Sol-gel Processed Zinc Oxide for Third Generation Photovoltaics

Elva Xin Zou
St. Cross College
30/03/2012



A thesis submitted for the Degree of

D.Phil. in Materials

University of Oxford

Abstract

This thesis presents an experimental study of the incorporation and optimization of sol-gel processed aluminum doped zinc oxide (AZO) thin films in solar cell devices.

I first optimized the optoelectronic properties of AZO thin films by manipulating the dopant incorporation, choice of precursor chemicals and post deposition anneal treatments. Results showed that improved performance could be attributed to several factors, including improved charge carrier concentration, mobility and conductivity. AZO thin films with transmittance of over 90% and resistivity values of the order of 10^{-2} Ω·cm have been achieved. I also demonstrated the successful application of these AZO thin films in organic photovoltaics (OPV), to serve as an alternative to ITO electrodes.

I demonstrated greater than 2-fold improvement in device efficiency through the modification of the front contact/polymer interface using zinc oxide buffer layers. This improved the charge selectivity of the electrodes and energy level alignment at the interface while reducing the recombination of separated charges and the device's series resistance.

Finally, I showed that the efficiency of inverted ZnO/PbS quantum dots solar cells can be enhanced by optimizing the *p*-type PbS thickness, UV treating the *n*-type ZnO layer and exposing the devices in the dark to nitrogen. Both ZnO and AZO systems were studied, and efficiency enhancement were demonstrated for a range of Al content from 0 to 0.4at.%.

Acknowledgements

First and foremost I want to thank my supervisors, Dr. Andrew Watt and Professor Chris Grovenor, it has been an honour and pleasure to work with you both. I am immensely grateful to all your guidance, discussions, and great contribution of time, ideas and effort to make my D.Phil experience productive and stimulating. The joy and enthusiasm you have for your research was contagious and motivational for me, even during the tough times in the pursuit of my D.Phil. I also thank you both for the exceptional work atmosphere you have fostered in the group and department.

I thank the Department of Materials for accepting me into the program and providing this valuable opportunity. I am very grateful to Oxford University for providing me with a Clarendon Scholarship and to the donors of the fund, and I am also thankful to the Clarendon Council that maximized my professional and social experience with scholars from various backgrounds.

Thank you to the members of the Solar Energy Materials Initiative group, who have contributed immensely to my personal and professional time at Oxford. I am very lucky to be part of such a fun-loving and supportive group, which has been a source of great friendships as well as good advice and collaboration. I am especially grateful to Jenna Holder, who is always there for me with a bright smile, thank you for the wonderful time we shared. I would like to acknowledge Cheng Cheng, for the collaboration on QDs devices. Thank you Peter Kovacik, I very much appreciated your enthusiastic discussions. Thank you Major Shawn Willis, for the excellent example you set, as a successful researcher and teacher. Thank you Laura Droessler, for setting up the abandoned SKP and your kind help, and also your talented ability to make any conversation enjoyable. Thank you Chris Cattley, for your very kind offer

in checking my first year report, and fun explanations of English terms and culture to me. I also thank Dr. Richard Beal and Dr. Alexandros Stavrinadis for showing me around the lab when I had just arrived. Other past and present group members that I have had the pleasure to work with: Christo, Tom, Daniel, Maria, Assia, Miriam, Anna, Lou and Shek. I would also like to thank our Engineering neighbours who have been very helpful and sociable: Di and Jay, thank you for the biscuits and coffee whenever I needed any.

I am grateful to Dr. Paul Warren for setting up all the computers and software, and Laurie Walton for the help in the machine workshop. Thanks go to Richard Turner and Dr. John Topping for help with odds-and-ends around the lab. I thank the EM group, Alison, Hugh, Clive, Gabriella and Sverre for advising me on the characterization equipment.

Special thanks go to Yanjun, for always being happy and being by my side with all the emotional support, continuous love, great entertainment and sound advice she provided. I wish to thank Lu, for his continuous encouragement, caring and camaraderie. I also want to thank all my other wonderful friends who have made life in Oxford enjoyable and sociable.

Finally, I thank my parents who raised me with lots of love and trust, and supported me in all my pursuits. I am very lucky and proud to have such wonderful, understanding, considerate and lovely parents. This is for you both.

Declaration of Originality

This thesis is an account of work carried out by the author under the supervision of Dr. Andrew Watt and Prof. Chris Grovenor, in the Materials Department, University of Oxford. Any work of others has been drawn upon this is duly acknowledged in the text, and a list of references is presented at the end of the thesis. No part of this thesis has been submitted towards the completion of another degree at this university or elsewhere. Parts of this thesis have been submitted or in preparation to the following scientific journals or conference proceedings:

Elva X. Zou, Chris R. M. Grovenor, Andrew. A. R. Watt, *Aluminium Doped Zinc Oxide – Conducting Polymer Composite Heterojunction Photovoltaics*, Conference Proceedings: Science and Technology of Synthetic Metals (ICSM), Japan. Oral presentation, July 2010.

Elva X. Zou, Chris R. M. Grovenor, Andrew. A. R. Watt, *Aluminium Doped Zinc Oxide – Conducting Polymer Composite Heterojunction Photovoltaics*, Conference Proceedings: The 17th Joint Conference of CSCST & SCI, Oxford. Oral presentation, October 2010.

Elva X. Zou, Chris R. M. Grovenor, Andrew. A. R. Watt, *Transparent Conductive Electrodes for Photovoltaics*, Conference Proceedings: Annual Meeting on Opto-Electronic Processes in Organic Materials, Oxford. Poster presentation, April 2011.

Elva X. Zou, Cheng Cheng, Chris R. M. Grovenor, Andrew. A. R. Watt, *Solution-Processed Photovoltaics Employing Doped Zinc Oxide*, Conference Proceedings:

Advances in Photovoltaics, Institute of Physics (IOP), London. Poster presentation, September 2011.

Elva X. Zou, Chris R. M. Grovenor, Andrew. A. R. Watt, *Improving the efficiency of inverted P3HT:PCBM solar cells by AZO buffer layer modification*, in preparation.

Elva X. Zou, Chris R. M. Grovenor, Andrew. A. R. Watt, *Thickness dependence of the aluminum doped zinc oxide buffer layers on inverted organic photovoltaic devices*, in preparation.

Elva X. Zou, Chris R. M. Grovenor, Andrew. A. R. Watt, *Preparation of aluminum doped zinc oxide films for the application of transparent conducting oxide in organic photovoltaic devices*, in preparation.

Table of Contents

Abstract i

Acknowledgements ii

Declaration of Originality iv

Table of Contents vi

List of Abbreviations xi

Chapter 1 – Introduction 1

1.1 Motivation 1

1.2 Historical Background 2

1.3 The State of the Art 3

1.4 Roles of Zinc Oxide Materials 5

1.5 Thesis Outline 7

Chapter 2 – Photovoltaic Device Operation and the Incorporation of Zinc Oxide 8

2.1 Conventional Photovoltaic Devices 8

2.2 Organic Photovoltaic Devices 10

2.2.1 Device architecture and working principle of organic solar cells 10

2.2.2 Homojunction organic solar cells 12

2.2.3 Heterojunction organic solar cells 14

2.3 Properties of ZnO 16

2.3.1 Crystallographic properties of zinc oxide 16

2.3.2 Optoelectronic properties of zinc oxide 19

2.3.3 Doping of zinc oxide 22
2.3.4 Aluminum-doped Zinc Oxide (AZO) 24
2.4 Growth of ZnO Thin Films 28
2.4.1 Early technologies 28
2.4.2 Sol-gel technique 29
2.4.3 Spin coating 31
Chapter 3 – Experimental Techniques 33
3.1 Photovoltaic Device Fabrication 33
3.1.1 Substrate cleaning 33
3.1.2 AZO fabrication by sol-gel processing 33
3.1.3 ITO/AZO patterning 35
3.1.4 PEDOT:PSS and polymer layer deposition 36
3.1.5 Metal electrode deposition 38
3.1.6 Thermal annealing 39
3.2 Materials Characterization 40
3.2.1 Dektak profilometry measurements 40
3.2.2 X-ray diffraction (XRD) 40
3.2.3 Atomic force microscopy (AFM) 41
3.2.4 X-ray photoelectron spectroscopy (XPS) 42
3.2.5 Scanning electron microscopy (SEM) 43
3.3 Optoelectronic Characterization 43

3.3.1 UV-Visible absorption spectra....43
3.3.2 Four-point probe resistivity measurements....45
3.3.3 Hall carrier and mobility measurements....47
3.4 Photovoltaic Device Testing and Characterization....48
3.4.1 Current-voltage (IV) measurements....48
3.4.2 External quantum efficiency (EQE) measurements....50
Chapter 4 – Aluminium Doped Zinc Oxide for the Application of Transparent Electrode in Organic Solar Cells....52
4.1 Introduction....52
4.1.1 Transparent conducting oxides (TCO)....52
4.1.2 P3HT:PCBM solar cells employing sol-gel processed AZO....55
4.2 Experimental Details....56
4.2.1 AZO thin film preparation and characterization....56
4.2.2 Device fabrication and characterization....57
4.3 Results and Discussion....58
4.3.1 The influence of Al doping concentration on the properties of AZO thin films....58
4.3.2 The influence of precursor solution concentration on the properties of AZO thin films....71
4.3.3 The influence of post-annealing on the properties of AZO thin films....75
4.3.4 Solar cell efficiency characterization....81
4.4 Conclusion....85

Chapter 5 – The Improvement of Organic Solar Cell Performance by Introducing Interfacial Buffer Layers 87

5.1 Introduction 87

5.1.1 The role of buffer layers 87

5.1.2 Material selection for buffer layers 88

5.1.3 Inverted organic solar cells and their advantages 97

5.1.4 The limitation of inverted device architecture and potential improvements 99

5.2 Experimental Details 103

5.2.1 EIL deposition and characterization 103

5.2.2 Device preparation 103

5.2.3 Device testing 104

5.3 Results and Discussion 104

5.3.1 Characterization of various ZnO cathode buffer layer materials 104

5.3.2 A comparison of various ZnO cathode buffer layers 111

5.3.3 Characterization of AZO buffer layer materials of various thicknesses 118

5.3.4 Thickness optimization of the AZO cathode buffer layers 124

5.4 Conclusion 130

Chapter 6 – Solution-processed Inverted ZnO/PbS Heterojunction Quantum Dot Solar Cells 132

6.1 Introduction 132

6.1.1 The application of solution processed ZnO as junction layer 132

6.1.2 PbS QDs and their synthesis 134

6.1.3 Inverted ZnO/PbS heterojunction devices 136

6.2 Experimental Details 141

6.2.1 The deposition of ZnO thin films on ITO substrate 141

6.2.2 Synthesis and LBL deposition of PbS quantum dots 142

6.2.3 The fabrication of the back electrode 145

6.2.4 Material characterization and device testing 145

6.3 Results and Discussion 146

6.3.1 Size and energy band gap of the PbS QDs 146

6.3.2 Thickness optimization of the *p*-type PbS QDs layer 148

6.3.3 The influence of Al-doping concentration in the ZnO film on the device performance 156

6.3.4 The influence of UV exposure on the device performance 159

6.3.5 The influence of N_2 exposure on the device performance 161

6.4 Conclusion 166

Chapter 7 - Summary 167

7.1 Conclusion 167

7.2 Suggestions for Future Investigations 169

Bibliography 171

List of Abbreviations

A	Electron acceptor
AFM	Atomic force microscopy
Ag	Silver
Al	Aluminium
AM1.5	Air mass 1.5
Au	Gold
BHJ	Bulk-heterojunction
Ca	Calcium
ca.	Approximately
CB	Chlorobenzene
CdTe	Cadmium telluride
CIGS	Copper indium gallium diselenide
CQD	Colloidal quantum dot
CuSCN	Copper thiocyanate
D	Electron donor
e^-	Electron
EDXD	Energy-dispersive x-ray diffraction
E_F	Fermi energy
E_f	Formation energy
E_g	Electrical band gap energy
eg.	For example
EQE	External quantum efficiency
ESRF	European synchrotron radiation facility
et al.	and the rest
etc.	and so on
FF	Fill factor
Ga	Gallium
h^+	Hole
HOMO	Highest occupied molecular orbital
HWHM	Full width at half maximum
i.e.	that is
IEA	International energy agency
In_2O_3	Indium oxide
I_{sc}	Short circuit current
ITO	Indium-tin oxide
J_{sc}	Short circuit current density
LCAO	Linear combination of atomic orbitals
LED	Light emitting diode
LiF	Lithium fluoride
LUMO	Lowest unoccupied molecular orbital
MDMO-PPV	Poly(2-methoxy-5-(3'-7'-dimethyloctyloxy)-1,4-

	phenylenevinylene)
MEH-PPV	Poly[2-methoxy-5-(2’-ethylhexyloxy)-p-phenylene vinylene]
Mg	Magnesium
MoO_x	Molybdenum oxide
n	Carrier concentration
N_a	Acceptor concentration
NC	Nanocrystal
N_d	Donor concentration
nm	Nanometer
NREL	National Renewable Energy Laboratory
OLED	Organic light emitting diodes
OPV	Organic Based Photovoltaic
P3HT	Poly(3-hexylthiophene)
PbS	Lead sulphide
PCBM	[6,6]-Phenyl-C61 butyric acid methyl ester
PCE	Power conversion efficiency
PEDOT:PSS	Poly(3,4-ethylenedioxythiophene) : poly(styrenesulfonate)
PV	Photovoltaic
QD	Quantum dot
RMS	Root mean square
R_s	Series resistance
R_{sh}	Shunt resistance
R_{sheet}	Sheet resistivity
SnO_2	Tin dioxide
TCO	Transparent conducting oxide
TEM	Transmission electron microscopy
TiO_2	Titanium dioxide
UV-Vis	Ultraviolet-Visible
V_{bi}	Built-in voltage
V_{oc}	Open circuit voltage
XPS	X-ray photoelectron spectroscopy
XRD	X-ray Diffraction
ZnO	Zinc oxide
ρ	Resistivity
ω	Depletion width
μ	Mobility
ε	Permittivity
Ω	Ohm

Chapter 1 – Introduction

1.1 Motivation

The increase in the world's energy demand and the international recognition of global warming are driving growing academic and industrial effort to replace conventional fossil fuels with alternative energy sources which are more environmentally, economically and politically favourable. Fossil fuels are being consumed at a breath-taking rate and it is estimated that resources will start to run out in the next 50 years.[1] At the same time, the combustion of fossil fuels has harmful effects on the delicate balance of life on earth. Over 20 teratons (10^{12} tons) of carbon dioxide is released into the atmosphere each year by burning fossil fuel, which accelerates the greenhouse effect.[2] The International Energy Agency (IEA) reported in 2011 [3] that around 20% of the world's population do not have access to electricity and ~85% of these people live in rural areas (Figure 1.1), requiring energy sources that do not rely on grid connection. These facts urge humanity to search for clean and renewable energy alternatives for a low-carbon future.

One promising solution is to utilise solar energy in photovoltaic devices. Becquerel first noted the photovoltaic effect in 1839 when he observed that certain materials produce an electric current when exposed to light.[4], [5] Photovoltaic devices take semiconducting materials with good optical absorption properties and make junctions with other semiconductors. These junctions create a potential difference which can sweep charge carriers generate by the absorption of light without the need to apply an external field.

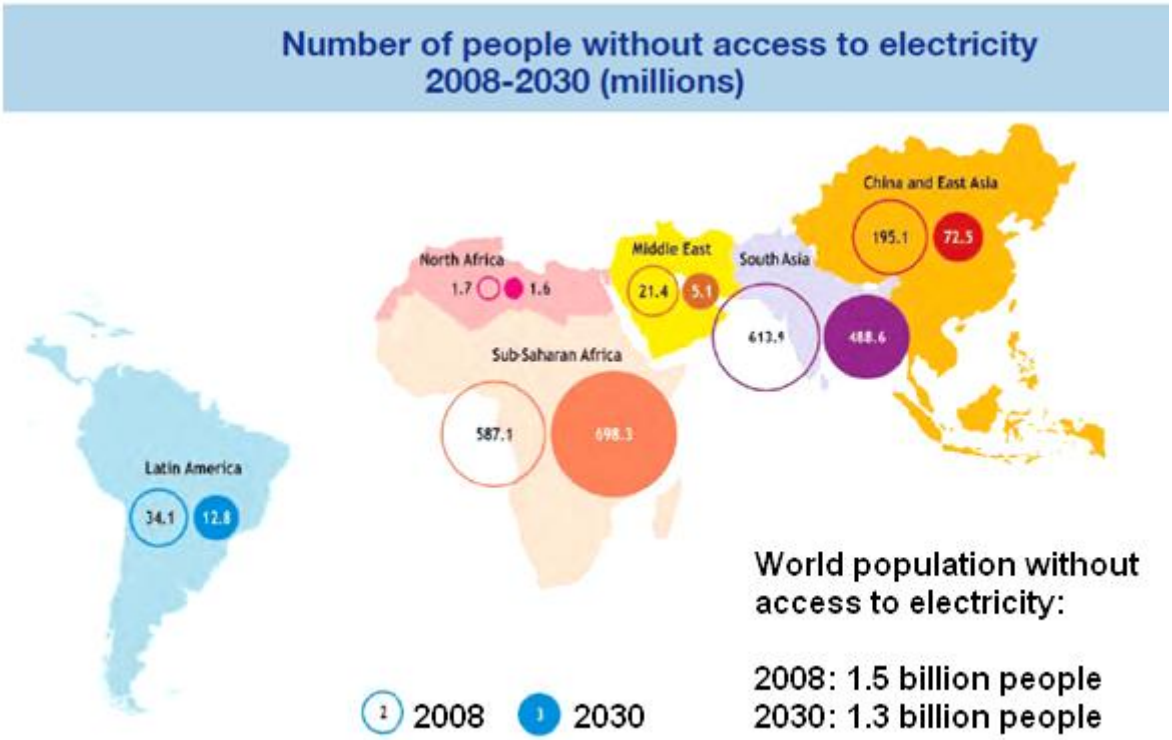


Figure 1.1. The IEA estimates that, in 2008, there were 1.5 billion people, 22% of the world's population, who do not have access to electricity, and 85% of these people live in rural areas. Note: the boundaries and names shown and the designations used on maps included here do not imply official endorsement of acceptance by the IEA.(after reference [6]*)*

1.2 Historical Background

The abundance of solar energy is clearly shown in Figure 1.2, yet the wider deployment of conventional inorganic based technologies remains constrained by expensive starting materials and fabrication requirements making them a less attractive proposition than more traditional hydrocarbon energy technologies. As such, the fortune of the photovoltaic industry has been volatile, depending on governmental policy to provide subsidies to establish economical viability. In order for photovoltaics to impact the global energy markets it requires scientists and engineers to develop new high-performance and low-cost photovoltaic technologies.

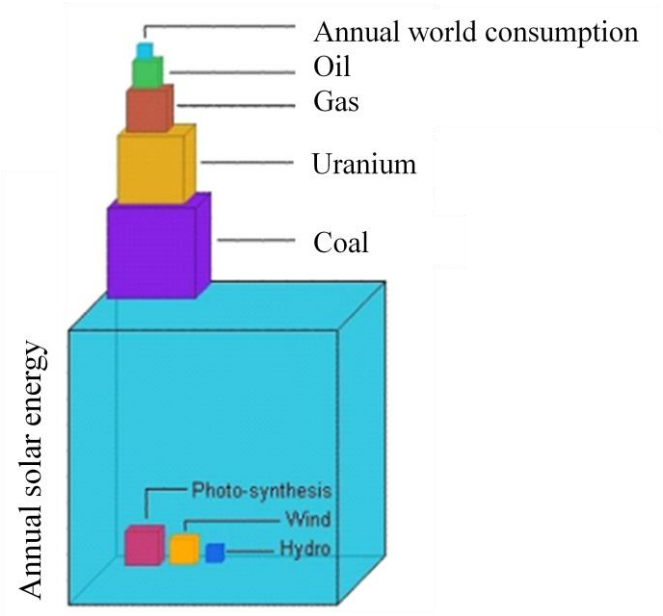


Figure 1.2. The WEC (world energy council) estimation of energy demand (~20 terawatts, TW, 1TW = 10^{12}W) and the energy supply.(after reference [6]*)*

Three generations of solar cells currently exist, based on silicon wafers, thin film technology (such as cadmium telluride, CdTe and copper indium gallium diselenide, CIGS) and emerging thin film technologies (such as organic molecules and quantum dots, QDs) respectively.[7] Silicon based solar cells dominate the market and typically have power conversion efficiency of 10~20% in commercial devices. However, these traditional photovoltaic panels rely on high temperature, high vacuum, batch-based manufacturing technology that is complex and cost-intensive. A transformative approach is third generation thin film solution-processed photovoltaics which are cost-effective and highly-versatile in converting solar energy into affordable electricity.

1.3 The State of the Art

Organic solar cells (OSCs) have attracted much attention in the past decade as an alternative clean energy source as they can be fabricated from relatively cheap materials in

large areas onto flexible substrate via roll-to-roll printing techniques.[8] They have the advantages of being transparent, light weight, variable band gap and have the freedom of product design for a wide range of applications.[9] These significant advantages demonstrate that OSCs are a promising avenue to low cost next generation renewable energy.

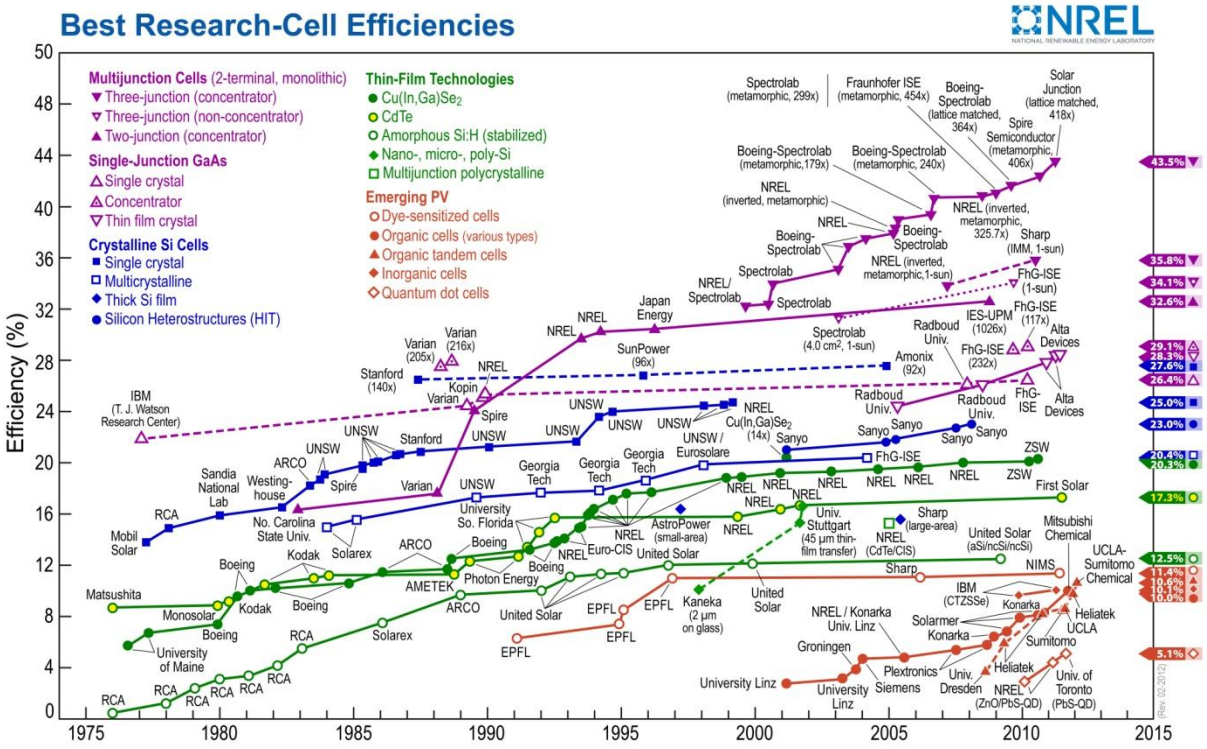


Figure 1.3. Conversion efficiencies of the best research solar cells worldwide from 1976 through 2011 for various photovoltaic technologies; efficiencies determined by certified agencies/laboratories.[10] *(Reprinted from reference* [11]*)*

One challenge for organic solar cells is their low power conversion efficiency; the maximum power conversion efficiency (PCE) of polymer solar cells must rise above 15% in the laboratory (corresponding to a module efficiency of ~10-12%) before they can become practically useful.[12] Thus, tremendous efforts have been devoted to improve the power conversion efficiency over the last decade. Today, solution processed polymer solar

cells with power conversion efficiencies from 3% to almost 9% have been accomplished with either new materials or novel device optimization concepts.[12–20] In particular, a recent NREL-certified solution processed tandem cell with PCE of 10.6% was demonstrated (Figure 1.3).[11]

1.4 Roles of Zinc Oxide Materials

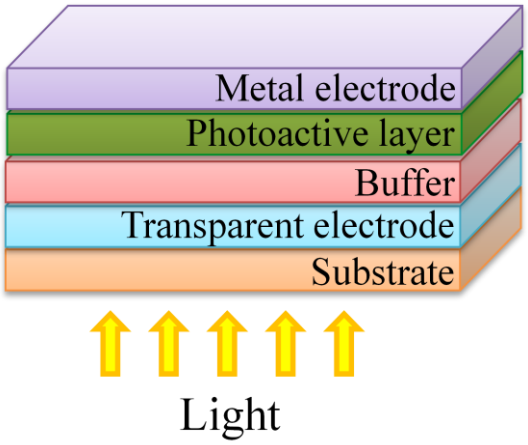


Figure 1.4. A schematic representation of a typical device structure of thin film solar cells. The active layer may comprise of one or more semiconducting layers, a blend or a combination of these.

Figure 1.4 shows the device structure of a typical organic/quantum dot device. Photons are absorbed by the active thin film layer (organic or quantum dots) generating a bound electron-hole pair (exciton). The electron-hole pairs are then separated and transported to respective electrodes and into the external circuit generating a direct current (DC). Zinc oxides, intrinsic or doped, can play a number of different roles in thin film photovoltaics. The examples addressed in this thesis are introduced here:

Transparent electrodes For incident light to be transported to the photoactive layer, at least one of the electrodes must be transparent in devices where carrier conductivity and mobility are low. Such transparent electrodes can be made using transparent conducting oxides (TCOs). The most widely used TCOs are tin-doped indium oxide (ITO) and fluorine-doped tin oxide (FTO). Other materials, such as aluminum-doped zinc oxide (AZO) have attracted remarkable interest during the last decade as an alternative owing to its comparable optoelectronic properties, chemical functionality and wider availability as compared with ITO.[21] An in-depth investigation on the fabrication and characterization of AZO transparent electrodes and their application in organic solar cells is presented in Chapter 4 of this thesis.

Buffer layers One primary cause of inefficiency in PV devices stems from leakage current, which is a result of reduced photocurrent due to charges generated in the device recombining with those injected by the electrodes. This problem is especially significant in organic devices, where a bulk heterojunction consisting of a blend of donor/acceptor materials leads to the direct contact of both active materials to both electrodes. This problem can be addressed by inserting a buffer layer between the active layer and the electrodes, which favors the transport of electrons and blocks holes, or vice versa. This helps to make the electrodes more selective by directing the charges towards their respective electrode, therefore reducing recombination and leading to improved photocurrent generation.[22] AZO thin films have just started to be used as a buffer layer in inverted OPV devices.[23] To the best of my knowledge, no study has yet explored how the AZO buffer layer thickness influences device performance, and this is addressed in Chapter 5.

Junction materials Junction materials form electric fields at the interface with the photoactive semiconductor. Light absorbed by the photoactive layer in PV devices,

creates electron-hole pairs, which remain bound as an exciton until a potential difference separates them. The two main modes for charge carrier separation in a solar cell are drift and diffusion. In excitonic devices, such as most polymer devices, diffusion of excitons due to random thermal motion dominates until they are either dissociated by the electrical fields existing at the edges of the photoactive region (the interfaces of electrode/photoactive polymer in homojunction devices or donor/acceptor in heterojunction devices). In *p-n* junction devices, such as most silicon devices, drift of charge carriers driven by an electric field established at junction region (i.e. space charge region) dominates the charge separation process. Some oxide/quantum dot (QD) devices arguably exhibit both excitonic and *p-n* junction behavior, depending on the doping present in the oxide.[24] In Chapter 6 of this thesis, a comprehensive investigation on manipulating ZnO junction material in order to improve inverted oxide/QD device performance is presented.

1.5 Thesis Outline

Following from and adding to this brief discussion of PV materials and devices, Chapter 2 examines the operation of various device architectures and some fundamental knowledge of transparent conducting oxides. This is to provide some technical background for, and to highlight the importance of, the areas investigated in the course of this work. Chapter 3 discusses the experimental methods and techniques used. The following chapters then describe the use of ZnO as a transparent electrode, buffer layers and junction materials.

Chapter 2 – Photovoltaic Device Operation and the Incorporation of Zinc Oxide

This chapter introduces the basic device design and operation of solar cells, giving an in-depth review of the rapidly developing PV field. The state of the art of conventional solar cells is introduced first, to provide some operational understanding of the commercial devices. The fabrication and properties of organic solar cells are then explained to demonstrate their promising potential. Finally, the properties and processing of aluminium doped zinc oxide (AZO) in solar cell devices are explained, including its fundamental structural and physical properties, the nature of the doping process to generate conductivity, and the most up-to-date advances reported in the literature.

2.1 Conventional Photovoltaic Devices

Most solar cells in commercial production today, including silicon solar cells as discussed in Chapter 1 that currently enjoy the largest PV market share (~80%),[25] operate based on a *p*-*n* junction,[26] and this is also the mechanism that produces the highest performing cells. While the *p*-*n* junction classification is broad, including *p*-*n* homojunction, *p*-*n* heterojunction and a wide selection of materials and device architectures, the basic operation mechanism of all *p*-*n* junction devices is the same.

In both homojunction (oppositely doped, same semiconductor material) and heterojunction (oppositely doped, different semiconductor materials) devices, a *p*-*n* junction is formed when *p*-type and *n*-type semiconductor layers are brought into contact. The discontinuity in the Fermi level at the interface between the two semiconductors will cause the flow of

charge across this interface until the Fermi levels on both sides are equal. This generates an excess of negative charges in the *p*-type semiconductor and an excess of positive charges in the *n*-type semiconductor, creating an electric field pointing from the *n*-type semiconductor to the *p*-type semiconductor.

Under illumination, photons absorbed in either the *p*- or *n*-type semiconductor generate electron-hole pairs. These electrons and holes can (i) recombine with each other (geminate recombination), (ii) recombine with other electrons and holes (bimolecular recombination), or (iii) diffuse to the *p*-*n* junction interface. In case (iii), the electric field present at *p*-*n* junction interface will sweep photogenerated electrons to the *n*-type material and holes to the *p*-type material, where they both become majority carriers. The electrons and holes must then migrate through the *n*- and *p*-type layer to their respective electrode, where they travel through the external circuit and recombine eventually. This process completes the circuit and therefore generates electricity. Figure 2.1 displays the simple case of *p*-*n* homojunction as an illustration.

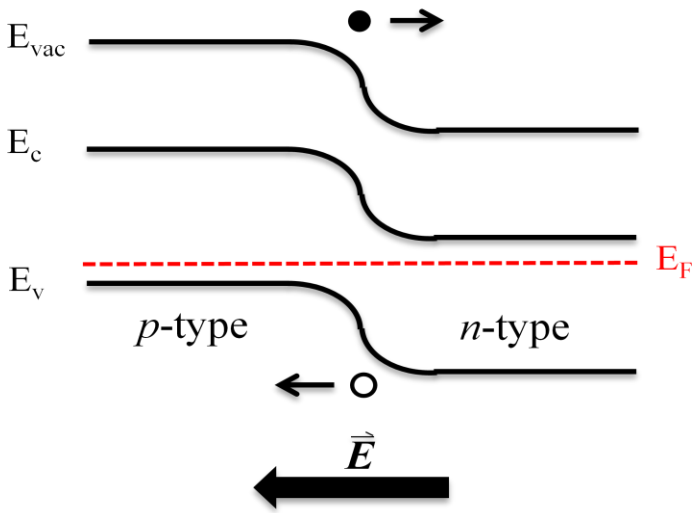


Figure 2.1. A schematic illustration of energy level diagram of a p-n homojunction in equilibrium.

2.2 Organic Photovoltaic Devices

As discussed in Chapter 1, organic solar cells are attracting considerable scientific and economic interest as a promising route to capture sunlight to generate low-cost renewable energy, as the power conversion efficiencies have been steadily increasing since the introduction of the donor-acceptor device concept by Tang.[27] To this end, although power conversion efficiency in excess of 10% have been accomplished (as mentioned in Chapter 1), this value is still far from that of their inorganic counterparts (10–20%). Nevertheless, the possibility of low-cost and flexible production drives the development of organic photovoltaic devices in a dynamic way. In the following sections, I briefly introduce the basic physics of organic photovoltaic devices and review the device architectures.

2.2.1 Device architecture and working principle of organic solar cells

The most simple organic solar cell device can be constructed by sandwiching an organic active layer between two electrodes: one with a higher work function (anode) for hole collection and one with lower work function (cathode) for electron collection, as shown in Figure 2.2a. The organic materials are primarily molecules or extended delocalized π -electron systems or conjugated polymer-based materials. The anode materials are normally transparent metal oxides with combined properties of high conductivity and transparency in the visible regime as well a higher work function. Aluminium or magnesium-silver alloys with a lower work function are normally used as the cathode for electron-injecting electrodes.

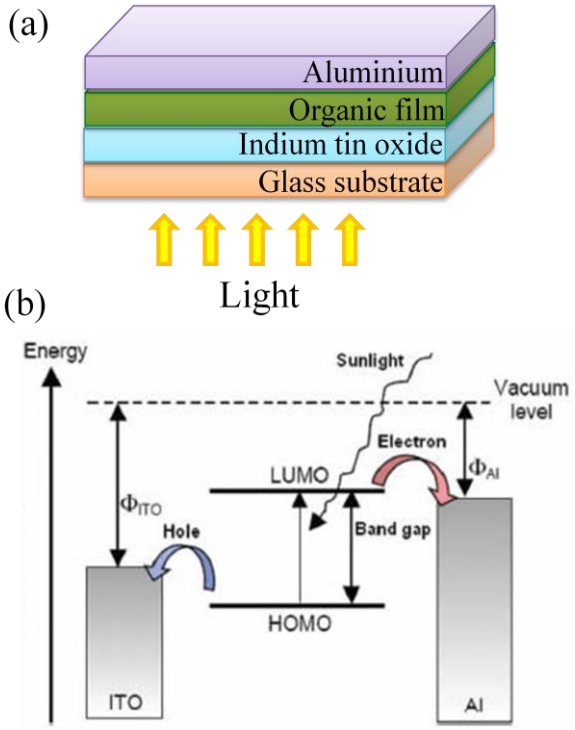


Figure 2.2. Device structure of a typical organic solar cell (a) and its working principle (b, reprinted from reference[28]*).*

Figure 2.2b shows the basic working principle of an organic photovoltaic cell. Generally, the process of converting light into electric current is accomplished by four consecutive steps: (i) Absorption of a photon leading to the formation of an excited state, the electron-hole pair (exciton). (ii) Exciton diffusion to a region, where (iii) charge separation occurs. Finally, (iv) charge transportation to the anode (holes) and cathode (electrons), to supply a direct current for the consumer load. Unlike inorganic materials, the interactions between organic materials are primarily weak intermolecular van de Waals forces; this results in the electronic states being localized on individual molecules, rather than forming a continuous band. Thus the diffusion of charges in organic species is based on a hopping mechanism. Consequently, organic materials have relatively lower mobility and very short diffusion lengths. Furthermore as the exciton binding energy in organic semiconductors is generally large (0.1–2 eV)[29], [30] compared to those of inorganic

semiconductors, the built-in electric field (in the order of 10^6 - 10^7 V/m) is usually not high enough to dissociate the excitons directly.[31] Hence, a process has to be introduced to efficiently separate the bound electron-hole pairs. This can be achieved by deliberately designing the device architectures. In the following sections, we will review two basic device architectures and examine their advantages and disadvantages. Their main difference lies in the exciton dissociation or charge separation process, which occurs at different locations within the photoactive layer.

2.2.2 Homojunction organic solar cells

A homojunction is the simplest device structure for PV applications, including organic solar cells. It is based on a structure consisting of two electrodes with an organic material (active layer) sandwiched in between (as shown in Figure 2.3).

The active layer is responsible for generating excitons by absorbing photons with energies larger than its band gap. However, the generated excitons can only diffuse for very short distances (1-10nm)[32] and they have a strong possibility to radiatively recombine rather than to form free carriers.[33] Only those excitons generated within a distance of their diffusion length from the electrode-organic interfaces can dissociate into free carriers. Excitons in organic materials are difficult to separate (~100 meV is needed, compared to a few meV in crystalline semiconductor materials). Moreover, organic materials are generally less ordered and this makes their mobility even lower. Combined with other factors such as the exciton recombination taking place at impurities and interface traps, homojunction organic solar cells have very limited efficiencies.

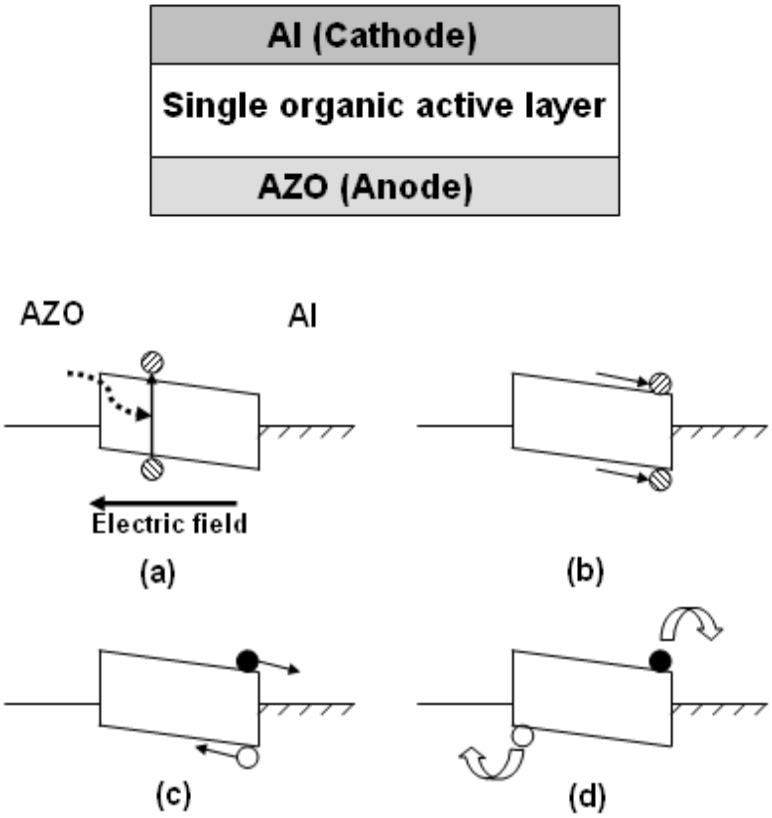


Figure 2.3. An illustration of a typical homojuction organic solar cell consisting of two electrodes with a single organic active layer in between, and its energy band diagrams (a-d). Upon contact, there is an electric field generated by the difference in the work function between the two electrodes, ~ 4.7 eV for AZO and ~4.2 eV for Al. The actual work function depends on many factors including morphology, oxidation etc. Photon energy can be absorbed by the active layer and therein generate an exciton (a). The exciton can diffuse to one or another electrode (b) before it can dissociate at the metal-organic interface to yield a charge carrier pair consisting of an electron and a hole (c). Driven by the electric field, the electron diffuses to the cathode (Al) while the hole diffuses to the anode (AZO) (d).

Consequently, the following considerations need to be specifically addressed to improve organic solar cells. Firstly, thinner films are required to compensate for the low mobility and short diffusion length. Secondly, a large driving force such as an electric field is necessary to assist the transition from exciton to charge carriers (i.e. charge separation), as well as to promote the diffusion of charge carriers (charge transportation). Both of these two factors can be better achieved in the so-called heterojunction organic solar cells.

2.2.3 Heterojunction organic solar cells

Heterojunction devices utilize electron donor and accepter materials to enhance charge separation (Figure 2.4).[34] The electron donor material has a lower electron affinity and ionization energy compared to the electron acceptor material, and thus is prone to donate electrons. At the donor-accepter interface a large electric field is built up capable of dissociating excitons as long as the potential difference is larger than the exciton binding energy. Particularly in some high purity devices, such significant enhancement in charge separation can greatly improve the overall cell efficiency.

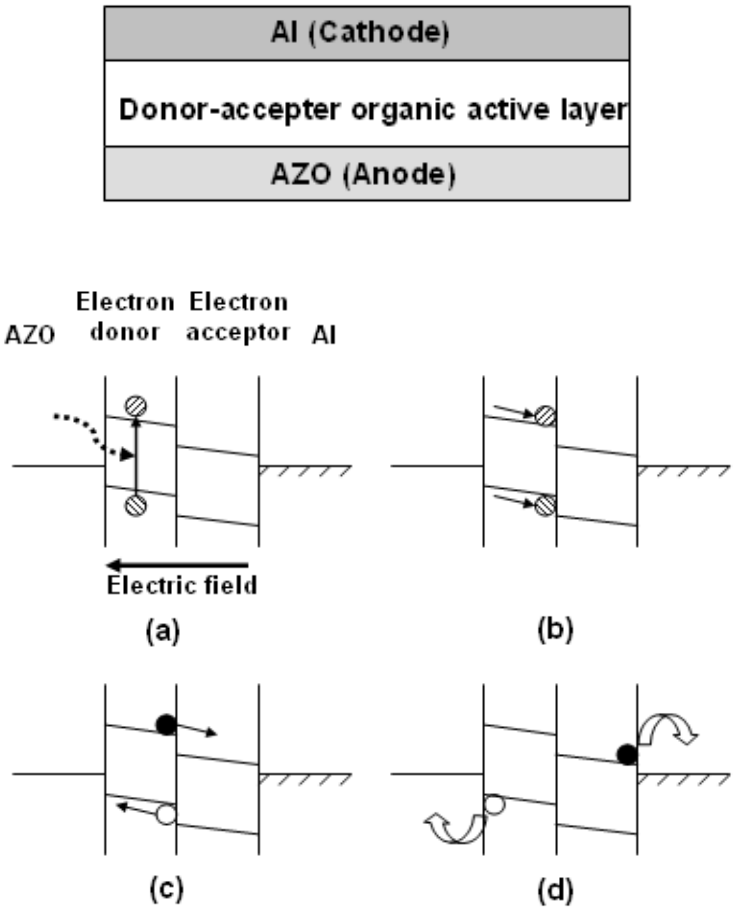


Figure 2.4. An illustration of a typical heterojuction organic solar cell consisting of two electrodes with an electron donating and accepting structure sandwiched in between, together with its energy band diagrams (a-d). The physics of the device working principle is similar to that of a homojunction device (refer to the explanations in Figure 2.3). The difference lies in the more efficient charge separation at the donor-acceptor interface, as compared to the charge separation that takes place at the metal-organic interface in a homojunction device.

Bulk heterojunction solar cells

Further efficiency enhancement was realised by blending the electron donating and accepting materials, namely the dispersed or bulk heterojunction device (Figure 2.5). Yu *et al.*[35] and Halls *et al.*[36] in 1995 reported greatly improved device efficiency by using composite structures. In 1997, Yoshino *et al.*[37] reported a further improved PV performance by using tri-layer structure with donor-acceptor blending.

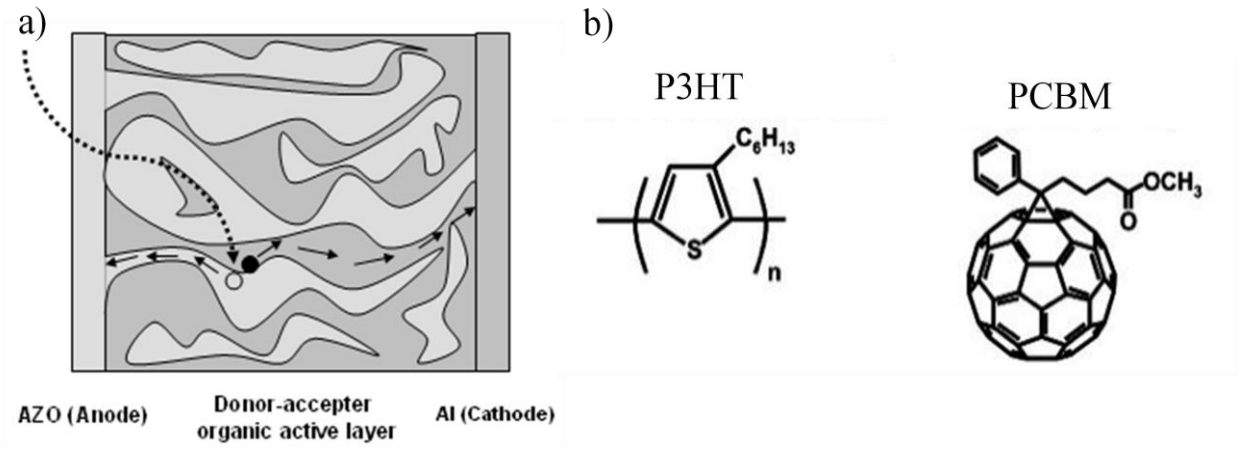


Figure 2.5. An illustration of a dispersed heterojunction device consisting of blended electron donor and acceptor materials (a), and an example of one of the most commonly used material systems – P3HT:PCBM (b). An exciton is generated by the incident photon and dissociation takes place at the readily available interface. With continuous pathways (preferably perpendicular to the electrodes) for both electrons and holes, they are transported to their respective electrodes effectively. Otherwise, recombination can take place and decrease the efficiency of photocurrent collection. Note that it is a challenge to control the degree of dispersion, as uniform blending at exciton diffusion length scale without significant segregation is necessary for photocurrent generation, while continuous pathways from interface to electrode are necessary for photocurrent transportation.

The most significant advantage of dispersed heterojunction devices is the enhanced exciton dissociation into free charge carriers at the readily available donor-acceptor

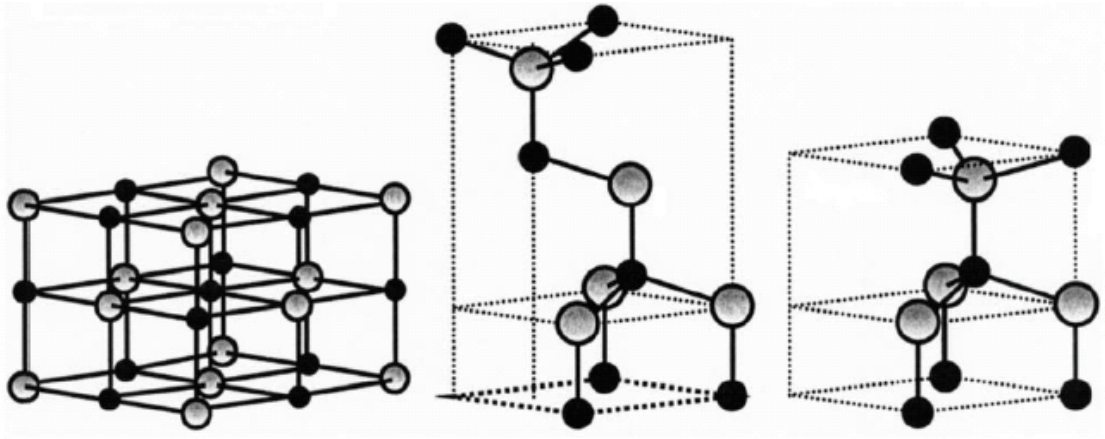
interfaces. Two positive effects are achieved by blending the donating and accepting organic materials. Firstly, length scale of both the donor and acceptor is reduced. Secondly, the amount of interface is increased. For the first effect, as long as the length scale of the individual phase is in the same order as the exciton diffusion length, theoretically, all the excitons can diffuse to the donor-accepter interfaces for dissociation. For the second effect, the increased amount of interfaces with electrostatic force provides much higher driving force for charge separation.

If the blended donating and accepting materials can form a continuous path to their corresponding electrodes, the separated charge carriers can then be more efficiently transported to their respective electrodes with very reduced losses. Therefore the dispersed heterojunction device offers improved performance.

2.3 Properties of ZnO

2.3.1 Crystallographic properties of zinc oxide

Like most group II-VI binary compound semiconductors, ZnO can crystallize into the wurtzite, zinc blende, or rocksalt structures, as illustrated in Figure 2.6. The wurtzite structure is the most thermodynamically stable phase at ambient conditions, where each cation is surrounded by four anions located at the corners of the tetrahedron, and vice versa. By repeating this arrangement, a hexagonal wurtzite structure is formed. Although this tetrahedral coordination is normally sp^3 covalently bonded, at the same time it is accompanied by some substantial ionic character. Thus, ZnO has an ionicity somewhere in between that of a typical covalent and ionic semiconductor.



(a) rocksalt (b) zinc blende (c) wurtzite

Figure 2.6. Stick and ball representations of ZnO crystal structures: (a) cubic rocksalt, (b) cubic zinc blende, and (c) hexagonal wurtzite. The shaded gray and black spheres denote Zn and O atoms respectively (reprinted from reference [38]*).*

2.3.1.1 ZnO wurtzite lattice parameters

Table 2.1. Measured and calculated lattice parameters a and c of wurtzite ZnO structures (Reprinted with modification from reference [38]*).*

***a* (Å)**	***c* (Å)**	***c/a***	**Method**	**reference**
3.2496	5.2042	1.6018	Measured by using XRD	[39]
3.2501	5.2071	1.6021	Measured by using XRD	[40]
3.2860	5.2410	1.5950	Calculated by using LCAO method	[41]
3.2498	5.2066	1.6021	Measured by using EDXD	[42]
3.2475	5.2075	1.6035	Measured by using XRD	[43]
3.2497	5.2060	1.6020	Measured by using powder XRD	[44]

The hexagonal unit cell of the ZnO wurtzite structure is characterized by its lattice parameters, *a* and *c*. The ratio of *c/a* is equal to $(8/3)^{1/2}$ for an ideal ZnO wurtzite structure and the exact values of *a* and *c* as suggested by different researchers are listed in Table 2.1. The difference in lattice parameters (either experimental or theoretical values) is likely to be the result of three major mechanisms, the difference in the lattice stability and ionicity, lattice expansion induced by free charges, and lattice defects (point defects such as oxygen vacancies and zinc interstitials and line defects such as dislocations). Despite these minor deviations from the ideal crystal lattice, it is well accepted that the value of parameter *a* is ~3.2 Å, and that of *c* is ~5.2 Å.

2.3.1.2 Other ZnO crystal structures

ZnO wurtzite structure may be reversibly transformed to the rocksalt structure by applying an external hydrostatic pressure.[42] This is caused by a reduction of the lattice parameters, which enhances the inter-ionic coulomb interaction. This provides a much stronger ionicity character than covalent character and results in the rocksalt structure.[38]

The other ZnO crystal structure, zinc blende, is metastable and can only be obtained by heteroepitaxial growth on existing cubic substrates or buffer layers such as ZnS.[45] Because ZnO has a tendency to form a thermodynamically stable wurtzite structure, the zinc blende phase grown on highly mismatched substrates is normally separated from the wurtzite phases. The zinc blende phase is also tetrahedrally coordinated, that is there are four atoms per unit cell and each group II atom is surrounded by four group VI atoms, and vice versa. The major difference between the wurtzite phase and the zinc blende phase lies in the stacking sequence of the close packed planes. For the wurtzite structure, the

stacking sequence of the close packed (0001) planes has an ABAB… pattern in the <0001> direction, whereas for the zinc blende structure, the stacking sequence of the close packed (111) planes has an ABCABC… pattern in <111> direction.

2.3.2 Optoelectronic properties of zinc oxide

2.3.2.1 Optical properties

The transmittance of ZnO in the visible region can be as high as ~90% [46] owing to its wide semiconducting band gap (~3.3eV). This is important for applications such as solar cells, because light energy (photons) can be effectively delivered to the photoactive region for charge creation. However, photon energy transmittance can be limited by the onset of a high reflectivity below the conduction electron plasmon frequency, which is determined by the carrier concentration. Since a typical carrier concentration of 10^{20} is generally obtained in AZO thin films,[47], [48] the low energy absorption is in the infrared regime.[49], [50]

In addition, the morphology, texture and thickness of the films can affect transmittance.[51] Habibi *et al.*[52] suggested films with rough and porous surfaces combined with large cluster grains have much lower transmittance, resulting from the enhanced scattering events. Thicker films can result in decreased transmittance due to scattering as well.

2.3.2.2 Electrical properties

Stoichiometric zinc oxide is a transparent insulator, owing to its wide band gap energy.[46], [53] However, it usually demonstrates a high electron concentration and thus

electrical conductivities owing to deviation from its stoichiometric state. Undoped ZnO exhibits *n*-type semiconductor characteristics due to unintentional doping. It has been shown that both intrinsic (oxygen vacancies, Zn interstitials) and extrinsic defects (hydrogen) induce shallow impurity states close to the bottom of the conduction band of ZnO and act as electron donors.[54] The concentration of defects in the ZnO lattice is related to their formation energy E_f by:

$$c = N \exp\left(-\frac{E_f}{k_B T}\right) \qquad \text{Equation 2.1}$$

where N is the concentration of the defect sites. One can conclude from this equation that a low formation energy results in a high defect concentration and vice versa. Kohan *et al*.[55] and Walle [56] have calculated the formation energy by using a first principles approach. It was suggested that the oxygen vacancy has a lower defect formation energy than the zinc interstitial, and thus should be present in larger amounts inside the ZnO lattice, especially in zinc-rich conditions. In contrast, zinc vacancies should form preferentially in oxygen-rich conditions, because of its relatively low defect formation energy. The first principles calculations of hydrogen in ZnO have shown a unique result. While it usually present as H^+ in *p*-type materials and H^- in *n*-type materials, hydrogen is found exclusively present in ZnO as positive charge state (H^+) and always act as a donor.[56] Owing to the low formation energy of hydrogen in ZnO, the O-H bond can be easily formed by the strong bonding between H and O atoms.

Having described the formation of defects in ZnO, one may ask what role the defects are playing and how these defects can act as donors in the ZnO crystals. This has been an

intensively debated research topic for the last decade. It is generally accepted that excess zinc at interstitials and loss of oxygen are the most common donors. Zinc interstitials and oxygen vacancies have ionization energies of about 30-50meV[57–60] and ~140-500meV[61], [62] respectively, thus they can be easily activated. However, Look *et al.* [63], [64] have pointed out that rather than oxygen vacancies, the zinc interstitial is the major native donor in undoped ZnO. Even more controversially, Kohan *et al.*[55] have carried out an in-depth first principles study and have pointed out that none of the native defects (oxygen vacancy or zinc interstitial) can result in high-concentration donor characteristics. Instead, some researchers [55], [56], [65], [66] suggest that only hydrogen with ionization energy of about 30 meV can act as a shallow donor and thus induce the *n*-type behavior for undoped ZnO. This suggestion was justified by claiming that hydrogen is always present in all growth methods and due to its good mobility can easily diffuse into the growing thin film in a relatively large amount. They behave like shallow donors in ZnO and are the origin of the high conductivity of undoped ZnO, as also suggested by first principles studies by Walle.[67]

The conductivity of undoped ZnO is not stable, since pure ZnO thin films are very sensitive to oxidation. Degradation of electrical conductivity is possibly induced by the reduction of oxygen vacancies by the adsorption of oxygen in the ZnO films. Intentional and substitutional Al or Ga doping of ZnO provides one of the most effective ways to obtain highly conductive and stable ZnO electrodes and has attracted intense research interests in recent years.[68], [69] In the following section, we will discuss the doping of ZnO.

2.3.3 Doping of zinc oxide

Ideally, both *n*- and *p*-type doped ZnO are desired to maximize the potential of ZnO in practical applications. *n*-type ZnO can be routinely obtained by doping ZnO with group III elements to produce excess electrons that can be activated to the conduction band. It has been shown that highly degenerate doped ZnO can be achieved by Al doping.[70] However, it remains a challenge to achieve high quality *p*-type doping of wide band gap semiconductors, like many other wide band gap compound semiconductors, such as GaN and ZnS.[54], [71–75]

2.3.3.1 n-type doping of ZnO

It is much easier to obtain *n*-type ZnO by substituting Zn with group III elements such as Al, Ga, and In, or by substituting O with group VII elements such as Cl and I.[76] Among these, doping with Al, Ga and In have been determined to be the most suitable dopants due to the resulting lower resistivity and good transmission in the visible region, therefore are well established by many research groups.[51], [69], [77–80] A high density of free electrons capable of charge transport is created with a small amount of substitution by Al (1-2%),[81–84] since each shallow trivalent Al can donate one excess electron to occupy the conduction band of ZnO. In 1996, Suzuki *et al.*[85] reported the production by pulsed laser deposition (PLD) of the first Al impurity doped ZnO thin films that have comparable resistivity (1.43×10^{-4} Ω·cm) with ITO, and later in 2003 Agura *et al.*[86] prepared AZO films with an ultra low resistivity of 8.5×10^{-5} Ωcm by PLD as well. These films have a high carrier concentration of 1.5×10^{21} cm^{-3} and good Hall mobility of 47.6 cm^2/Vs. Ga doped ZnO (GZO) films were reported to have a low resistivity of ~10^{-4} Ω·cm when grown by chemical vapor deposition (CVD) [87] or plasma assisted MBE.[77]

Compared to its main competitors, such as impurity doped SnO_2 and doped In_2O_3, the resistivity of impurity doped ZnO shows the potential to be further reduced. As shown in Figure 2.7, the obtained minimum resistivities of impurity doped SnO_2 and In_2O_3 films have essentially remained unchanged for the past 20 years, whereas the minimum resistivity of impurity doped ZnO films is still decreasing with more or less a constant rate. In the last decades, it has been evident that impurity doped ZnO has shown promising applications in a wide field including LED and PV, and an in-depth explanation of Al doping in ZnO will be discussed in section 2.3.4.

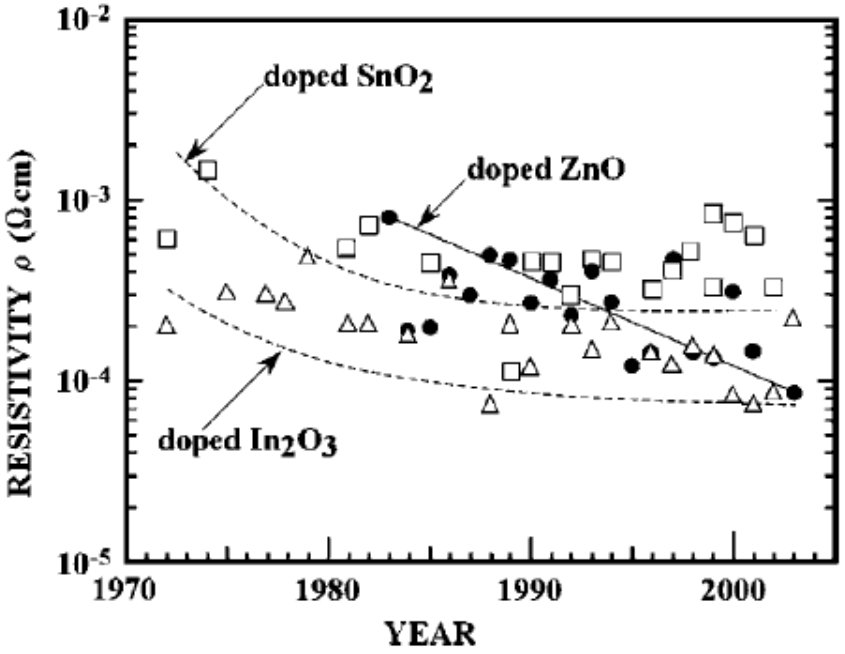


Figure 2.7. Reported resistivities of impurity doped binary compound TCO films, 1972 - 2005. Impurity doped SnO_2 is denoted by (□), In_2O_3 by (Δ) and ZnO by (●).(reprinted from reference [70]*)*

2.3.3.2 p-type doping of ZnO

In principle, *p*-type ZnO can be achieved by either substituting Zn with group I elements such as Li, Na and K or substituting O with group V elements such as N, P and As. Each

substitution will result in the loss of one conduction electron. In other words, one extra hole will be created at valence band, which gives rise to the *p*-type character of ZnO.

The *p*-type doping of ZnO is however difficult to achieve. Park *et al.*[88] have suggested that the bond lengths between the substitutional impurities and the nearest-neighbour atoms are significantly larger (e.g. 2.03 Å, 2.10 Å and 2.42 Å for Li-O, Na-O and K-O bond respectively) than the ideal Zn-O bond length (1.93 Å). Consequently, this deviation can induce lattice strain around the impurities and increase the possibility to form compensating defects such as vacancies. These defects act as donors and compensate the intentionally doped acceptors. This is the major reason why it is difficult to attain *p*-type doped ZnO. The same problem exists for group V elements except N. The bond lengths of Zn-N, Zn-P and Zn-As are 1.88 Å, 2.18 Å and 2.23 Å, respectively. It seems that N is the best candidate to achieve *p*-type doping of ZnO, as predicted by Kobayashi *et al.*[89] However, due to the limited solubility of N in the host ZnO, it is difficult to achieve *p*-type doing of ZnO by using a pure N source as well.[90]

2.3.4 Aluminum-doped Zinc Oxide (AZO)

2.3.4.1 The band structure and doping mechanism of AZO

As explained in section 2.3.2.2, excess electrons present in undoped ZnO can be thermally activated into the conduction band at room temperature to make the host oxide conductive. By increasing doping or impurity concentration, the bottom of conduction band can be continuously occupied by donor electrons. A degenerate electron gas is created at the conduction band edge with the Fermi level pinned above the bottom of conduction band,

giving rise to high electronic conductivity. At the same time, the band gap of the host material is slightly increased depending on the doping level, which retains the optical transparency in the visible region.

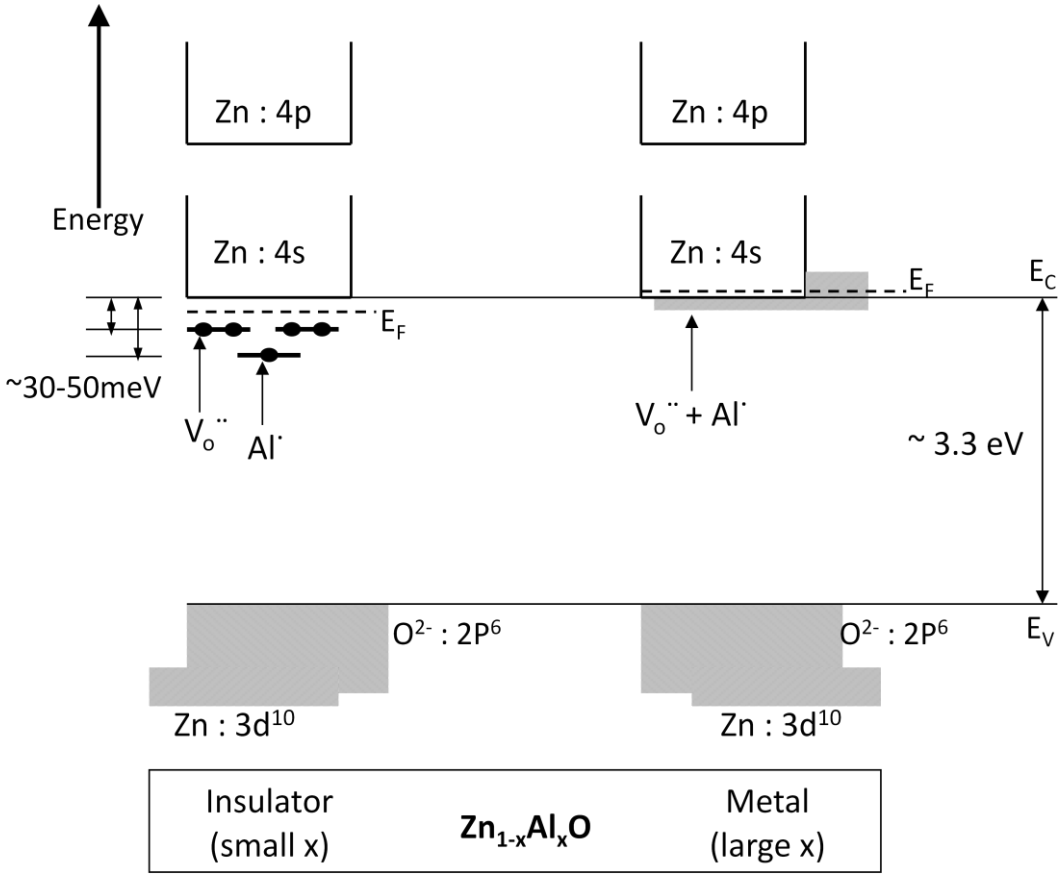


Figure 2.8. Illustration of electronic energy band structure of both lightly doped (small x, insulator) and heavily doped (larger x, metal) AZO (after reference [91]*).*

The one electron energy band model developed by Fan and Goodenough [91] can be used to describe the electronic energy band structure of pure, lightly doped and heavily doped oxide materials. Figure 2.8 shows a schematic band structure and the formation of a degenerate gas of electrons upon sufficient doping, where ZnO acts as host oxide material and Al is used as dopant. The valence band of ZnO is primarily derived from the filled oxygen $2p^6$ states. The filled zinc 3d levels lie beneath the valence band edge. The

conduction band is mainly formed by the zinc 4s electrons, with some contribution from zinc 4p electrons. The Fermi energy level of stoichiometric pure ZnO is located right in the middle of the band gap, and assuming there are no defects such as oxygen vacancies or zinc interstitials it should be an insulator. By substituting a small amount (small x value, 0-1% Al)[92] of the host atoms (Zn^{2+}) with higher valence dopant atoms (Al^{3+}) or creating oxygen vacancies, charged donor ($Al^{\cdot}$) or O vacancy ($V_o^{\cdot\cdot}$) states are formed close to the conduction band of the ZnO (left panel of Figure 2.8). Subsequently, ZnO becomes a lightly *n*-type doped semiconductor, and the Fermi level which was located half way between the conduction band and valence band of pure ZnO is raised close to the conduction band.

Upon further Al doping (large x value, 1-3% Al),[93], [94] more impurity or donor states will be created and the bottom of conduction band can be continuously occupied by donor electrons, giving rise to a degenerate gas of electrons (right panel of Figure 2.8). Ultimately, the degenerately doped ZnO shows a metallic character exhibiting high electronic conductivity, which can be described by the well-known Drude model.[95], [96] The Fermi level is raised much closer to the host conduction band, and the exact location depends on the degree of doping. As such, the conductivity can be improved by increasing the carrier concentration in the film.

2.3.4.2 Mott criteria

An important factor for consideration is how much the host oxide material must be doped to act as metallic conductor. In other words, what the critical carrier concentration is for the insulator-metal transition. Mott [97–99] first developed the idea of a compositionally

induced transition from nonmetallic to metallic behavior which occurs at a critical concentration of states at T = 0 K . The critical carrier concentration, denoted as n_c, is given by:

$$n_c^{1/3} a^* = K \qquad \text{Equation 2.2}$$

where a^* is the Bohr radius of the donor and K varies from 0.18 to 0.376 depending on the model.[100] The above criteria tell us that upon sufficient doping, when the carrier concentration is greater than this critical value ($n > n_c$), the host nonmetallic (insulating) material can be modified to become metallic.

Since the resistivity is temperature dependent, metallic (itinerant electrons) or nonmetallic (localized electrons) materials can be classified by plotting the temperature dependent electrical resistivity (or conductivity), and extrapolating the curve to 0K. Metallic materials will always display finite conductivities at absolute zero, whereas nonmetallic materials exhibit zero conductivity when the temperature is equal to absolute zero, i.e.

Metallic materials: $\sigma \neq 0$ at $T \rightarrow 0K$

Nonmetallic materials: $\sigma = 0$ at $T \rightarrow 0K$

Thus, the temperature dependent resistivity (conductivity) provides an effective way to characterize the metallic or nonmetallic behaviors of degenerately doped semiconductors. By applying the above Mott criteria, the required carrier concentration in ZnO for the nonmetallic-metallic transition can be calculated. The Bohr radius a* can be obtained from

the effective mass approximation in the relation:

$$a^* = (\varepsilon/m^*)(h^2/\pi e^2) \qquad \text{Equation 2.3}$$

where ε is the dielectric constant of ZnO and is equal to $8.65\varepsilon_0$, *h* is Planck's constant and m* is the appropriate effective mass. For ZnO, the reported effective mass is $0.28m_0$ for electrons and is $0.59m_0$ for holes.[101] Thus a* is ~2 nm at room temperature.[38], [102] The different values of K give an n_c value in a range from 1.33×10^{18} to 1.21×10^{19} cm^{-3}. Therefore, in order to tune ZnO to have a metallic behavior, a minimum carrier concentration of ~1.33×10^{18} cm^{-3} has to be reached.

2.4 Growth of ZnO Thin Films

2.4.1 Early technologies

ZnO thin films (both undoped and doped) can be grown with strong (0001) preferential orientation on substrates such as glass,[103] sapphire [104] and diamond [105] by various techniques. Early ones included magnetron sputtering [105], [106] and chemical vapor deposition (CVD).[107], [108] However, these techniques have difficulties growing high quality single crystal films, and polycrystalline films have poorer optical and electrical performance and this reduces the potential applications. Therefore, other techniques which allow improved control over growth have been investigated, including RF magnetron sputtering,[109] molecular beam epitaxy (MBE),[110] pulsed laser deposition (PLD) [111] and metal organic chemical vapor deposition (MOCVD).[112] The much finer

control associated with these techniques provides the possibility of higher quality, single crystal ZnO films. These improved film qualities have opened up opportunities for applications as UV light emitters [113] and transparent electrodes.[70], [114] However, these high cost complex techniques are hitting their performance-price limits, although they are currently dominating the field.[115]

2.4.2 Sol-gel technique

The cost of photovoltaic electrodes is one of the most important limiting factors influencing the uptake of commercial PV systems.[116], [117] In recent years, sol-gel methods that employ colloidal solutions and thermal decomposition have been widely investigated, since they require less complex deposition and are lower cost compared to the early technologies.[118–120]

Sol-gel refers to the simple chemical solution technique where deposition is accomplished by a gelation process, and has been widely used to fabricate metal oxides.[51], [84], [121–133] It starts with a liquid-phase mixture (sol), through an intermediate bi-phase gel (both liquid and solid phases), until a final solid-phase discrete particle or continuous network product. Precursors used to fabricate metal oxides are primarily metal alkoxides and metal chlorides. For the growth of AZO, precursors normally consist of Zn^{2+} salts and counter anions such as nitrate and acetate.[121], [130], [132], [134] In addition, very small amounts of dopant precursors can be uniformly dispersed in the starting sol, which is the basis to achieve effective doping in the final product. By going through various types of hydrolysis and polycondensation reactions,[125] metallic elements can be connected either by –O– or –OH– bridges from which small particles of metal oxide can start to form inside

the solution. Under appropriate conditions, successive reactions in the solution can result in large amounts of metal oxide with controllable microstructures; including shape, morphology and size. The solvent in which the sol-gel process is taking place should eventually be removed and leaves only the desired metal oxide product, and this can be achieved through a drying process.[122], [131] Drying significantly affects film quality, particularly defect density, and ultimately it effects the evolution of the microstructure, and thus also the properties and performance of the final product.

Finally, a firing process is carried out for decomposition, polycondensation and crystallization.[126] Grain growth at elevated temperatures can result in a reduced density of grain boundaries,[52] which contributes to both optical transparency and electrical conductivity by reducing grain boundary scattering. These three sub-processes can change the physical characteristics of the deposited film, improve the structural stability, as well as enhance the mechanical, optical and electrical properties.

Sol-gel processing has distinct advantages over other techniques. The homogeneous precursor solution makes the controllable chemical composition much easier.[52], [126], [135] Moreover, as eventually we intend to build solar cells based on inexpensive and flexible polymeric substrates, the processing should not employ high temperatures.[136] This restriction motivates the development of sol-gel processing,[121], [126] which is also a high yield, fast throughput method that offers the possibility of fabrication of low cost solar cells with performance characteristics suitable for large-scale industrial applications.[118–120], [137]

2.4.3 Spin coating

For the sol-gel technique, the precursor solution can be deposited onto a substrate by dip coating, spin coating, doctor blading or spray techniques, which are considered to be less expensive and are especially promising for fabricating high quality films.[115], [138] In particular, spin coating is able to fabricate highly controllable and reproducible films with excellent uniformity on large areas.[139]

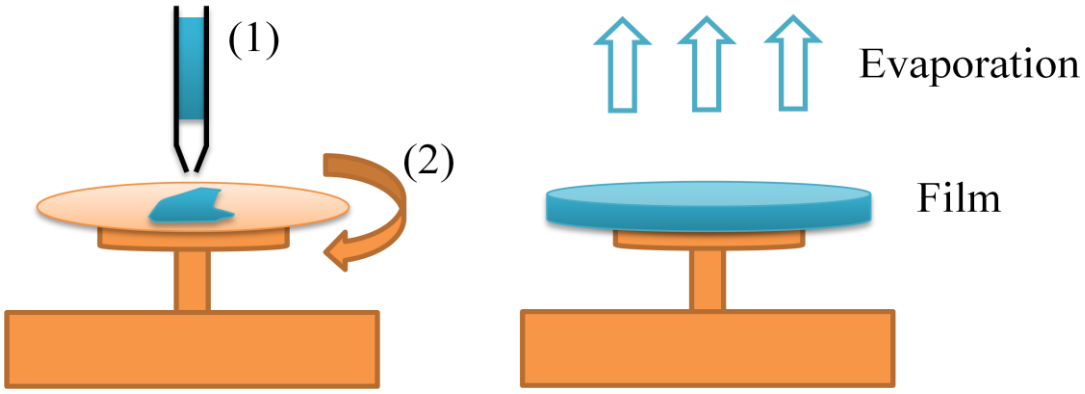


Figure 2.9. An illustration of a spin coating process.

In a spin coating process, the precursor solution is firstly dropped onto the substrate and wets the surface (step 1, left panel, Figure 2.9). The spin coater then rotates the substrate at a speed of around 2000-4000rpm for 10-30 seconds [122], [131], [140] (step 2, left panel, Figure 2.9). Two forces are acting on the solution during spin coating; the adhesive forces at the solution-substrate interface and the centrifugal forces resulting from the high-speed rotation. These two competing forces will result in a strong shearing action at the interface which causes the solution to form a thin film with controllable thickness,[139] depending on angular velocity, solution concentration and viscosity. The correlation between these parameters and the resulting film thickness has been empirically established in previous work.[141–144] Next, depending on the solution system, a drying process at a temperature in the range 100-300°C for around 5-20 minutes is necessary before the next round of

deposition to evaporate solvent and remove organic residuals (right panel, Figure 2.9).[125], [131] By repeating this coating-drying procedure, a desirable film thickness from a few tens of nanometers to a few micrometers can be obtained.[122], [131] Figure 2.10 illustrates the three major steps during this process, namely nucleation, crystal growth and film formation. At the same time, these processes allow Al atoms to relocate at positions with lower free energy.[124]

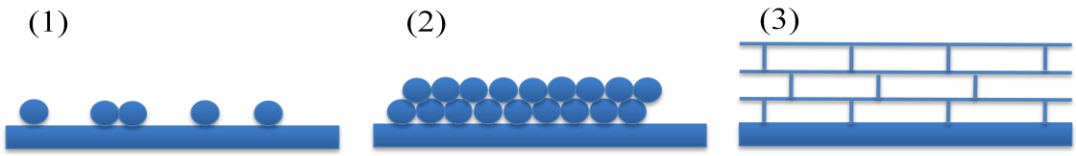


Figure 2.10. An illustration of the process of nucleation (1), crystal growth (2) and film formation (3).

In conclusion, sol-gel spin-coating is a simple and cost-effective approach to fabricate AZO thin films. However, challenges encountered by this approach include the current immature understanding of the process parameters as well as the relatively poor performance compared with sputtered ITO. Today, AZO thin films with low resistivity in the order of 10^{-4} Ω·cm are achieved; some representative results include 7.40×10^{-4} Ω·cm by DC magnetron sputtering,[145] 4.62×10^{-4} Ω·cm by thermal evaporation [146] and 4.00×10^{-4} Ω·cm by PLD.[147] It is worth mentioning that, sol-gel processed AZO thin film with a low resistivity of 5.79×10^{-4} Ω·cm has been made possible recently using spin coating technique,[148] comparable to the early technologies. This motivates further investigation so that much higher quality films can be achieved with simpler techniques. In Chapter 4, I will look into some major factors affecting the thin film quality, and design experiments to improve the film performance.

Chapter 3 – Experimental Techniques

The main techniques used in the preparation and characterization of the thin films and devices studied in this thesis are described in this chapter.

3.1 Photovoltaic Device Fabrication

3.1.1 Substrate cleaning

Thin film fabrication starts with sheets of soda-lime glass substrates (Fisherbrand, FB58624), which are cut into 12 × 14mm rectangles. The cleaning process consisted of sonication in a diluted detergent solution (Decon 90 : de-ionized water = 800mL : 5mL) and de-ionized water (DI water) for 5 minutes each, followed by soaking in acetone and isoproponal at ~50ºC for 3 minutes each, and then dried in air.

3.1.2 AZO fabrication by sol-gel processing

AZO thin films were grown on glass substrates in an ambient environment by the sol-gel spin-coating technique. Precursor solutions were formed by dissolving zinc acetate dihydrate ($Zn(CH_3COO)_2 \cdot 2H_2O$, Riedel-de Haën) and aluminium nitrate ($Al(NO_3)_3 \cdot 9H_2O$, Sigma-Aldrich) in 2-methoxyethanol ($HOCH_2CH_2OCH_3$, Fisher) combined with monoethanolamine (MEA, $HOCH_2CH_2NH_2$, Sigma-Aldrich), as described by Xu *et al.*[149] MEA was added to the suspension to stabilize the aluminium doped ZnO complex.[150] The molar ratio of MEA to zinc acetate was maintained at 1.0 and the concentration of zinc acetate was in the range of 0.2 to 1.5M, within typical literature values.[130], [140] The content of aluminium dopant in the solution was varied from 0 to 3at.% (Al/Zn) depending on the application. This doping level lies within the typical range

used in the literature (0.5-2 at.% Al/Zn),[81], [121], [127] as Tang *et al.*[121] suggested that after a certain level of doping, no more dopant atoms can occupy zinc site because of the limited solubility of Al in the ZnO lattice. The solution was thoroughly refluxed at 75ºC for about an hour until clear as shown in Figure 3.1.[52], [131] This solution was then aged at room temperature for 2 days before deposition to stabilize the colloidal with an improved uniformity [151] and to obtain a low resistivity.[129], [131], [152]



Figure 3.1. AZO precursor solution.

Glass substrates were cleaned as described in section 3.1.1. The AZO precursor solution was dropped onto the glass substrates using a pipette to give a full coverage, followed by spin coating at 3000 rpm for 20 seconds. The coated substrates were dried at 250ºC for 10 minutes on a hot plate in air after each coat to evaporate the excess solvent (drying process). By repeating the procedure of spin coating and drying, AZO thin films of different thicknesses were obtained. The specimens were then decomposed in air at 500ºC for 1 hour [52], [81], [94], [140]) using a Carbolite RWF12/23 furnace, with a ramp rate of 10ºC/min.

Afterwards, if annealing was necessary, it was carried out either in vacuum (~10^{-5} torr) or forming gas ($90N_2/10H_2$) at 500ºC for 1 hour using a Carbolite 15/450 tube furnace, with a ramp rate of 20ºC/min. Vacuum and forming gas atmosphere were formed in a quartz tube (Robson Scientific) located inside the furnace as shown in Figure 3.2, and a Swagelok tube fitting (SS-25M0-1-8KT, Swagelok London) was used at the two ends for the vacuum application. A NXL 776000 BOC Edwards pump was used to generate vacuum atmosphere and this was monitored by a Center One vacuum gauge controller (Oerlikon Leybold Vacuum GmbH).

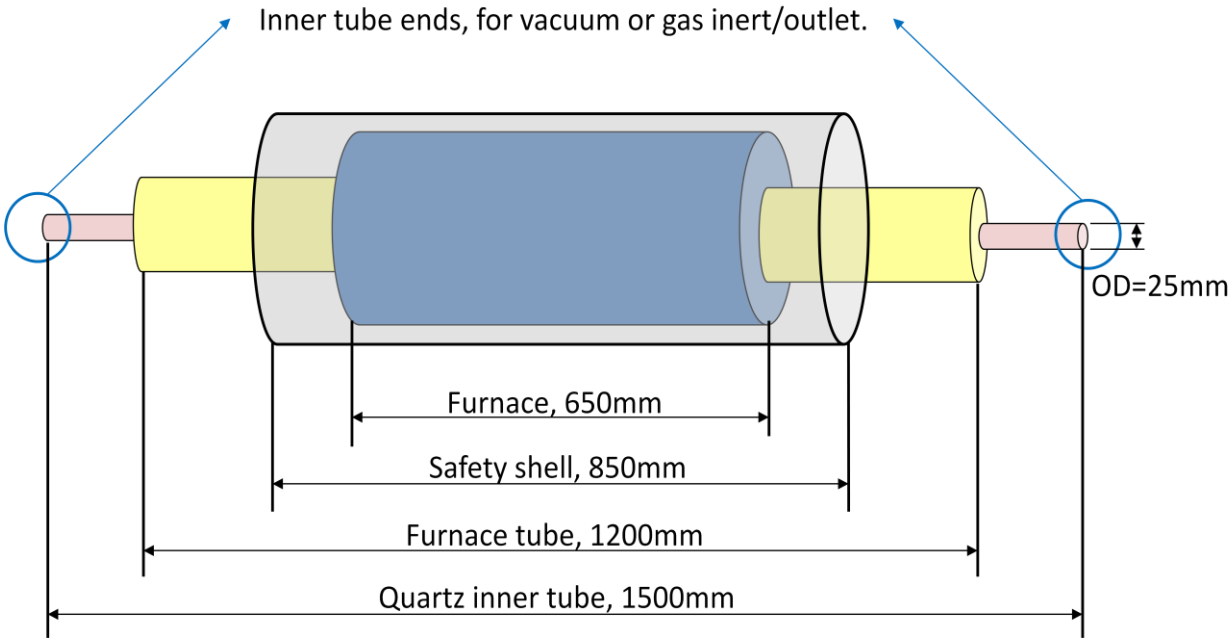


Figure 3.2. An illustration of the tube furnace system.

3.1.3 ITO/AZO patterning

The sol-gel processed AZO and commercially available ITO substrates must be patterned to give a stripe running the length of the substrate (Figure 3.3). To do this, the ITO or AZO substrate was firstly cleaned with isoproponal and dried in air, followed by masking

the 2mm stripe with a self adhesive tape. A Roland Stika cutting printer was used to prepare the adhesive masks that are applied to the AZO and ITO films. The substrates were then immersed in an etchant solution consisting of 10 DI water: 9 HCl: 1mL HNO_3. The etching process was carried out at 40 - 60ºC on a hotplate for 5 minutes. The substrates were then removed from the acid bath, immersed in water for 30 seconds and rinsed thoroughly with running water to remove any residual acid. The adhesive mask was removed and any residual adhesive removed mechanically, by gently rubbing the sample surface with cotton buds soaked in acetone. The substrates were then rinsed successively in acetone and isopropanol.

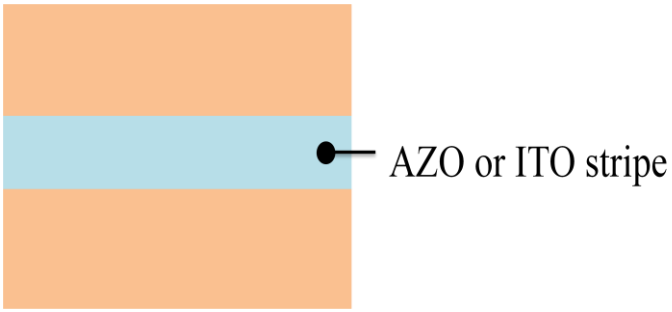


Figure 3.3. AZO or ITO pattern (middle strip) on glass substrate.

3.1.4 PEDOT:PSS and polymer layer deposition

In Chapter 4 and 5, PEDOT:PSS was employed as a buffer layer to smooth the ITO substrate and block the flow of electrons to the anode. The only difference between the conventional and inverted device fabrication in terms of PEDOT:PSS/polymer processing is the order in which it is deposited. In devices with a conventional geometry (Chapter 4), the PEDOT:PSS/polymer layer interface was created by coating a solution of P3HT:PCBM on the surface of a solid PEDOT:PSS film, and using an Al electrode. In

contrast to this, devices employing an inverted geometry (Chapter 5) were prepared by coating a dispersion of PEDOT:PSS onto the surface of a solid P3HT:PCBM film, and using an Au electrode. The processing of both architectures was described below (processing of PbS quantum dot layers will be discussed in Chapter 6).

3.1.4.1 Blending P3HT:PCBM solutions

First, the BHJ P3HT:PCBM solution was prepared in a low-moisture nitrogen glove box operating at <100 ppm (parts per million) O_2 and <150 ppm H_2O. P3HT (Reike Metals Inc.) and PCBM (Nano-C) were dissolved in chlorobenzene (Sigma-Aldrich) with a weight ratio of 1:0.8 (i.e., with a small excess of P3HT), as widely used by other authors to ensure a good phase separation between the two materials.[153][154][155] The solution was kept in the glove box and continuously stirred overnight at ambient temperature, with the vial covered with aluminum foil to prevent light soaking.

3.1.4.2 Conventional device fabrication

Once the P3HT:PCBM solution was well-mixed, the ITO- or AZO-coated substrates were cleaned as described above for subsequent deposition. An oxygen plasma treatment was first performed for 30 seconds to smooth the surface, improve sheet resistance and film transmission.[156] Next, a blocking layer of PEDOT:PSS in aqueous solution (a conductive and transparent polymer, H.C. Starck GmbH) was deposited onto the ITO or AZO substrate by spin coating. In general, a few droplets of the solution were applied to the substrate using a variable pipettor, the substrate was then spun at 5000rpm for 30 seconds. Following deposition of the PEDOT:PSS the films were heat treated on a hot plate at 140°C for 10 minutes to remove residual moisture before being transferred to a

low-moisture glove box. The pre-mixed photoactive P3HT:PCBM layer was then spin coated on top of the PEDOT:PSS at 700rpm for 15 seconds.

3.1.4.3 Inverted device fabrication

For the inverted devices, the ITO substrates that were coated with ZnO blocking layers were firstly cleaned as described in section 3.1.1. Next the substrates were transferred into the glove box where the pre-mixed P3HT:PCBM solution was spin cast onto the substrates at 700rpm for 15 seconds, followed by drying on a hotplate located inside the glove box at 70°C for 2 minutes. Next, one droplet of the PEDOT:PSS solution (hole-injection layer, HIL) was dropped onto the spinning substrate and spin cast at 5000rpm for 1 minute, then dried at 45ºC on a hotplate for 5 minutes.

3.1.5 Metal electrode deposition

The cells were transferred into a vacuum chamber, and aluminum or gold electrodes were thermally evaporated through a shadow mask (to define the electrode dimensions) by using an Edwards E04 evaporator for conventional and inverted devices respectively. A tungsten boat (Umicore) was used and evaporation was performed in a vacuum environment of ~10^{-6} torr. The first 30 seconds of evaporation was shuttered to avoid any impurities being deposited onto the substrate. Next, the shutter was removed and evaporation was performed at a rate below 2Å/s to reach a total thickness of 100±5nm. The deposition rate was monitored using a calibrated Edwards FTM 5 quartz crystal growth monitor. The top view of the final cell geometry is shown in Figure 3.4a, where each substrate contains three different pixel cells defined by the overlap of the two electrodes (i.e. ITO and Au strips in this case). A set of 10 images taken by optical

microscopy have shown that each pixel cell has an area of ~0.02 cm^2 and Figure 3.4b displays one of the images.

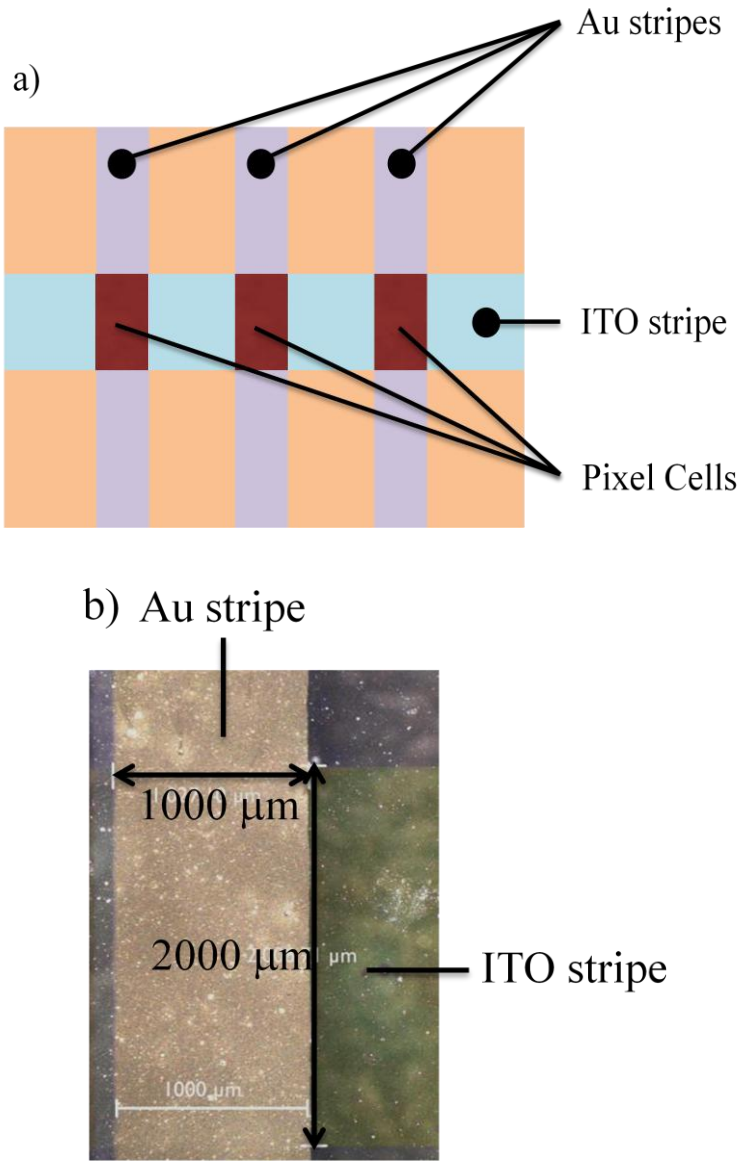


Figure 3.4. (a) Three solar cells (termed pixel cells) per substrate are defined by the overlapping area of the ITO and Au strips. (b) An optical microscope image of one of the pixel cells, showing the two stripes and their dimensions.

3.1.6 Thermal annealing

Once the devices had been removed from the vacuum chamber, most were submitted to a thermal annealing treatment at 150ºC for 10 minutes on top a digital hotplate (Fisher

Scientific) within the glove box. This is to obtain optimized phase separation in the P3HT:PCBM layers by increasing the nanodomains sizes, in order to match the corresponding exciton diffusion lengths in each material (around 3-30nm).[157]

3.2 Materials Characterization

3.2.1 Dektak profilometry measurements

The thicknesses of these solution processed ZnO thin films were measured by surface profilometry (Veeco Dektak 6M Stylus Profiler). A diamond tipped stylus is scanned across the surface of the sample with a given contact force. The vertical movements of the tip on the sample can be translated into an electrical signal and give 2D plots of the topography of the sample surface.

For measuring the thickness of AZO thin films and polymer layers, a step is formed by scratching off a portion of the film with cotton tip (soaked with etchant in the case of AZO films). This step height is then measured to give the reading of film thickness.

3.2.2 X-ray diffraction (XRD)

X-ray diffraction (XRD) is a very widely used and efficient non-destructive tool to investigate the structure and microstructures of bulk materials as well as surface layers. It utilizes the elastic scattering of X-rays as they pass by the electron cloud of individual atoms. The wavelength of X-rays is in the range of 1 - 500Å, ideal for examining inter-atomic spacing of individual atoms in a crystal lattice.

XRD patterns were recorded to study the crystal structure and phase composition of undoped and Al doped ZnO thin films on a Philips PW1820 system with a PW1727 X-ray generator with monochromated Cu Kα radiation (λ = 1.5418Å) at room temperature. The scans were carried out in the range of 2θ between 10° and 70° with a scan rate of 0.02 degree per second. The data is then analyzed on Philips X'Pert software.

3.2.3 Atomic force microscopy (AFM)

Atomic force microscopy (AFM) provides very useful numerical data on surface height for characterization of thin film surfaces. This involves rastering a cantilever with an ultra fine tip across the sample surface, the interactions between the cantilever tip and the sample surface lead to deflections which are measured by a laser beam and detected by a photodiode array. Various analyses have been developed to utilize the data obtained from AFM scans, including the root mean square (rms) heights. These analyses are useful to relate the evolution of surface morphological parameters to the physical properties of the thin films, in order to optimize the growth mechanism of thin films.

AFM (Veeco Park CP-II AutoProbe SPM) images were recorded at ~4 different regions of each sample. This equipment was operated in tapping mode with a 'J' scanner having a lateral range of approximately 100 µm and a vertical range of 6 µm. MikroMasch silicon beam-shaped probes with a thin coating of aluminium to act as a mirror for the laser beam were used. Calibration of the AFM was accomplished by scanning a 2.5 µm pitch 200 nm depth reference sample from TopoMetrix Corporation.

3.2.4 X-ray photoelectron spectroscopy (XPS)

X-ray photoelectron spectroscopy (XPS) is a quantitative spectroscopic technique that can be used to examine the elemental composition of a material, as well as the chemical and electronic state of the elements. The sample is irradiated by a beam of X-rays, which cause core electrons to be ejected from the sample surface. A spectrum of the energies of these ejected electrons is recorded. The electron energies of interest usually lie in the range of 0 - 1500 eV, since the escape depth of electrons at these energies is typically between 2 and 8 monolayers, XPS is surface specific (in the top 1-10nm of the sample). The identification of individual species and their elemental and chemical states are based on the fact that the emitted electron have a characteristic binding energy (BE), corresponding to the atom's electron shell structure (1s, 2s, 2p, 3p etc).

The equipment used in this work was a VG nine channel CLAM4 electron energy analyzer, fitted with a 200Watt unmonochromated MgKα X-ray source and argon ion gun, in a ultra high vacuum chamber (5×10^{-10} mTorr). The analyzer was operated at constant pass energy of 100 eV for wide scans and 20eV for detailed scans, and the C1s peak at BE 284.8eV was used to overcome any sample charging. For some samples, consecutive ion beam etching was carried out by sputtering using the ion gun to clean off the surface contamination, enable the examination of the composition below the surface. Analysis of the peaks was performed using the CASA XPS software package.

Hard X-ray photoemission spectra (HXPS) at hν=6000.0 eV were measured on Beamline ID16 on the ESRF (European Synchrotron Radiation Facility, Grenoble, France) with an overall energy resolution of 0.35 eV.

3.2.5 Scanning electron microscopy (SEM)

A scanning electron microscope (SEM) is used to image a sample by scanning it with a beam of electrons in a raster scan pattern under vacuum. The electron beam is thermionically emitted from an electron gun fitted usually with a tungsten filament cathode, and the beam is then focused by condenser lenses to a fine spot (~4 - 5nm) giving rise to a high spatial resolution. The interaction of electrons with the atoms present in the sample will produce signals that contain information on surface topography and composition. The energy exchange between the electron beam and the specimen will result in the generation of low energy secondary electrons and high energy backscattered electrons, which can be detected by specific detectors and used to create images of the specimen surface.

The cross-sectional information, include thickness and device structures, was examined using a JEOL 840F SEM operated at 6 keV, a relatively low voltage to avoid charging. Cross-sectional specimens were prepared by cutting the backside of the substrate using a fine diamond cutter and breaking the substrate into half by leveraging against a sharp edge (such as a needle).

3.3 Optoelectronic Characterization

3.3.1 UV-Visible absorption spectra

UV-Vis spectroscopy refers to absorption spectroscopy or reflectance spectroscopy in the ultra violet and visible spectral regions. The measured UV-Vis spectrum can be viewed as an absorption spectrum or as a transmission spectrum. The transmission spectrum gives

the percentage of the incoming light that actually travelled through the sample. The spectrum can be analyzed to obtain information such as the energy band gap and thickness of the thin films. The optical gap is defined as the minimum energy needed to excite an electron from the valence band to the conduction band.[158] Intrinsic absorption of photons by a semiconductor occurs when the photon energy is located in the vicinity of the energy band gap of the material. In other words, absorption happens when the incident photon energy, $h\nu$, is greater than the semiconductor's band gap energy between the bottom of the conduction band and top of the valence band, E_g. The optical absorption coefficient α is calculated using Lambert's law:

$$\alpha = - \ln(1/T) / t \qquad \text{Equation 3.1}$$

where T is the transmittance and t is the film thickness. The maximum absorption occurs at high energy and decreases with optical energy. For the direct-transition semiconductors, the relation between α and E_g can be determined by Tauc's relation:[159], [160]

$$\alpha \propto (h\nu - E_g)^{1/2} \qquad \text{Equation 3.2}$$

where, h is the Planck's constant and ν is the frequency of the incident photon.

In the work presented in this thesis, a Cary 5000 UV-Visible-NIR spectrophotometer was used to obtain the optical absorption parameters of the films in air. It utilizes tungsten halide or deuterium light sources which pass through a monochromator, then split into two beams that travel through a sample and a blank glass slide reference, respectively. The

instrument software then compares the two signals in order to determine the transmission of the sample.

3.3.2 Four-point probe resistivity measurements

A four-point probe technique is an electrical impedance method that uses separate pairs of current and voltage electrodes to measure the sheet resistance of thin films. It removes the effects of contact resistance from the measurements, thus giving more accurate reading than traditional two- terminal sensing techniques. As shown in Figure 3.5, one can imagine that when current is supplied via the outer pair of probes, a voltage drop across the inner pair of the probe will be generated and can be measured.

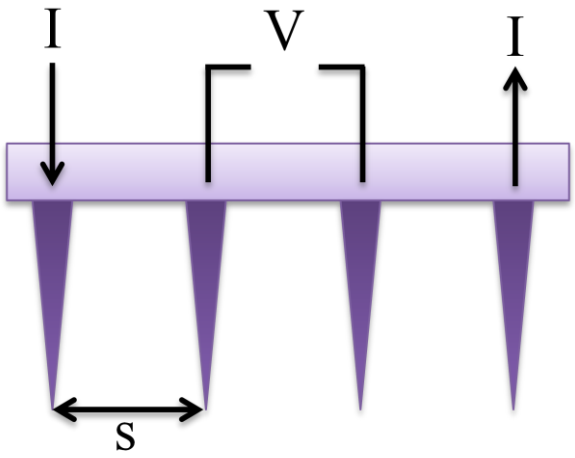


Figure 3.5. Illustration of a four point probe resistivity measurement arrangement for sheet resistance calculations.

The electrical resistance of a given object depends primarily on two factors, the material and the shape. For a given material, the resistance is proportional to the length, which by Ohm's Law: [161]

$$R = \frac{V}{I} = \rho \frac{d}{A} \qquad \text{Equation 3.3}$$

where R is resistance measured in ohms (Ω), V is the potential difference measured in volts (V), I is the current measured in amperes (A), ρ is the resistivity measured in Ω·m, *d* is the length of the material measured in metres and A is the cross-section area of the material measured in square metres. For the measurement of electrical resistivity of thin films by a four-point probe method, the relation can be expressed as follows:

$$\rho = t \frac{\pi}{ln2} \left(\frac{\Delta V}{I} \right) \qquad \text{Equation 3.4}$$

where ΔV is the potential difference of voltage probes, I is the current flow of current probes, t is the thickness of the thin film coating and π/ln2 is a correction factor that should be taken into account for sheet resistance of thin films with finite sample size and geometric shape effects, and itself is a product of a number of variables that take into account factors such as thickness, proximity to sample edge and temperature. The approximation of CF values for all geometric possibilities is beyond the scope of this thesis, but can be found in the literature.[162], [163] The sheet resistance, R_{sheet}, is defined as resistivity divided by thickness giving:

$$R_{sheet} = \frac{\rho}{t} \qquad \text{Equation 3.5}$$

R_{sheet} is measured in Ω/□ (which is dimensionally equal to Ω, but is exclusively used for sheet resistance to avoid confusion.[164] Measurements were performed using a Keithley 220 current source and an Agilent 34420A Voltage meter. The probe spacing was 1mm, and the sample sizes were typically around 12×12mm.

3.3.3 Hall carrier and mobility measurements

Hall probes are based on the principle of the Hall effect, discovered by Hall in 1879.[165] The Hall effect in a semiconductor refers to the phenomenon that upon the application of an orthogonal magnetic field on a current-carrying semiconductor, the charge carriers experience a force in the direction perpendicular to both the magnetic field and the current. This force then results in the movement of positive and negative charge carriers in opposite directions, leading to a potential difference across the material, which is known as the Hall voltage.

The resulting electric field is recorded to obtain information such as Hall carrier concentration and mobility. The Van der Pauw method was employed because it enables accurate properties measurements of any arbitrary 2D shaped samples, such as thin films. When using this method, four Ohmic contacts were formed on the sample edges as shown in Figure 3.6. A current is driven through two contacts (for example contacts 1 and 4) and the resulting voltage across the other two contacts (contacts 2 and 3) was recorded. Repeating the measurements by swapping the current and voltage edges, as well as reversing the magnetic polarity, accurate measurements may be obtained.

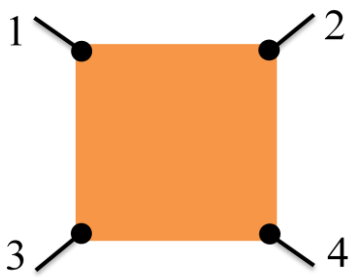


Figure 3.6. An illustration of the sample configuration for Hall effect measurements.

Hall effect measurements in this work were carried out on an Ecopia HMS-3000 Hall system at room temperature. Silver dag was used to form contact at the four corners of the sample. Current – voltage characteristics were measured prior to Hall analysis to ensure the contacts formed were Ohmic over the range of measured current.

3.4 Photovoltaic Device Testing and Characterization

3.4.1 Current-voltage (IV) measurements

The most important figures of merit distinguishing the performance of a solar cell are its short circuit current (I_{sc}), open circuit voltage (V_{oc}), fill factor (FF) and power conversion efficiency (PCE, as shown in Figure 3.7).

The I_{sc} is the maximum current flowing through a solar cell when the voltage across which is zero (i.e., when the solar cell is short circuited). The V_{oc} is the maximum voltage available from a solar cell when the current is zero (i.e., when the solar cell is at the open circuit condition). However, at both of these operating stages, the power from a solar cell is zero. The FF is the ratio of the maximum power (P_{max}) from a solar cell to the product of

I_{sc} and V_{oc} (the light green shaded area divided by the light pink shaded area as shown in Figure 3.7), and therefore in conjunction with I_{sc} and V_{oc} determines the maximum power from a solar cell. The efficiency of a solar cell is then defined as the fraction of incident power which is converted into electricity:

$$\eta = (V_{oc} \times I_{sc} \times FF) / P_{in} \qquad \text{Equation 3.6}$$

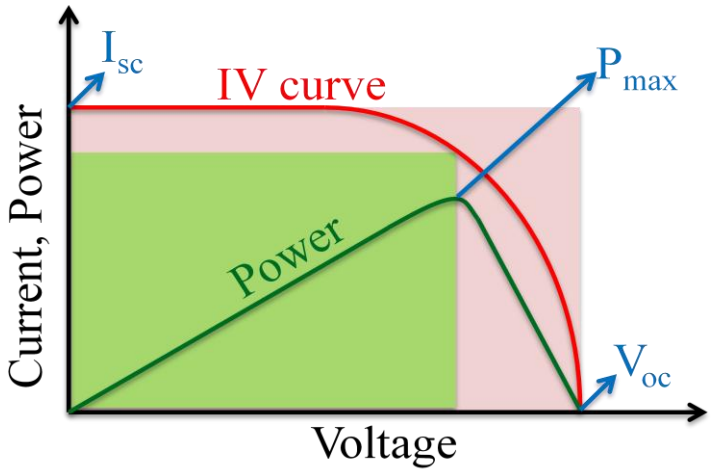


Figure 3.7. An illustration of the IV curve (red line) of a solar cell, showing I_{sc}, V_{oc} and P_{max}, and the power (green line) as a function of voltage.

In addition, the efficiency of a solar cell is affected by parasitic resistances. The most common parasitic resistances are series resistance (R_s) and shunt resistance (R_{sh}, as shown in Figure 3.8). A high series resistance causes power losses in a solar cell by resisting current flow, which will reduce the FF value and excessively high values may reduce I_{sc} as well. A low shunt resistance has a negative impact on solar cells by providing alternative current pathways for the photogenerated current, reducing the amount of the current flowing through a solar cell junction as well as the voltage from the cell. Therefore, for an

ideal device, we want low series resistance and high shunt resistance values. The illuminated IV curves were used to obtain the R_s and R_{sh} by using Co-content function, as described by Ortiz-Conde *et al.* (the excel worksheet used was developed by Shawn Willis from our group).[166]

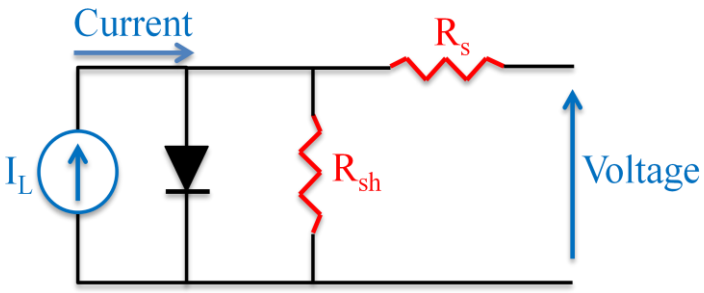


Figure 3.8. An illustration of parasitic series and shunt resistances in a solar cell circuit.

The devices were placed in a testing holder inside the glove box and sealed by using a rubber ring. The nitrogen atmosphere was maintained throughout the device-testing period by continually flowing nitrogen gas through the holder. A Newport 67005 solar simulator was used to simulate AM1.5 illumination. The solar cells were positioned such that the incident power density from the solar simulator was 100mW/cm^2. This incident light intensity was monitored regularly using a D3MM thermal sensor (Thorlabs Instrumentation). IV curves were recorded with a Keithley 2400 SourceMeter between -0.4V and +1 V, in step size of 12.5 mV with 20 milliseconds per step.

3.4.2 External quantum efficiency (EQE) measurements

EQE refers to the ratio of the number of charge carriers collected by the solar cell to the number of incident photons. This parameter is wavelength dependent and describes how efficiently the device can convert solar energy into electrical energy. For instance, if every

incident photon with a certain energy (i.e., at a given wavelength) is absorbed and collected, the EQE at that wavelength is one.

The same holder that was used for IV measurement was used for external quantum efficiency (EQE) measurement, with nitrogen gas flushing throughout the experiment. Illumination was provided by a halogen lamp and Oriel Cornerstone 130 monochromator. When illuminating at longer wavelengths, a 400, 610 or 1000nm filter was used to clock the higher orders of the monochromator grating. Calibration of the light intensity at each wavelength was performed using a Newport 818 UV enhanced silicon photodetector and a Newport 918 IR germanium photodetector. The current signal from the solar cell was measured with a Keithley 6845 picoammeter, and the entire process was controlled by a LabVIEW virtual instrument.

Chapter 4 – Aluminium Doped Zinc Oxide for the Application of Transparent Electrode in Organic Solar Cells

As mentioned in Chapter 1, transparent metal oxides (TCOs) play an important role as hole-collecting electrodes in determining the performance of solar cell devices, such as the conversion efficiency, device stability and lifetime. Therefore, a fundamental understanding of the physical origins of the unique combination of high electrical conductivity and optical transparency in these materials is crucial to satisfy the ever-increasing demand for high device performance. In this chapter, investigations of the preparation conditions, including the influence of Al doping concentration, precursor solution concentration and post annealing, on the structural and optoelectronic properties of AZO films were performed. Then, a series of organic solar cells were fabricated employing either solution-processed AZO or sputtered ITO (commercially available) thin films as the front electrode, in order to study the capability of solution processed AZO in the photovoltaic industry.

4.1 Introduction

4.1.1 Transparent conducting oxides (TCO)

Recent progress in the photovoltaic and optoelectronic industries has shown a rapid increase in the demand for thin-film transparent electrodes. TCOs are important functional oxides with applications as the optical window electrode for photovoltaic devices (PV), liquid crystal displays (LCD) and light emitting diodes (LED). In the field of photovoltaics,

it is important to develop TCO materials that are electronically tailored to enhance charge extraction and transport. The TCO front contact in solar cells acts both as a window for light transmission to the photoactive layer for absorption and charge generation as well as an electrode for charge carrier collection and transport out of the solar cell.

In general, photovoltaic applications require TCO materials to have a band gap greater than 3.27eV (less than 380nm) to avoid the absorption of light,[70] therefore making better use of the solar irradiance spectrum to improve absorption in the photoactive layer. In addition, TCO material resistivities lower than 10^{-3} Ω·cm are preferred for effective charge transport.[167] By impurity doping, the electrical properties can be enhanced dramatically by increasing the carrier concentration. For photovoltaic electrode applications, generally a minimum carrier concentration of ~10^{20} cm^{-3} is required to provide good conductivity.[70]

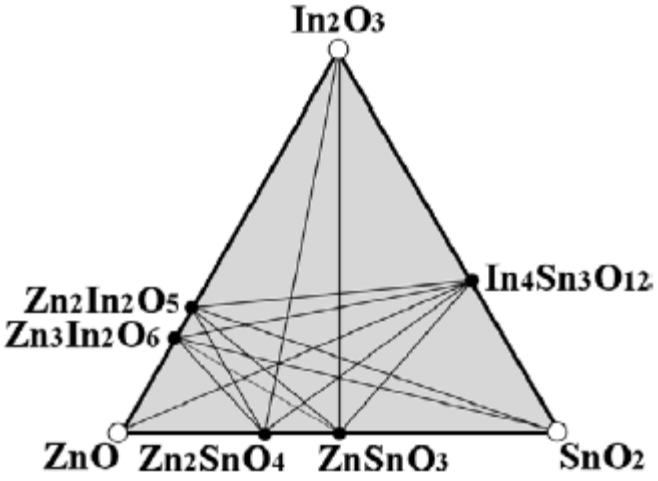


Figure 4.1. TCO semiconductors for practical transparent electrodes (reprinted from reference [70]*)*

TCO semiconductors for transparent electrode applications have been widely developed from metal oxides containing at least one of the following materials: Zn, Cd, In and Sn. Cd-containing TCOs can have low resistivities; however they have little practical value because Cd is very toxic and so environmental regulations will make commercial exploitation difficult. Minami[70] has suggested that only ZnO, In_2O_3 and SnO_2 and their multicomponent compounds are of practical use (as illustrated in Figure 4.1). To date, tin doped indium oxide (ITO) is most widely used by industry owing to its low resistivity of ~10^{-4} Ωcm[168][169] and high transmittance of ~90% in the visible region.[170]

ITO, however, is not an ideal transparent electrode given that indium, the principal component of ITO, is a scarce rare earth metal with some toxicity; making ITO based devices expensive and potentially harmful to the environment. Therefore, considerable effort has been directed towards the discovery of a sustainable alternative,[126] for both environmental and economical reasons. A number of avenues have been investigated for the identification of doped binary compounds, and AZO is recognized as a promising alternative due to its low-cost, non-toxicity, bio-compatibility and comparable properties to that of ITO.[171] Zinc, the primary element in AZO, is the 24th most abundant element in the Earth's crust.[172] Indium, composes 90 at.% of the metal in commercial ITO, cost $580/kg in 2012,[173] whereas zinc at <$0.95/kg [174] makes up ~98 at.% metals in AZO, giving an obvious commercial driver to use more Zn based TCOs.[137]

In addition, the anode work function is a very important factor because a higher work function can lower the hole injection barrier, and at the same time results in better energy matching between the anode and the highest occupied molecular orbital (HOMO) of the

organic electron donor. This improves the solar cell conversion efficiency.[175] AZO makes a good anode material, as it possess a relatively high work function (from 4.7[176] to 5.2 eV[177]) for hole extraction with a high barrier for electron injection. Furthermore, the potential of AZO can be maximized by optimizing the chemistry and manufacturing process, as is addressed further in the later sections of this Chapter.

4.1.2 P3HT:PCBM solar cells employing sol-gel processed AZO

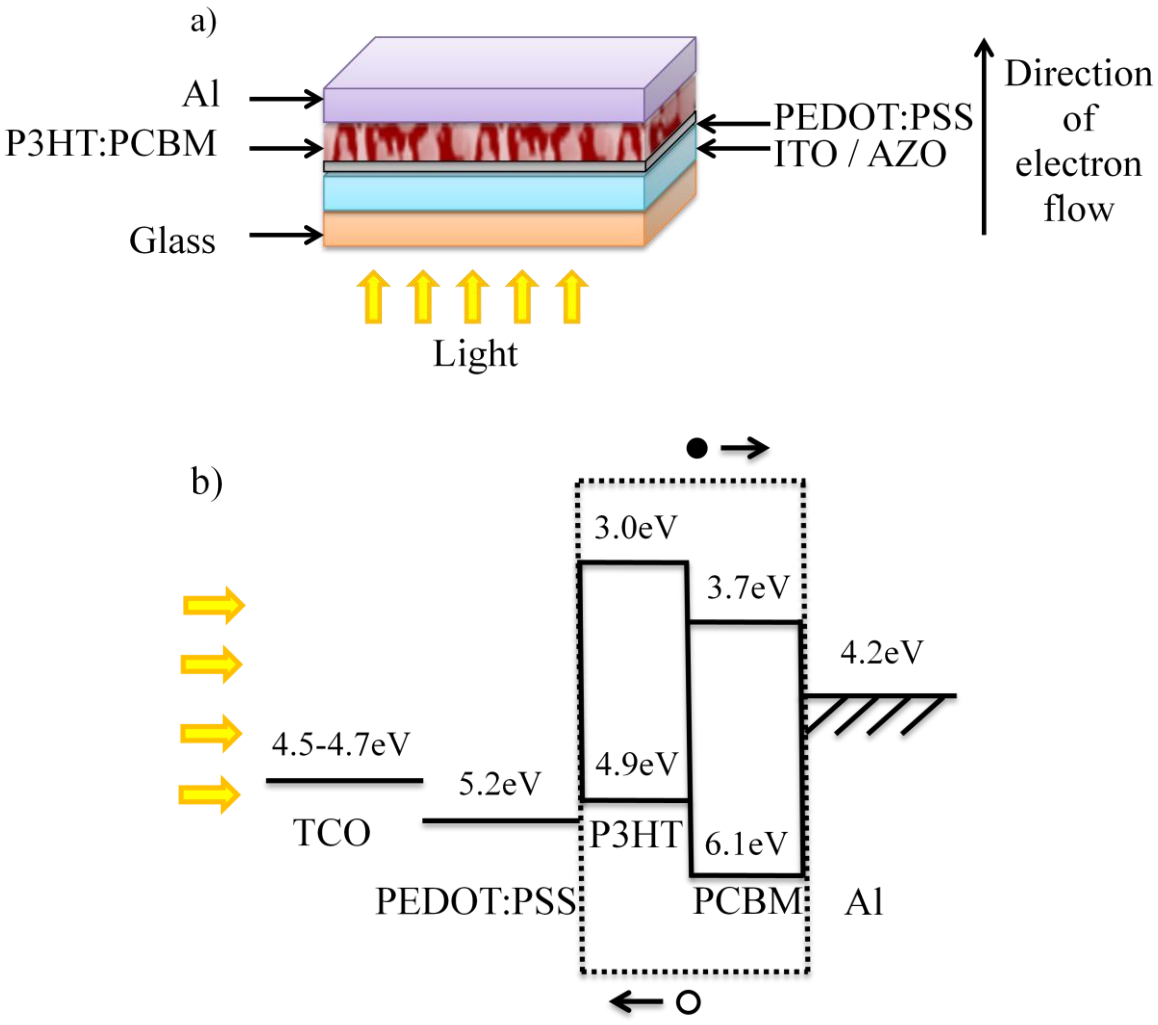


Figure 4.2. (a) Cross section structure and (b) the corresponding simplified energy band diagram of the AZO – P3HT:PCBM bulk heterojunction solar cell devices fabricated.

As test beds for the AZO transparent electrode technology, a series of solution-processed small-molecule bulk heterojunction photovoltaic cells were fabricated using poly(3-hexylthiophene) (P3HT) as the electron donor and [6,6]-phenyl C61-butyric acid methylester (PCBM) as the electron acceptor. A conventional device structure (TCO/PEDOT:PSS/ P3HT:PCBM/Al) was employed, and the device performance employing sol-gel processed AZO was compared to that employing sputtered ITO. Figure 4.2a is a schematic drawing of the device structure and direction of illumination (from the glass substrate of the device). Figure 4.2b shows the corresponding simplified energy band structure.

4.2 Experimental Details

4.2.1 AZO thin film preparation and characterization

The preparation of AZO thin films with thickness of ~480±30nm on glass substrates was performed by the sol-gel technique as described in section 3.1.2. The precursor thin films were decomposed in air at 500ºC for 1 hour using a Carbolite RWF RWF12/23 furnace, with a ramp rate of 10ºC/min. Some samples went through a post annealing treatment, either in flowing forming gas ($90N_2/10H_2$) or in vacuum (~10^{-6} torr) at 500ºC for 1 hour using a Carbolite 15/450 furnace, with a ramp rate of 20ºC/min.

As described in Chapter 3, the film thickness was measured using surface profilometry, and confirmed by examining the cross-sectional view of specimens using SEM. The structural features were studied by XRD, the morphological characteristics were studied by AFM, and the material chemical analyses were performed by using XPS and

synchrotron on the ESRF (Grenoble, France). Finally, the optoelectronic properties were investigated by UV-Vis spectrometer and Hall measurements, respectively.

4.2.2 Device fabrication and characterization

4.2.2.1 Substrate cleaning and treatment

The AZO and ITO thin films were firstly cleaned with isoproponal and dried in air. They were then etched to stripes 2mm wide as described in section 3.1.3, followed by a cleaning process. Then, oxygen plasma treatment of AZO and ITO was carried out for 30 seconds before depositing PEDOT:PSS.

4.2.2.2 Device fabrication

As described in section 3.1, a layer of PEDOT:PSS was applied on top of the ITO or AZO by spin coating. Then, P3HT:PCBM solution was spin coated at 700rpm for 15s and annealed on a hotplate at 140°C for 10 minutes. Next, the cells were transferred into a vacuum chamber located inside the glove box, and Al electrodes (~100nm) were thermally evaporated through a shadow mask.

4.2.2.3 Device characterization

The devices were placed in a testing holder with continuous nitrogen gas flushing throughout the experiment. Current density-voltage (IV) and external quantum efficiency (EQE) characteristics were recorded as described in section 3.4.

4.3 Results and Discussion

As discussed, the properties of AZO anodes are strongly dependent on the deposition process, the post-deposition annealing and the presence of impurities.[81], [127], [129] This can be controlled by many process parameters, such as Al doping concentration, precursor solution concentration and annealing.

4.3.1 The influence of Al doping concentration on the properties of AZO thin films

As explained in Chapter 2, Al doping has a significant impact on the film electrical properties. AZO thin films with various Al doping concentrations of 0, 0.5, 1.5 and 3at.% were fabricated and characterised to optimize their optoelectronic performance. All thin films were grown by decomposing 1.5M (molar) precursor solution in air at 500°C on glass substrates without annealing treatment. A set of 24 thin films were fabricated for this study (6 samples at each doping concentration). All the thin films studied have an average thickness of around 480±30nm, as measured by Dektak surface profiler and confirmed by SEM cross sectional images. As an example, the film prepared with 1.5at.% Al doping from 1.5M precursor solution is shown in Figure 4.3, and the thickness is about 485nm.

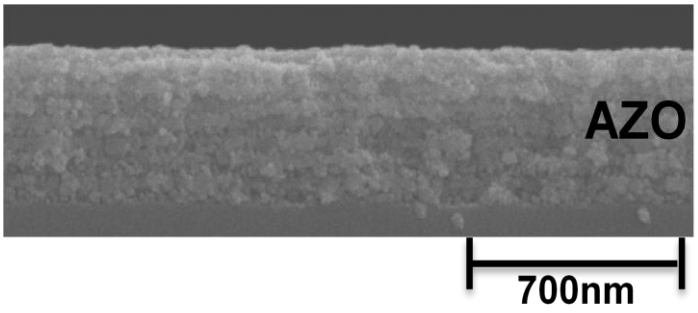


Figure 4.3. Cross-sectional SEM image of as as-grown AZO film prepared with 1.5at.% Al doping from 1.5M precursor solution, showing the films thickness of ~485nm.

4.3.1.1 Structural properties of AZO films with various Al doping concentrations

The literature notes a crystal structural change in AZO films upon doping.[49] As such, θ-2θ X-ray diffraction (XRD) spectra were measured to determine any effect that the Al doping may have on the structural properties of the AZO films.

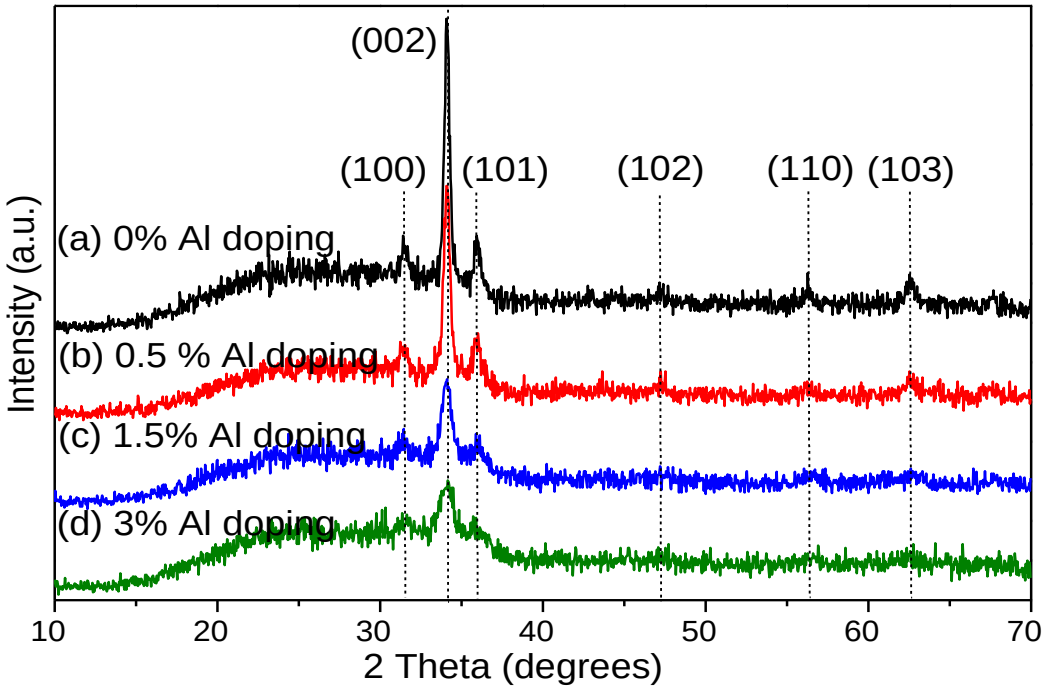


Figure 4.4. X-ray diffraction profiles of as-grown AZO thin films prepared from 1.5M precursor solution with Al doping concentrations ranging from 0 to 3 at.%.

Figure 4.4 displays typical XRD patterns, showing the structural implications of Al dopant incorporation into the ZnO lattice. At all doping levels, the main characteristic peaks corresponded to the zinc oxide reflections from a hexagonal wurtzite phase regardless of the degree of doping. As can be seen, there is no other crystalline phase observable, such as insulating aluminium oxide (Al_2O_3) [178] or gahnite ($ZnAl_2O_4$), [179] which were reported to be present in the grain boundary regions in AZO films as secondary phases when ZnO is heavily doped. This suggests that the Al is incorporated into the lattice as a subsitutional ion.[180] In addition, all films have reasonably sharp (002) diffraction peaks

while the other peaks appear relatively weak, indicating that the films are oriented with their c-axis perpendicular to the substrate.[181], [182] It is believed that this preferential orientation is due to the minimization of surface energy and internal stress.[183] Furthermore, the highest peak value from the XRD measurement was obtained from the undoped ZnO film, demonstrating that films deposited without doping have a superior degree of preferential orientation and a more ordered crystal lattice structure.[181]

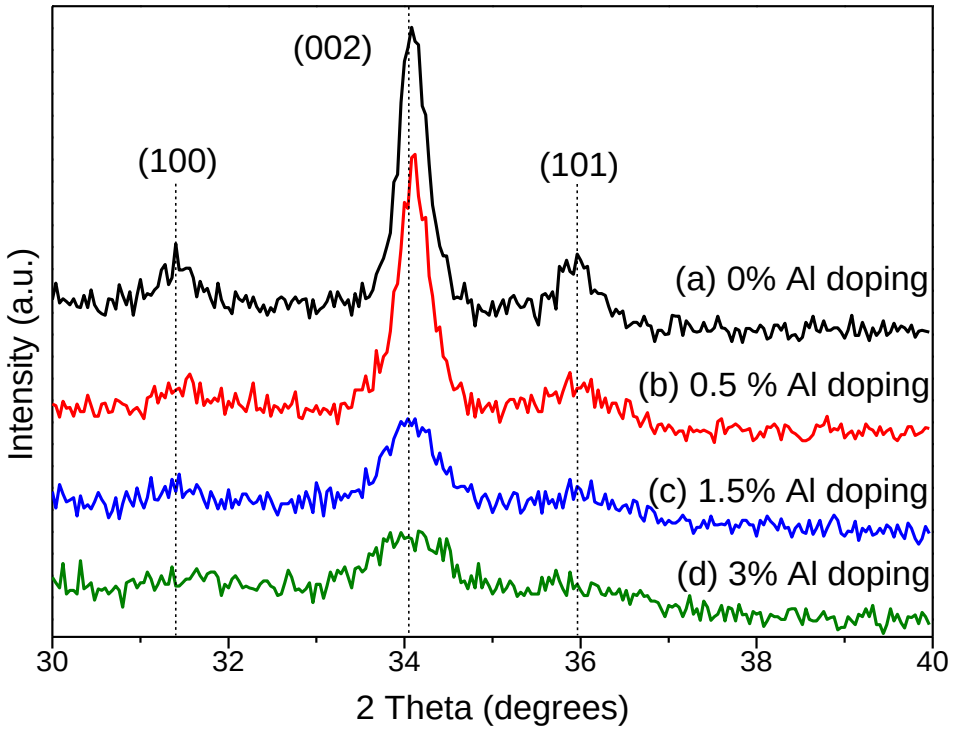


Figure 4.5. A narrow-scan of X-ray diffraction profiles of as-grown AZO thin films prepared from 1.5M precursor solution with Al doping concentrations ranging from 0 to 3 at.%, showing the peak broadening and intensity reduction upon Al doping.

In order to study the effect of Al doping, a detailed analysis of the XRD peaks shown in Figure 4.5 was carried out by fitting the peaks using a Gaussian function. It was found that there is a significant peak broadening (as shown by the FWHM values in Table 4.1, a well-defined number used to compare the quality of data), intensity reduction, as well as an insignificant shift in (002) peak position toward higher 2θ value with increasing Al

content. Similar observations have been reported upon the increase of Al content in ZnO [184][185] and Co content in ZnO films as well.[180] Zhou *et al.*[184] suggested that an increase in doping concentration deteriorates the film quality and crystallinity, this was explained by the formation of stress induced by the ionic radius difference between Al and Zn, and the possible segregation of Al in grain boundaries for high doping concentrations. Furthermore, although not obvious in Figure 4.5, the (002) diffraction peak position of 2θ increases a little bit from 34.08±0.01° in the undoped ZnO films up to a higher angle of 34.16±0.03° in the 3at.% Al doped AZO films. This behaviour of the (002) peak shift upon doping can be further understood by using Bragg's law:[186], [187]

$$n\lambda = 2d\sin\theta \qquad \text{Equation 4.1}$$

Where λ is the X-ray wavelength (0.154nm), θ is obtained from diffraction angle of the (002) peak. By rearranging the equation as discussed in Chapter 3, the *c*-axis lattice parameters of the films were derived from the 2θ readings and are listed in Table 4.1.

Table 4.1. Variation of lattice parameters derived from as-grown AZO films prepared from 1.5M precursor solution with different Al content.

Al Doping (at.%)	2θ (degrees)	Lattice Constant, *c* (Å)	FWHM
0	34.08±0.01	5.255±0.006	0.39±0.05
0.5	34.10±0.01	5.243±0.006	0.45±0.01
1.5	34.12±0.02	5.231±0.012	0.79±0.01
3.0	34.16±0.03	5.209±0.016	0.97±0.02

A decrease in *c* value with increasing aluminium doping concentration was observed. This contraction of the ZnO lattice upon Al doping was also reported by other authors,[49] and is likely to be due to the difference in the ionic radius of the aluminium ion (Al^{3+}, 0.53 Å) and zinc ion (Zn^{2+}, 0.60 Å). When the smaller Al^{3+} replaces the bigger Zn^{2+}, the ZnO lattice will contract, with the degree of contraction dependent on the level of doping. As a consequence, the microstructural parameters of AZO films are altered.

4.3.1.2 Elemental composition of AZO films with various degrees of Al doping

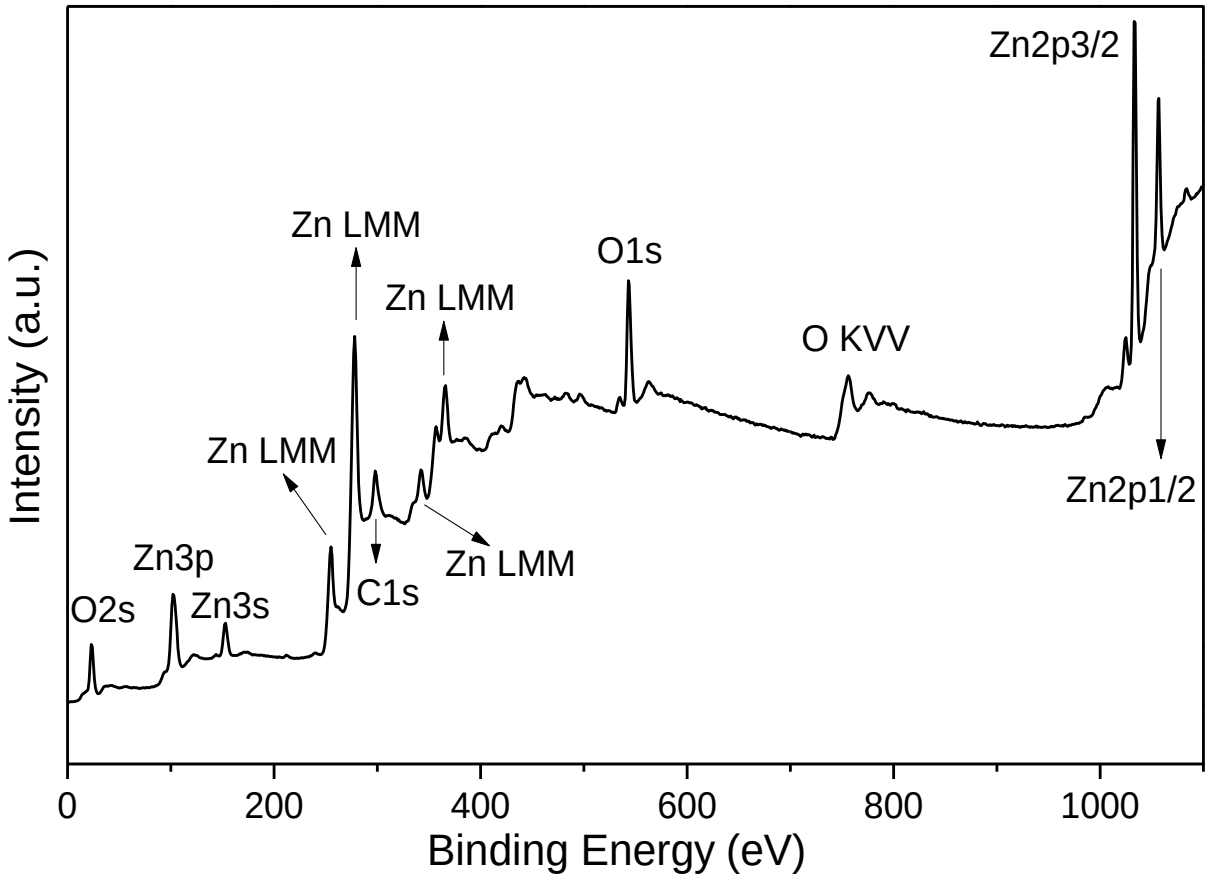


Figure 4.6. XPS spectrum of an AZO thin film with 1.5at.% doping film (XPS performed by Dr. Hugh Bishop).

The chemical composition of the AZO thin films was determined by X-ray photoelectron spectroscopy (XPS) with 4kV Ar^+ sputtering for 2 minutes to remove the surface layer to investigate the bulk material (the etching rate of the sample was around 1nm/min, the position of the C1s peak was taken as a standard). As an example, Figure 4.6 shows the XPS spectra of an AZO film with ~1.5at.% Al doping. A Zn $2p_{3/2}$ peak and the principal contribution to the O 1s peak are observed at 1021.8 and 530.3eV in binding energy, respectively, both typical for ZnO.[188]

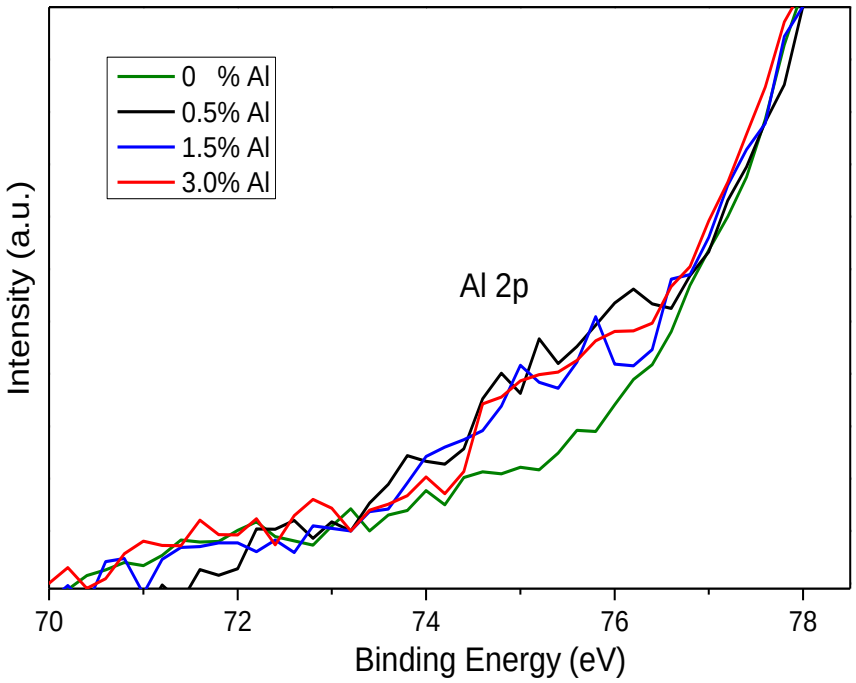


Figure 4.7. XPS spectra of Al 2p core level, showing the Al doping (range from 0 to 3at.%) in the ZnO thin film (XPS performed by Dr. Hugh Bishop).

A narrow scan of the Al $2p_{3/2}$ peak, centred at ~74.6eV (characteristic peak position corresponds to Al-O bonding [189] and the metallic Al peak at 72.4±0.3eV is not observed[190], [191]), was performed for AZO thin films with Al doping concentration of 0 to 3at.% (Figure 4.7). The XPS spectra revealed a clear Al $2p_{3/2}$ peak for the doped AZO

film as compared to the undoped i-ZnO film, with very low intensity. However, we cannot distinguish the amount of various doping concentration, as shown by the similar level of peak intensity. This is probably due to the low concentration of Al in the ZnO matrix and its low ionization value.[190] Other authors have had a great deal of difficulty to detect the Al 2p peak at these low doping concentrations.[192]

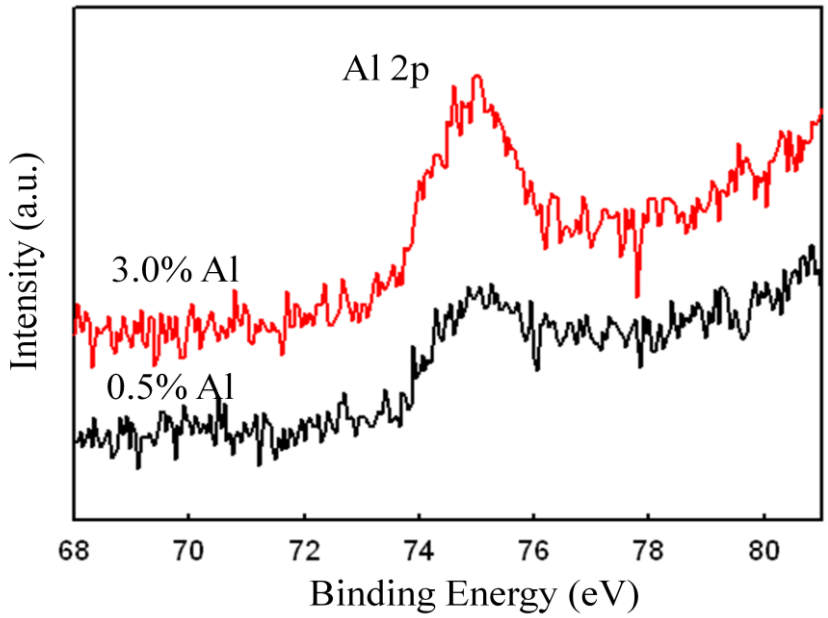


Figure 4.8. Synchrotron spectra of 0.5 and 3at.% Al doped AZO films, showing the increase in the Al 2p peak intensity (Synchrotron measurements were performed by Kelvin Zheng).

In order to further investigate the Al doping, we were able to send two samples with 0.5 and 3at.% Al doping concentration for synchrotron X-ray photoemission studies on the ESRF (Grenoble, France), as shown in Figure 4.8. The Al 2p peak centred at around 75eV is found while no metallic aluminium peak centred at 72.4±0.3eV is observable. In addition, we observe an increase in the Al 2p peak intensity with increase in Al doping from 0.5 to 3at.%.

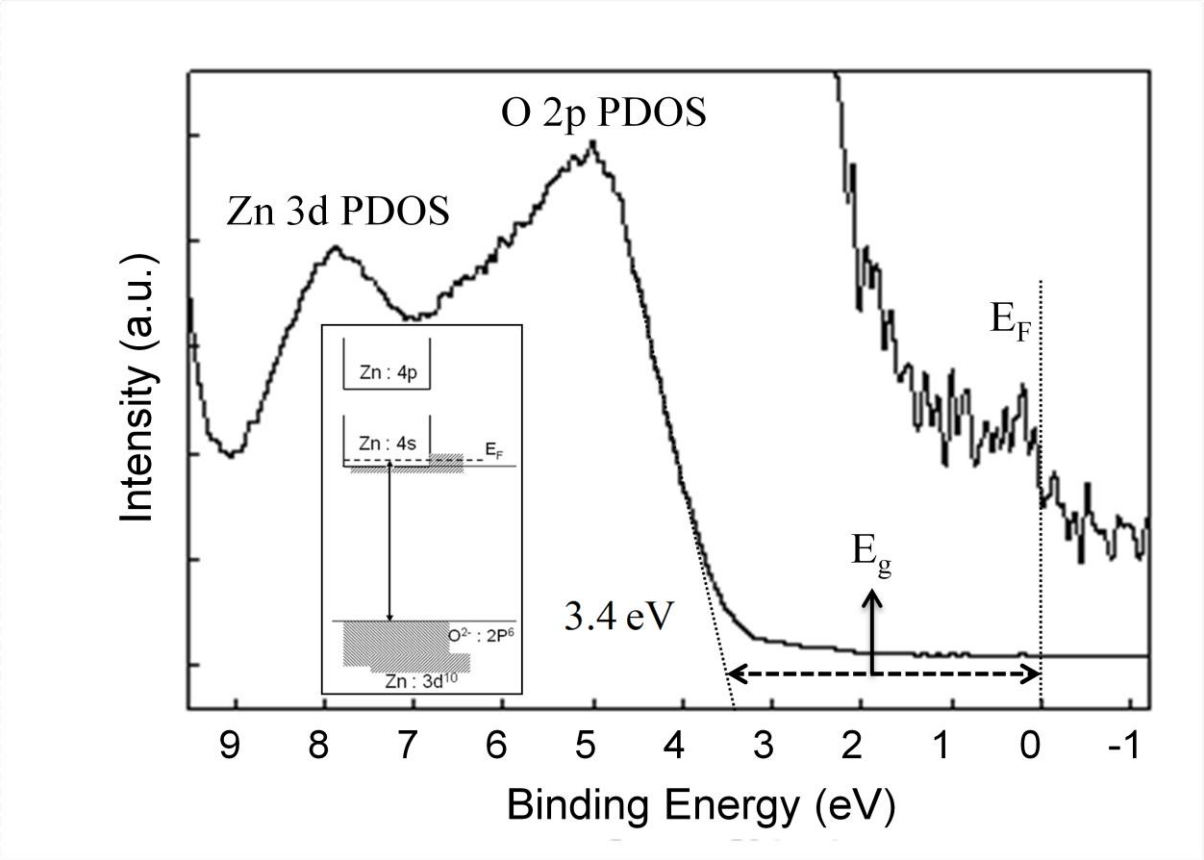


Figure 4.9. Valence band photoemission spectra of 0.5% Al doped ZnO thin film, showing part of valence band, including the O 2p partial density of states and Zn 3d partial density of states (PDOS). The conduction band emission near the Fermi energy is magnified, showing the occupation of conduction band upon doping. (Synchrotron measurements were performed by Kelvin Zheng).

The 0.5at.% Al doped sample was then sent for further hard X-ray photoemission synchrotron measurements on the ESRF, in order to gain a better understanding of the energy band structure. Figure 4.9 shows the valence band photoemission spectra. The sharp increase in intensity beyond ~3.4eV illustrates the top of the valence band of the AZO thin film. By extrapolating the peak edge, we are able to obtain the E_g of the film of around 3.4eV. Furthermore, the distinct peak shown at around 0eV (by enlarging the vertical scale) proves that Al is effectively doping the ZnO lattice, which results in the formation of a free electron cloud hence the peak. The inset shows the physical origin of

this observation, as discussed in Chapter 2. Together, these XPS results indicate the high quality of these AZO thin films, and the effective doping achieved by the addition of Al.

4.3.1.3 Optical properties of AZO films with various degree of Al doping

Optical transmission spectra of the above AZO films were studied by using the UV-Vis technique, as shown in Figure 4.10. All of the films exhibited high average optical transmittance of 85-95% in the visible region of the spectrum despite the degree of Al doping concentration. This high level of transparency and the similarity among various doping levels have also been observed by other authors.[181], [193], [194]

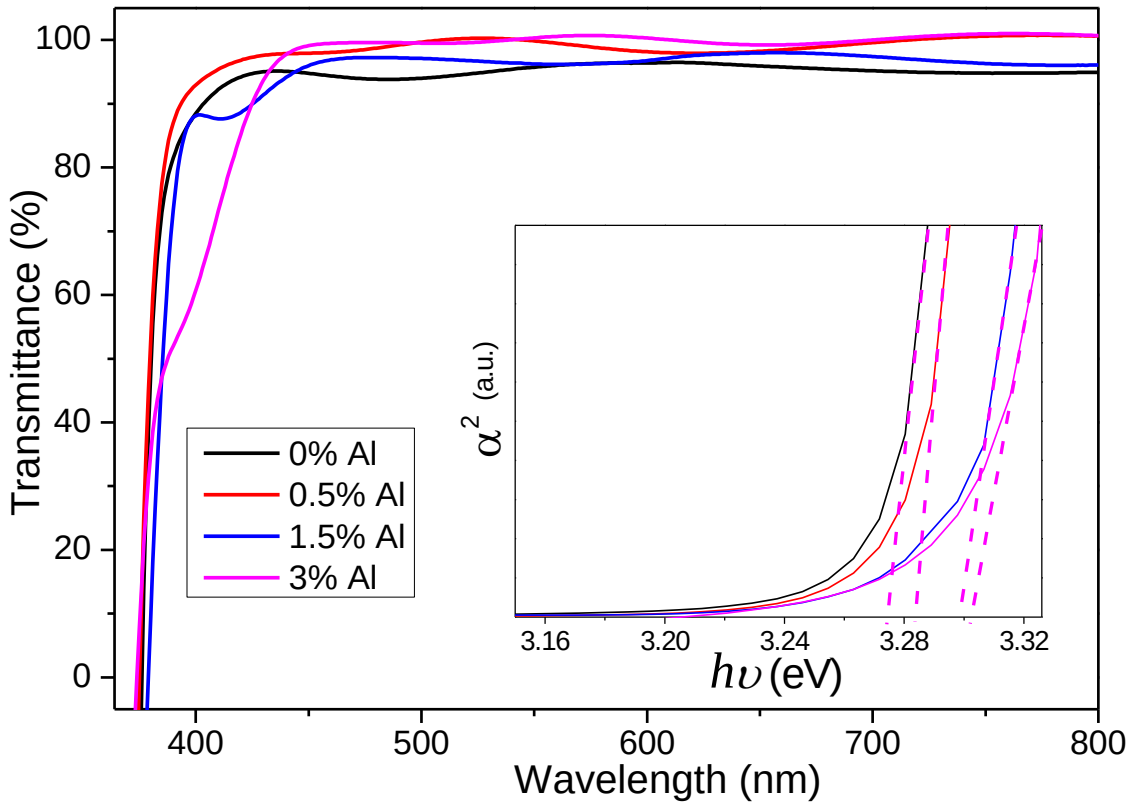


Figure 4.10. Optical transmission spectra of as-grown AZO films prepared from 1.5M precursor solution containing various degrees of Al doping (0, 0.5, 1.5 and 3at.%). The inset is the plot of the square of the absorption coefficient, α^2, vs. photon energy, $h\nu$, of un-doped ZnO and 0.5at.% doped AZO thin films deposited from 1.5M precursor solutions without annealing.

As discussed in section 3.3.1, ZnO is a direct-transition semiconductor and its absorption coefficient, α and band gap energy, E_g obey Tauc's relation:[159], [160]

$$\alpha \propto (h\nu - E_g)^{1/2} \qquad \text{Equation 4.2}$$

By plotting α^2 vs. $h\nu$ as shown in the inset of Figure 4.10, we observe a linear dependence of α^2 on $h\nu$ at higher photon energies (which is due to the fact that AZO films are direct band gap semiconductors[195]). By extrapolating this straight-line portion of the curve towards zero absorption coefficient (α=0), we are able to estimate the E_g values.[196]

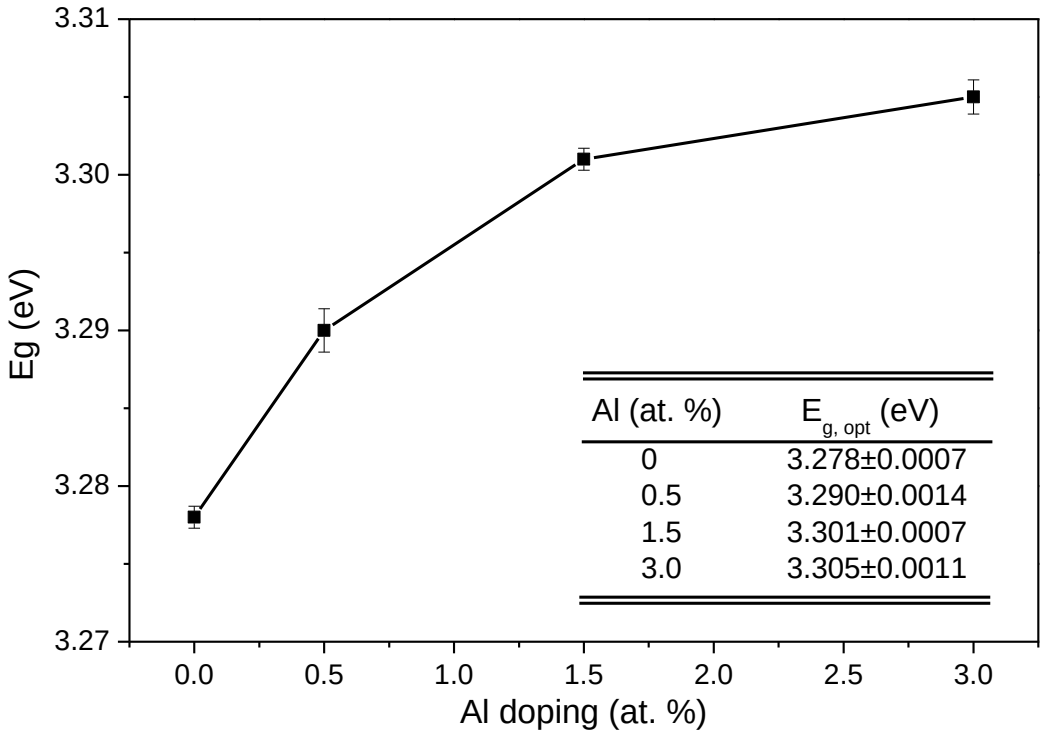


Figure 4.11. The energy band gap (E_g) dependence on the degree of aluminium doping of as-grown AZO films prepared from 1.5M precursor solutions. Data points and error bars correspond to the average and standard deviation of four to five films. Inset is a table showing the extrapolated optical band gaps of these AZO thin films.

As a quantitative summary, Figure 4.11 displays the effective band gap of undoped i-ZnO and 0.5, 1.5 and 3at.% Al doped AZO films obtained by extrapolation, and the E_g values are summarized in the inset table. It is observed that the E_g values estimated from the absorption edges vary depending on the degree of Al doping, and increased from ~3.278eV for the undoped i-ZnO film to ~3.290, ~3.301 and ~3.305eV for the 0.5, 1.5 and 3at.% Al doped films, respectively. This trend of E_g increment with Al doping was consistently observed across all tested films, Milliron *et al.*[49] and Lu *et al.*[197] have reported similar results. It is suggested that the changes of the optical band gap are due to the Burstein-Moss effect,[193][198] which causes the Fermi level to move into the conduction band due to changes in the carrier concentration.[158] This theory suggests that upon heavy doping, the bottom of conduction band is occupied by excited electrons (as illustrated in Figure 4.12 and Figure 4.9). Further electrons from the valence band thus need higher excitation energies to be promoted to the conduction band, hence effectively enlarging the E_g of doped zinc oxide films compared to undoped ones.

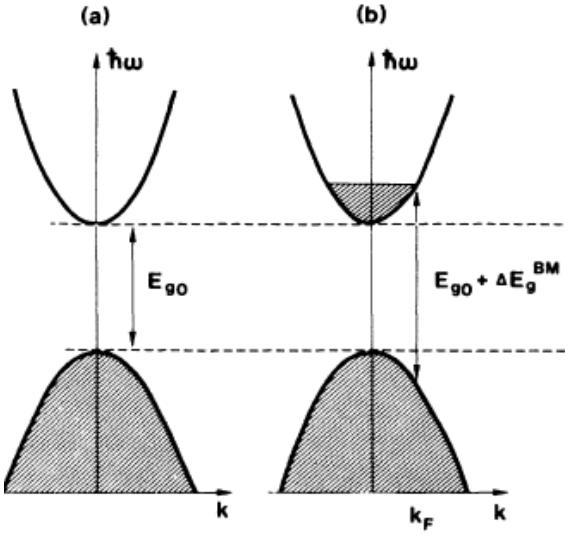


Figure 4.12. Schematic band structure with parabolic conduction and valence bands separated by E_{g0} (a) and after heavy doping assumed to have the effect of blocking the lowest states in the conduction band so that the optical gap is widened by a Burstein-Moss shift ΔE_g^{BM} (b). Shaded areas show the occupied states, and the Fermi wave vector k_F is indicated. (reprinted from reference [158]*)*

4.3.1.4 Electrical properties of AZO films with various degrees of Al doping

The dependence of electrical resistivity (ρ), carrier concentration (n), and mobility (μ) on the varying degrees of Al doping was studied using Hall measurements (as shown in Figure 4.13). A remarkable increase in free carrier concentration was demonstrated with increases in Al doping concentration, from ~2.59×10^{13} for undoped ZnO films to ~1.78×10^{17}, ~4.92×10^{17} and ~1.09×10^{18} cm^{-3} for 0.5, 1.5 and 3at.% Al doped films. This suggests that a small amount of Al dopant can introduce a large concentration of free charge carriers consistent with the XPS data and the E_g widening results discussed in previous sections, both as suggested by Sernelius *et al.*[158] (Figure 4.12). Similar observations were also reported upon the increase in indium doping concentration from 0 to 9at.% in sol-gel processed ZnO thin films.[199] Furthermore, the density and molar mass of ZnO is 5.606 g/cm^3 and 81.408 g/mol, and the Al doping concentration was between 0 and 3 at.%. If we assume that each Al atom added effectively provides one depant electron and no other doping mechanism is present, then the carrier concentration would be 0, 2.07, 6.22 and 12.45×10^{20} cm^{-3} for 0, 0.5, 1.5 and 3at.% Al doped films, respectively. This give us a rough idea about the effectiveness of Al doping, which is around 1% of Al atoms added are effectively donating electrons (not considering any other doping mechanism).

In addition, a decrease in mobility with increasing Al concentration was observed in Figure 4.13. This may be attributed to excessive lattice distortion at higher doping concentrations or simply the ionized impurities at higher carrier concentration [38] that increase the scattering events, and in turn deteriorate the electronic properties. Moreover, heavy doping can result in the segregation of the dopants at the grain boundary,[184] leading to increased scattering centres.

Combining the effect of both the carrier concentration and mobility changes, the resistivity of the films was reduced from ~1.70±0.15×10^5 to ~6.84±0.01×10^1 and ~3.38±0.01×10^1 Ω·cm with an increase in the Al concentration from 0 to 0.5 and 1.5at.%, representing a optimum value at 1.5at.% Al doping. Then the resistivity increased to 2.03±0.03×10^2Ω·cm with a further increase of the Al doping to 3at.% as a result of the low mobility (as shown in Figure 4.13). Such trends are not unusual and are frequently interpreted as being due to neutralization of the dopant atoms.[82], [195], [200–203]

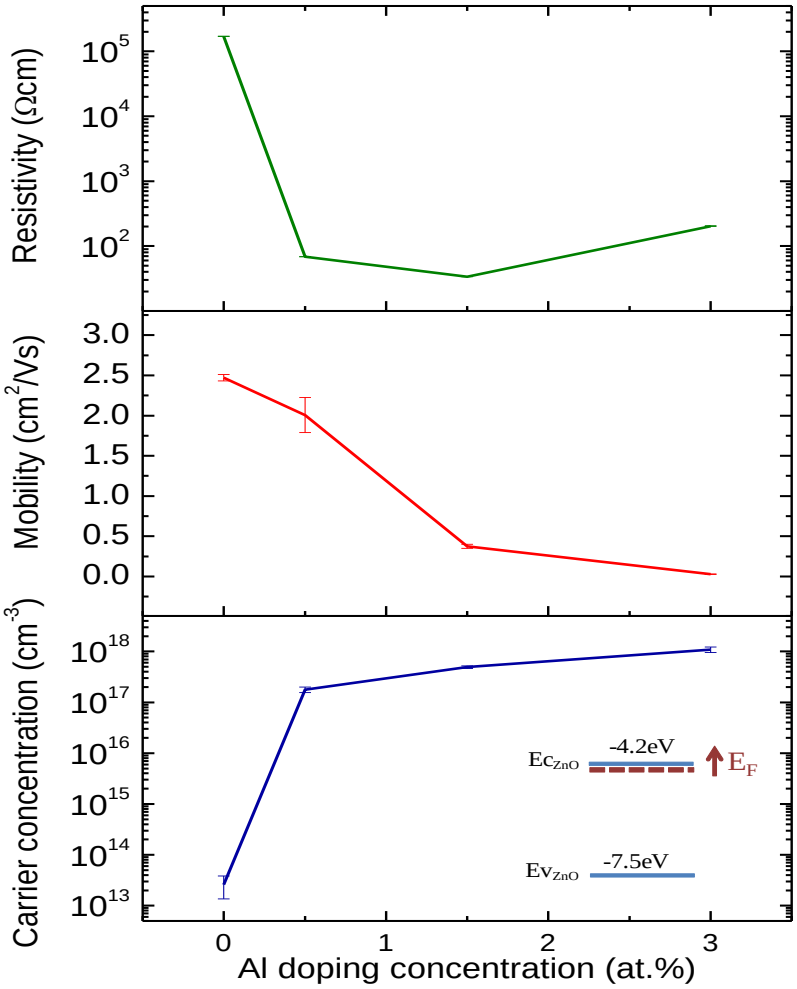


Figure 4.13. Electrical performance characteristics of as-grown AZO films prepared from 1.5M precursor solution with various Al doping concentrations (ranging from 0 to 3at.%). Data points and error bars correspond to the average and standard deviation across five to six thin films. Lines serve as a guide to the eye. A resistivity minimum is achieved at 1.5at.% Al doping concentration, with n = 4.92±0.3×$10^{17}$$cm^{-3}$, μ = 0.38±0.03 cm^2/V·s, and ρ = 3.34±0.01×10^1 Ω·cm.

4.3.2 The influence of precursor solution concentration on the properties of AZO thin films

As explained in section 2.4.2, the precursor solution concentration has a significant impact on the film performance. AZO thin films derived from various zinc acetate precursor solution concentrations (0.2, 0.7, 1.0 and 1.5M) were fabricated and tested to optimize the optoelectronic performance. The Al doping concentration is kept at ~1.5at.% because it was found to give rise to the lowest resistivity (as discussed in section 4.3.1.4). All thin films studied were as-grown by decomposing the precursor solution in air at 500°C. A set of 20 thin films were fabricated for this study (5 samples for each solution concentration).

4.3.2.1 Surface morphologies of AZO films derived from various precursor solution concentrations

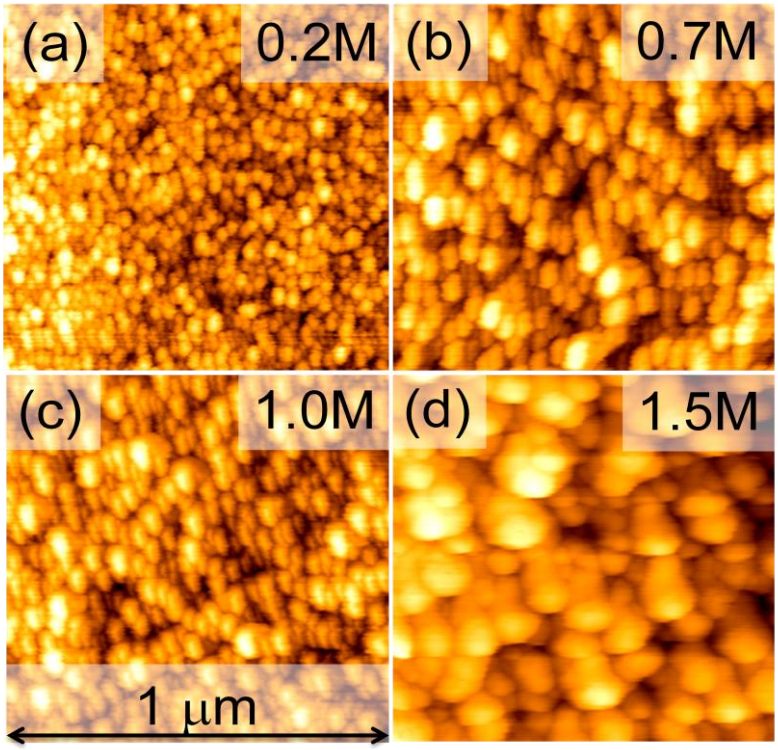


Figure 4.14. 1 µm × 1 µm topographic AFM images of as-grown 1.5at.% doped AZO thin films from (a) 0.2M, (b) 0.7M, (c) 1M and (d) 1.5M precursor solutions.

The surface morphologies of all the films were studied using AFM. Figure 4.14 displays AFM micrographs (1 × 1 μm) of AZO thin films grown from 0.2 to 1.5 M precursor solutions. It can be seen that the AZO particle size increased with an increase in the precursor solution concentration. It was found that the surface particles grown from lower concentration solutions (Figure 4.14a) have a lateral dimension typically of the order of 25-30 nm and a root mean square (rms) roughness of ~2.18 nm. The lack of grain growth is possibly due to the limited surface diffusion length of the Zn and O ad-atoms.[204]

Comparatively, we observed an increase in the particle size with increasing precursor solution concentration. Surface particles grown from 0.7, 1 and 1.5M solution were found to be ~60, ~60 and ~180 nm, much bigger than those from 0.2M solution (Figure 4.14 b, c and d). Furthermore, it was suggested that larger values of particle size can lead to increasing rms values of the AZO thin films,[205] and they were found to be ~3.04, ~3.86 and ~13.82 nm for the AZO thin films grown from 0.7, 1 and 1.5M solution. This implies a reduced grain boundary density which could be beneficial for mobility improvement.

4.3.2.2 Optical properties of AZO films derived from various precursor solution concentrations

Figure 4.15 displays the optical transmission spectra of AZO films prepared with 1.5 at.% Al doping concentration using precursor solutions of various molarities (0.2 to 1.5M). All of the films exhibit high average transmittance of ~90% in the visible range regardless of precursor solution concentration. This result also indicates that the difference in the initial precursor solution concentration (range from 0.2 to 1.5M) has little impact on the optical properties of AZO films.

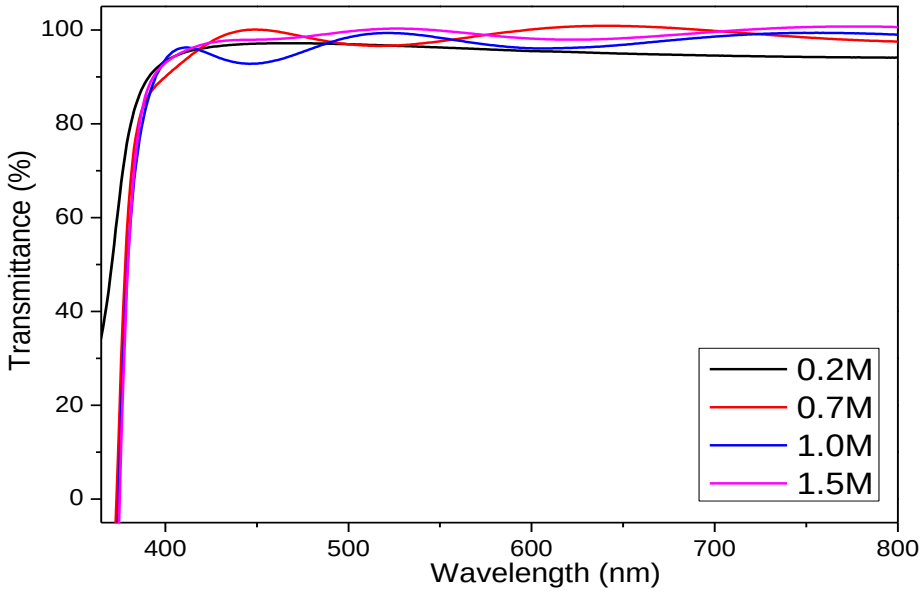


Figure 4.15. Optical transmission spectra of 1.5 at.% aluminium-doped zinc oxide films deposited from different zinc acetate solution molarities at a decomposition temperature of 500ºC for 1 hour without annealing.

4.3.2.3 Electrical properties of AZO films derived from various precursor solution concentrations

The dependence of electrical resistivity (ρ), carrier concentration (n), and mobility (μ) on various concentration of precursor solution was studied using Hall measurements and is shown in Figure 4.16. A significant increase in mobility was found with the increase in solution concentration, from ~0.16 $cm^2/V{\cdot}s$ for AZO films derived from 0.2M precursor solution to ~0.31, ~0.38 and ~2.01 $cm^2/V{\cdot}s$ for AZO films derived from 0.7, 1.0 and 1.5M precursor solution, respectively. This is in good agreement with the increase in particle size as shown by the AFM images in Figure 4.14,[206] which indicates a reduction in the likelihood of grain boundary scattering events. As a consequence, the resistivity was reduced primarily by the improved mobility up to 1M. The carrier concentration of AZO films was slightly decreased in 1.5M films. Bruneaux *et al.*[207] and Amalina *et al.*[208] suggested that charge trapping at grain boundaries will be the main reason for increased

resistivity at low carrier concentrations, and this perhaps is the cause in the increased resistivity in my results. From this data we can conclude that solution concentration has been demonstrated to be a critical parameter for the AZO sol-gel process.

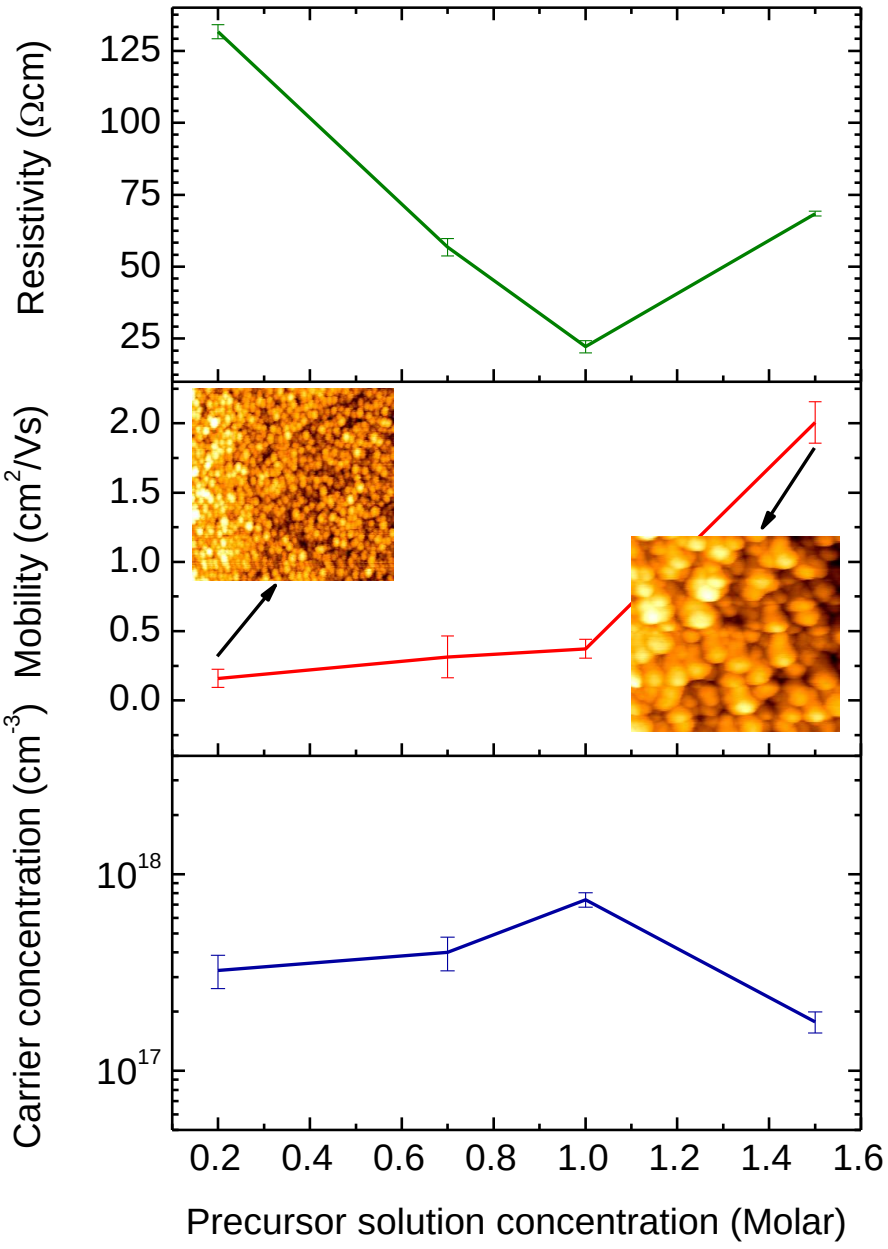


Figure 4.16. Electrical performance characteristics of as-grown AZO films prepared with 1.5at.% Al doping concentration from various precursor solution concentrations (ranging from 0.2 to 1.5M). Data points and error bars correspond to the average and standard deviation across five thin films. Lines serve as a guide to the eye. A resistivity minimum is achieved at 1M precursor solution concentration, with $n = 7.41\pm0.6\times10^{17} cm^{-3}$, $\mu = 0.38\pm0.06\ cm^2/V{\cdot}s$, *and* $\rho = 2.22\pm0.2\times10^{1}\Omega{\cdot}cm$.

4.3.3 The influence of post-annealing on the properties of AZO thin films

Annealing has a significant impact on lattice microstructure, thin film morphology, and therefore on the device efficiency. By optimizing the annealing conditions, a 1-2 orders of magnitude enhancement in the electrical conductivity of sol-gel processed AZO films can be achieved.[121], [127–129] Around 30 AZO thin films were characterized for the investigation of the effect of annealing. The 1.5at.% Al doped AZO thin films studied were derived from 1M precursor solution concentration. These AZO thin films were studied once upon decomposition in air at 500°C, then half of the samples were annealed in $90N_2/10H_2$ atmosphere and the other half were annealed in vacuum (~10^{-5} torr with ~10 samples for each condition). The evolution of the performance characteristics of various AZO thin films before and after annealing is presented below.

4.3.3.1 Structural properties of AZO films employing various post-annealing treatments

Figure 4.17 shows the XRD patterns from as-grown AZO thin films, annealed in $90N_2/10H_2$ atmosphere and in vacuum, respectively. It is noticed that all the films exhibit only the ZnO (002) peaks (as shown in the right inset), without any detectable peaks from possible secondary phases such as Zn, Al, Al_2O_3 or ternary phase of $ZnAl_2O_4$.[209] As discussed in section 4.3.1.1, this shows that these orientated films have grown with the *c*-axis perpendicular to the substrate. In addition, it was found that the quality and crystallization of the thin films were influenced greatly by the annealing conditions.

The results displayed in Figure 4.17 clearly show that (002) peak intensity is increased when the AZO film is annealed, with the highest value obtained for the vacuum annealed sample. Moreover, the position of the (002) peaks slightly shift towards higher 2θ values

upon annealing (left inset), from 34.05° for the as-grown thin film to 34.31° and 34.41° with annealing in $90N_2/10H_2$ and vacuum. This observation was also reported by other authors,[77] and was interpreted as more Al^{3+} ions substituting for Zn^{2+} ions upon annealing. In addition, another effect that should be taken into account is the reduction of residual stress of the films that built during growth, as suggested by Wang *et al.*[182] They attribute this to the increase in grain size, and also the small pores in the films combine into big holes. Such stress release by annealing therefore results in a peak shift to higher 2θ values.[210] Moreover, Marrocchelli *et al.*[211] have suggested that oxygen vacancy formation results in lattice contractions, this may have contributed to the observation in my sample as well, while the quantitative contributions of each of the above factors are not certain.

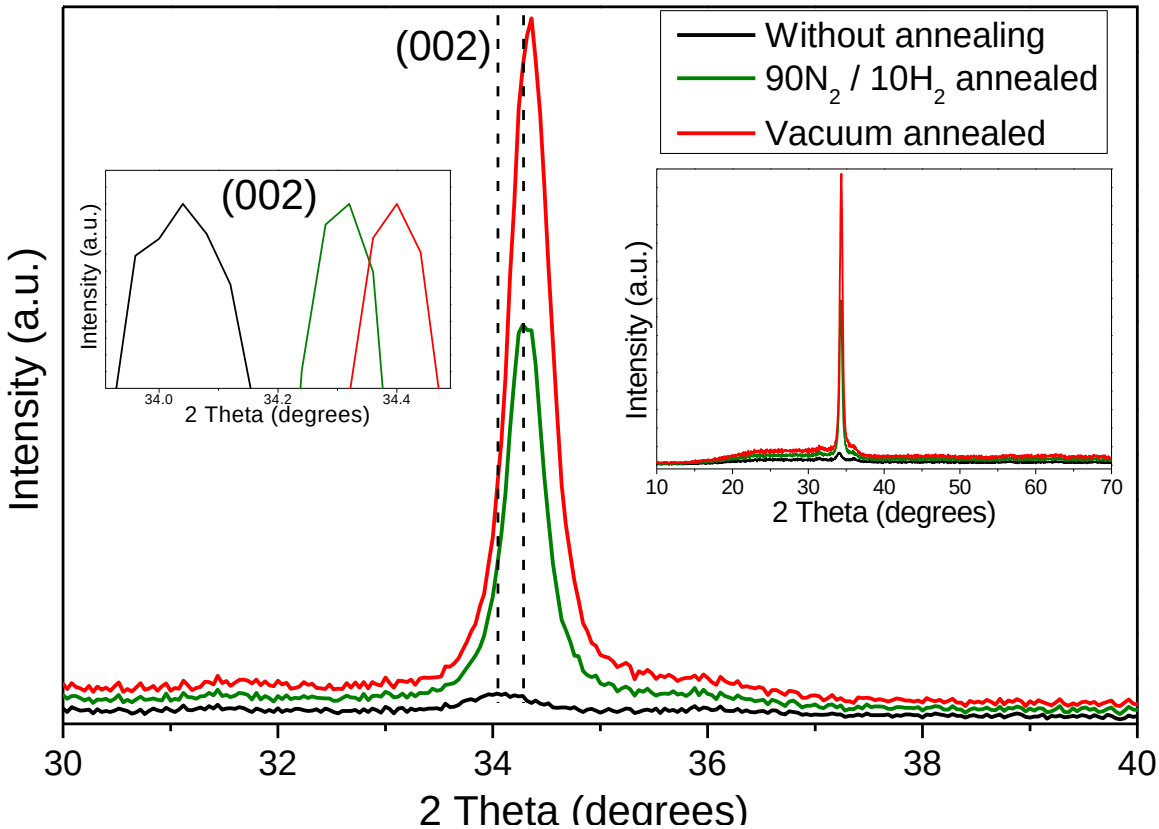


Figure 4.17. X-ray diffraction profiles of 1.5at.% Al-doped AZO thin film prepared from 1M precursor solution with various annealing conditions: before (black line), after annealing in $90N_2/10H_2$ (green line) and after annealing in vacuum (red line). The dashed lines serve as a guide to the eye. The left inset is a normalised scan shows the peak shift upon annealing, and the right inset shows a wide-scan.

4.3.3.2 Surface morphologies of AZO films employing various post-annealing treatments

The AFM images shown Figure 4.18 demonstrate the influence of annealing on the surface morphology of the AZO films.

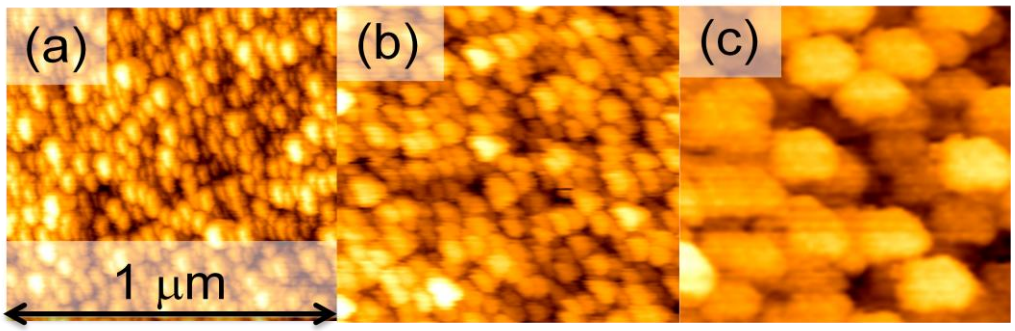


Figure 4.18. 1 × 1 μm topographic AFM images of 1.5at.% Al-doped AZO thin films prepared from 1M precursor solution with various annealing conditions: before (a), after annealing in 90N_2/10H_2 (b) and after annealing in vacuum (c).

The surfaces of the as-grown films present morphologies composed of closely packed small nano-grains as shown in Figure 4.18a (not treated samples). These nano-grains were found to grow laterally upon annealing in the 90N_2/10H_2 atmosphere (Figure 4.18b) and ultimately coalesce into more continuous thin films with high crystalline quality upon annealing in vacuum (Figure 4.18c), consistent with the XRD observations in section 4.3.3.1. It was found that the AZO particle size increased from ~60nm to about ~100 and ~300nm upon annealing in 90N_2/10H_2 and vacuum, leading to an increase in rms surface roughness from 3.03 to 3.17 and 4.28 nm. This process of coalescence causes major grain growth, which has been suggested to be strongly related to the migration of surface atoms.[181] Taken together, the AFM results and XRD data presented in Figure 4.17 suggest that grain growth and stress relaxation result in improved surface morphology and crystallinity, owing to the extra thermal energy provided by the annealing treatment.

4.3.3.3 Optical properties of AZO films employing various post-annealing treatments

Figure 4.19 shows the optical transmission spectra of AZO films prepared from 0.2 to 1.5M precursor solutions with 1.5at.% aluminium doping concentration after various annealing conditions (annealed in $90N_2/10H_2$ and vacuum, and compared to the sample without annealing).

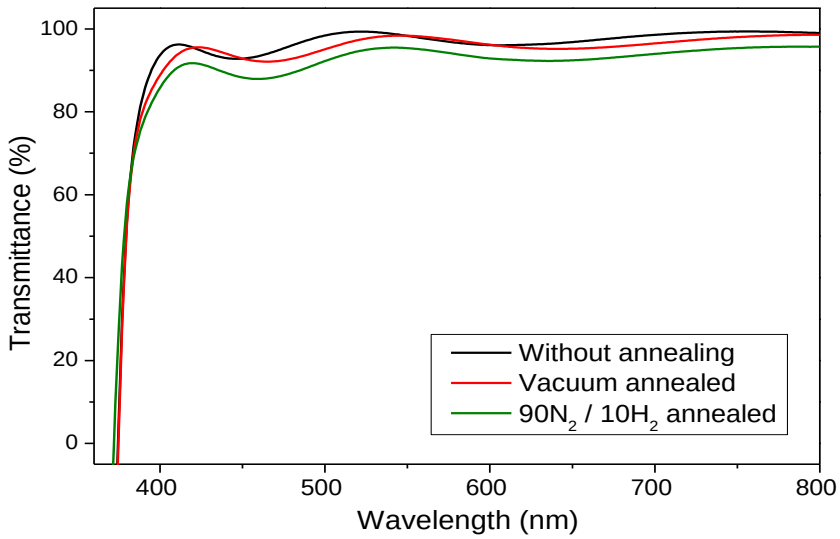


Figure 4.19. Optical transmission spectra of 1.5at.% Al-doped AZO thin film prepared from 1M precursor solution with various annealing conditions.

All of the films exhibited high average transmittance of 85-95% in the visible range despite the annealing conditions, with a slight reduction in transmittance for annealed samples as compared to the as-grown ones. This observation has been reported by other authors as well,[212] and was interpreted as higher scattering of the incident beam from the structural defects caused by Al doping. In addition, it was reported [193] that annealing in hydrogen can damage the surface of AZO films, although this damage does not affect the achieving of high transparency in the range of 390-1100nm. Together, these results imply that annealing does not have significant impact on obtaining high optical transparencies of AZO films, and they all demonstrate sufficiently good optical quality to be used as front electrode in solar cells.

4.3.3.4 Electrical properties of AZO films employing various post-annealing treatments

The dependence of electrical resistivity (ρ), carrier concentration (n), and mobility (μ) on various annealing conditions was studied using Hall measurements, as shown in Figure 4.20.

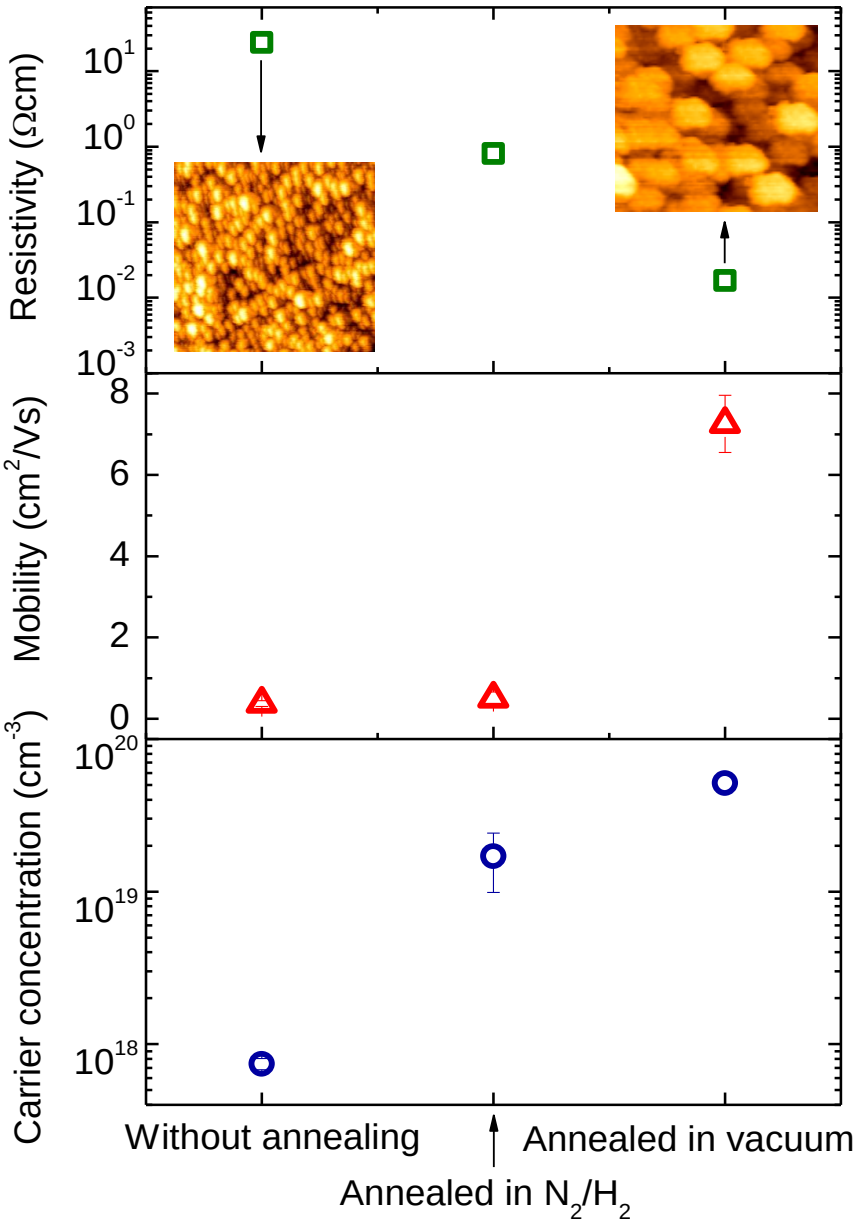


Figure 4.20. Electrical performance characteristics of AZO films prepared with 1.5at.% Al doping from 1M precursor solution, with various annealing conditions. Data points and error bars correspond to the average and standard deviation across around five thin films. Lines serve as a guide to the eye. A resistivity minimum is achieved when the AZO thin film is annealed in vacuum, with $n = 5.14\pm0.6\times10^{19} cm^{-3}$, $\mu = 7.25\pm0.7\ cm^2/V{\cdot}s$, and $\rho = 1.68\pm0.3\times10^{-2}\Omega{\cdot}cm$.

A significant increase in mobility was found, from 0.38 $cm^2/V{\cdot}s$ for the as-grown AZO films to 0.50 and 7.25$cm^2/V{\cdot}s$ for the AZO films annealed in $90N_2/10H_2$ and vacuum (Figure 4.20). This result is consistent with the XRD (002) peak shift towards higher angles as shown in Figure 4.17, as well as the increase in particle size as shown by the AFM images in Figure 4.18. This is likely to be due to the reduced grain boundary scattering events as discussed in section 4.3.2. Similarly, Lee *et al.*[122] observed that the grain size was increased upon annealing AZO in $95N_2/5H_2$, leading to reduced resistivity. In addition, we observed an increase in the (002) XRD peak intensity (Figure 4.17) upon annealing which indicates the lattice is re-arranged to achieve better crystallinity with improved *c*-axis orientation, and this is suggested to decrease the effect of grain boundary scattering on the resistance.[182] As suggested, thin film resistivity and (002) peak intensity is inversely proportional.[122] Furthermore, Chen *et al.*[126] suggested that annealing AZO thin films at 530°C can result in homogeneous and dense microstructure with decreased crystal defects. The healing of stress and increased crystallinity is also indicated by a shift and narrowing of the ZnO (002) peak in X-ray diffraction (XRD) spectra (consistent with my XRD data), resulting in enhanced carrier mobility.

As shown in Figure 4.20, a significant increase in carrier concentration from ~$7.41\times10^{17}cm^{-3}$ for the as-grown AZO films to ~1.70 and ~$5.14\times10^{19}cm^{-3}$ for the AZO films annealed in $90N_2/10H_2$ and vacuum atmosphere was observed. Similar observations have been reported by Musat *et al.*,[84] who achieved improved film conductivity when the films were annealed in forming gas (N_2/H_2 atmosphere) compared to those processed in air. In addition, annealing in vacuum is known to induce additional oxygen vacancies into the oxide lattice,[124], [127] owing to oxygen annihilation from the ZnO crystals [122] via desorption from the AZO surface, pores and grain boundaries.[121] It was suggested

by Fang *et al.*[213] that the more the oxygen vacancies exist in AZO thin films, the higher the electrical conductivity will be, owing to the fact that one oxygen vacancy can effectively donate two electrons. Moreover, annealing in vacuum or inert environment [126] have been suggested to improve conductivity by not only providing more oxygen vacancies but also activating Al donors more effectively.

The above-mentioned combined effects eventually lead to a significant reduction in the film resistivity, from ~23.9 to ~8.11×10^{-1} and ~$1.68\times10^{-2}\Omega\cdot$cm. This value is higher than the best resistivity obtained in the literature, where Agura *et al.*[214] demonstrated $8.54\times10^{-5}\Omega\cdot$cm (and average transmittance of over 88%) by using pulsed laser deposition technique on Corning #7059 glass substrate. However, the utilization of laser, magnets and high vacuum limited their practical application. Last but not least, it is worth mentioning that the carrier concentration in the annealed films is typically around 1.7 to 5.2×10^{19}cm^{-3}, which is above the critical value of ~1.33×10^{18} cm^{-3} to meet the Mott criterion for the onset of metallic behaviour (as explained in section 2.3.4). This means that these AZO films have the electronic quality to be used as transparent electrode in solar cells.

4.3.4 Solar cell efficiency characterization

A set of fifteen TCO/PEDOT:PSS/P3HT:PCBM/Al solar cell devices (10 AZO and 5 ITO devices) were fabricated to study the performance characteristics of sol-gel processed AZO films as front electrode, and to compare to the reference ITO devices (using commercial ITO films). Two cells were found defective and are not included in the discussion. From the previous discussions in this chapter, AZO thin films with 1.5 at.% Al doping derived from 1M precursor solution concentration demonstrate the best electronic

performance after annealing in vacuum. Thus all the AZO devices employed these optimized processing parameters. Devices were tested under simulated sunlight (AM 1.5G). The overall device properties are summarized in Table 4.2.

Table 4.2. Performance characteristic of P3HT:PCBM devices employing AZO or ITO as transparent conducting electrode.

TCO	J_{sc} (mA/cm^2)	V_{oc} (V)	FF	PCE (%)	R_s ($\Omega \cdot cm^2$)	R_{sh} ($\Omega \cdot cm^2$)
AZO	2.74±0.52	0.64±0.02	0.31±0.03	0.53±0.03	53.4±0.3	319±9
ITO	10.48±0.13	0.61±0.005	0.57±0.01	3.63±0.09	1.45±0.2	416±8

AZO based devices exhibit a typical performance of 0.53±0.03% in terms of power conversion efficiency (PCE), and the reference devices fabricated with ITO gave a typical performance of 3.63±0.09%, representing a ~7-fold efficiency difference. Since AZO thin films were shown to demonstrate good optical properties, this difference in device performance is most likely caused by the electronic properties of AZO as compared to ITO electrode. This was investigated using Hall measurement and is shown in Table 4.3.

Table 4.3. Electrical properties of sol-gel processed AZO films prepared from 1M solution precursor with 1.5at.% Al doping after annealing in vacuum, and sputtered ITO films obtained by commercial means.

Thin film	Carrier conc., n (cm^{-3})	Mobility, μ ($cm^2/V \cdot s$)	Resistivity, ρ ($\Omega \cdot cm$)
AZO	$5.14\pm0.6\times10^{19}$	7.25±0.7	$1.68\pm0.03\times10^{-2}$
ITO	$1.17\pm0.1\times10^{21}$	36.7±0.1	$1.45\pm0.01\times10^{-4}$

It can be seen that both the carrier concentration (n) and mobility (μ) of ITO thin films are considerably higher than that of the AZO thin films, resulting in a much lower electrical resistivity (ρ) of $1.45\pm0.01\times10^{-4}$ as compared to the optimized AZO, $1.68\pm0.03\times10^{-2}\Omega\cdot$cm. This is consistent with the device series resistance values observed in Table 4.2, which are ~53.4 and ~1.45 $\Omega\cdot cm^2$ for AZO and ITO based devices, respectively, leading to the significant difference in J_{sc}. This indicates higher resistivity of AZO thin film caused parasitic losses in the device. We can also notice the difference in shunt resistances for AZO and ITO based devices, which are ~319 and ~416 $\Omega\cdot cm^2$, respectively, similar to what have been reported in literature.[215] This is likely the cause of the difference in FF (shown in Table 4.2) between the two types of devices.

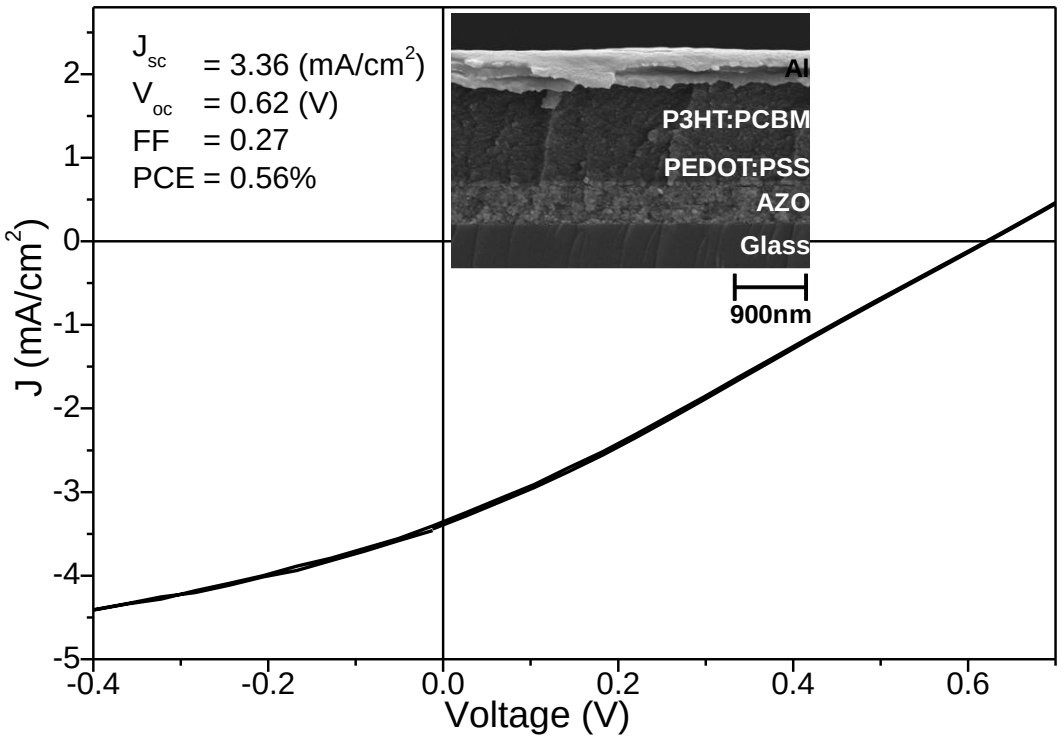


Figure 4.21. IV performance characteristics of a typical solution processed AZO (1.5at.%Al, 1M sol concentration) / PEDOT:PSS / P3HT:PCBM / Al solar cell. The inset is an example showing the cross sectional view of such devices.

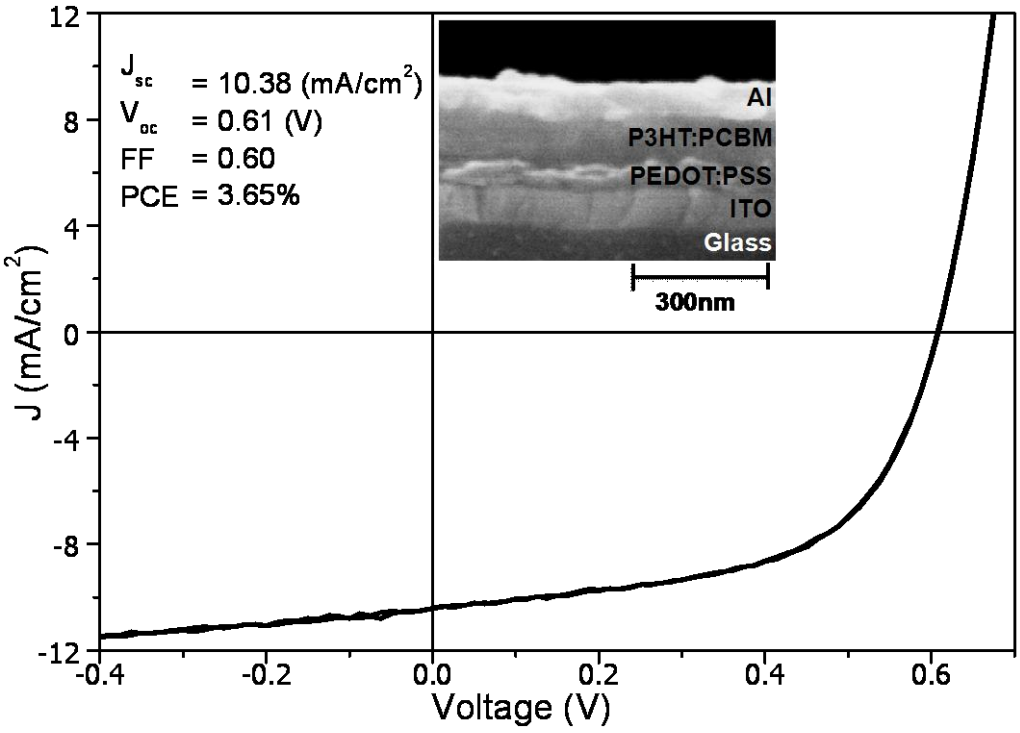


Figure 4.22. IV performance characteristics of a typical sputtered ITO / PEDOT:PSS / P3HT:PCBM / Al solar cell. The inset is an example showing the cross sectional view of such devices.

Figure 4.21 and 4.22 displays the current density - voltage curve of a typical AZO and ITO devices respectively, and their corresponding SEM cross sectional images. The SEM images shown that both the solution processed AZO and sputtered ITO layers demonstrate uniform morphology. Therefore the improved IV curve presented in Figure 4.22 for the ITO device compared to Figure 4.21 for the AZO device lies mostly in the better electronic properties. However, the sol-gel processed AZO devices employed far less technical processing and materials cost, therefore it is appealing to serve as an effective alternative to ITO, with a 2 orders of magnitude improvement in resistivity.

4.4 Conclusion

The growth of AZO thin films using the sol-gel spin-coating technique has been investigated and optimized, including the influence of Al-doping concentration, precursor solution molarity and post-annealing on the film properties. AZO thin films with transmittances of ~90% and resistivity of the order of $10^{-2}\Omega\cdot$cm have been achieved. The electronic properties show a strong Al-doping, sol-concentration and post-annealing dependence. The effective incorporation of aluminium was proved by XPS spectra, and shown to cause a widening in AZO band gap. Around 1.5 at.% aluminium dopant incorporation optimized the metallic behaviour which can be attributed to the generation of abundant free electrons.

Furthermore, it was demonstrated that solution molarity and post-annealing have a remarkable impact on film morphology and electrical properties. Low molarity growth (0.2 M) without annealing leads to a nano-grain structure, giving rise to low carrier mobility due to grain boundary scattering. By increasing the solution molarity to 0.7M and above, or upon annealing, nano-grains collapsed into micron-sized morphology, leading to improved mobility and better film conductivity. XRD revealed that upon annealing, the grain growth is associated with a release of tensile stress as shown by the peak shift as well as an improvement in crystallinity as shown by the peak intensity increment, leading to a ~3 orders of magnitude reduction in resistivity upon post-annealing in vacuum compared to the as-grown films.

Lastly, AZO based OPV devices were investigated by comparing to those fabricated with sputtered ITO. The poorer electrical performance of AZO thin films results in a ~7-fold

device efficiency difference. However, utilizing of AZO thin films removes the need for costly ITO material and complicated sputtering processing. Outright performance may have reduced slightly, but this may be outweighed by the benefits of far less material usage and simpler processing.

Chapter 5 – The Improvement of Organic Solar Cell Performance by Introducing Interfacial Buffer Layers

From the discussion of organic solar cell performance in Chapter 2, it is well known that charge carrier extraction at the organic material/electrode interface has a great impact on the overall device performance. In this chapter, I will discuss more specifically the possibility of optimizing the interfacial layers in order to improve device performance. I will focus on inverted devices which offer additional advantages such as improved stability compared with the regular device structure.[8], [22] A review of previous work from the literature and results of my own work will be discussed in order to define a route towards gaining a better understanding of the interfacial behaviour and how to enhance device performance.

5.1 Introduction

5.1.1 The role of buffer layers

The performance of solar cells is greatly affected by the quality of electrodes, which are responsible for efficient charge extraction and transportation. To improve this function, buffer layers have been utilised at the anode/semiconductor and the cathode/semiconductor interfaces; primarily to promote charge exchange and improve the overall cell performance.[216] These functional buffer layers (also known as interfacial layers, interlayers, selection layers, injection layers, blocking layers) are essential to achieve optimized device performance. They are introduced to engineer the active layer/electrode interfaces by inducing interfacial charge redistribution, geometrical

modifications, and/or chemical reactions.[217] Figure 5.1 illustrates two commonly studied structures (conventional and inverted) for single junction polymer solar cells, where buffer layers are introduced at the anode, as a hole-injection layer (HIL) and at the cathode as an electron-injection layer (EIL).

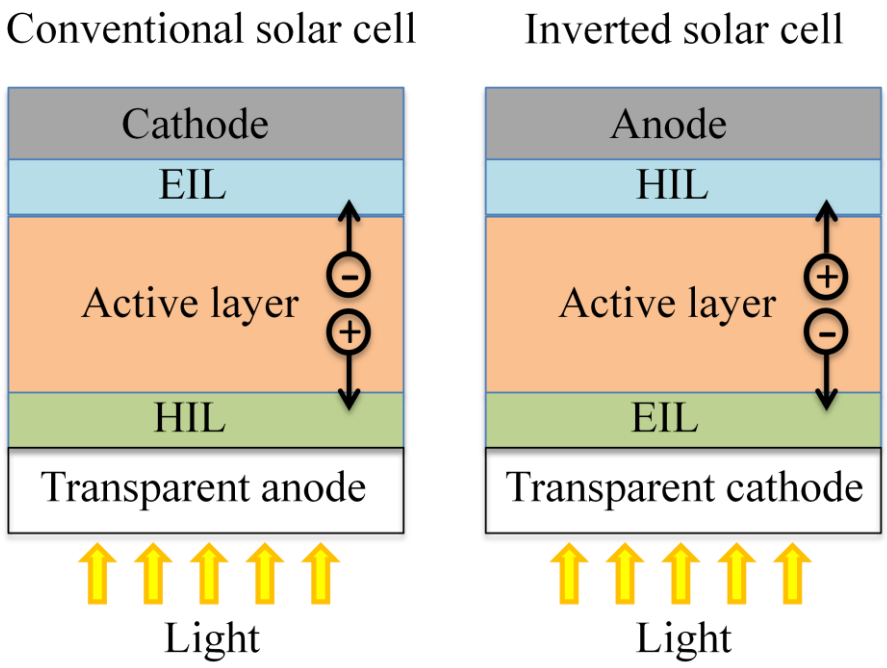


Figure 5.1. Typical device geometry of single junction conventional and inverted polymer solar cells. EIL: electron injection layer, HIL: hole injection layer. (after reference [216]*)*

5.1.2 Material selection for buffer layers

The materials used as buffer layers in a particular device structure are mainly selected based on the alignment of energy levels and charge transport properties. In addition, they can also smooth rough substrate surfaces [218] and block the migration of electrode materials through to the photoactive layer by stopping impurity migration.[219] Furthermore, they have been shown to protect the photoactive layer from the diffusion of oxygen and water.[220], [221] Finally, buffer layers can be used to reverse the device polarity, enabling ITO to be used as a cathode in the inverted device structure.[22], [222]

5.1.2.1 Anode buffer layers

Most of the polymer solar cells currently being fabricated use ITO substrates, both in conventional and inverted architectures. ITO has a work function of around 4.7 eV,[223] which is not well aligned with either the HOMO level of common donor polymer materials or with the LUMO level of fullerenes, as shown in Figure 5.2 and Table 5.1. The resulting non-Ohmic junctions at the ITO/donor or ITO/acceptor interfaces causes the optimal open circuit voltage (V_{oc}) value to deteriorate; since V_{oc} is determined by the energy levels of the donor and acceptor materials in the case of Ohmic contacts.[224], [225] This allows ITO to be used as either an anode or cathode, but its selectivity (the ability of an electrode to distinguish between the different charged carrier types, i.e. to either extract electrons and block holes, or extract holes and block electrons) has to be improved. This can be achieved by inserting a buffer layer.[226], [227]

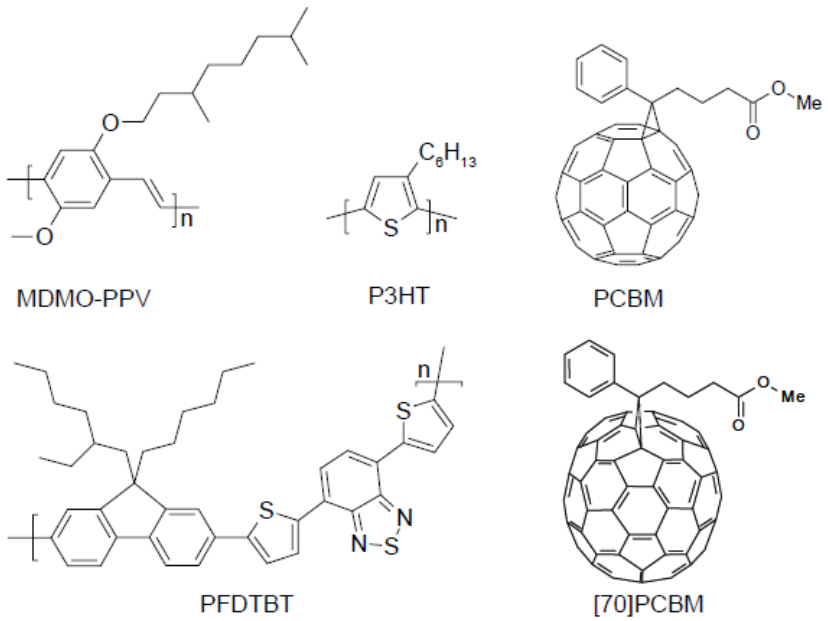


Figure 5.2. Donor and acceptor materials used in polymer-fullerene bulk-heterojunction solar cells. Donors: MDMO-PPV = poly[2-methoxy-5-(3´,7´-dimethyloctyloxy)-p-phenylene vinylene]; P3HT= poly(3-hexylthiophene); PFDTBT: poly[2,7-[9-(2´-ethylhexyl)-9-hexylfluorene]-alt-5,5-(4´,7´-di-2-thienyl-2´,11´,3´-benzothiadiazole)]. Acceptors: PCBM: 3´-phenyl-3´H-cyclopropa[1,9][5,6]fullerene-C60-Ih-3´-butanoic acid methyl ester; [70]PCBM: 3´-phenyl-3´H-cyclopropa[8,25][5,6]fullerene-C70-D5h(6)-3´-butanoic acid methyl ester. (re-printed from reference [228])

Table 5.1. The HOMO and LUMO levels of the above listed polymer materials.

Material	HOMO (eV)	LUMO (eV)	Ref.
P3HT	-5.2	-3.0	[229]
PCBM	-6.1	-3.7	[230]
MDMO-PPV	-5.2	-2.7	[231]
PFDTBT	-5.0	-3.3	[232]
[70]PCBM	-6.1	-4.3	[233]

The main role of an anode buffer layer is to improve the anode electrode efficiency in collecting and extracting positive carriers (i.e. holes).[226] For this purpose, the ideal requirements for materials selection of the HIL can be summarized as:

1. well aligned energy levels which provide Ohmic contacts at the HIL/donor material interface,
2. good hole conductivity which will not increase the device series resistance (R_s),
3. good carrier selectivity which will block electron transport,
4. good transparency which allows the incident light to reach the active layer when used at the front contact (in conventional device structures as shown in Figure 5.1),
5. diffusion barrier to prevent the migration of materials from electrode to active layer (eg. stop the indium migration from ITO to the polymer [234]),
6. ideally can act as barrier layers to prevent the ingress of oxygen and water which degrade organic materials.[235]

In order to achieve these goals, some popular materials that have been used are PEDOT:PSS,[236] modified PEDOT:PSS [237] and metal oxides.[238]

PEDOT:PSS

The first device performance improvement upon the insertion of conducting polymers as HILs was reported in the late 1990s,[239] after the success in modifications to OLED designs.[240] The work showed that PEDOT:PSS improved the hole injection properties at the ITO contact when compared to devices without PEDOT:PSS. PEDOT has the advantage of low toxicity and high transparency; mixing with PSS subsequently circumvented its solubility problem. This combination of PEDOT:PSS thus results in a more soluble mixture in aqueous solution with good film conductivity and visible light transmissivity,[241], [242] making it a widely used material choice. A more comprehensive review of its synthesis, properties and application can be found in other references.[243] Here I have reviewed work incorporating PEDOT:PSS by other authors and summarized the main results into Table 5.2, where the advantages of introducing different kinds of HILs are listed.

MoO_3

Similarly, MoO_3 has been widely used as a buffer layer to reduce the contact resistance by altering the energy barrier between the conducting polymer and electrode.[244] It has been demonstrated as an efficient hole-injection material for organic devices,[245], [246] and promotes the collection of photogenerated charges and decreases the leakage current.[247] Some authors reported a similar, or even better, performance compared to the devices using a PEDOT:PSS buffer layers (the 5^{th} and 6^{th} examples in Table 5.2).[248] A summary of a few reports on the effect of using various HIL buffer layers is shown in Table 5.2.

Table 5.2. A summary of solar cell performance utilizing various anode buffer layers (HILs). The photovoltaic parameters are compared to those measured for a reference cell (values in parentheses), when available, made with an anode without HIL.

HIL	Cell architecture	J_{sc} (mA/cm^2)	V_{oc} (V)	FF	PCE (%)	Ref.
PEDOT:PSS (Baytron P)	ITO/PEDOT:PSS/ P3HT:PCBM/Al	8.72	0.615	0.609	3.27	[249]
PEDOT:PSS (Baytron PH500)	ITO/PEDOT:PSS/ P3HT:PCBM/Al	9.27	0.596	0.641	3.54	[249]
PEDOT:PSS: Glycerol (6%)	ITO/PEDOT:PSS:Glycero/ P3HT:PCBM//LiF/Al	9.06	0.60	0.54	2.92	[237]
PEDOT:PSS: Au NPs (20%)	ITO/PEDOT:PSS:Au NPs/ P3HT:PCBM//Ca/Al	10.18	0.59	0.70	4.19	[250]
PEDOT:PSS (Baytron P4083)	ITO/ PEDOT:PSS /P3HT:PCBM/ Ca	8.95 (7.82)	0.59 (0.49)	0.60 (0.51)	3.18 (1.96)	[248]
MoO_3	ITO/MoO_3/P3HT:PCBM/ Ca	8.94 (7.82)	0.60 (0.49)	0.62 (0.51)	3.33 (1.96)	[248]
MoO_3	ITO/MoO_3/P3HT:PCBM/ LiF/Al	8.20 (7.95)	0.60 (0.58)	0.67 (0.62)	3.31 (2.85)	[251]
MoO_3	FTO/ZnO/P3HT:PCBM/ MoO_3/Ag	8.59 (8.69)	0.62 (0.57)	0.57 (0.47)	3.09 (2.30)	[153]

The high electrical conductivity and solution processability of PEDOT:PSS mixture have made it a widely used material choice. MoO_3 is usually deposited via evaporation introducing an additional complex processing step and increased cost compared to PEDOT:PSS. Overall, we can see from Table 5.2 that a significant enhancement of J_{sc}, V_{oc}

and FF is observed upon the incorporation of buffer layers, which leads to an enhanced power conversion efficiency.

5.1.2.2 Cathode buffer layers

Cathode buffer layers, also termed electron injection layers (EILs), improve the efficiency of collecting and extracting negative carriers (i.e. electrons). For this purpose, the ideal requirements for materials selection of EILs can be summarized as (very similar to those for HILs):

1. well aligned energy levels which provide Ohmic contacts at the EIL/acceptor material interface,
2. good electron conductivity which will not increase the series resistance (R_s) of the device,
3. good carrier selectivity to block hole-transport,
4. good transparency to allow incident light to reach the active layer when used as the front contact (in inverted device structures as shown in Figure 5.1),
5. diffusion barrier to prevent the migration of materials from electrode to active layer,
6. ideally able to prevent the diffusion of oxygen and water.

In addition, because of the high electron affinity of fullerene molecules,[252] cathode materials with high work functions, such as Au or Pd are required to extract electrons. However, the energy level of the cathode material has to be aligned with the LUMO level of the acceptor material to provide an Ohmic contact because this influences the open-circuit voltage and thus the overall device performance. Therefore, the role of the buffer

layer is particularly important to achieve good charge collection and extraction performance. Some popular materials that have been used in this application are alkali metal compounds, such as lithium fluoride (LiF),[253] and metal oxides.[254]

Alkali metal compounds

In conventional organic solar cells, a very thin layer of LiF is placed between the Al electrode and the organic layer to block holes and inject electrons. This principle was first established in OLEDs,[255–258] and later applied to polymer/fullerene solar cell devices.[259], [260] Brabec *et al.*[260] first showed that the inclusion of an ultrathin layer of LiF (<1nm) between the MDMO-PPV:PCBM BHJ and the Al electrode improved both FF and V_{oc}, and in turn led to an efficiency improvement of 20% (more details in Table 5.3). It was proposed that the formation of a dipole layer upon inclusion of LiF led to the performance enhancement,[260], [261] because it lowers the electrode work function [262] and therefore establishing an improved energy level alignment at the polymer/cathode interface. At the same time, it was suggested that LiF dissociation and the subsequent chemical reaction (doping) of the organic layer also played a major role in the charge transfer process at organic/metal interface.[253], [262–264]

Similar to LiF, a thin layer of CsF has also shown improvements on V_{oc} and FF, thus benefiting the cell performance. Furthermore, unlike LiF, Jiang *et al.* have demonstrated that the advantage of adding a CsF EIL is almost independent of film thickness.[265] Jiang *et al.* show that the device efficiency improved from 1.4% without the CsF layer to 2.2% with CsF, but kept at around 2.2% when CsF thickness was increased from 0.4 to 3nm.[266] In this case, the CsF layer had an effect on interface modifications caused by dipole-induced charge redistribution as well as modification of the organic layer.

Metal oxides

Titanium sub-oxide (TiO_x) has been widely used to inject electrons at cathodes. TiO_x has a wide energy band gap (~3.7eV)[267] and this provides good transparency for use in inverted devices. TiO_x has valence and conduction band edges at ~4.4 and ~8.1eV respectively,[266] which allows an Ohmic contact to be formed with fullerenes [268] as well as forming a high energy barrier for the diffusion of holes (hole-blocking).[269] Furthermore, its solution processability via the sol-gel method is compatible with most organic device technology, which is normally based on wet solution processing.[270] Finally, the mobility of negative charge carriers in amorphous TiO_x is around 1.7×10^{-4} $cm^2V^{-1}s^{-1}$,[271] which implies it is very suitable as an electron transporter. Kim *et al.* have demonstrated that upon insertion of a TiO_x layer, device efficiency can be improved from 2.3% to 5%, mainly contributed by the ~50% improvement in J_{sc},[268] as shown in Table 5.3. Hayakawa *et al.*[268] also demonstrated that by inserting a TiO_x layer R_{sh} has been improved leading to an enhanced performance, owing to effective hole-blocking performance at the TiO_x interface.

Similar to TiO_x, ZnO is another good option to use as an EIL owing to its good electrical and optical properties, especially in inverted structures. It is an *n*-type semiconductor with wide energy band gap (~3.3 - 3.4eV). Its conduction band edge is at ~4.1eV [272] which aligns well with the fullerene material, which enables the formation of an Ohmic contact. From a review of published work on EIL materials, I have summarized some representative results into Table 5.3.

Table 5.3. A summary of the performance of solar cells utilizing various cathode buffer layers (EILs). The photovoltaic parameters are compared to those measured for a reference cell (values in parentheses), when available, made with a cathode without EIL.

EIL	Cell architecture	J_{sc} (mA/cm^2)	V_{oc} (V)	FF	PCE (%)	Ref.
LiF	ITO/PEDOT:PSS/MDMO-PPV:PCBM/LiF/Al	5.25	0.82 (0.76)	0.61 (0.53)	3.30	[260]
CsF	ITO/PEDOT:PSS/MEH-PPV:PCBM/CsF/Al	(5.26)	(0.72)	(0.37)	2.20 (1.40)	[260]
TiO_x	ITO/PEDOT:PSS/P3HT:PCBM/ TiO_x/Al	11.10 (7.50)	0.61 (0.51)	0.66 (0.54)	5.00 (2.30)	[266]
TiO_x	ITO/TiO_x/P3HT:PCBM/ PEDOT:PSS /Au	9.00	0.56	0.62	3.10	[268]
ZnO	ITO/ZnO/P3HT:PCBM/ Ag	11.22	0.56	0.48	2.97	[22]
ZnO	ITO/ZnO(120nm)/P3HT:PCBM/ MoO_3/Ag	8.86	0.62	0.57	3.09	[273]
ZnO NRs	ITO/ZnO(50nm)/P3HT:PCBM/ PEDOT:PSS/Ag	10.69	0.62	0.54	3.61	[274]
Al_2O_3	ITO/Al_2O_3(0.5nm)/P3HT:PCBM/ PEDOT:PSS/Ag	10.1 (10.4)	0.57 (0.63)	0.64 (0.58)	5.34 (5.49)	[8]

From Table 5.3, we can see that compared to the unmodified devices, the incorporation of a buffer layer generally leads to improved J_{sc}, V_{oc} and FF values, which then result in an enhanced device performance. Alkali metal compounds (eg. LiF) are most widely used in conventional structures, and metal oxides (eg. TiO_x) are more widely used in inverted

structures. This is probably due to better alignment of energy level of alkali metal compounds with metal electrodes and metal oxides with ITO electrodes (as discussed in the next section). Overall, the incorporation of buffer layers is shown to be critical to establish an improved device performance because they enhance the charge extraction from active layer to electrode, block leakage of photogenerated counter charge carries flow, and provide good optical and electrical properties.[226]

5.1.3 Inverted organic solar cells and their advantages

Many polymer solar cells have a typical stacking sequence of ITO (or AZO)/PEDOT:PSS/ polymer blend/Ca (or LiF)/Al.[275–277] In this structure, the *p*-type PEDOT:PSS buffer layer is used at the anode to smooth the electrode surface [278] as well as to block the flow of electrons to the anode. [236], [279] A low work function metal, typically Al, is used as the cathode to collect electrons. However, the combination of ITO/PEDOT:PSS electrode and a low work function metal are known to result in poor device stability[280–282] for the following reasons. First of all, the ITO/PEDOT:PSS interface is not stable because of the acidic nature of PEDOT:PSS (a typical aqueous PEDOT:PSS solution has a pH value of ~1.2 at 20°C).[283] This instability comes from In_2O_3, which has a relatively high solubility in acidic solution,[234], [284] and results in the progressive etching of the ITO during the PEDOT:PSS spin coating process. Second, indium diffusion into PEDOT:PSS and even into the polymeric active layer is potentially detrimental to the device characteristics.[285], [286] Furthermore, low work function metals are easily oxidized, which increases the series resistance at the metal/BHJ interface and degrades device performance. It was also shown that both molecular oxygen and water will diffuse through the aluminum electrode to all the underlying layers in the device all the way to the

ITO interface.[287–289] All polymeric active layers will react with molecular oxygen and water in varying degree causing oxidation and thus degradation.

In principle, ITO can be used as either a cathode or an anode, because its work function (ca. 4.5 to 4.9eV) lies between the typical HOMO and LUMO values of common organic photovoltaic materials. This allows ITO to be used as either a cathode or anode by coating the ITO surface with other materials that can modify the polarity of the electrode. For instance, by coating with a high work function layer, such as PEDOT:PSS, ITO can act as an anode to collect holes [282] due to the formation of an Ohmic contact with *p*-type polymer donor materials. On the other hand, to serve as a cathode, low work function ITO can be created by molecular scale engineering. Osikowicz *et al.* have demonstrated a low ITO work function of 3.7eV can be achieved through a redox reaction between a monolayer of electron-donor molecules, tetrakis(dimethylamino)ethylene, and the ITO surface.[290] Another route to achieve low work function ITO is by coating its surface with a metal oxide such as TiO_x and ZnO, as previously mentioned in section 5.1.2.

This tunability of the work function of ITO has enabled an alternative architecture for polymer solar cells – the inverted structure – as introduced in 2005.[283], [291] In the inverted configuration, the ITO substrate is covered by a low work function compound serving as the cathode, resulting in the efficient collection of electrons. One of the biggest advantage of this structure is that it can be modified to avoid the potential interface instability of ITO-based devices (such as the PEDOT:PSS etching) by using alternative functional buffer layers at the ITO electrode (instead of PEDOT:PSS), such as low work function metal compounds.[292], [293] These functional buffer layers are ultrathin (at the

nm scale) and highly transparent (E_g>3 eV) to minimize any optical losses. The anode in this case is substituted with either PEDOT:PSS or a high work function transition metal oxide such as vanadium oxide (V_2O_5) or molybdenum oxide (MoO_3), coupled with a stable metal electrode such as Au or Ag. The use of a stable electrode in the inverted geometry brings additional benefits, i.e. the device is not susceptible to oxidative degradation when stored in the dark.[294] Furthermore, the Au or Ag electrodes are effective at preventing the diffusion of air and moisture into the organic active layer,[295] which improves the stability of the devices. Last but not least, the vertical phase separation of the polymer blends has proven to be advantageous in the inverted structure.[296] As a consequence, the inverted structure opens a route for fabrication of more stable photovoltaic devices by preventing the acidic PEDOT:PSS destroying ITO,[282], [297] and providing a stable electrode that at the same time acts as a form of encapsulation. As a result, it has been suggested by Dang *et al.* in 2011 that the inverted structure will become the dominant geometry in the next few years.[298]

5.1.4 The limitation of inverted device architecture and potential improvements

Although inverted structures can potentially provide better stability by reversing the electrodes in OPV devices, one of the main challenges is to prepare selective and transparent cathode contacts for efficient electron collection and light transmittance.[299] This is due to the poor charge extraction ability associated with the small difference in work function of the ITO and Au/Ag electrodes (the work function of ITO is ~4.7,[244] Ag is ~4.4-4.7,[154], [300], [301] and Au is ~5.1eV[302]). This makes ITO a poor choice of cathode material, because it forms a non-selective interface that results in surface recombination. Therefore, further improvement of the inverted geometry can be expected by inserting functional buffer layers and improving the conductivity of these buffer layers,

as well as by optimizing the energy alignment between the acceptor/buffer layer interfaces.[303]

One of the key factors to achieve high performing inverted polymer devices is the selection of an electron injection buffer layer to improve the electron-extracting and hole-blocking capability at the cathode (as previously discussed). ZnO has been demonstrated to be an attractive material because of the various nanostructures [304], [305] with good electron mobility that can be easily achieved via solution processing for more efficient charge extraction and transportation. The energy levels of ZnO fit very well to the requirements as an electron injection layer, its work function is well matched to the LUMO of PCBM for electron-injection and its valence band is deep below the HOMO of P3HT for hole-blocking (as shown in Figure 5.3b). Furthermore, its wide band gap has ensured good transmittance in the visible wavelength range as a front window buffer layer.[306]

However, the low conductivity of intrinsic ZnO (i-ZnO) limits its application as an efficient electron injection layer.[38] The free electrons at the acceptor/buffer interface must travel through the buffer layer in order to be collected by electrode; the conductivity of the buffer layer is therefore crucial for an efficient charge collection process. The poor conductivity can result in increased series resistance and lead to a poor charge collection in the devices, thus reducing the short-circuit current density. As a consequence, i-ZnO imposes a requirement of depositing a very thin film for effective charge transportation. This causes various problems to the manufacturing of the OPV devices. First, very thin films may result in a relatively high density of pinholes, leading to increased shunt

paths.[307], [308] Second, ultra thin films appear to be less robust and can become a potential challenge for the deposition of subsequent layers.

In light of the above limitations, doping zinc oxide with aluminum (AZO) might be a suitable solution to be used as a cathode buffer layer instead of i-ZnO, owing to its lower resistivity and high transmittance.[150] In addition, AZO can be fabricated by low-cost solution methods as well, which are compatible with solution based BHJ solar cell processing. By manipulating the buffer layer's doping level and thickness, the short-circuit current density (J_{sc}) and the overall device performance are expected to be enhanced.

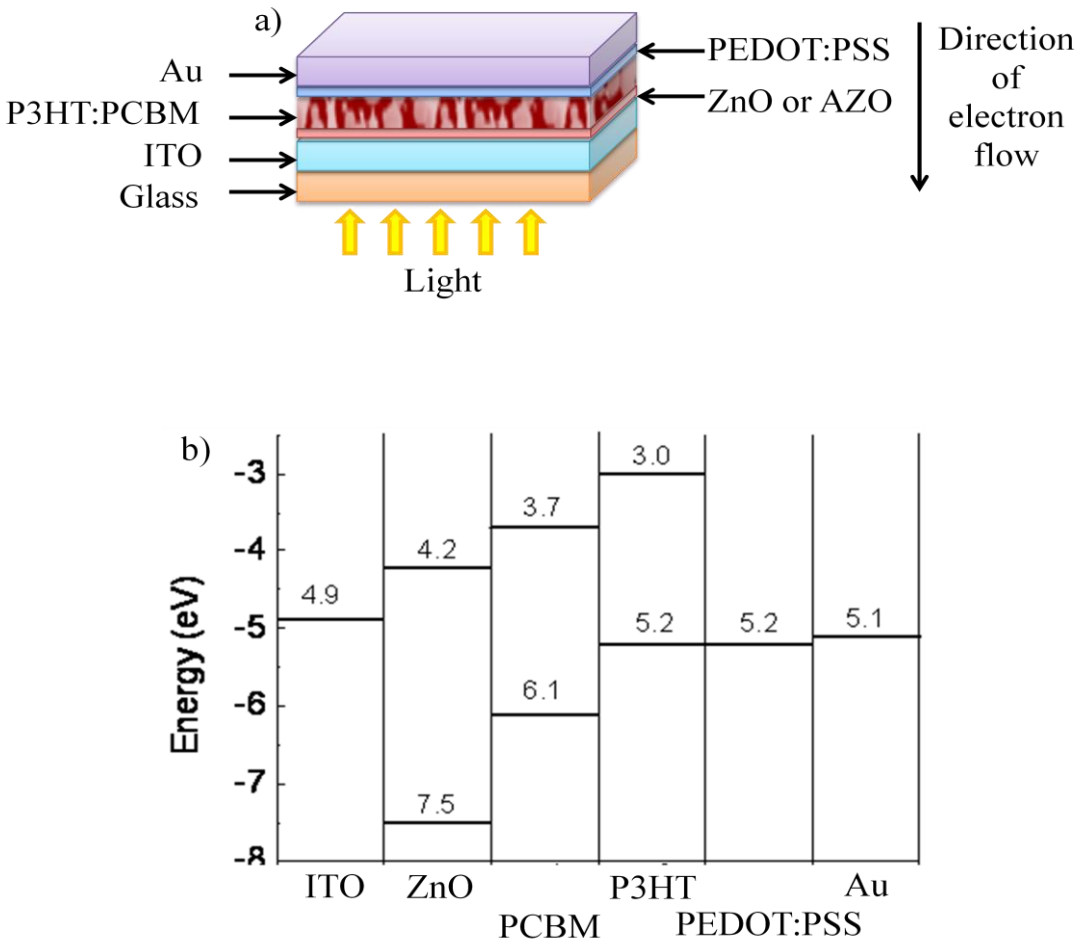


Figure 5.3. Schematic of the inverted solar cell employing either EIL or HIL or both, with structure of ITO/EIL/P3HT:PCBM/HIL/Au (a) and its corresponding simplified energy band diagram (b).

The above discussion promotes the fabrication of the inverted OPV structures shown in Figure 5.3a, employing various ZnO buffer layers at the ITO cathode. High carrier injection efficiencies can be achieved by decreasing the energy barriers that charged carriers must overcome, or tunnel through, at the interface between the relevant active layer and electrode.[245] The barrier to electron injection originates from the energy level difference between the LUMO of the polymer and the work function of the cathode (in this case PCBM and ITO). Similarly, the barrier to hole injection originates from the energy level difference between the HOMO of polymer and the work function of the anode (in this case P3HT and Au).

In this chapter, I report the fabrication and characterisation of a series of inverted polymer composite photovoltaic devices, with a focus on the comparison between i-ZnO and AZO cathode buffer layer materials, as well as the effect of various AZO thicknesses on the device performance. The device architecture studied is displayed in Figure 5.3 with its proposed corresponding energy band diagram.

Most of the excitons are generated in the irradiated polymer P3HT, followed by diffusion to and separation at the P3HT:PCBM interface. The holes are then transported to the anode and the electrons are accepted by the PCBM. As shown in Figure 5.3b, the conduction band of ZnO is located at ~4.2eV, representing an increased difference in the energy levels between ZnO and the Au (~5.1eV) to that between ITO (~4.7-4.9eV) and Au. Accordingly, it is energetically favoured for the excitons generated in the polymer materials to dissociate and be extracted to their respective electrodes, owning to the better positioned ZnO energy levels and the good electron mobility in ZnO.[309] This is because

the electrons located at the lowest unoccupied molecular orbital (LUMO) level of PCBM (-3.7eV) [309] can be effectively extracted to the conduction band of ZnO (-4.2eV), then rapidly transported to the ITO electrode.

The interfacial area between the donor P3HT and acceptor PCBM is much greater than that of P3HT and ZnO due to the formation of a bulk heterojunction (as illustrated in Figure 5.3a). Therefore, the ZnO buffer layer is primarily acting as an electron collector rather than electron acceptor and does not form an appreciable heterojunction structure with P3HT.

5.2 Experimental Details

5.2.1 EIL deposition and characterization

The preparation of ZnO and/or AZO (1.5at.% doped) thin films with the desired thickness on ITO substrates by the sol-gel technique was described in section 3.1.2. The precursor thin film was decomposed in air at 500ºC for 1 hour using a Carbolite RWF RWF12/23 furnace, with a ramp rate of 10ºC/min. The techniques described in Chapter 3 are used to characterise the optoelectronic properties here, namely AFM, XRD, Scanning Kelvin Probe (SKP), Hall measurement, 4-point probe, UV-Vis, and Dektak surface profiler.

5.2.2 Device preparation

First the BHJ P3HT:PCBM solution was prepared as described in section 3.1.4. Once the solution is well-mixed, the ZnO EIL coated on ITO substrates were cleaned for the deposition of P3HT:PCBM thin films as described in section 3.1.1. Next the substrates

were transferred into the glove box where the P3HT:PCBM solution was spin cast onto the substrates at 700 RPM. The HIL materials that were used are PEDOT:PSS in aqueous solution (from H.C. Starck GmbH) and were deposited as described section 3.1.4.3 in the glove box. One droplet of PEDOT:PSS solution was dropped onto the spinning substrate (coated with ZnO and P3HT:PCBM already) and spin casted at 5000 RPM for 1 minute, then dried at 45ºC on a hotplate for 5 minutes. Following this, the devices were transferred into a vacuum chamber and gold electrodes were thermally evaporated through a shadow mask before they were annealed at 150ºC for 10 minutes.

5.2.3 Device testing

The devices were placed in a testing holder, which was continuously flushed with nitrogen gas throughout the experiment. Current-voltage (IV) and external quantum efficiency (EQE) characteristics were recorded as described in section 3.4.

5.3 Results and Discussion

5.3.1 Characterization of various ZnO cathode buffer layer materials

The following section characterises the materials properties of the i-ZnO (intrinsic ZnO), AZO + i-ZnO (a layer of 1.5at.% aluminium doped ZnO on top of i-ZnO) and AZO (1.5at.% aluminium doped ZnO). These materials were chosen because ZnO enables an improved energy alignment in the inverted P3HT:PCBM devices as described in Figure 5.3, and 1.5at.% Al doping concentration has been shown to give the best electrical properties in Chapter 4. The difference between these buffer layers and the AZO films fabricated for

the application of TCO is that these buffer layers are significantly thinner (~60nm versus ~400-500nm) and no post annealing (eg. vacuum treatment) was performed.

Morphology characterization by AFM

The atomic force microscope (AFM) was used to study the morphology of the buffer layers, and typical results are shown in Figure 5.4.

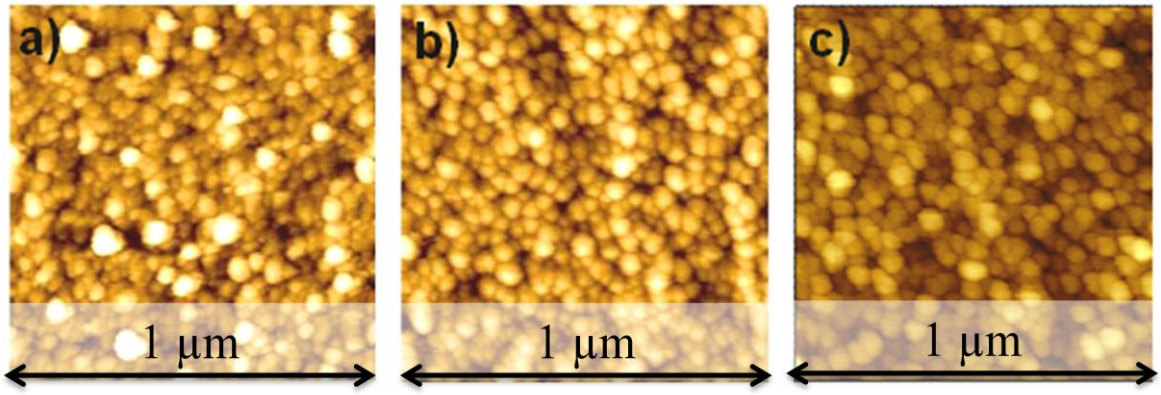


Figure 5.4. 1 µm × 1 µm topographic AFM images of buffer layers a) AZO, b) i-ZnO and c) AZO+i-ZnO thin films for application as buffer layers.

The morphology of the buffer layers showed little difference in terms of rms roughness and crystal size (as shown in Figure 5.4 and summarized in Table 5.5). The thin films were relatively smooth with rms roughness values of ~3.3, ~3.0 and ~2.1nm for AZO, i-ZnO and AZO+i-ZnO buffer layers respectively. Comparing these values to the results discussed in section 4.3.2, where AZO films were fabricated from same solution concentration (1M) and same processing method (without post annealing), a consistent rms roughness of ~3.3nm was obtained. It demonstrates that these AZO films exhibit very similar morphological properties (in terms of surface roughness). This implies that the three buffer layers are likely to result in a similar influence on the physical contact at the

active layer/electrode interface (in terms of how smooth the contact is). In addition, these rms roughness values are also very close to the ZnO films studied by other authors,[294] where a result of about 2.6nm was reported. Furthermore, the small rms roughness values of these films prevents shorting between the cathode and anode, which has been reported for rougher surfaces (rms roughness of around 10.38nm),[294] lowering shunt resistance. The particle sizes on the surface of the thin films were measured and are summarized into Table 5.5. Average sizes of around 40nm for all three types of films were observed, again close to those found in Chapter 4 (ca. 30-60nm). This as well, identified the small morphological difference across the three films.

Optical characterization by UV-Vis

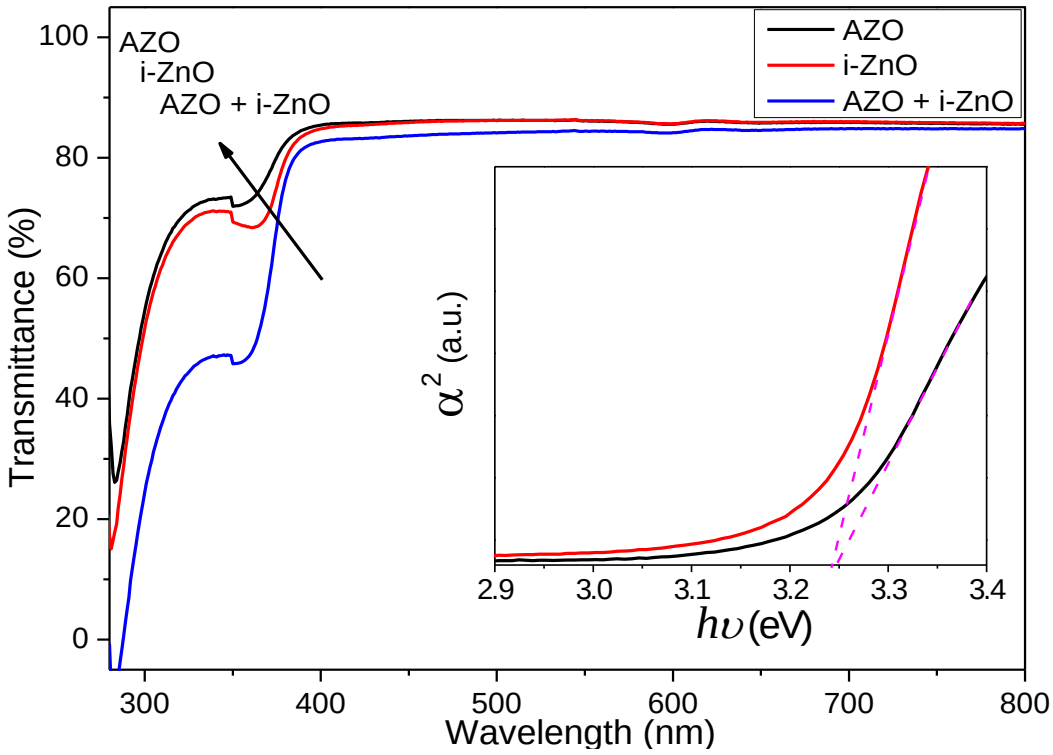


Figure 5.5. The transmission spectra of buffer layers derived from various sols: AZO, i-ZnO and AZO+i-ZnO. The inset is the estimation of E_g values by extrapolating the straight-line portion towards zero absorption coefficient (α=0) for the three types of thin films.

The optical transparencies of the buffer layers were analysed using UV-Vis and the results are displayed in Figure 5.5. The three buffer layers have demonstrated transparencies of around 85% over the visible range. The AZO film had a slightly higher transmittance over a broad range of wavelengths compared to the i-ZnO films. This is likely to be due to the slightly enlarged E_g upon Al doping, which is consistent with the results discussed in Chapter 4 and with the literature.[49] The E_g of different films are therefore calculated for comparison.

The thicknesses of the buffer layers were measured by using a Dektak surface profiler. Both AZO and i-ZnO layers have a thickness of ~60nm, and the combined AZO+iZnO layers have a thickness of ~90 nm, and this thicker film might account for the slightly reduced transmittance. The optical absorption data displayed in Figure 5.5 were further analyzed using the formula discussed in section 3.3.1:

$$\alpha \propto (h\nu - E_g)^{1/2} \qquad \text{Equation 5.1}$$

The results are summarized in Table 5.5. The 1.5% doped AZO film has shown an insignificant E_g increment of ~0.004eV compared to the i-ZnO (undoped) film. This rather small blue shift possibly implies a small improvement in conductivity for the AZO film analyzed compared to the undoped ZnO film.

Structural characterization by XRD

These solution processed ZnO buffer layer thin films were analyzed by XRD to analyze their structural properties.

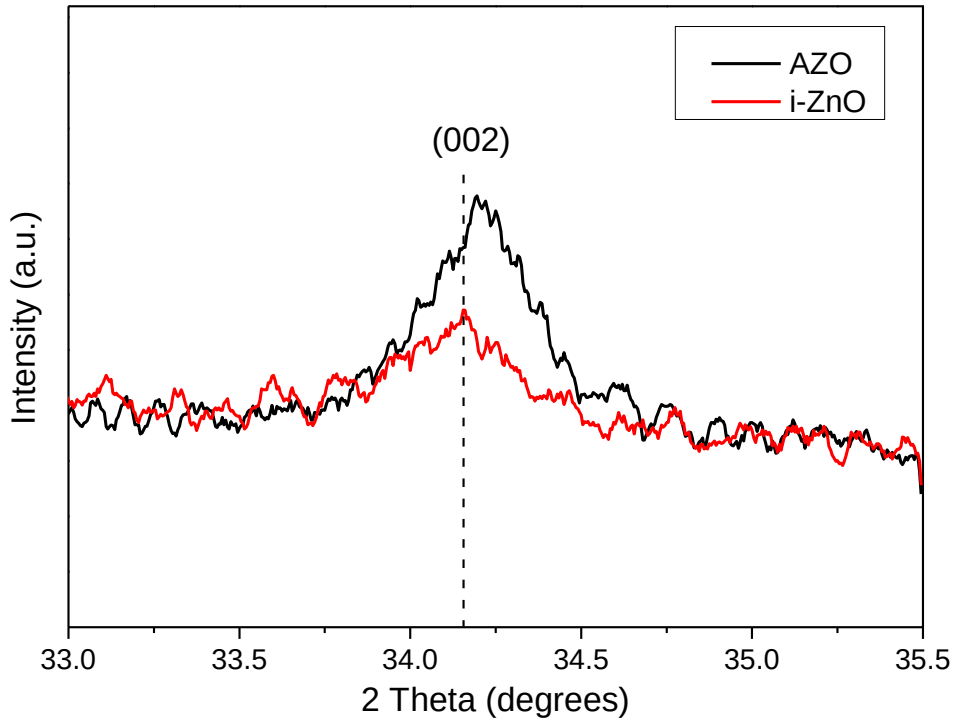


Figure 5.6. XRD spectra displaying the (002) peak of ZnO thin films derived from different sols: AZO and i-ZnO. Dashed line is serving as a guide to the eye.

The (002) characteristic peak corresponds to the ZnO lattice and a shift of this peak is observed upon Al doping, which is consistent with the results presented in section 4.3.1. The degree of the (002) peak shift is extracted using Bragg's law, $n\lambda = 2d\sin\theta$, as described in Chapter 4. By rearranging the equation, the *c*-axis lattice parameters of the films were derived from the 2θ readings and are listed in Table 5.4.

Table 5.4. Lattice parameters of as-grown AZO and i-ZnO thin films prepared from 1M precursor solution with Al doping concentration of 1.5 at.%.

Thin Film	2θ (degrees)	Lattice Constant, *c* (Å)
AZO	34.198±0.005	5.19±0.003
i-ZnO	34.158±0.01	5.21±0.006

A decrease in lattice parameter upon Al doping is observed, consistent with the trend observed in Chapter 4 and other reports.[49] It is believed to be the result of the same mechanism - that a slight contraction of ZnO lattice is due to the substitution of smaller Al^{3+} ions (radius 0.53Å) on Zn^{2+} (radius 0.60Å) lattice sites.

The work function of the front electrode is not usually considered in device optimization, but is indeed an important parameter to take into account in order to achieve the best device performance.[310] The work function of ITO and Au measured by the SKP (primarily taken by Laura Droessler) are 4.9 and 5.15eV respectively. This rather small energy offset might result in lower charge carrier extraction ability thus imposing a negative impact on V_{oc} value, because it was pointed out that V_{oc} is correlated with the work function difference of the electrodes.[311], [312] In order to improve the charge extraction, low work function buffer layers can be used to modify the ITO electrode, which can potentially increase the V_{oc} of inverted P3HT:PCBM devices.[313] The work functions of i-ZnO, AZO and AZO+i-ZnO buffer layers measured by SKP are ~4.76, ~4.70 and ~4.70 respectively (as shown in Table 5.5). By incorporating one of these buffer

layers, the difference between the two electrodes is increased to around 0.45eV as compared to in the absence of a buffer layer (in which case the difference between ITO and Au is 0.25eV). This implies an improved and rather similar electron extraction capability of AZO, i-ZnO and AZO+i-ZnO buffer layers. In addition, the separation of the ZnO conduction band edge (around 4.2eV) from the LUMO of the PCBM (3.7eV) is 0.5eV, permitting the development of an Ohmic contact with the LUMO level of the acceptor material for electron transportation.

Together, the improved energy structure upon the insertion of AZO, i-ZnO or AZO+i-ZnO film suggests that these buffer layers can offer improved electron extraction ability without imposing an injection barrier. Besides acting as an electron injection layer, these ZnO based layers function as hole blocking layers due to the fact that the valence band edge of ZnO lies at ~7.5eV, much deeper than that of HOMO of PCBM (6.1eV) and the ITO cathode (Figure 5.3b). This barrier height represents an improved hole-blocking property (from HOMO of PCBM to ITO) as compared to devices lacking a buffer layer.

Electron mobility, carrier concentration and resistivity values on the three types of films were obtained by Hall measurements as described in section 3.3.3, and are summarized in Table 5.5. The AZO film has the lowest resistivity owing to it higher carrier concentration. Unfortunately the i-ZnO thin film's electrical properties are not measurable, most likely due to its large resistivity. Other techniques, such as four-point probe resistance measurement, were used to examine the i-ZnO film, although no data could be obtained. The overall optoelectronic and morphological properties of three types of thin films are summarized in Table 5.5.

Table 5.5. Comparison between the thin film properties of AZO, i-ZnO and AZO+i-ZnO buffer layers.

Thin Film	Optical Bandgap (eV)	Crystallite Size (nm)	Rms Roughness (nm)	Work Function (eV)	Resistivity (Ω•cm)	Carrier Conc. (cm^{-3})	Mobility (cm^2/Vs)
AZO	3.247	~40±5	3.3	4.70	1.52E+02	4.19E+16	0.98
i-ZnO	3.243	~40±5	3.0	4.76	*	*	*
AZO+i-ZnO	3.229	~40±5	2.1	4.70	1.67E+02	1.54E+15	24.33

*. Not measurable by Hall measurement and 4-point probe, indicating large resistivity.

It was also noted that, the fabrication of ZnO or AZO films on ITO glass substrates led to the degradation of the ITO resistivity from 1.53×10^{-4} to 6.07×10^{-4} Ω•cm. This is most likely due to the diffusion of indium ions into the glass substrate under the elevated-temperature conditions (500°C for 1 hour) required for the decomposition of ZnO or AZO layer on ITO substrate. Other authors also observed similar degradation.[150], [294] This degradation is not likely to result in an impact in terms of the comparison among various buffer layers because all the buffer layers were fabricated through the same method, but will lead to efficiency decreases through series resistance losses.

5.3.2 A comparison of various ZnO cathode buffer layers

Systematic experiments have been performed on the inverted device geometry shown in Figure 5.7, to study the effect of different EIL cathode buffer layers on device performance. The buffer layer materials studied include i-ZnO, AZO+i-ZnO and AZO (as

characterized in section 5.3.1), and compared with devices fabricated without an EIL as a reference. PEDOT:PSS was used as an anode buffer layer to inject holes (HIL) into the Au electrode.

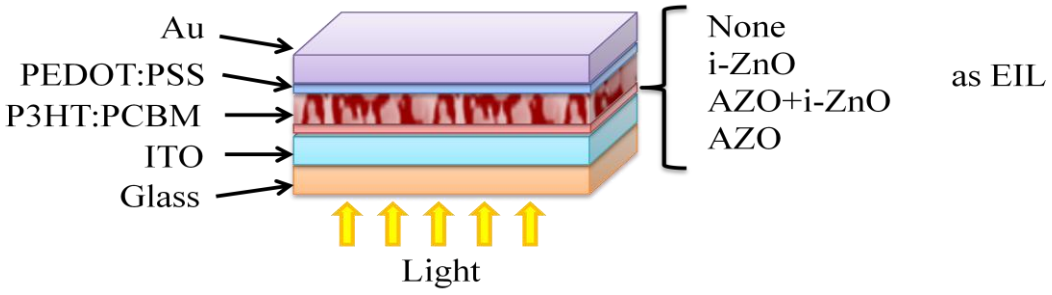


Figure 5.7. Inverted BHJ OPV structure, showing various EIL analyzed, including i-ZnO, AZO+i-ZnO and AZO, compared with device made without EIL (none).

A set of 20 devices was fabricated for this investigation (5 identical cells for each type of EIL buffer layer conditions) 3 devices were found to be defective and are not included in the comparison. Solar cell devices were tested under simulated sunlight (AM 1.5G, 100mWcm^{-2}), the overall results of all devices are displayed in Figure 5.8. I noted a significant deterioration of the J_{sc} performance upon the insertion of the i-ZnO layer. This is most likely due to the insulating nature of the i-ZnO layers, which leads to poor charge transportation and increased recombination.[303] By replacing i-ZnO with more conductive AZO+i-ZnO or AZO film, J_{sc} was significantly improved. Such improvement demonstrates the importance of the buffer layer conductivity. V_{oc} of the devices employing all three types of buffer layer was considerably improved, and the degree of enhancement is nearly the same when employing the three different types of buffer layers. The V_{oc} enhancement is primarily caused by the improved energy level alignment by introducing ZnO buffer layer (as described in section 5.1). However, compared to the large energy level difference between the ITO substrate and ZnO buffer layer, the rather insignificant

difference in the energy levels among the three types of ZnO buffer layers as discussed in section 5.3.1 results in comparable influence on V_{oc} enhancement. The change in FF is less significant as compared with that of J_{sc} and V_{oc}. Overall, the changes in the above parameters have led to a significant enhancement in PCE, and the best performance was achieved for the devices employing AZO buffer layers (with nearly 2-fold increment in PCE).

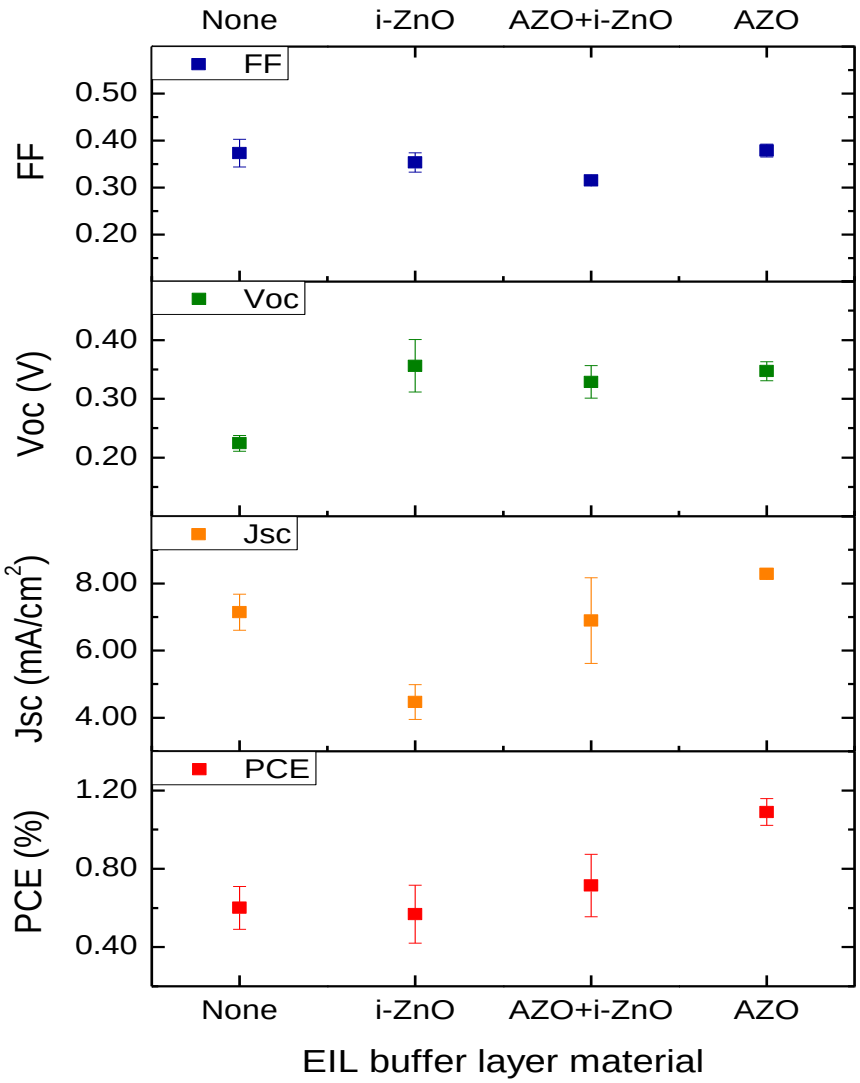


Figure 5.8. Performance characteristics of inverted ITO/EIL/P3HT:PCBM/PEDOT:PSS /Au devices employing a PEDOT:PSS HIL, and EILs of varying materials: none, i-ZnO, AZO+i-ZnO and AZO. Data points and error bars correspond to the average and standard deviation of four to five cells. An efficiency maximum is achieved for a device employing AZO EIL, with J_{sc} = 8.15 ± 0.05 mA/cm^2, V_{oc} = 0.36 ± 0.005 V, FF = 0.39 ± 0.002, and PCE = 1.15 ± 0.01%.

The J-V (current density – voltage) characteristics and EQE (External Quantum Efficiency) spectra of one typical set of the above inverted OPV devices are analyzed as described in section 3.4 and results are displayed in Figure 5.9, for a more in depth comparison. The specific performance parameters are extracted into Table 5.6, where R_s (series resistance) and R_{sh} (shunt resistance) values calculated from the light IV curves are included for further investigation. For an efficient cell, we want R_s to be as small and R_{sh} to be as large as possible.[26]

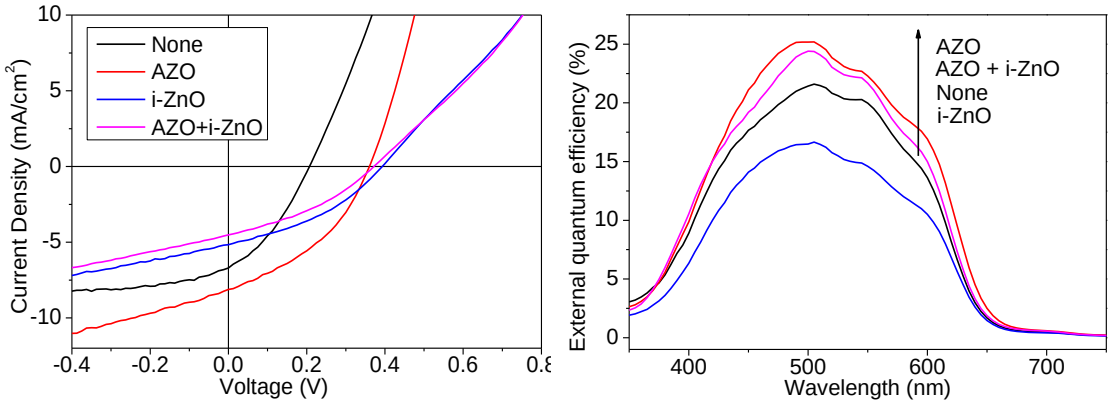


Figure 5.9. The J-V characteristics (left) and EQE spectra (right) of inverted ITO/EIL/ P3HT:PCBM/PEDOT:PSS/Au solar cells employing a PEDOT:PSS HIL, and EIL of varying materials: none, i-ZnO, AZO+i-ZnO and AZO.

As shown in Figure 5.8, devices without any EIL modification exhibit poor device performance. Figure 5.9 displays a poor JV character that is consistent with the trend observed in Figure 5.8. Low J_{sc} and V_{oc} are observed, which indicates the presence of serious recombination events.[154] This is probably due to the relatively small difference between the work function of ITO (4.9eV) and Au (5.1eV), which exerts insufficient driving force for charge carriers to travel to the respective electrodes. This poor electrode selectivity, the so-called extraction ability, leads to increased recombination. The EQE

spectrum of the device without EIL shown in Figure 5.9 is also consistent with the observed poor J_{sc} value.

Table 5.6. A summary of the performance characteristics of inverted devices ITO/EIL/P3HT:PCBM/PEDOT:PSS/Au employing a PEDOT:PSS HIL, and EIL of varying materials: none, i-ZnO, AZO+i-ZnO and AZO.

EIL material	PCE (%)	J_{sc} (mA/cm^2)	V_{oc} (V)	FF	R_s (Ω·cm^2)	R_{sh} (Ω·cm^2)
None	0.49	6.68	0.28	0.35	19.8	65.2
i-ZnO	0.76	5.17	0.39	0.37	27.3	181
AZO+i-ZnO	0.88	7.40	0.37	0.32	24.9	70.5
AZO	1.15	8.18	0.36	0.39	4.6	128

The insertion of the i-ZnO HIL significantly improves the V_{oc} of all the devices, although J_{sc} suffered at the same time due to increased resisitivity. The devices show relatively poor FF of ~0.3±0.02, probably due to the significant R_s (as shown in Table 5.6) as a result of the rather insulating i-ZnO (as shown in Table 5.5). In addition, it was suggested that J_{sc} is essentially reduced by the series resistance R_s as well.[314] For instance, as shown in Table 5.6, the reduction of J_{sc} from 6.68 to 5.17 mA/cm^2 is likely to be due to the increased R_s from 19.8 to 27.3 Ω cm^2. In addition, the EQE spectra shown in Figure 5.9 reveals a lower value of 15% maximum for the device using an i-ZnO buffer layer, which is likely to be due to poor charge transportation caused by the high resistivity (as shown in Table 5.5). In fact, the much improved EQE performance of the AZO devices confirmed

that the resistance of the buffer layer plays an important role in device performance. Although i-ZnO has a relatively low conductivity, electrons can tunnel though the thin layer (around 60nm). Therefore, compared to the devices without EILs, devices employing a thin layer of ZnO EILs provide better charge selectivity and transport.[154] One way to overcome the poor conductivity of i-ZnO is by depositing an ultra thin layer so charge carriers can tunnel through more easily. However, ultra thin films pose increased possibility of pin-hole formation, which give rise to short circuits in the devices. As shown in Table 5.6, V_{oc} was increased from 0.28 to 0.39V upon insertion of i-ZnO, resulting in an overall increased PCE from 0.49% to 0.76%. This represents a 1.5-fold enhancement as compared to the devices without EIL modification. These values are comparable to the results reported by other authors, where inverted P3HT:PCBM cells employing ZnO buffer layers have yielded V_{oc} values near 0.25V for devices with a planar ZnO buffer layer, and ~0.4V for devices employing nanopillar ZnO buffer layers.[154] Together, it was demonstrated that the ZnO HIL plays an important role in cell design.

As previously shown in Figure 5.8, the introduction of AZO+i-ZnO further improves the device performance. For example, V_{oc} has been improved from 0.28 to 0.37V as compared to the devices without buffer layers (Table 5.6). The same mechanism as inserting i-ZnO buffer layers is believed to apply here - the establishment of an improved energy alignment. Furthermore, R_{sh} has been improved from 65.2 to 70.5$\Omega \cdot cm^2$ (as shown in Table 5.6), indicating an enhanced hole-blocking property as well. J_{sc} has improved slightly from 6.68 to 7.40mA/cm^2, which is consistent with the improved EQE performance shown in Figure 5.9. However, the degree of improvement is insignificant; this is likely to be due to the relatively high resistance associated with the i-ZnO portion

that hinders the charge transport. FF on the other hand did not show an appreciable change. Overall, the PCE was improved from 0.49 to 0.88%, representing a 1.8-fold enhancement.

Finally, the introduction of AZO buffer layer developed the most significant device improvement, as shown in Figure 5.8. Specifically, a further increase in J_{sc} from 6.68 to 8.18mA/cm^2 is achieved (Table 5.6), primarily as a result of the reduced R_s, from 19.8 to 4.6Ω·cm^2, which is due to the improved conductivity upon Al doping in the AZO film. The substantial further improved performance of AZO devices compared with i-ZnO devices is probably due to a more efficient electron transport properties owning to their relatively low resistivity (as shown in Table 5.5). Thus photogenerated electrons can readily move towards the ITO electrode once captured by the AZO layer. This can reduce the probability of free carrier recombination. Furthermore, an improved EQE maximum at ~510nm from 21% for the device without EIL to 26% for the devices with an AZO buffer layer is observed. This improved EQE is likely to be the result of enhanced charge collection in the device. It is clear from the EQE results why J_{sc} values exhibit significant differences for the various cells. The improved EQE response of devices employing AZO or AZO+i-ZnO shown in the EQE spectra is expected to increase the J_{sc} as compared to that employing i-ZnO or without buffer layer. In fact, other authors have reported similar observations, that the addition of buffer layer can improve the J_{sc} compared to the reference devices without modification.[280], [315], [316] Both V_{oc} and FF have shown considerable improvement, with V_{oc} increasing from 0.28 to 0.36V and FF increasing from 0.35 to 0.39. This is likely to be a result of improved R_{sh} (from 65 to 128 Ω·cm^2) due to the improved hole-blocking property brought by the AZO buffer layer, which suppressed charge carrier recombination. In addition, the better energy alignment of AZO

as discussed earlier in section 5.3.1 further improves charge extraction. Together, an improved PCE from 0.49 to 1.15% was achieved, a 2.3-fold increment.

In summary, the introduction of EIL buffer layers has improved the performance of devices. These ZnO based buffer layers have the dual-function of electron-transport and hole-blocking. The good hole blocking properties arise from the fact that its valence band (7.5eV) is much deeper than the HOMO of acceptor/donor (6.1eV/5.2eV) as shown in Figure 5.3b. Therefore the improved V_{oc} and FF can be attributed to the suppression of back current (versus photocurrent) at the active layer/ITO interface. Therefore, the improved performance is likely to be due to the improved charge selectivity upon the insertion of EIL buffer layers. Furthermore, AZO was shown to be a more efficient EIL material owning to its reduced resistivity. In the next section, thickness optimization of the AZO buffer layers is discussed, in terms of material characterization and device optimization.

5.3.3 Characterization of AZO buffer layer materials of various thicknesses

The thickness of the buffer layer is a critical parameter, and there is a compromise between the risks of pinhole formation and introduction of parasitic series resistance if the film is too thick.[317] It is clear from the above analysis that the AZO buffer layers result in better device performance. In this section, I will focus on studying the influence of various AZO buffer layer thicknesses (ranging from 0 to 150nm) on device performance. A combination of AFM, 4-point probe, UV-Vis, and Dektak surface profiler are employed to study the properties of these solution-processed AZO buffer layers.

Morphology characterization by AFM

Atomic force microscope (AFM) was used to study the morphology of the AZO buffer layers of different thicknesses, and the results are shown in Figure 5.10. As mentioned in section 5.3.2, other authors have suggested that ultra thin films are prone to pinhole formation that will lead to increased recombination (leading to short circuit). Particular attention is therefore drawn to look at the ultra thin films to find out if such failure is observed.

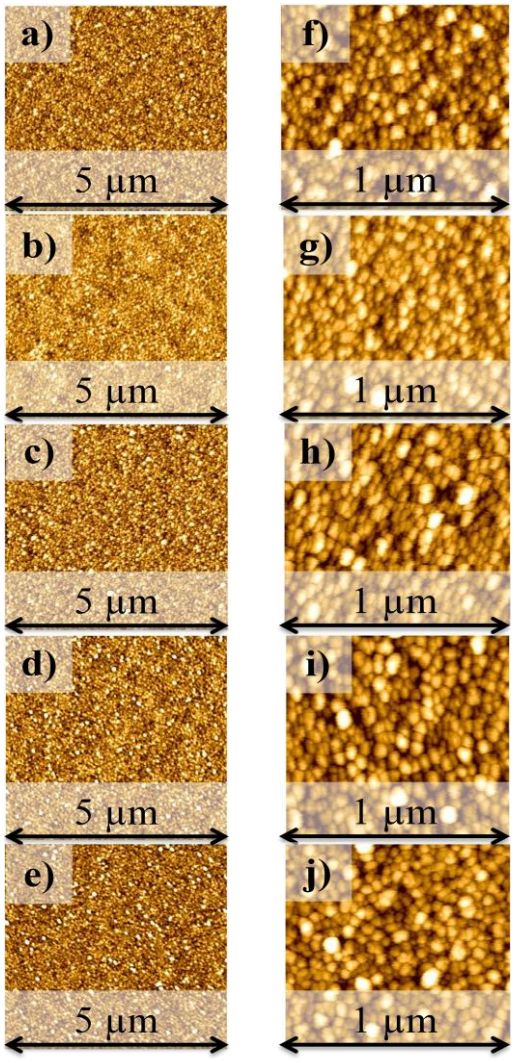


Figure 5.10. 5 × 5 µm (left) and 1 × 1 µm (right) topographic AFM images of AZO buffer layers with thicknesses 40±3, 60±5, 90±5, 120±3 and 150±5nm as displayed in images a) to e) on the left and images f) to j) on the right, respectively.

Film thickness was measured by using Dektak surface profiler, and read 40±3, 60±5, 90±5, 120±3 and 150±5nm from thinnest to thickest, respectively. Films with thin thicknesses of 40±3nm showed a few scratch-like line defects on the surface, as shown in Figure 5.11a. A depth profile of the defect is studied and shown in Figure 5.11b.

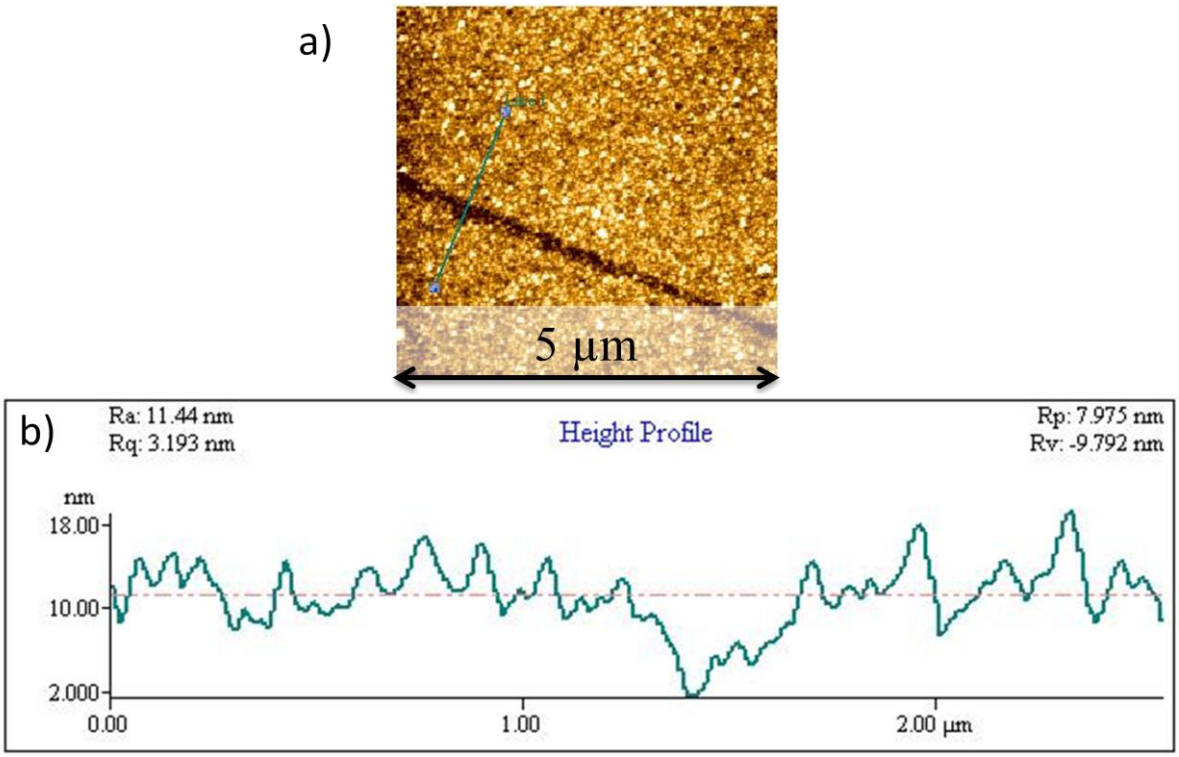


Figure 5.11. 5 × 5 µm AFM image of a 40±3nm AZO buffer layer featuring a line defect (a) and the depth profile of this defect (b).

We found that the line defect have an average depth of ~8 to 10nm, comparing to the film thickness (~40nm), and can be considered a shallow defect. Thus they are not expected to cause severe shorting problems due to pinhole formation. The shallow depth of the defects also implies that scratching probably is not the origin, because much deeper scratches should be caused otherwise. Such line defects are found at several locations in ultra thin films (i.e. on ~40nm films, and also on a ~30nm thick AZO film deposited for comparison), while thicker films showed a more consistent surface. The rms roughness

has increased from ~2.74nm to ~3.19nm locally, which is insignificant when compared to the much higher roughnesses reported by other authors that will be discussed later. The origin of these line defects is unclear. It is possible that any surface defects that remain in the substrate[318] may lead to a more significant impact on the thinner films due to the lack of abundant material during crystal growth. Overall, it seems that these ultra-thin films (~40nm) are not expected to suffer greatly from pinhole failures, although shallow defects are prone to form in thinner films as compared to the thicker ones. Next, the rms roughness of films with various thicknesses is investigated and shown in Table 5.7.

Table 5.7. rms roughness of AZO films of various thicknesses.

AZO film thickness (nm)	rms roughness of 5×5μm scan (nm)	rms roughness of 1×1μm scan (nm)
40±3	3.10	2.77
60±5	2.86	3.22
90±5	3.77	2.82
120±3	3.16	3.23
150±5	3.38	3.50

The rms roughnesses of these AZO films are around 3.3±0.4nm, which is comparatively very smooth as compared to the literature where 12.7 and 67.5nm were reported for applications in transistors and TCOs.[319], [320] Comparing these values to the results discussed earlier in section 5.3.1 of this chapter and in section 4.3.2 of Chapter 4, a

consistent rms roughness near ~3-4nm is obtained. The similar values in rms roughness among these films with various thicknesses again demonstrate that they exhibit similar morphological properties and thus similar active layer/electrode interfacial properties in terms of a physical contact, as discussed in section 5.3.1. Also, the small rms roughness values imply a relatively low probability of direct contact between the cathode and anode as discussed in section 5.3.1. Overall, the similar values in the rms roughness of various thin films and the shallow defect depth of ultra-thin films suggest that the morphology probably is not going to affect the device property as a primary factor.

Electrical characterization by 4-point probe

Table 5.8. Sheet resistance of AZO films of various thicknesses.

AZO film thickness (nm)	Sheet resistance (MΩ/□)
40±3	68.8±5
60±5	27.3±2
90±5	35.7±2
120±3	41.1±1
150±5	43.0±4

The electrical property of AZO buffer layers is an important factor. It influences the device parasitic resistance, as electrons have to travel past these layers (through their

thickness direction) in order to be collected by the electrode. Therefore, both the resistance and thickness of buffer layer play an important role in determining the device parasitic resistance. The precise resistance that these buffer layers enforce on the transportation of electrons is extremely difficult to be obtained. In this chapter, sheet resistance of the AZO films at various thicknesses was measured in order to infer the impact of resistance associated with several buffer layers on the device parasitic resistance. Using the four-point probe measuring technique, the sheet resistance of AZO thin films was studied as a function of the film thickness, a factor which affects the film conduction process drastically. The results are shown in Table 5.8, along with the thickness data obtained by using Dektak surface profiler. The sheet resistance of AZO films increased with increasing thickness, except the ultra-thin film of 40±3nm that exhibited highest resistance. Minami *et al.*[321] reported that, an ultra-thin film would result in increased resistivity; in particular, thin films with a thickness below about 50nm were very unstable. It was interpreted as the carrier transport being dominated by trapping of free electron due to oxygen adsorption on the film surface and grain boundaries which increased scattering.[322] This is consistent with our result shown in Table 5.8, and explained the observation of highest AZO film resistance at ~40nm. Together, it would not be unreasonable therefore to predict that the parasitic resistance in my devices could be affected by variations in thickness (thus motivates me to carry out a systemic study on the effect of thickness and results are presented in the following section). This is another compromise in solar cell design, since you cannot easily achieve excellent hole-blocking properties while keeping a low material resistance for efficient electron-transporting which in turn affects the parasitic resistance. In summary, it appears that the AZO buffer layer morphology is not likely to be a primary factor in influencing the device performance, more so resistance.

5.3.4 Thickness optimization of the AZO cathode buffer layers

A set of 26 devices was fabricated for this study, (4 to 5 identical cells for each type of EIL buffer layer conditions). 4 devices were found to be defective and are not included in the comparison. Figure 5.12 displays the performance characteristics of devices employing AZO buffer layers with thicknesses ranging from 0 to 150nm.

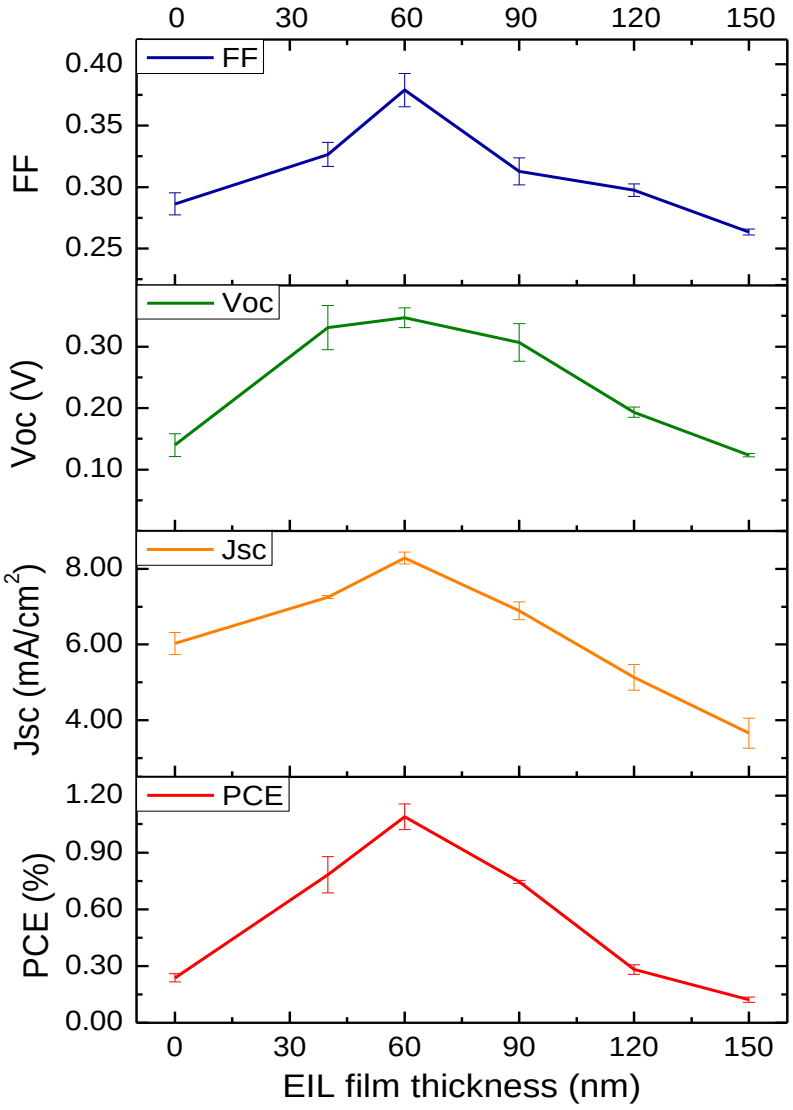


Figure 5.12. Performance characteristics of inverted ITO/AZO/P3HT:PCBM/PEDOT:PSS /Au devices employing an AZO EIL of varying thicknesses (ranging from 0 to 150nm). Data points and error bars correspond to the average and standard deviation across three to five cells. Lines serve as a guide to the eye. An efficiency maximum is achieved when employing ~60nm thick AZO EIL, with J_{sc} = 8.15 ± 0.05 mA/cm^2, V_{oc} = 0.36 ± 0.005 V, FF = 0.39 ± 0.002, and PCE = 1.15 ± 0.01%.

Devices which do not employ an AZO buffer layer leave the ITO electrode in direct contact with the polymer active layer. This means that there is no hole-blocking capability at that electrode. Due to the similar band edge of ITO and PEDOT:PSS/Au as shown in Figure 5.3b, holes can migrate from the highest occupied molecular orbital of P3HT to either the Au or ITO electrode. This decrease in electrode selectivity can effectively increase the probability of bimolecular recombination either at the ITO interface or within the active layer itself.[323]

For the devices employing AZO buffer layer, the AZO acts as an electron-transporting, hole- and exciton-blocking layer, leading to an increase in J_{sc}. It was also noted that devices employed ~60nm AZO buffer layer outperformed the rest, in good agreement with the resistance data discussed in the last section. Similarly, it was reported [324] that the insertion of sufficiently thick Ta_2O_5 into the OLED device can improve the hole-blocking property and enhance the device performance. Hayakawa *et al.*[325] also demonstrated in conventional P3HT:PCBM devices that the insertion of ~10nm TiO_x (thicker films, eg. 50nm, cannot be used as a hole blocking layer because of the resulting low conductivity of the TiO_x film leading to low I_{sc}, V_{oc} and FF) has significantly improved rectification compared to devices lacking a TiO_x layer. They claimed that the TiO_x layer not only serves as a hole blocking layer but also prevents contact between the electrode and active layer which otherwise will result in diffusion of electrode material (Al) into active layer and reaction of the active layer with Al. For a further understanding of the impact of AZO buffer layer thickness on the OPV devices, the performance parameters from one set of the devices shown in Figure 5.12 are extracted and summarized in Table 5.9. R_s and R_{sh} were calculated from the current density-voltage (J-V) curve and listed in the table as well.

Table 5.9. A summary of inverted ITO/AZO/P3HT:PCBM/PEDOT:PSS/Au device performance characteristics that employ AZO EIL of varying thicknesses (ranging from 0 to 150nm).

Thickness (nm)	PCE (%)	J_{sc} (mA/cm^2)	V_{oc} (V)	FF	R_s ($\Omega \cdot cm^2$)	R_{sh} ($\Omega \cdot cm^2$)
0	0.24	6.03	0.14	0.29	24.0	15.4
40±3	0.61	6.83	0.28	0.31	23.2	92.3
60±5	1.15	8.18	0.36	0.39	4.6	128
90±5	0.48	6.32	0.24	0.31	29.2	78.6
120±3	0.28	5.13	0.19	0.30	33.7	25.8
150±5	0.12	3.66	0.12	0.26	39.7	25.3

It has been reported that in organic bulk heterojunction solar cells shunt pathways initially exist through the interpenetrating network from one electrode to the other, and this can lead to a reduced V_{oc}.[326], [327] However, these shunt pathways can be reduced by i) annealing, which produces a vertical segregation of the blended material[328] that reduces the formation of shunt pathways, and/or ii) blocking layers which inhibit the flow of holes to the cathode. Both exhibit beneficial effects that improve V_{oc}.[329] The left panel of Figure 5.13 shows the dependence of AZO sheet resistance, device shunt resistance (R_{sh}) and V_{oc} values on AZO film thickness. It is known that an extreme drop in R_{sh} will reduce V_{oc}.[314] In the results presented here, the significant improvement of V_{oc} from 0.14 V for the device without EIL, to 0.28, 0.36 and 0.24V for the devices with ~40, ~60 and ~90nm AZO respectively, provide evidence for removal of shunt pathways from the active layer

to the ITO electrode. This is consistent with the improved R_{sh} values shown in Table 5.9 and Figure 5.13, from 15.4 for the device without EIL to 92.3, 128 and 78.6Ω·cm^2 for devices employing a ~40, ~60 and ~90nm AZO respectively. However, devices employing even thicker AZO layers (such as 120 and 150nm) have suffered from reduced shunt resistance as compared to devices employing a thinner AZO and this has led to a decrease in the device performance (Figure 5.12).

It was also noted that the V_{oc} value of all the devices are generally lower than literature expectation, which should be primarily determined by the LUMO level of acceptor and HOMO level of donor.[323], [330] Nevertheless, similar lower values were also reported for inverted devices employing ZnO nanopillars,[331] and this was explained by the defect states derived from the chemical reactions at the organic/electrode interface that can contribute to interface barriers or mid-gap states, which can pin the Fermi level and might have influenced the open circuit voltages. In our experiment, the buffer layers were deposited without post annealing in vacuum (as compared to the AZO films discussed in Chapter 4 for application as TCOs), thus there might not be sufficient energy for the AZO films to release the strain and defects built up during Al doping and crystallization (as discussed in Chapter 4). Defects that are generated upon doping may cause increased mid-gap states [235] which lead to recombination or parasitic resistive losses at the AZO/P3HT interface instead of P3HT:PCBM interface, resulting in a decrease in V_{oc}. These results suggest that AZO films with improved microstructure and decreased defect states may yield improved V_{oc} and FF values. Therefore, in order to further optimize performance, understanding of the influence of EIL microstructures and defect states on the interface properties and device performance needs to be further researched.

From Table 5.9, it is seen that the fill factor (FF) of the devices slightly increased initially with the increase in AZO thickness, and decreased for films greater than ~90nm thick. Other authors who are working on inverted OPVs using ZnO and MoO_3 as EILs and HILs have reported similar FF values (in the range of 0.26 to 0.44),[323] where a dependence of FF on R_{sh} has been demonstrated with various buffer layer thicknesses caused by the presence of electrical shunt paths due to their rough ZnO surfaces. Therefore, the reason for the relatively low FF is likely due to the relatively low R_{sh} of our devices, which one may ascribe to charge carrier recombination and hole shunt paths.

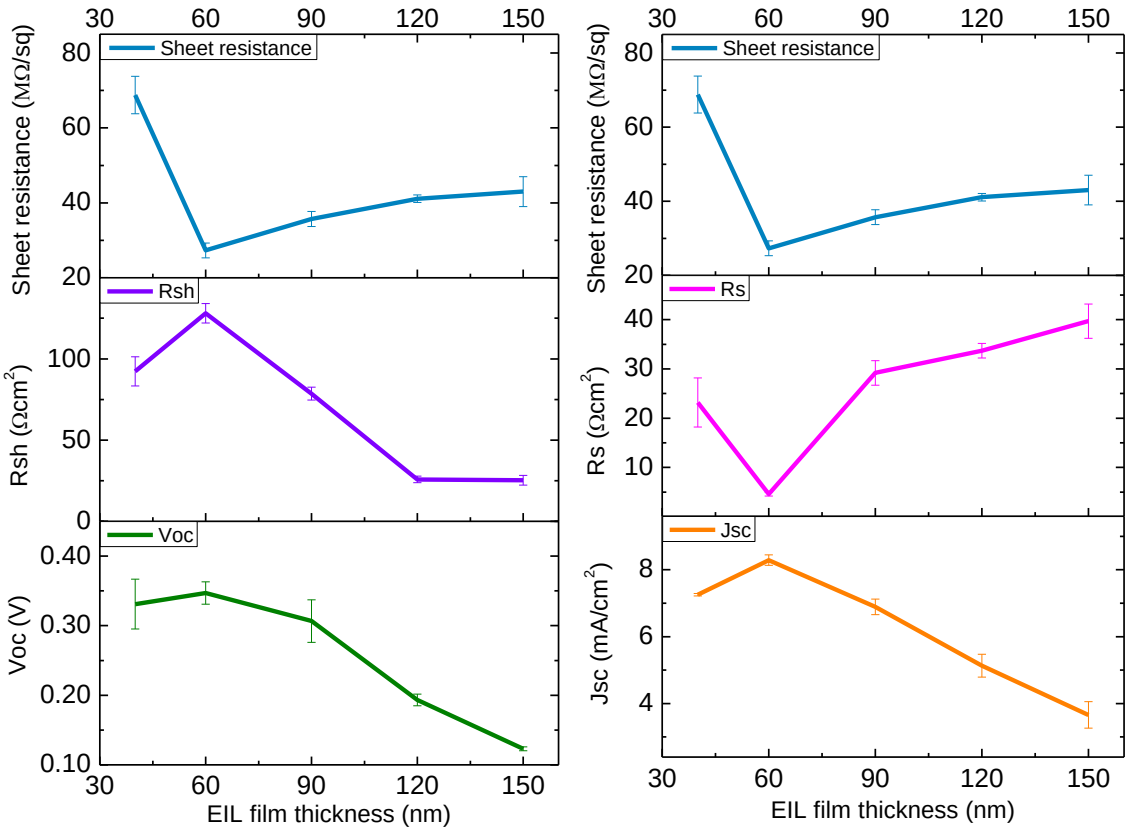


Figure 5.13. Dependence of sheet resistance, R_{sh} and V_{oc} on AZO buffer layer thickness (left), and dependence of sheet resistance, R_s and J_{sc} on AZO buffer layer thickness (right) of inverted ITO/AZO/P3HT:PCBM/PEDOT:PSS/Au devices employing an AZO EIL of varying thicknesses (ranging from 0 to 150nm). Data points and error bars correspond to the average and standard deviation across three to five cells. Lines serve as a guide to the eye.

Furthermore, besides improving electron extraction from the acceptor material through the use of a low work function AZO buffer layer (as discussed in section 5.3.2), the incorporation of the AZO film with optimized thickness (~60nm) is beneficial also because of a reduction in device series resistance. This is a result of the relatively low resistance of ~60nm AZO films as compared to those ultra-thin and ultra-thick ones (as discussed in section 5.3.3). The right panel of Figure 5.13 displays a combined plot illustrating the dependence of AZO sheet resistance, device series resistance (R_s) and J_{sc} values on AZO buffer layer thickness. Here, a dependence of R_s and J_{sc} on AZO sheet resistance is observed.[14] With ultra-thin AZO buffer layers (~40nm), the devices suffer from high series resistance, exhibiting low J_{sc} values of 6.83 mA/cm^2. The performance increases significantly when a ~60nm AZO buffer layer is inserted, demonstrating reduced R_s values (from 23.2 to 4.6 Ω·cm^2) and improved J_{sc} values (from 6.83 to 8.18 mA/cm^2). In contrast, further increasing the buffer layer thickness has led to deteriorated device performance (R_s and J_{sc}, shown in Figure 5.13), associated with the degraded charge transport properties shown by the increased AZO sheet resistance. This results in increased R_s from 4.6 to 29.2, 33.7 and 39.7 Ω·cm^2 as well as reduced J_{sc} from 8.18 to 6.32, 5.13 and 3.66 mA/cm^2 for devices employing an AZO buffer layer of 60, 90, 120 and 150nm thick, respectively. These suggest the significant dependence of device performance on the buffer layer sheet resistance. Based on the above-mentioned discussions, ITO covered with ZnO acts well as a cathode for electron collection, and the optimized thickness was found to be ~60nm. Similar observations have been reported for hole-injection layer upon the insertion of MoO_3,[332] where the lowest series resistance of 4.7Ω•cm^2 has led to highest J_{sc} of 21.3mA/cm^2. They claim this was due to a reduction in the back contact resistance, and showed that inserting thicker MoO_x layers deteriorated the device

performance due to additional series resistance, as MoO_x is essentially an insulating material.

It is worth mentioning that the reduction in series resistance is comparatively small in our case, as compared to the significant impact on the improved in shunt resistance. This probably suggests that the primary contribution of incorporating the AZO buffer layer is from its good hole-blocking character. Similar to the report by other authors upon the insertion of MoO_x,[323] where they claim that the main influence to the performance of their devices is the improved R_{sh}. In summary, the device performance presented here are in good agreement with the material characterization data discussed in section 5.3.3. Overall, they demonstrated the tremendous influence of AZO buffer layer thickness on device design by modifying the blend/electrode interface.

5.4 Conclusion

The concept of polymer:fullerene BHJ solar cells has opened up a promising avenue to develop low cost photovoltaic devices, although the common aspect of great difficulty in controlling the blend/electrode interface remains a challenge. The main issue is the fundamental understanding of the energy alignment at these interfaces and the prevention of material diffusion and unwanted charge carrier transport between electrode and active layer. This has been studied in this chapter by introducing buffer layers that result in significant improvement in device performance. The buffer layer materials were chosen with a good knowledge of the HOMO and LUMO values of the organic materials and the work function of the electrodes, in order to build device architectures with good physical configurations and electrical properties. I have demonstrated that the introduction of ZnO

based buffer layers between the polymer blend and the cathode results in a considerable device performance enhancement attributed to improved charge carrier selectivity. The well-aligned energy level of ZnO/acceptor has established an Ohmic contact to allow efficient extraction of electrons to the cathode, as discussed in section 5.3.1. By doping the ZnO layer with Al, the electronic conductivity has been improved, as shown by the reduced device R_s values in Table 5.6 (section 5.3.2) for the devices employed AZO as compared to those employing ZnO buffer layers. Next, I have shown the importance of AZO buffer layer thickness by relating the AZO resistance as studied in section 5.3.3 to the device performance as presented in section 5.3.4. Finally, an optimized AZO buffer layer thickness of about 60nm was found due to reduced device series resistance and efficient electron-extraction and hole-blocking properties as discussed in section 5.3.4. In conclusion, the results presented in this chapter prove that the incorporation of buffer layer with appropriate doping level and thickness is critical for the device performance.

Chapter 6 – Solution-processed Inverted ZnO/PbS Heterojunction Quantum Dot Solar Cells

This chapter discusses the application of sol-gel processed *n*-type ZnO to form inverted heterojunction solar cells with *p*-type lead sulphide quantum dots (PbS QDs). The work contained in this chapter focuses on manipulating the ZnO:PbS junction by varying the aluminium content in the ZnO, optimizing film thicknesses, and using post fabrication treatments on both the *n*- and *p*-type materials to improve charge transportation and hence device efficiency.

6.1 Introduction

6.1.1 The application of solution processed ZnO as junction layer

Zinc oxide is widely used as transparent conducting film as discussed in Chapter 4, however, its application as a junction layer in the active region is relatively rare to date. In addition to the beneficial properties discussed earlier (e.g. abundance), ZnO is a useful junction material because it exhibits high electron mobility that is favourable for electron transport, leading to reduced recombination losses.[333], [334] ZnO can be produced in a wide variety of nanostructures, thus presenting tunable properties. ZnO also has a direct band gap that encourages efficient energy transitions in solar cell applications. Other favourable attributes of ZnO include its broad chemical processibility leading to many opportunities for wet chemical etching, stability when exposed to high-energy radiation and biocompatibility.[335]

There has been work carried out to apply ZnO films as components of extremely thin absorber (ETA) solar cells.[336–339] For instance Mora-Sero and co-workers [336] have presented ETA solar cells based on ZnO nanowires sensitized with a thin layer of CdSe, using CuSCN as the hole transporting material (Figure 6.1). Electron-hole pairs are generated in the CdSe semiconductor absorber layer. Then, the electrons are injected into the ZnO nanowires that are employed as an electron conductor, and transported to the transparent conducting oxide, FTO. Holes are injected into the CuSCN and are transported to the counter electrode, Au, leading to an efficiency of ~1.5%.

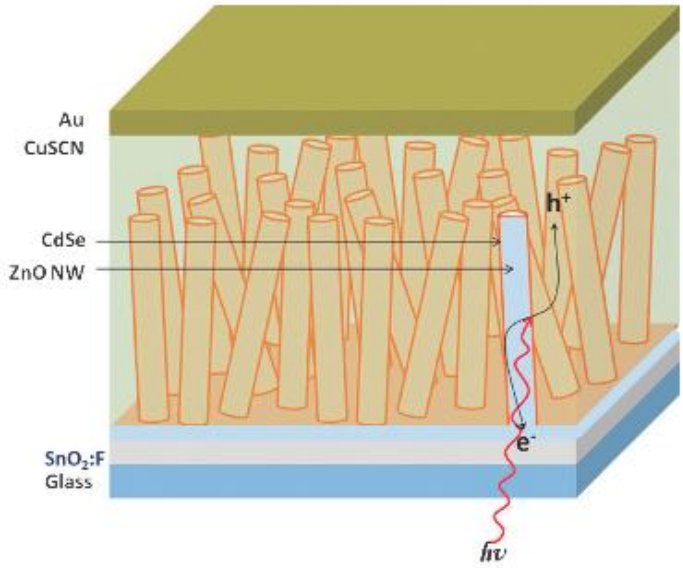


Figure 6.1. Schematic illustration of the ETA solar cells employing ZnO nanowires. (reprinted from reference [336]*)*

In the field of hybrid solar cells, *n*-type ZnO is a useful material when used in conjunction with a *p*-type conjugated polymer, forming a heterojunction structure.[340] Beek *et al.*[341], [342] have demonstrated 1.6% efficient conventional bulk heterojunction devices by blending ZnO nanoparticles with MDMO-PPV and 0.9% efficiency with P3HT.

Another application of zinc oxide is in nanoparticle-sensitised ZnO nanorod cells.[343–346] For instance, Leschkies *et al.*[346] demonstrated the application of ZnO nanowires in CdSe quantum dot devices, where CdSe inject electrons across the quantum dot-nanowire interface upon illumination, and ZnO provides a direct pathway for electrons to be transported to the electrode. They obtained a power conversion efficiency of ~0.4% with ~12µm long ZnO nanowires.

In this chapter, a very similar device structure as presented in Figure 6.1 will be employed. A ZnO thin film will be fabricated next to the ITO substrate, with light entering the cell through the ITO substrate, in order to allow longer wavelength photons to reach the QD layer. Further review of the QD material and the device architecture will be discussed below.

6.1.2 PbS QDs and their synthesis

Lead sulphide (PbS) was chosen as the *p*-type inorganic material in our devices for a number of reasons. First of all, it has tunable broad band absorption due to quantum confinement,[347], [348] which can be altered to match the solar spectrum. Secondly, it does not show the strong carrier recombination associated with surface states and defect centers.[349], [350] Thirdly, both electrons and holes demonstrate long excited state lifetimes.[351] Furthermore, looking at the materials resource aspect, PbS is an abundant and inexpensive semiconductor material that may be able to contribute to meeting global electricity needs.[352] Together, these properties make PbS nanocrystals a promising candidate for the engineering of low cost photovoltaic devices. However, this potential is limited by the band gap of the material in its bulk form (E_g = 0.41eV), which is too small for efficient photovoltaic applications. Henry[353] suggested that when $E_g > h\nu$ (incident

photon energy), energy loss is caused by photons that are not absorbed. When $E_g < h\nu$, energy loss is caused by the carriers relaxing to energies near the band edges almost immediately after generation. The highest efficiencies for a single junction solar cells are found at around E_g = 1.35eV.[354], [355]

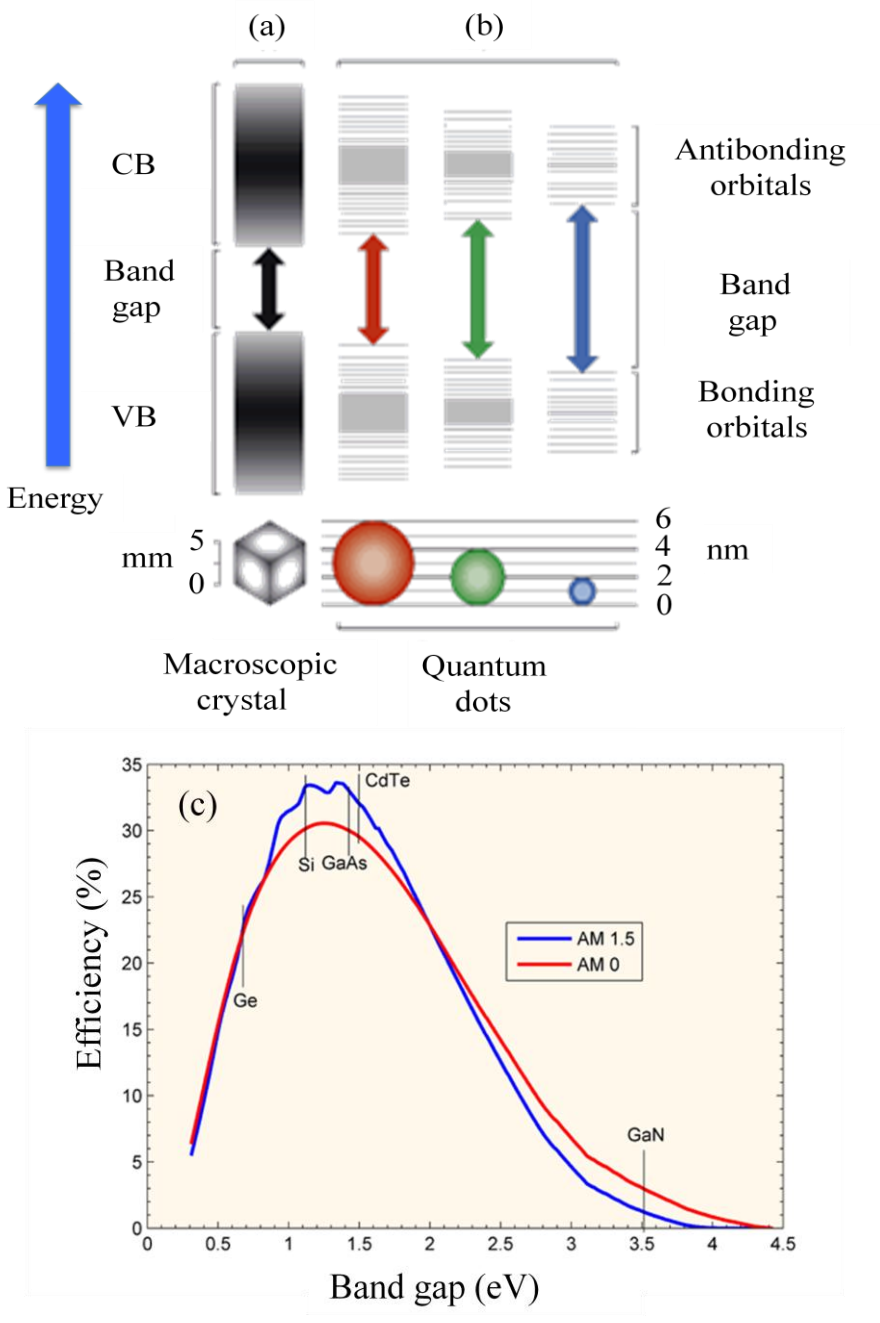


Figure 6.2. (a) Schematic illustration of the energy band diagram of a macroscopic crystal and (b) the corresponding discretization of the energy levels arising from quantum confinement for quantum dots (reprinted with modification from reference [356]*). (c) The limiting efficiency for a single band gap solar cell (reprinted from reference* [357]*).*

The E_g of PbS QDs, can be easily tuned to between 1 to 1.4eV, (Figure 6.2a and b) well matched with the solar spectrum (Figure 6.2c). Figure 6.2c displays the limiting solar cell efficiency as a function of the material band gap for one-sun illumination.[357] The calculation is based on the assumption that the only recombination is radiative. However, in actual devices, other mechanisms of recombination and resistance will result in lower efficiencies.

The PbS quantum dots (QDs) used in my experiments were synthesized by Cheng Cheng in our laboratory. A solution based method based on the work reported by Luther *et al.*[358] was employed, where lead oxide and hexamethyldisilathiane were used as precursors. The ratio of Pb to S precursor used was 2:1, which lies within the typical range used to synthesize cadmium chalcogenide and lead chalcogenide nanocrystals.[359] In order to achieve a narrow size distribution and a well-defined excitonic structure, relatively fast cooling was used following rapid sulfur precursor injection. The PbS QDs were capped with butylamine to prevent agglomeration and facilitate subsequent further manipulations such as cross-linking or densification of films.[360]

6.1.3 Inverted ZnO/PbS heterojunction devices

The evolution of PbX QD solar cells

PbX (PbS, PbSe) QDs solar cells were first made using the structure of ITO/PbX/metal, where a low work function metal such as Ca, Mg or Al was used to form a Schottky contact.[361–363] However, Schottky junction solar cells often suffer from low built-in voltage values, which in turn limit the efficiency of the device. The maximum possible V_{oc} in Schottky devices is likely to be limited to $E_g/2q$,[364] where q is the charge of an

electron. This is probably due to the Fermi-level being pinned at the metal/semiconductor junction. Furthermore, since the Schottky junction is formed at the metal electrode opposite to the side on which the light is incident, minority carriers (electrons) recombine or are trapped at the defect states, preventing them reaching the electrode.

In addition, Schottky junction QD solar cells require the use of thinner active layers to enable the maximum number of photons to be absorbed within the depletion region located at the rear metallic non-transparent contact.[365] To overcome this limitation, heterojunction devices are employed: an *n*-type material is inserted next to the *p*-type PbX QDs material.[366–368] For instance, by introducing an *n*-type ZnO film beneath the *p*-type PbX QD film, a *p*-*n* junction is formed. Here, minority carriers travel toward ITO while holes are extracted to the metal electrode. This structure offers improved V_{oc} values compared with the Schottky junction QD devices, because V_{oc} is now determined by the difference in the quasi-Fermi levels of the *n*- and *p*-type materials.[364], [369] By using the quantum confinement effect, Luther *et al.* reported a metal oxide/QD device with a V_{oc} that is greater than the PbS bulk band gap.[358] Similarly, Choi *et al.* have demonstrated a V_{oc} of 0.44V in a device based on PbSe,[366] close to twice the band gap value in bulk PbSe, 0.27eV.[370]

The efficiency of the QD PV devices has progressed rapidly during the past few years, from only 1% in some early reports [371–373] to the improved performances of ~5%,[369], [374–376] and most recently a 6% device was reported.[377] This rapid progress has resulted from improved knowledge of materials properties, such as the electronic transport and recombination,[378], [379] as well as the device engineering such

as the evolution from Schottky[380] to heterojunction,[358] to QD-sensitized solar cells[373], [381] and tandem cells.[382], [383]

Inverted structure

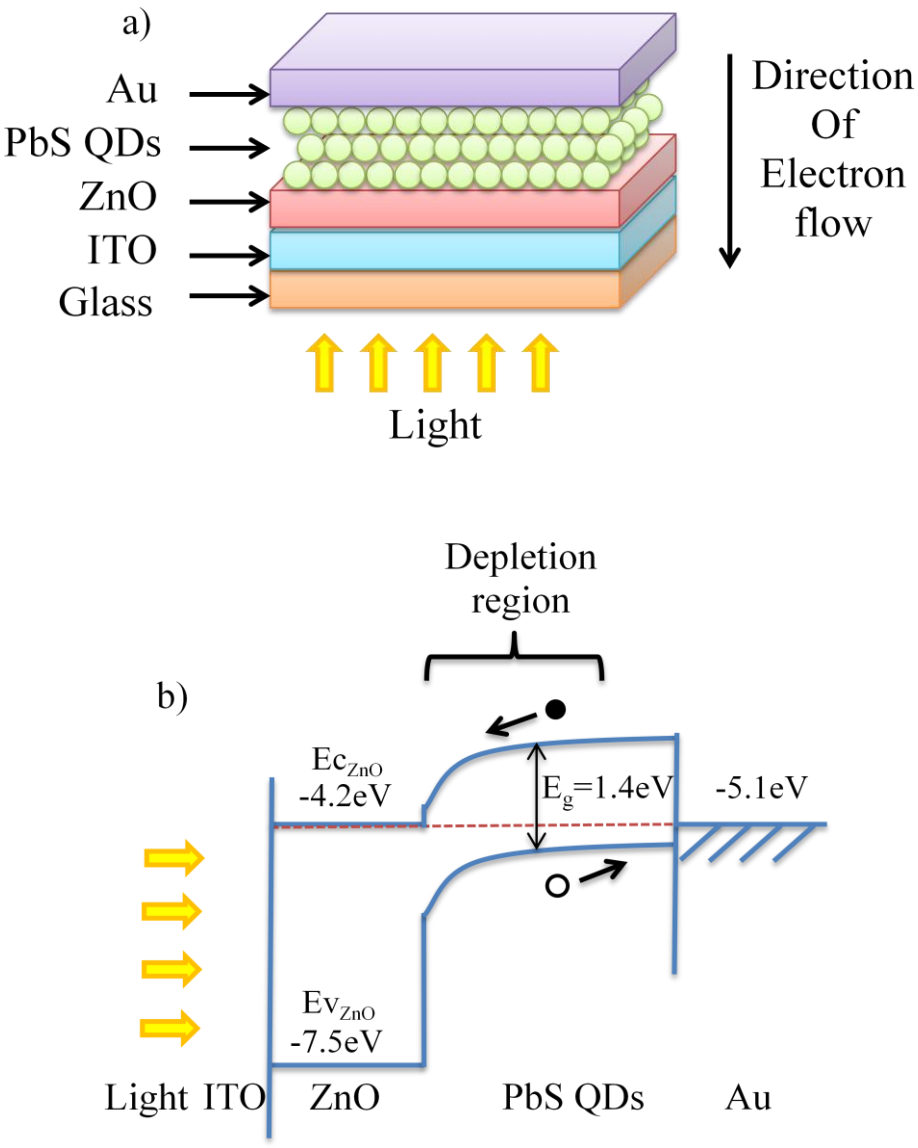


Figure 6.3. (a) An illustration of the inverted ITO/ZnO/PbS/Au heterojunction device structure employed in this chapter, showing the direction of electron flow towards the ITO substrate. (b) Proposed corresponding energy band diagram for the operation of the device at equilibrium.(after Luther et al.[358] *)*

Inverted QD solar cells have been fabricated according to the structure shown in Figure 6.3a, using either lightly doped AZO or undoped ZnO as the *n*-type material, and PbS as the *p*-type material. The *n*-type ZnO film is placed below the *p*-type PbS QDs film to, together with the use of the high work function metal electrode, invert the polarity of the device.[364] This is termed the 'inverted structure' following the naming in OPV (as mentioned in Chapter 5).

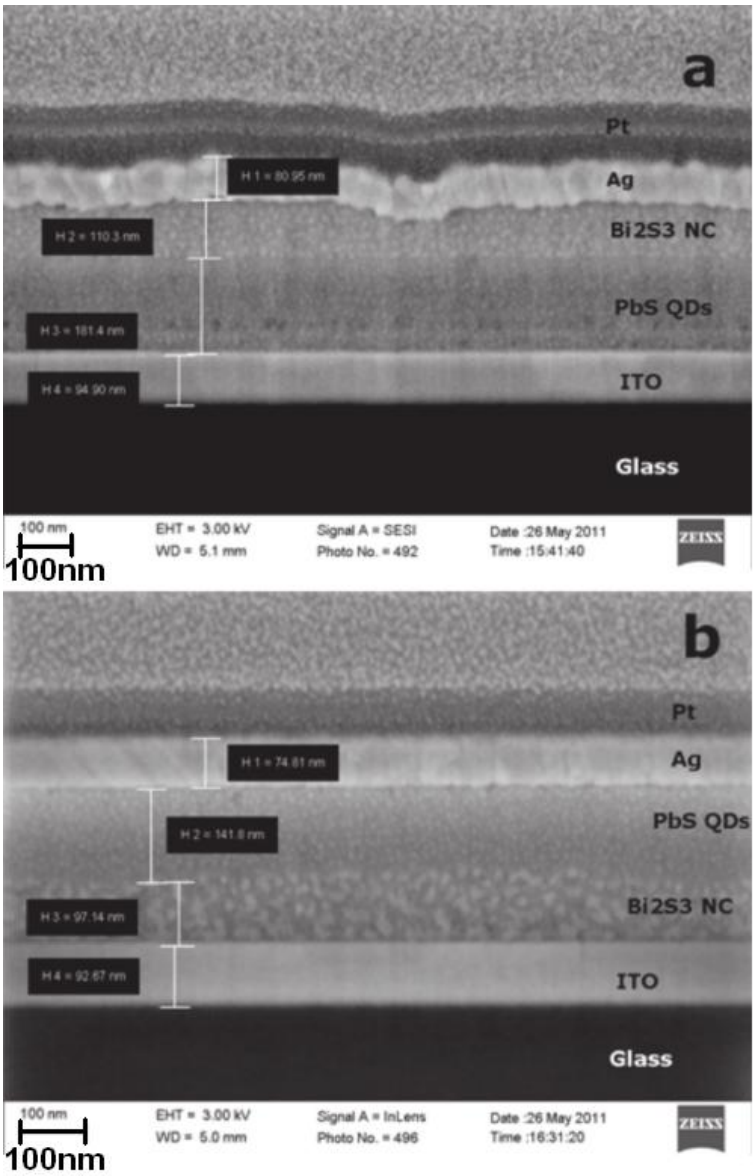


Figure 6.4. Cross sectional SEM images of conventional (a) and inverted structures (b) consisting of 5 LBL Bi2S3 NC and 7 LBL of PbS QD layers. The microscopy images clearly show the 2 distinct regions of the two phases. (reprinted from reference [384]*)*

For PbX QD solar cells, this inverted layout offers the advantage of increased light absorption as compared to the regular device structure, by locating the depletion region adjacent to ITO substrate. This layout also permits the positioning of the illuminated optical field maximum within the depletion region of the PbS layer (as shown in Figure 6.3b). It enables high charge carrier collection efficiency without sacrificing the absorption of photons by allowing the use of thicker, highly absorptive films.[365], [385] In addition, Rath *et al.*[384] demonstrated that inverted structures yield higher FF values than conventional structures. They attributed this to the higher quality metal-semiconductor interfaces in the inverted structures as evidenced by the lower series resistance compared to conventional structures. Furthermore, they also demonstrated that inverted structures exhibited larger shunt resistances compared to conventional structures because of a more robust morphology as evidenced by the cross sectional SEM images (Figure 6.4). In addition, the inverted structure also benefits from better stability by using high work function metal electrodes such as Au or Ag instead of Al or Ca, avoiding the degradation caused by the oxidation of electrodes.

Depletion region

Figure 6.3b shows a schematic energy band diagram of the device at equilibrium. The band alignment formed between *n*-type ZnO and *p*-type PbS QDs allows the formation of a built-in electric field that drives the photogenerated electrons to the *n*-type ZnO and holes to the *p*-type PbS QDs. The impact of the depletion region on the *p*-*n* junction devices can be explained by the charge extraction mechanism, where the built-in electric field is necessary for charge transportation and to prevent recombination. According to Nelson's book,[26] for a *p*-*n* junction device the depletion width inside the *p*-type region, ω_p, and inside the *n*-type region, ω_n, are given by:

$$\omega_p = \frac{1}{N_a}\sqrt{\frac{2\varepsilon V_{bi}}{q(\frac{1}{N_a}+\frac{1}{N_d})}} \qquad \text{Equation 6.1}$$

$$\omega_n = \frac{1}{N_d}\sqrt{\frac{2\varepsilon V_{bi}}{q(\frac{1}{N_a}+\frac{1}{N_d})}} \qquad \text{Equation 6.2}$$

And the total width of the space charge region, ω_{scr}

$$\omega_{scr} = \omega_p + \omega_n = \sqrt{\frac{2\varepsilon}{q}\left(\frac{1}{N_a}+\frac{1}{N_d}\right)V_{bi}} \qquad \text{Equation 6.3}$$

Where ε is the permittivity of the semiconductor, V_{bi} is the built-in voltage, N_d and N_a are the donor and acceptor concentrations. We can tell that the depleted width of either *p*- or *n*-type material increases as either the *p*- or *n*-doping is reduced. This results in a compromise in cell design, since it is not feasible to have a *p*-*n* junction with both a wide depleted region that improves carrier collection and a high doping level that improves cell voltage.

6.2 Experimental Details

6.2.1 The deposition of ZnO thin films on ITO substrate

Pre-patterned ITO substrates were purchased from Xin Yan Technology Limited. The preparation of ZnO and AZO (0.5at.% Al doping) thin films with desired thickness on the ITO substrate by the sol-gel technique has been described in section 3.1, including

substrate cleaning, ZnO and AZO precursor solution preparation and deposition. The deposited precursor thin films were decomposed in air at 500ºC for 1 hour using a Carbolite RWF12/23 furnace, with a ramp rate of 10ºC/min.

6.2.2 Synthesis and LBL deposition of PbS quantum dots

Synthesis of PbS QDs

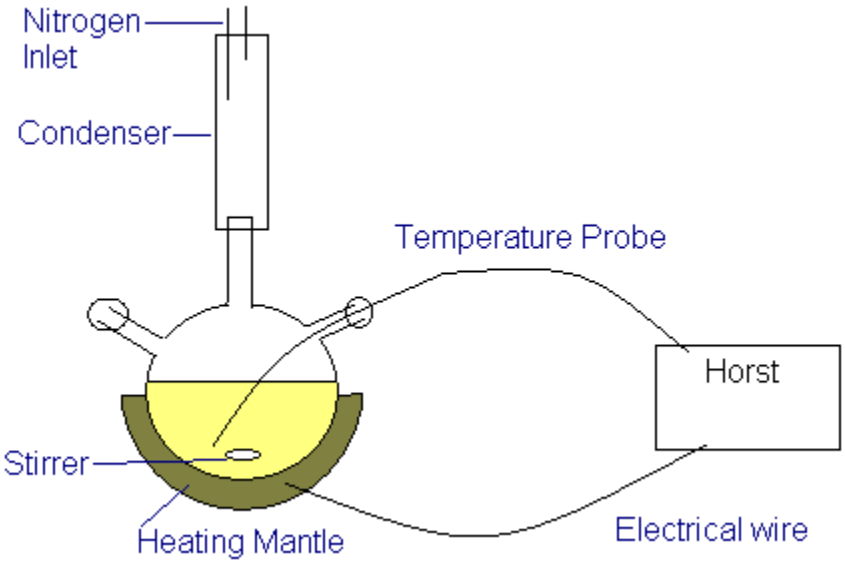


Figure 6.5. An illustration of the experimental set-up to synthesize PbS QDs, heating process is controlled by a Horst temperature regulator.

Synthesis of ~1.45eV band gap PbS nanocrystals was performed in a standard Schlenk line according to recipes in the literature.[358] As illustrated in Figure 6.5, a mixture of 0.47 g lead oxide yellow (PbO, ≥99%, Sigma-Aldrich), 2 mL oleic acid (OA, technical grade 90%, Sigma-Aldrich), and 10 mL 1-octadecene (ODE, tech. grade 90%, Sigma-Aldrich) was stirred in a three-neck round bottomed flask using a magnetic stirrer. This solution is

heated to 120°C using a heating mantle for 2 hours with the protection of N_2 flow. In the meantime, 180 µL hexamethyldisilathiane (TMS, technical grade, 90%, Sigma-Aldrich) and 3 mL ODE were mixed in a separate vial inside a glove box. Once ready to proceed, this TMS mixture was transferred into a syringe and then injected swiftly into the flask at 100°C. The solution turned a brownish colour immediately suggesting a nucleation burst.[386] The heating mantle was removed after 1 minute to allow PbS QDs growth, followed by quenching the flask in an ice water bath.

PbS NCs were precipitated by mixing the reaction solution with 35mL 1:1 ethyl-acetate (Romil): methanol (HPLC grade, Fisher Scientific). The NCs were separated by centrifuging at 4000rpm for 5 minutes. The supernatant was discarded and the sediment was dried under N_2 flow. Two additional purification steps were carried out by re-dispersing the PbS NCs in 5mL hexane (HPLC grade, Fisher Scientific), and precipitated again through a combination of methanol and centrifugation. This procedure is repeated to precipitate any aggregations and/or reaction side-products.[386] Finally, the NCs dispersed in hexane were filtered through a 0.45 µm PTFE filter. The actual PbS NCs were collected at the bottom of the test tube.

Next, ligand exchange was carried out by dispersing the precipitated NCs in 5 mL butylamine (99.5%, Sigma-Aldrich) and ultrasonicating for 30 minutes. Then, the NCs were precipitated by using isopropanol (HPLC grade, Fisher Scientific); followed by re-dispersing in 5 mL butylamine and ultrasonication for 30 minutes. The NCs were finally precipitated by isopropanol with centrifuging, and dried under N_2 flow. The weight of the dry PbS NCs was measured, to calculate the amount of hexane to be added for dispersing

the NCs into the desired concentration. PbS QDs capped with butylamine molecules were then suspended in hexane to produce 25mg/mL stock solution. This solution was stored in a glove box until use.

LBL spin casting of PbS QDs film

PbS QDs films were fabricated by employing a layer-by-layer (LBL) spin casting technique, which permits controlled thickness deposition of nanocrystal layers with pinhole-free structures.[384] 1,2-ethanedithiol (EDT, ≥98%, Sigma-Aldrich), methanol, and acetonitrile (anhydrous, 99.8%, Sigma-Aldrich) were used as received. ITO substrates which were pre-coated with ZnO were cleaned for the deposition of PbS thin films. The cleaning process consisted of sonication in a diluted detergent solution and DI water for 5 minutes each, then soaked in 50ºC acetone and isopropanol for 3 minutes each. Next the substrates were transferred into a glove box where diluted PbS QDs solution (25 mg/mL) was spin cast onto the substrates at 2000 RPM for 60 seconds.

For the assembly of the nanocrystalline PbS films, EDT molecules are employed to replace the electrically insulting butylamine and at act as an agent to cross-link the nanocrystals. The replacing of long insulating ligands with a cross-linking agent can dramatically enhance conductivity and energy transfer in the nanocrystalline films[387–390]. By cross-linking the colloidal PbS QDs into nanocrystalline film structures, unique optoelectronic properties can be obtained, which in turn affect the photocurrent, charge-transport and conversion efficiency to a great extent.[391] This is a result of increased internanoparticle electronic coupling[392] and carrier mobility upon EDT ligand

exchange.[393] In addition, EDT can also render the nanocrystals insoluble in common solvents. The ligand exchange treatment was done by immersing the PbS thin film into 0.01 vol% EDT in acetonitrile solution for 30 seconds. Then the film is soaked in methanol followed by hexane for 30 seconds each in order to wash off any residual EDT and butylamine. The process of PbS spin casting, EDT ligand exchange and methanol/hexane cleaning has been repeated various times to achieve the desired film thickness, as measured by DEKTAK and confirmed using SEM cross section images.

6.2.3 The fabrication of the back electrode

Immediately after the deposition of the PbS thin film, the cells were transferred into a vacuum chamber located inside the glove box and gold electrodes were thermally evaporated through a shadow mask, as described in section 3.1.5.

6.2.4 Material characterization and device testing

As described in section 3.3, a Cary 5000 UV-Vis spectrophotometer was used to obtain absorption spectra of the quantum dots in hexane at room temperature. Measurements were taken in a 10mm quartz cuvette, at a scan rate of 600nm per minute using a 1nm interval. The spectral response was adjusted using a hexane reference. Transmission electron microscopy (TEM) was carried out using a JEOL 2000FX TEM by Cheng Cheng, to investigate the size distribution and structure of individual quantum dots. TEM specimens were prepared by taking the cleaned product, diluting it and placing a drop on an ultra thin carbon grid. The devices were placed in a testing holder with continuous nitrogen gas flushing throughout the experiment. Current-voltage (IV) and external quantum efficiency (EQE) characteristics were recorded as described in section 3.4.

6.3 Results and Discussion

6.3.1 Size and energy band gap of the PbS QDs

The tunability of QDs enables optical matching of the absorbance of single-junction solar cells to the solar spectrum and allows the design of multi-junction devices for further efficiency improvement.[377] Consequently, the size of the QDs used in the devices is crucial, since it determines the degree of the quantum confinement effect, which controls the band gap of the PbS layer and hence the open circuit voltage of the device. UV-Visible and TEM characterization of the PbS QDs solution was performed to study the optoelectronic and physical properties of the QDs, and the data are presented below.

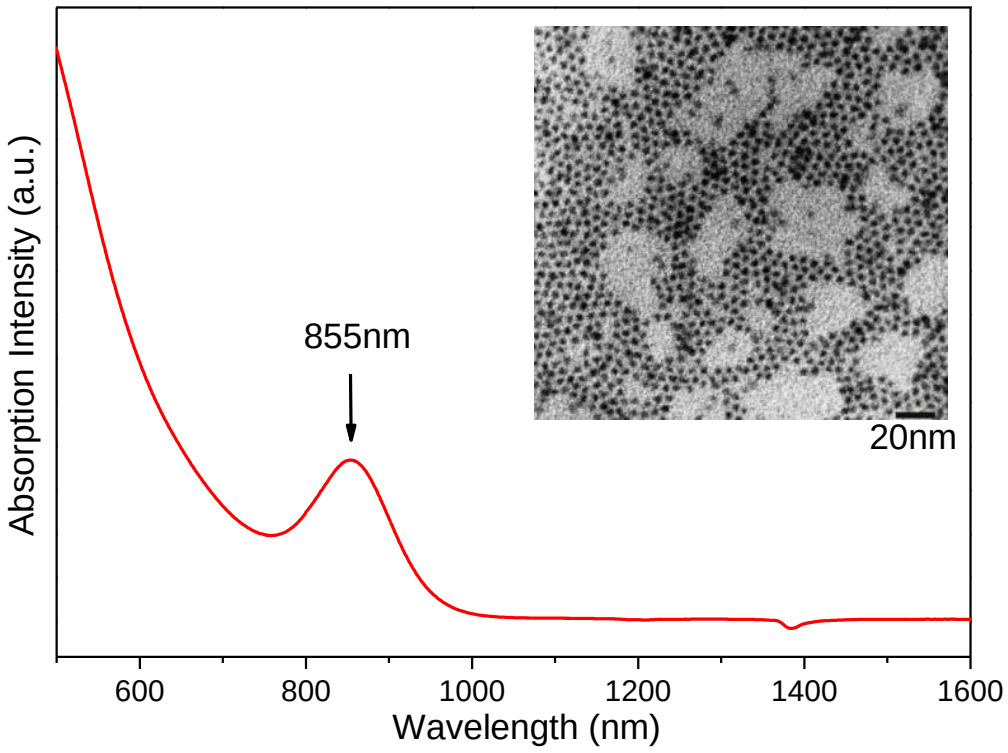


Figure 6.6. Absorption spectrum of as-synthesized PbS QDs in hexane. The inset shows the transmission electron micrograph (TEM) of an ensemble of PbS QDs in a film (spherical black dots are the QDs, TEM photo was taken by Cheng Cheng).

From data like that shown in Figure 6.6, we found that as-synthesized PbS NCs show a well-defined excitonic peak centred at 855nm. We use this excitonic peak value to calculate the band gap, E_g in eV: [394]

$$\text{Band gap energy } (E_g) = h*c/\lambda \qquad \text{Equation 6.4}$$

Where *h* is Plancks constant and is equal to 6.626×10^{-34} Joules sec, c is the speed of light and is equal to 3.0×10^{8} metres/sec, λ is the excitonic peak wavelength and is equal to 855×10^{-9} metres in our case. Knowing 1eV = 1.6×10^{-19} Joules (conversion factor), we obtained:

$$E_g = 1.45\text{eV}$$

Next, the average size of the PbS NCs was calculated based on the method used by Jiang Tang *et al*.[386] that was first proposed by Iwan Moreels *et al*.[395]:

$$E_g = 0.41 + (0.0252d^2 + 0.283d)^{-1}$$

A value of 2.73nm can be calculated for the average QD size. TEM was employed to gain an understanding of the nanocrystal growth and quality. The inset in Figure 6.6 shows a high magnification image of the film composed of individual quantum dots. We can also see that these PbS QDs show a spherical shape with a mean diameter of approximately 2.7 ± 0.3nm. This value is in good agreement with the size calculated from the distinct excitonic peak observed in Figure 6.6. In addition, these nanoparticles formed periodic arrays with a hexagonal packing pattern on the TEM grids, suggesting that the particles are rather uniform in size.[396] A similar monodispersity has been reported for QDs used as

solar light harvesters,[397] which is an important factor for QD applications because size determines energy levels, therefore alters the effective band alignment. [371] Furthermore, the TEM image also reveals that the PbS nanocrystals are non-aggregated, which is an important factor for device fabrication. In summary, these QDs demonstrated monodispersity in nanoparticle size distribution and have an energy band gap of approximately 1.45eV, implying a high limiting efficiency as a single band gap solar cell that matches well with the solar spectrum, as shown in Figure 6.2.

6.3.2 Thickness optimization of the *p*-type PbS QDs layer

Undoped ZnO as n-type material

Inverted ITO/ZnO/PbS/Au devices were fabricated using the LBL-processed PbS layers synthesized and tested in nitrogen atmosphere. Devices with various PbS active layer thicknesses were fabricated and tested to optimize the performance, while keeping ZnO layer at a constant thickness of 150±5nm. A set of 30 cells were fabricated for this study, from which 23 cells were selected. The 7 discarded cells were probably damaged by mis-handling during fabrication (such as uneven coating of each active layer) or testing errors during processing (such as exposing to air for an extended period before measurement).

In Figure 6.7, the performance characteristics of a set of inverted ITO/ZnO/PbS/Au heterojunction devices are displayed over a range of PbS active layer thicknesses. An increase in J_{sc} is observed with increasing PbS thickness up to 150nm. This result is consistent with Capacitance-Voltage (CV) measurements indicating a ~140 nm thick depleted region in the PbS at the heterojunction interface.[384] For a PbS thickness below

140nm, a dependence of the capacitance on the PbS thickness is observed, suggesting a fully-depleted PbS layer. However as the thickness of PbS increases, the devices enter a regime of incomplete depletion as evidenced by saturation of the capacitance decrease rate. This depletion width value is also close to that measured in PbS QD Schottky devices (~150nm).[380]

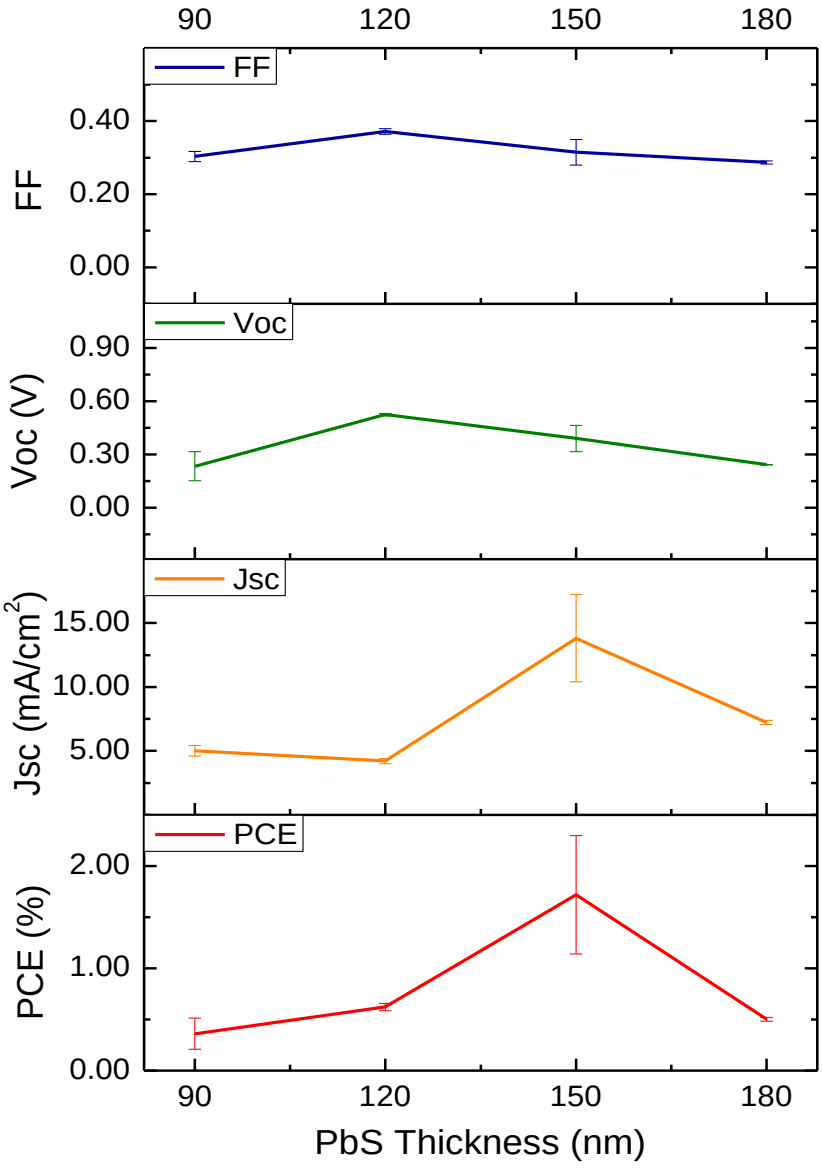


Figure 6.7. Performance characteristics of ITO/ZnO/PbS/Au devices employing a 150nm ZnO layer and PbS layer of varying thicknesses (ranging from 90 to 180nm). Data points and error bars correspond to the average and standard deviation across three to six cells. Lines serve as a guide to the eye. An efficiency maximum is achieved for a 150nm-thick PbS layer, with J_{sc} = 12.8 ± 0.6 mA/cm^2, V_{oc} = 0.48 V, FF = 0.36, and PCE = 2.23 ± 0.1%.

Devices with 240nm PbS layer were fabricated as well, but with this even thicker PbS layer, devices suffer from poor charge extraction, resulting in very poor IV performance. A cross-sectional SEM image is shown in Figure 6.8, featuring the optimized PbS thickness. This image also shows the uniformity of each deposited layer, as well as their reasonably well-controlled thicknesses.

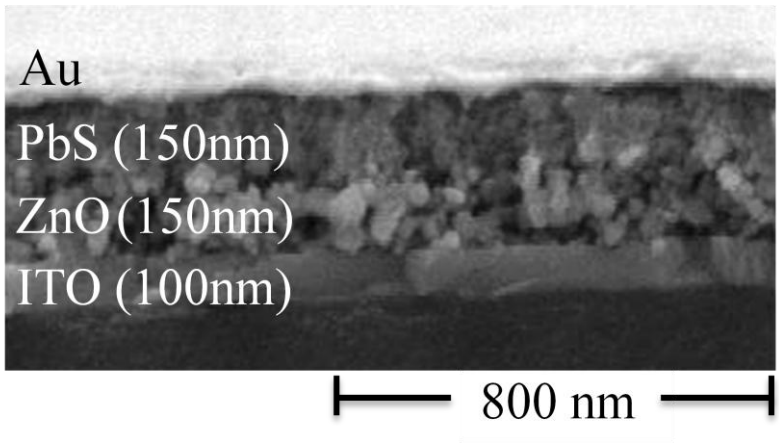


Figure 6.8. SEM cross sectional view of the device with optimized PbS thickness. The 150nm ZnO thin film is 0.3% doped with Al).

Aluminium doped ZnO (AZO) as n-type material

By doping the ZnO thin film with Al, I expected an increase in V_{oc} owing to the well known Burstein-Moss effect, more discussion is presented in section 6.3.3. Here, in order to investigate the effect of the PbS thickness on device performance and corroborate the estimate of the depletion width, we performed a similar study in inverted structures employing AZO instead of ZnO as the *n*-type material. Inverted ITO/AZO/PbS/Au devices were fabricated with various PbS thicknesses, all AZO layers were 0.5at.%Al doped and were 150±5nm thick. The results are summarized in Figure 6.9.

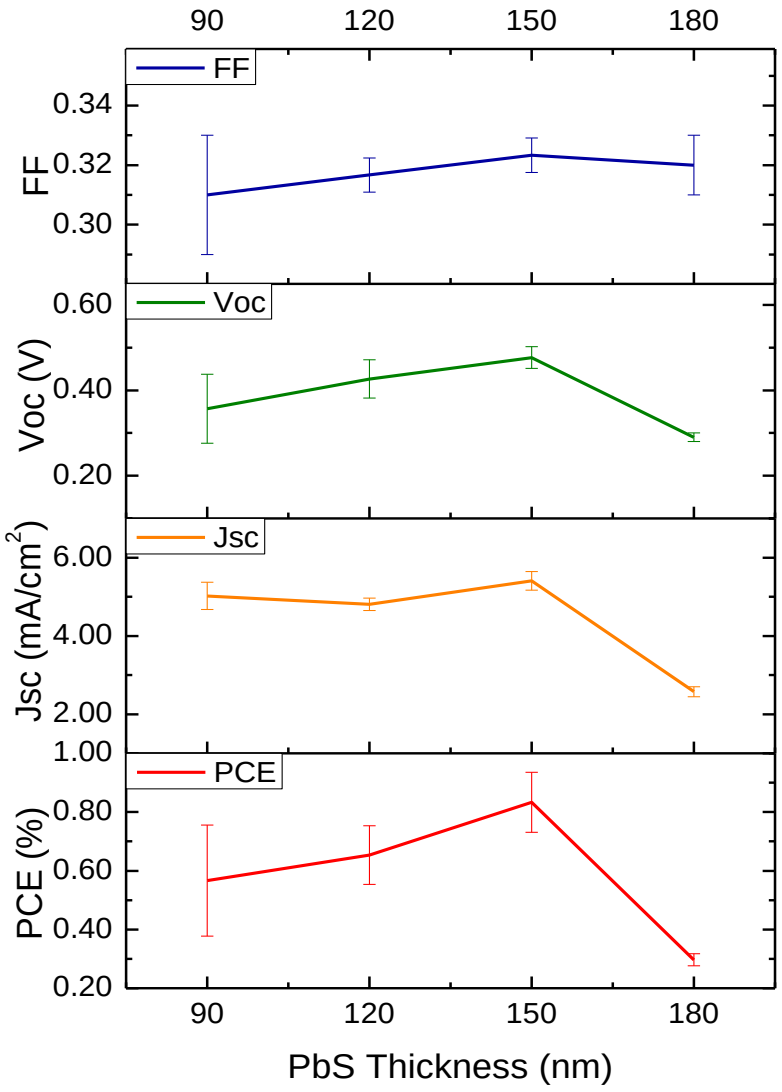


Figure 6.9. Performance characteristics of ITO/ AZO/PbS/Au devices employing a 150nm AZO layer 0.5at.% doped with Al, and a PbS layer of varying thicknesses (ranging from 90 to 180nm). Data points and error bars correspond to the average and standard deviation across three cells. Lines serve as a guide to the eye. An efficiency maximum is achieved for a 150nm-thick PbS layer, with J_{sc} = 5.2 ± 0.4 mA/cm^2, V_{oc} = 0.48 ± 0.2 V, FF = 0.325 ± 0.005, and PCE = 0.86 ± 0.06%.

The same trend is observed for the AZO devices as compared to the undoped ZnO devices: (i) a dramatic improvement in the IV performance was found up to 150nm, (ii) this improvement is mainly caused by the improved J_{sc}, (iii) for PbS thickness beyond ~150nm the J_{sc} values decrease sharply indicating a depletion width of around 140-150nm, in

agreement with ZnO devices and other reports.[380], [384] We indeed expect the AZO devices to demonstrate a similar trend as compared to the ZnO devices, because it is the doping concentration in the *p*-type material that determines the depletion width within the PbS layer.[24]

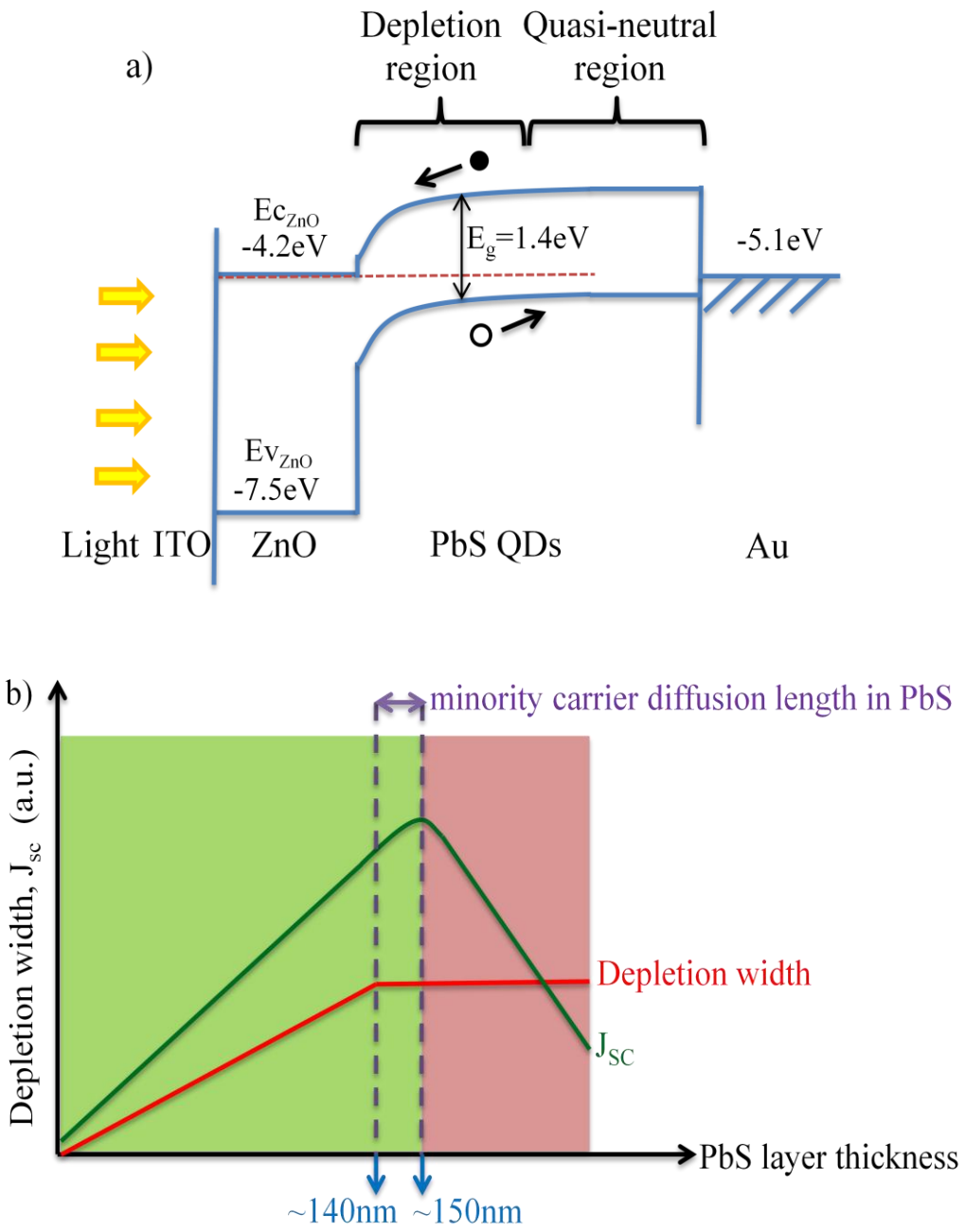


Figure 6.10. (a) Electron energy band diagram of a depleted heterojunction device (After Barkhouse et al. [398]*). (b) A schematic illustration of the relation between PbS thickness, depletion width and device J_{sc} in simplified cases.*

Heterojunction QD devices transport electrons and holes through a QD film consisting of various sub-layers, as suggested by Kramer and Sargent.[399] This transportation occurs efficiently over a distance equal to the sum of the depletion width (see Figure 6.10a) and the minority carrier diffusion length (Figure 6.10b). Unfortunately, because the diffusion length is limited to a few tens of nanometres in PbS,[398], [400] extraction is only efficient when there is a significant built-in electric field. That is, the majority of the current generated in QD devices to date is dominated by drift rather than diffusion.

As a consequence, those devices, with active layer thickness less than or equal to the sum of depletion width and minority carrier diffusion length, can achieve efficient charge carrier generation and transport throughout the entire active layer region. This efficient charge extraction originates from the built-in electric field from the depletion region and charge carrier diffusion from the small extra region beyond the depletion width (Figure 6.10b). This is the case for the devices with PbS thickness ≤150nm shown in Figures 6.7 and 6.9.

In addition, by comparing the normalized EQE and AM1.5 spectra, we found that the device with ~150nm thick PbS is most efficient in converting incident photons with ~425nm wavelength into charge carriers, which matches well to the peak (~450nm wavelength) of the solar spectrum, where there are most incident photons (Figure 6.11). This is an important beneficial character of these devices. Moreover, devices employing ~150nm PbS demonstrate efficient charge extraction ability as well, as discussed earlier. However, this efficient charge extraction is associated with less efficient photon absorption ability to make use of incident photons with longer wavelengths (Figure 6.11).

The limitation here is that, although visible wavelength photons can be absorbed efficiently in a single pass, these QD films are too thin to absorb most near-infrared photons.

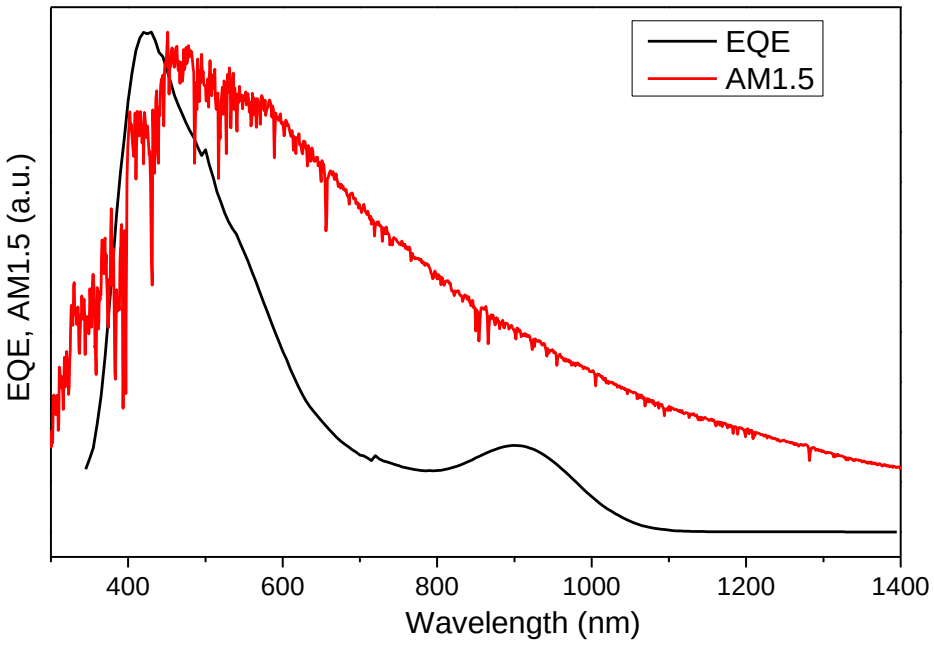


Figure 6.11. Normalized external quantum efficiency (EQE) spectrum of a 150nm PbS device, demonstrating poor long wavelength absorption. The sharp drop below 400nm is due to the ZnO absorption which is not expected to contribute much to the charge carrier generation.

On the other hand, if we want to improve the efficiency of absorption of the incident photons and fabricate devices employing an active layer with a thickness greater than the sum of depletion width and minority carrier diffusion length (such as the 180nm PbS devices), a widening of the quasi-neutral region at the rear of the device can be established (Figure 6.10a). In contrast to the depleted region closest to the interface with ZnO, where depleted majority carriers create a space charge region and charge extraction is most efficient due to the presence of the built-in electric field, this quasi-neutral region present

in the thick PbS layer is not fully depleted and thus shows significantly limited charge extraction. Photogenerated electrons and holes in the quasi-neutral region suffer from enhanced recombination [384] due to the lack of driving force, because charge extraction in this region relies on slow and spatially random minority carrier diffusion.[380], [385], [401]

For those even thicker PbS devices, formation of another region in addition to the depletion and quasi-neutral regions is possible. That is the region far from the depletion width (beyond the quasi-neutral region) and is termed the 'dead zone', where absorption remains strong but carrier extraction is negligible.[398] Such dead zones have important implications for device design, especially for the inverted structure where illumination is through the top contact. The poor performances of devices employing 240nm PbS layers perhaps results from the presence of a dead zone.

In conclusion, the two competing factors namely 'extraction' versus 'absorption' result in a compromise in cell design. This is one of the many trade-offs in solar cells. In sight of this limitation, the optimized PbS thickness is found to be approximately 150nm for my inverted ZnO/PbS devices. Those cells employing a thicker PbS layer (eg. 180nm as shown in Figures 6.7 and 6.9) suffer significantly reduced performance. Attempts to resolve the 'extraction vs. absorption' issue may be performed by improving the hole extraction layer. For instance, Gao *et al*. have demonstrated a significant improvement in device performance by inserting a MoO_x layer between the PbS and back electrode which improves hole extraction.[376]

6.3.3 The influence of Al-doping concentration in the ZnO film on the device performance

The hypothesis for the effect of Al doping on the device performance is based on the well known Burstein-Moss effect,[198] which has been explained earlier in Chapter 4. If sufficient Al doping is employed, it can possibly increase the carrier concentration. This might lead to a blue shift of the Fermi level, depending on the level of doping, which will then widen the band gap (Figure 6.12). However, only very low level of doping should be employed here in order to retain the *n*-type semiconductor properties for application in *p*-*n* junction devices. As explained in Chapter 4, ZnO is easily tunable to exhibit conductor behaviour upon Al doping which is not favourable here.

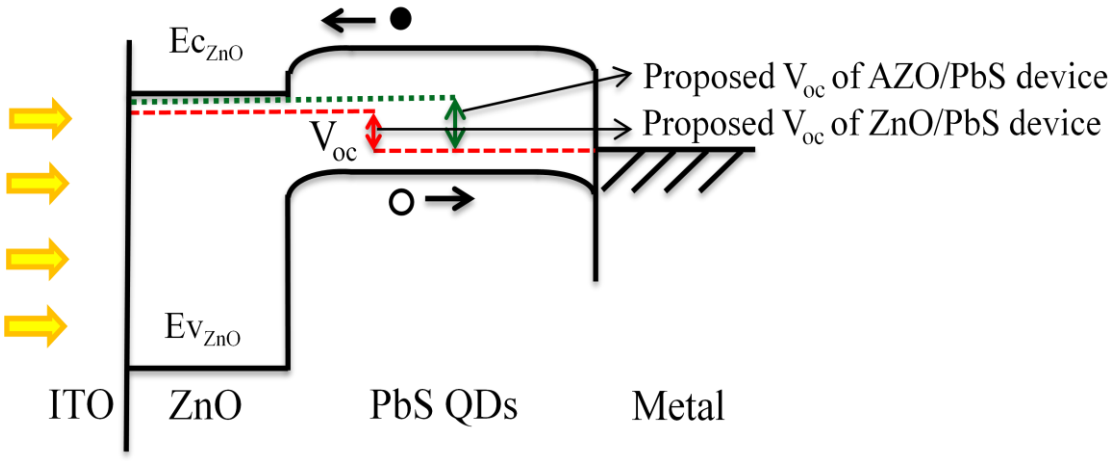


Figure 6.12. Schematic band diagram of inverted ITO/ZnO/PbS/Au solar cell under illumination, showing the potential shift of E_F before (dashed red line) and after (dotted green line) the small amount of Al doping. It illustrates the potential increment in V_{oc} that may be caused by the blue shift in ZnO layer up on Al doping.

Considering that Al doping can possibly raise the Fermi level of AZO thin films, and the difference in the quasi-Fermi levels in the AZO and PbS QD layers determines V_{oc} (Figure 6.12),[402] it was hypothesized that an improved V_{oc} might be observed upon the increase

of Al doping concentration in the ZnO layers. I therefore sought to investigate this hypothesis. Employing the same experimental and analytical methods, 150nm thick layers of PbS QDs of ~2.7nm were deposited onto 150±5nm thick AZO layers. A similar device architecture is adopted (i.e. ITO/AZO/PbS/Au), but with various low concentrations of Al doping in the AZO layers (0, 0.1, 0.2, 0.3, 0.4 and 0.5at.%). Figure 6.13 displays the performance characteristics of these devices.

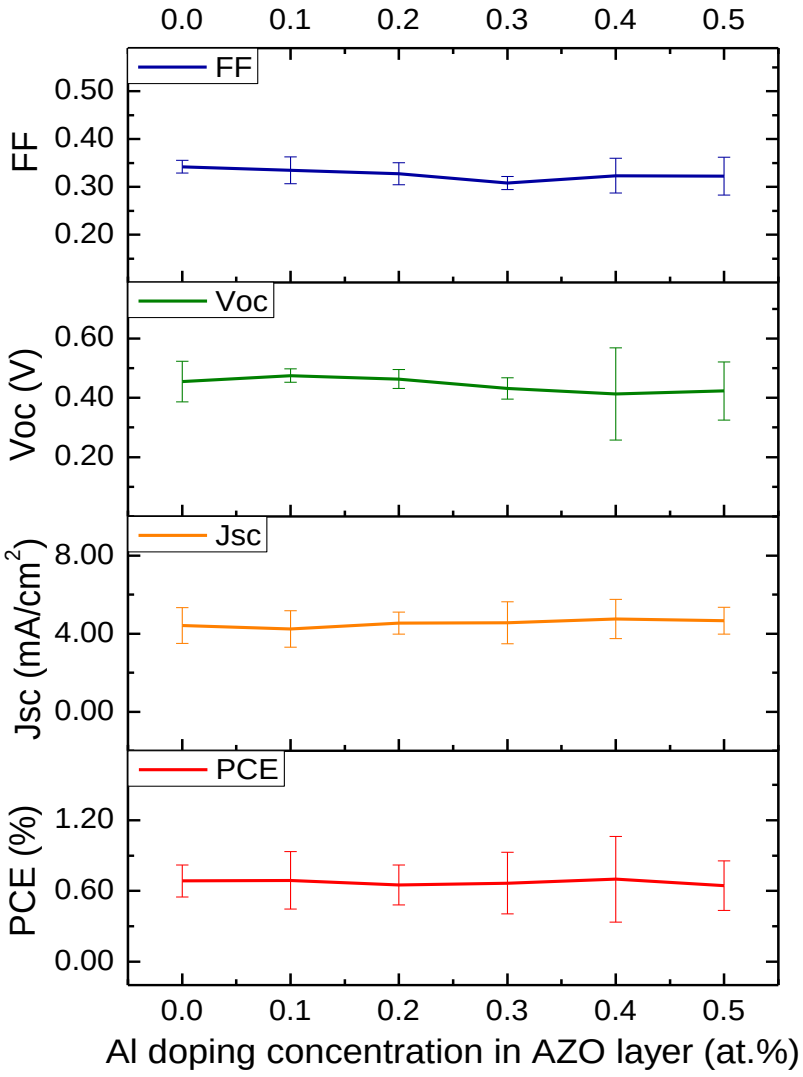


Figure 6.13. Performance characteristics of ITO/ AZO/PbS/Au devices employing an AZO layer of varying Al-doping concentration (ranging from 0 to 0.5at.%). Data points and error bars correspond to the average and standard deviation across five to seven cells. Lines serve as a guide to the eye.

Figure 6.13 shows that all the devices have virtually very close IV performances, with no obvious sign of improved V_{oc} upon increase in Al doping from 0 to 0.5%. This is possibly due to the fact that the nominally 'undoped' intrinsic ZnO crystals are unintentionally doped, and give a strong *n*-type conductivity.[403], [404] This is attributed to native point defects such as oxygen vacancies as deep donors, as well as hydrogen and the less energetically favourable zinc interstitials as shallow donors.[405] These defects are likely to form with a substantial concentration in *n*-type ZnO, leading to a significant concentration of donors. Lavrov *et al*.[406] observed a donor concentration as high as $10^{16}cm^{-3}$. Probably, this relatively rather heavy unintentional 'doping' thus does not allow the observation of small changes brought about by the very low Al doping concentration. As a consequence, this results in the insignificant change of overall performance upon the small amount of aluminium doping increment. Similar observations in inverted organic solar cells have also been reported by Oh *et al.*,[200] where little variation in the V_{oc}, FF and J_{sc} as a function of the degree of doping was observed. Another possible explanation for the lack of improved performance upon increasing Al doping concentration might be the reduced extraction efficiency. As the defect intensity can be increased upon Al doping, resulting in a large number of mid-gap trap states,[407] this leads to rapid recombination of photogenerated electrons with holes, which will significantly affect electron transport properties in AZO.[408] These traps would have to be saturated by electrons before an increase in conductance could be observed.[409]

Perhaps in consequence of the above-mentioned factors, one can infer that variation of the doping concentration between 0% and 0.5% has no major impact on the device performance. As a result, V_{oc} improvement upon doping can probably be ruled out as a potential cause of any subsequent changes in device efficiency.

6.3.4 The influence of UV exposure on the device performance

Ten inverted ITO/ZnO/PbS/Au devices were characterized for the investigation of the effect of UV exposure. The ZnO layers in all these devices are 150±5nm thick, with various degrees of Al doping. IV measurements were taken before and after 10 minute UV treatments. The same degree of improvement was consistently observed throughout entire set of devices. The evolution of the performance characteristics of various devices with and without UV treatment is summarized in Table 6.1.

Table 6.1. The influence of UV treatment on the performance characteristics of ITO/AZO/PbS/Au PV cells with different Al doping concentration.

	Al doping (at.%)	J_{sc} (mA/cm^2)	V_{oc} (V)	FF	PCE (%)
Before UV	0	5.57	0.55	0.39	1.18
After UV	**0**	**7.47**	**0.56**	**0.40**	**1.68**
Before UV	0.1	5.45	0.50	0.37	1.01
After UV	**0.1**	**6.53**	**0.53**	**0.38**	**1.31**
Before UV	0.2	5.22	0.50	0.37	0.97
After UV	**0.2**	**6.73**	**0.53**	**0.37**	**1.32**
Before UV	0.4	5.35	0.51	0.35	0.96
After UV	**0.4**	**7.83**	**0.53**	**0.36**	**1.48**

We can see from Table 6.1 that the introduction of a 10 minute UV treatment clearly improved the J_{sc} values for all devices, while V_{oc} and FF improved an insignificant amount. These result in an overall 1.4-, 1.3-, 1.3- and 1.5-fold enhancement in PCE for the devices with 0, 0.1, 0.2 and 0.4% Al doping concentration. We noticed that, regardless of the Al doping concentration, the degree of enhancement for various devices are almost the same. In another words, what we have observed are that (i) the performance enhancement is mainly induced by the improved J_{sc}, (ii) the degree of enhancement is independent of the degree of Al doping concentration in the AZO film.

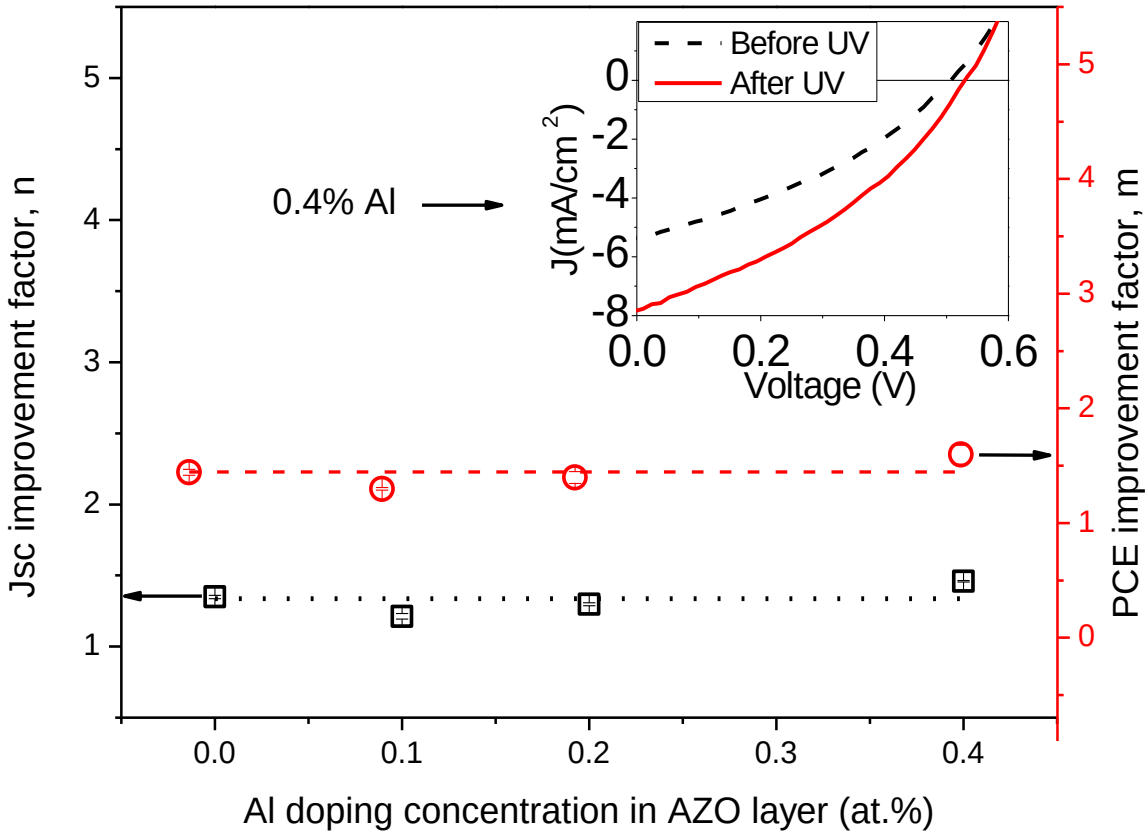


Figure 6.14. The influence of UV treatment on the performance characteristics of ITO/AZO/PbS/Au PV cells with different Al doping concentrations. The open squares represent the improvement factor of J_{sc} (the black dotted line is the fit by Origin for n), and open circles represent the improvement factor of PCE (the red color dashed line is the fit by Origin for m). The inset is an example showing the improvement in IV characteristics of a device before (dashed line) and after (solid line) the 10 minutes exposure to UV.

To further investigate these observations, two terminologies have been defined: the J_{sc} improvement factor n, denoting the J_{sc} after UV treatment divided by the original J_{sc}; and the PCE improvement factor m, denoting the PCE after UV treatment divided by the original PCE. Figure 6.14 displays a plot of these two factors, and it was found that the average J_{sc} improvement factor n is approximately 1.34, and the average PCE improvement factor m is approximately 1.45, as fitted by Origin. The UV response arises from the absorption of UV radiation by ZnO, which lead to the presence of photogenerated holes that can induce *n*-type doping in the ZnO nanocrystals.[410] It was suggested by Collins *et al*.[409] that those electron-hole pairs diffuse to the surface of ZnO and can be trapped by the oxygen ions. UV treatment can be used to free the charge carriers, by inducing desorption of oxygen molecules that are otherwise absorbed on the ZnO surface. This release of oxygen on the ZnO surface can enhance the concentration of mobile electrons originating from the native doping and photoexcitation of the ZnO nanocrystals. We also had hoped that the Al would effectively dope ZnO films to improve carrier concentration, but has either not happened or it does not affect J_{sc}.

6.3.5 The influence of N_2 exposure on the device performance

Devices were stored in N_2 and then in air with light shielding but without any encapsulation, and we tracked their performance in order to study their stability in N_2 and air. The glove box was used to provide the N_2 atmosphere with a low concentration of impurity gases (oxygen and water <100 ppm). A set of twelve devices was studied, employing the same device structure and processing method (ITO/ZnO/PbS/Au devices with ~150nm ZnO and ~150nm PbS). The IV characteristics were recorded once the devices were fabricated, after exposure to N_2 (for 1 hour, 24 hours, 72 hours, 168 hours and 336 hours), as well as after exposure to air (for 3 hours, 42 hours and 96 hours).

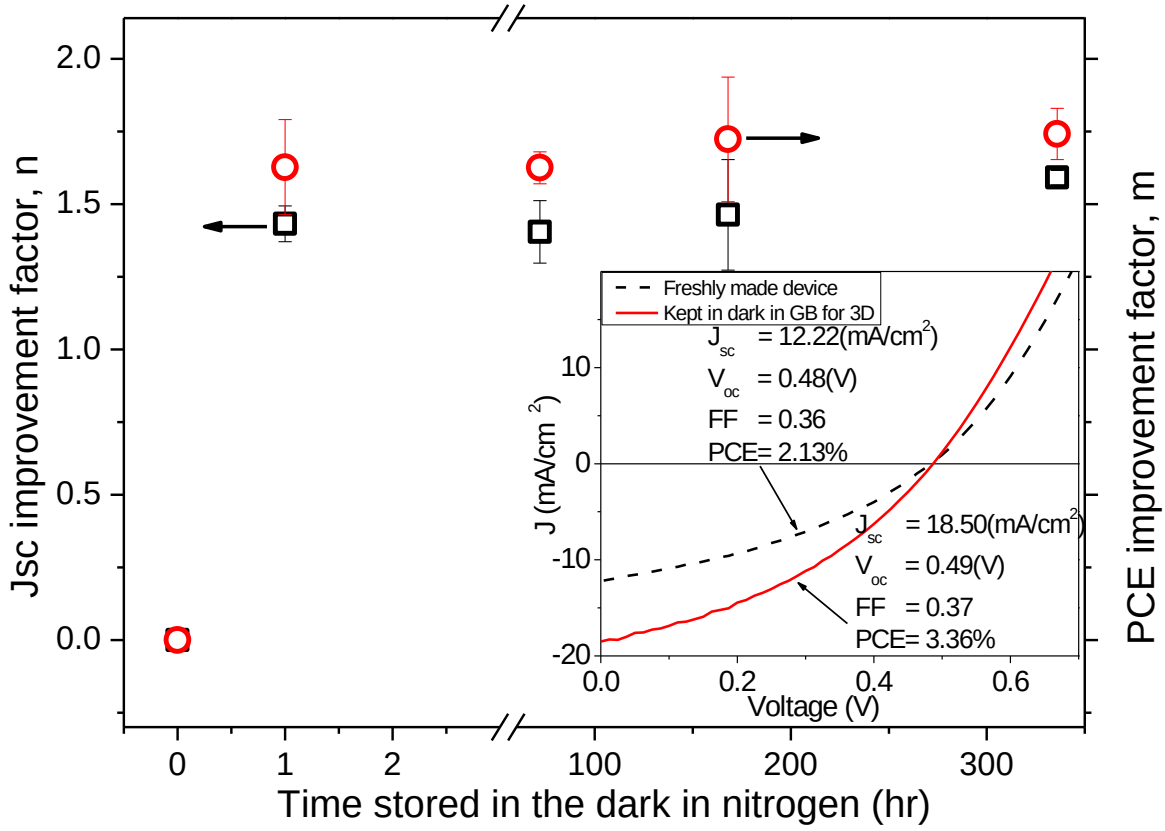


Figure 6.15. The improvement in performance of ITO/ZnO/PbS/Au devices as a function of N_2 exposure time, where open squares represent the improvement in J_{sc}, and open circles represent the improvement in PCE. The inset is an example showing the improvement in IV characteristics of a device before (dashed line) and after (solid line) exposure to N_2 for 72 hours.

N_2 exposure

The performance of freshly made devices is relatively poor, but can be improved upon N_2 exposure in the dark, surprisingly. The evolution of device performance over N_2 exposure time is shown in Figure 6.15. The impact of N_2 exposure on the IV performance is significant, leading to a 1.5±0.1-fold increment in J_{sc} (J_{sc} improvement factor n, as defined earlier). The improvements in V_{oc} and FF are negligible. Together, a 1.6±0.1-fold improvement of PCE was achieved (PCE improvement factor m). For instance, as we can see from the inset in Figure 6.15, a freshly made device was first tested in nitrogen, and

stored in the glove box immediately after testing. Interestingly, after 72 hours N_2 exposure we observed an increment in J_{sc} from 12.22 to 18.50mA/cm^2, while V_{oc} and FF remained nearly unchanged, leading to an enhanced PCE from 2.13% to 3.36%. The observation has demonstrated good N_2 stability of the devices up to 14 days (336 hours).

A similar observation was reported for PbSe QD field effect transistors (FETs),[411] where an improved charge mobility in the presence of N_2 was observed. They attribute this improvement to the passivation of electron trapping sites by N_2 molecules. Several possibilities could explain the improvement in performance in our devices. Firstly, the N_2 gas present in the glove box might have displaced some of the residual oxygen and water molecules that inevitably exist on the surface of the PbS crystals. Perhaps this reduction in oxygen and water has resulted in the improvement because PbS is prone to degradation in the presence of oxygen and water (discussed in the later section on air exposure). Secondly, the exposure to the N_2 atmosphere improved the electrical properties of the PbS films possibly by passivating trap sites, as a result of interactions between the N_2 molecules and the surface of the PbS QDs. Similar observation was reported for PbSe QD films,[412] where it was suggested that N_2 molecules may diffuse through the QD film and physically adsorb onto the surface of the QDs, resulting in the N_2 molecules occupying the electron trapping sites, leading to an improved charge carrier concentration and mobility. Likewise, the N_2 atmosphere present in our PbS films might have played an important role by passivating the trap sites that can otherwise capture the mobile charge carriers. This possibly improved the charge transportation properties of the PbS film, thus the observed J_{sc} increment. A third explanation is that the low oxygen environment of the glove box might probably result in a desorption of oxygen from the ZnO layer, which can lead to a further doping of ZnO because it is well known that oxygen vacancies are intrinsic

electron donors in ZnO.[306], [413] This *n*-type doping by oxygen vacancies can improve the carrier concentration in the ZnO layer,[295] which possibly contributed to the improvement of J_{sc} values in our devices.

Last but not least, we can tell from Figure 6.15 that the improvement of performance is significant once stored in nitrogen (1 hour), and no significant further improvement can be found. This time scale suggests that the improvement is strongly affected by relatively fast processes in the PbS film, which appear to be saturated after 1 hour of exposure to N_2.

Air exposure

Finally, although these devices are stable when stored and tested under O_2- and H_2O-free conditions, their lifetime is small – approximately 3 hours – when exposed to ambient conditions. These stability problems have also been reported before for lead chalcogenide nanocrystal cells[363] and for SnS/PbS nanocrystal cells.[414] In order to find out the stability in air, I have exposed the above devices to air in the dark and tested after 3 hours, 42 hours and 96 hours respectively. However, J_{sc} reduced from 6.5 mA/cm^2 to 2.9 mA/cm^2 after 3 hours exposure and to 1.9 mA/cm^2 after 42 hours exposure. V_{oc} reduced from 0.58V to 0.24V after 3 hours and 0.13V after 42 hours exposure to air. FF also reduced from 0.46 to 0.33 after 3 hours exposure and 0.25 after 42 hours. These have led to a PCE loss from 1.72% to 0.23% after 3 hours, 0.06% after 42 hours, and ~0% after 96 hours exposure to air. We observed that these devices lose nearly all their efficiency after ~42 hours exposure to air. This suggested that these devices are very sensitive in air, which is primarily due to reactions with oxygen and moisture.

It is generally understood that there might be several causes for this degradation. First of all, assemblies of QDs are inherently metastable, prone to oxidative degradation driven by their large surface to volume ratios and high surface energies, which also limit their use in practical devices.[380], [415] Ambient oxidation or reaction with moisture is usually detrimental to QD devices because these reactions introduce traps,[386], [416] giving rise to more recombination loss and mobility reduction.[377] Secondly, the QD films may lose passivation and/or develop mid-gap recombination centres.[415] Unstable ligands such as butylamine and ethanedithiol make the PbS films particularly sensitive to oxygen and moisture. The butylamine is suspected of reacting with the shallow work function metal contact. Koleilat *et al.*[362] have demonstrated improved lifetime in devices by passivating PbSe with more robust 1,4-benzenedithiol. This indeed suggests that the stability of passivation within the film may be a key factor for the stability of the devices. Furthermore, Buckner *et al.*[417] suggested that the penetration of water into the nanocrystal structure could create strain in the crystal, which creates trap sites for the exciton. Likewise, Somorjai [418] has suggested that the adsorbed oxygen traps photogenerated electrons, which decreases the free-electron lifetime by a few orders of magnitude.

Although these devices degraded rapidly during ambient storage, leading to almost complete loss of PCE over 42 hours, they actually compare favourably with PbSe-EDT devices for which nearly instantaneous degradation has been reported upon exposure to air.[380], [419] Comparing our butylamine capped PbS QDs devices with the first high-efficiency devices reported also employing butylamine,[420] their devices degraded in air within a few minutes. This slightly better stability in air of our devices might be a result of using a deep work function metal contact. Most devices reported employ a shallow work

function metal contact; these metals are known to oxidize rapidly. In contrast, our devices employ Au as the electrode, which is less reactive and improves the stability of the contact. This is consistent with other reports which employ deep work function metals such as Au and ITO, which also demonstrated much less degradation in air.[392], [421], [422]

6.4 Conclusion

In summary, the performance of inverted ZnO/PbS QD heterojunction photovoltaics was significantly enhanced by changing the *p*-type PbS QD thickness, UV treatment of the *n*-type ZnO layer, as well as storing the devices in the dark in nitrogen. The improved device exhibited a respectable 3.36% solar power conversion efficiency, with 150nm thick ZnO and PbS layers after exposing to N_2 atmosphere. The strategies presented in this chapter enable good compromise between solar absorption and charge transportation, as well as good device stability, whilst using inexpensive chemicals readily processed in solution. The work presented here provides a roadmap for the optimization of metal oxide/quantum dots solar cells. Further work may be performed in the area of device engineering, to design devices that increase absorption and decrease the demand for long distance transportation.

Chapter 7 - Summary

7.1 Conclusion

The aim of this thesis was to investigate zinc oxide in different photovoltaic device architectures as outlined in Table 7.1 in a bid to improve device performance.

Table 7.1. Summary of the application of zinc oxide in various photovoltaic architectures investigated in this thesis.

Function of ZnO	Device Architecture	Chapter
TCO electrode	Glass substrate/ZnO/PEDOT:PSS/P3HT:PCBM/Al	4
Buffer layer	Glass substrate/ITO/ZnO/P3HT:PCBM/ PEDOT:PSS/Au	5
Junction material	Glass substrate/ITO/ZnO/PbS /Au	6

From these studies, the following conclusions can be drawn:

Transparent electrodes Chapter 4 described the development of a simple and cost-effective way to manufacture AZO thin films by the sol-gel spin-coating method for the application as transparent electrodes in solar cells. Modifying thermodynamics and processing conditions optimised the optoelectronic properties. In particular, 1.5at.% Al doping improved carrier concentration as shown by Hall Measurements, while thin films grown from 1M precursor solution improved carrier mobility due to reduced grain boundary scattering as suggested by the AFM images. In addition, a vacuum-annealing treatment improved both carrier concentration and mobility by approximately two orders of magnitude. This was ascribed to three main factors;

improved crystallinity (enhanced *c*-axis orientation and relieved stress), larger grain size (reduced scattering and improved mobility) and increased oxygen vacancy concentration (one oxygen vacancy can effectively donate two free electrons). Finally, we successfully demonstrated the fabrication of OPV devices employing AZO electrodes. The AZO devices were less efficient than those made with sputtered ITO, a result of the higher electrical resistivity leading to parasitic resistive losses.

Buffer layers Chapter 5 addressed the leakage current issue in inverted OPV devices by inserting a zinc oxide buffer layer between the organic photoactive layer and ITO electrode, with different Al dopings and various thicknesses. The zinc oxide buffer layer favours the transport of electrons and blocks holes, owing to the well-aligned energy levels of ZnO and the electron acceptor material. In addition, device series resistance was reduced by doping the zinc oxide buffer layers with aluminum, owing to the lower resistivity of AZO. Next, the influence of AZO buffer layer thickness on the device performance was explored relating the AZO sheet resistance to device series resistance. At the optimized 1.5at.% Al doping, an AZO buffer layer of ~60nm thick was found to be optimum, due to its low resistance and high electron-extraction and hole-blocking properties. This improved electrode selectivity led to reduced charge carrier recombination and improved photocurrent generation.

Junction materials Chapter 6 investigated the application of zinc oxide as a type-II heterojunction material in conjunction with PbS quantum dots, in order to improve the inverted oxide/QD device performance. The effect of PbS thickness was

investigated in both undoped ZnO and 0.5% Al-doped AZO systems, and an optimized ~150nm PbS was found to improve device J_{sc}. A UV cure was demonstrated to consistently enhance the device J_{sc} regardless of the degree of Al concentration in AZO layer (0-0.4at.%), owing to the release of oxygen on ZnO surface which i) increased the concentration of mobile electrons (i.e., *n*-type doping) and ii) decreased the number of trap states. Lastly, these devices demonstrated a good stability when stored in the dark in N_2 atmosphere upto 336 hours, and an instant (within ~1 hour) performance boost was achieved upon such N_2 exposure, owing to the passivation of electron trapping sites by N_2 molecules. A respectable 3.36% power conversion efficiency was achieved.

7.2 Suggestions for Future Investigations

An in-depth investigation on optimizing the optoelectronic properties of AZO thin films was presented in Chapter 4, with the preliminary study carried out on the application of these AZO films as the transparent electrode in OPV devices. A thorough exploitation of other ways to optimize the device performance, such as adding various buffer layers and work function modification of AZO electrode could be an interesting topic.

In Chapter 5, I demonstrated the enhancement of charge extraction by inserting an AZO buffer layer. Further device improvement may be possible by treating the buffer layers in a reduced environment, as this is most likely to reduce the resistance and lead to further enhancements of device performance.

The inverted ZnO/PbS devices presented in Chapter 6 was optimized in three aspects, *p*-type material thickness, UV cure and N_2 exposure. Another interesting subject to explore will be device engineering in order to increase absorption and decrease the demand for long distance charge carrier transportation at the same time. Possible areas to study would be the examination of excitonic behaviour in ZnO/PbS devices by fabricating bulk heterojunction devices that aid charge separation, or the growth of ZnO nanorods/nanowires infiltrated with PbS QDs that aids charge transportation.

Bibliography

[1] N. Schlossman, “Green Energy - Alternatives To Fossil Fuels.” Green earth articles directory.

[2] Z. Cheng, Y. Ma, X. Li, W. P. Pan, and Z. Zhang, “Investigation of Carbon Distribution with 14C as Tracer for Carbon Dioxide (CO2) Sequestration through NH4HCO3 Production.” Energy and Fuels, 2007.

[3] “International energy agency, world energy outlook.,” 2011. [Online]. Available: http://www.iea.org/weo/electricity.asp.

[4] A. E. Becquerel, “Memoire sur les effects electriques produits sous l’influence des rayons solaires,” *Comptes rendus des seances hebdomadaires*, vol. 9, pp. 561-567, 1839.

[5] R. William, “Becquerel photovoltaic effect in binary compounds,” *Journal of chemical physics*, vol. 32, no. 5, 1960.

[6] “World Energy Council.” [Online]. Available: http://www.worldenergy.org.

[7] M. A. Green, “Third generation photovoltaics: solar cells for 2020 and beyond,” *Physica E*, vol. 14, pp. 65-70, 2002.

[8] S. K. Hau, H.-L. Yip, N. S. Baek, J. Zou, K. O’Malley, and A. K.-Y. Jen, “Air-stable inverted flexible polymer solar cells using zinc oxide nanoparticles as an electron selective layer,” *Applied Physics Letters*, vol. 92, no. 25, p. 253301, Jun. 2008.

[9] F. C. Krebs et al., “A complete process for production of flexible large area polymer solar cells entirely using screen printing—First public demonstration,” *Solar Energy Materials and Solar Cells*, vol. 93, no. 4, pp. 422-441, Apr. 2009.

[10] L. L. Kazmerski, “Conversion efficiencies of the best research solar cells worldwide from 1976 through 2011 for various photovoltaic technologies,” *National Renewable Energy Laboratory (NREL), Golden, CO*, 2011. [Online]. Available: http://upload.wikimedia.org/wikipedia/commons/c/c9/PVeff(rev111205).jpg.

[11] “www.nrel.gov/ncpv/images/efficiency_chart.jpg.”

[12] G. Li, R. Zhu, and Y. Yang, “Polymer solar cells,” *Nature Photonics*, vol. 6, no. 3, pp. 153-161, Feb. 2012.

[13] G. Li et al., “High-efficiency solution processable polymer photovoltaic cells by self-organization of polymer blends,” *Nature Materials*, vol. 4, no. 11, pp. 864-868, Oct. 2005.

[14] C.-J. Ko, Y.-K. Lin, F.-C. Chen, and C.-W. Chu, "Modified buffer layers for polymer photovoltaic devices," *Applied Physics Letters*, vol. 90, no. 6, p. 063509, 2007.

[15] W. Ma, C. Yang, X. Gong, K. Lee, and A. J. Heeger, "Thermally Stable, Efficient Polymer Solar Cells with Nanoscale Control of the Interpenetrating Network Morphology," *Advanced Functional Materials*, vol. 15, no. 10, pp. 1617-1622, Oct. 2005.

[16] W.-J. Yoon and P. R. Berger, "4.8% efficient poly(3-hexylthiophene)-fullerene derivative (1:0.8) bulk heterojunction photovoltaic devices with plasma treated AgOx/indium tin oxide anode modification," *Applied physics letters*, vol. 92, no. 1, p. 13306, 2008.

[17] S. H. Park et al., "Bulk heterojunction solar cells with internal quantum efficiency approaching 100%," *Nat Photon*, vol. 3, no. 5, pp. 297-302, 2009.

[18] H.-Y. Chen et al., "Polymer solar cells with enhanced open-circuit voltage and efficiency," *Nature Photonics*, vol. 3, no. 11, pp. 649-653, Oct. 2009.

[19] J. Gilot, M. M. Wienk, and R. A. J. Janssen, "Double and triple junction polymer solar cells processed from solution," *Applied Physics Letters*, vol. 90, no. 14, p. 143512, Apr. 2007.

[20] S. Sista et al., "Highly efficient tandem polymer photovoltaic cells.," *Advanced materials (Deerfield Beach, Fla.)*, vol. 22, no. 3, pp. 380-3, Jan. 2010.

[21] T. Minami, "Transparent conducting oxide semiconductors for transparent electrodes," *Semicond. Sci. Technol.*, vol. 20, p. S35-S44, 2005.

[22] C. Waldauf et al., "Highly efficient inverted organic photovoltaics using solution based titanium oxide as electron selective contact," *Applied Physics Letters*, vol. 89, no. 23, p. 233517, Dec. 2006.

[23] R. Søndergaard, M. Helgesen, M. Jørgensen, and F. C. Krebs, "Fabrication of Polymer Solar Cells Using Aqueous Processing for All Layers Including the Metal Back Electrode," *Advanced Energy Materials*, vol. 1, no. 1, pp. 68-71, Jan. 2011.

[24] S. M. Willis, C. Cheng, H. E. Assender, and A. A. R. Watt, "The Transitional Heterojunction Behavior of PbS/ZnO Colloidal Quantum Dot Solar Cells.," *Nano letters*, Feb. 2012.

[25] European Photovoltaic Industry Association, "Solar Generation 6 Solar Photovoltaic Electricity Empowering the World," 2011.

[26] J. Nelson, *The Physics of Solar Cells*. London: Imperial College Press, 2010.

[27] C. W. Tang, "Two-layer organic photovoltaic cell," *Applied physics letters*, vol. 48, no. 2, pp. 183-185, 1986.

[28] M. E. Kose, "The Future of Solar Energy in the Energy Market and Why We Need It More Than Ever," *Fountain Magazine*, p. 63, 2008.

[29] B. A. Gregg and M. C. Hanna, "Comparing organic to inorganic photovoltaic cells: Theory, experiment, and simulation," *Journal of Applied Physics*, vol. 93, no. 6, p. 3605, Mar. 2003.

[30] I. G. Hill, A. Kahn, Z. G. Soos, and J. Pascal, "Charge-separation energy in films of π-conjugated organic molecules," *Chemical Physics Letters*, vol. 327, no. 3-4, pp. 181-188, Sep. 2000.

[31] H. Hoppe and N. S. Sariciftci, "Organic solar cells: An overview," *Journal of Materials Research*, vol. 19, no. 7, pp. 1924-1945, Jul. 2004.

[32] Y. Terao, H. Sasabe, and C. Adachi, "Correlation of hole mobility, exciton diffusion length, and solar cell characteristics in phthalocyanine/fullerene organic solar cells," *Applied Physics Letters*, vol. 90, no. 10, p. 103515, Mar. 2007.

[33] L. T. Vuong, G. Kozyreff, R. Betancur, and J. Martorell, "Cavity-controlled radiative recombination of excitons in thin-film solar cells," *Applied Physics Letters*, vol. 95, no. 23, p. 233106, Dec. 2009.

[34] M. D. McGehee, "Organic solar cells: Overcoming recombination," *Nature Photonics*, vol. 3, no. 5, pp. 250-252, May 2009.

[35] G. Yu and A. J. Heeger, "Charge separation and photovoltaic conversion in polymer composites with internal donor-acceptor heterojunctions," *Journal of applied physics*, vol. 78, pp. 4510-4515, 1995.

[36] J. J. M. Halls et al., "Efficient photodiodes from interpenetrating polymer networks," *Nature*, vol. 376, no. 6540, pp. 498-500, 1995.

[37] K. Yoshino, K. Tada, A. Fujii, E. M. Conwell, and A. A. Zakhidov, "Novel photovoltaic devices based on donor-acceptor molecular and conducting polymer systems," *IEEE transactions on electron devices*, vol. 44, no. 8, pp. 1315-1324, 1997.

[38] Ü. Özgür et al., "A comprehensive review of ZnO materials and devices," *Journal of applied physics*, vol. 98, no. 4, pp. 41103-41301, 2005.

[39] H. Karzel et al., "Lattice dynamics and hyperfine interactons in ZnO and ZnSe at high external pressures," *Physics review B*, vol. 53, no. 17, pp. 11425-11438, 1996.

[40] E. H. Kisi and M. M. Elcombe, "u parameters for the wurtzite structure of ZnS and ZnO using powder neutron diffraction," *Acta Cryst.*, vol. 45, pp. 1867-1970, 1989.

[41] M. Catti, Y. Noel, and R. Dovesi, "Full piezoelectric tensors of wurtzite and zinc blende ZnO and ZnS by first-principles calculations," *Journal of physics and chemistry of solids*, vol. 64, pp. 2183-2190, 2003.

[42] S. Desgreniers, “High-density phases of ZnO: Structural and compressive parameters,” *Physical Reciew B*, vol. 58, no. 21, 1998.

[43] L. Gerward and J. S. Olsen, “The high-pressure phase of zincite,” *J. Synchrotron Rad.*, vol. 2, pp. 233-235, 1995.

[44] R. R. Reeber, “Lattice parameters of ZnO from 4.2 to 296 K,” *Journal of applied physics*, vol. 41, no. 13, pp. 5063-5066, 1970.

[45] A. B. M. A. Ashrafi et al., “Growth and characterization of hypothetical zinc-blende ZnO films on GaAs (001) substrates with ZnS buffer layers,” *Applied physics letters*, vol. 76, no. 5, 2000.

[46] Y.-J. Lin, C.-L. Tsai, Y.-M. Lu, and C.-J. Liu, “Optical and electrical properties of undoped ZnO films,” *Journal of Applied Physics*, vol. 99, no. 9, p. 093501, May 2006.

[47] H. Tanaka, K. Ihara, T. Miyata, H. Sato, and T. Minami, “Low resistivity polycrystalline ZnO:Al thin films prepared by pulsed laser deposition,” *Journal of Vacuum Science & Technology A: Vacuum, Surfaces, and Films*, vol. 22, no. 4, p. 1757, Jul. 2004.

[48] T. Minami, H. Sato, K. Ohashi, T. Tomofuji, and S. Takata, “Conduction mechanism of highly conductive and transparent zinc oxide thin films prepared by magnetron sputtering,” *Journal of Crystal Growth*, vol. 117, no. 1-4, pp. 370-374, Feb. 1992.

[49] R. Buonsanti, A. Llordes, S. Aloni, B. A. Helms, and D. J. Milliron, “Tunable Infrared Absorption and Visible Transparency of Colloidal Aluminum-Doped Zinc Oxide Nanocrystals.,” *Nano letters*, vol. 11, no. 11, pp. 4706-4710, Oct. 2011.

[50] K. M. Whitaker, S. T. Ochsenbein, V. Z. Polinger, and D. R. Gamelin, “Electron Confinement Effects in the EPR Spectra of Colloidal n-Type ZnO Quantum Dots,” *Journal of Physical Chemistry C*, vol. 112, no. 37, pp. 14331-14335, Sep. 2008.

[51] T. Schuler and M. A. Aegerter, “Optical, electrical and structural properties of sol gel ZnO□: Al coatings,” *Thin solid films*, vol. 351, no. 1-2, pp. 125-131, 1999.

[52] M. H. Habibi and M. K. Sardashti, “Structure and Morphology of Nanostructured Zinc Oxide Thin Films Prepared by Dip- vs. Spin-Coating Methods,” *Journal of the Iranian Chemical Society*, vol. 5, no. 4, pp. 603-609, 2008.

[53] J. E. Medvedeva and C. L. Hettiarachchi, “Tuning the properties of complex transparent conducting oxides: Role of crystal symmetry, chemical composition, and carrier generation,” *Physical Review B*, vol. 81, no. 12, Mar. 2010.

[54] T. Minami, H. Sato, H. Nanto, and S. Takata, “Group III impurity doped zinc oxide thin films prepared by RF magnetron sputtering,” *Japanese journal of applied physics*, vol. 24, no. 10, p. L781-L784, 1985.

[55] A. F. Kohan, G. Ceder, D. Morgan, and C. G. V. de Walle, “First-principles study of native point defects in ZnO,” *Physical Review B*, vol. 61, no. 22, pp. 15019-15027, 2000.

[56] C. G. V. de Walle, “Defect analysis and engineering in ZnO,” *Physica B: condensed matter*, vol. 308-310, pp. 899-903, 2001.

[57] A. Travlos, N. Boukos, and C. Chandrinou, “Zinc related defects in ZnO nanorods,” *physica status solidi (b)*, vol. 249, no. 3, pp. 560-563, Mar. 2012.

[58] D. Look, J. Hemsky, and J. Sizelove, “Residual Native Shallow Donor in ZnO,” *Physical Review Letters*, vol. 82, no. 12, pp. 2552-2555, Mar. 1999.

[59] J. Sann et al., “Zn interstitial related donors in ammonia-treated ZnO powders,” *Physical Review B*, vol. 76, no. 19, Nov. 2007.

[60] A. Hutson, “Hall Effect Studies of Doped Zinc Oxide Single Crystals,” *Physical Review*, vol. 108, no. 2, pp. 222-230, Oct. 1957.

[61] D. M. Hofmann et al., “Properties of the oxygen vacancy in ZnO,” *Applied Physics A*, vol. 88, no. 1, pp. 147-151, Apr. 2007.

[62] A. Janotti and C. G. Van de Walle, “Fundamentals of zinc oxide as a semiconductor,” *Reports on Progress in Physics*, vol. 72, no. 12, p. 126501, Dec. 2009.

[63] D. C. Look and J. W. Hemsky, “Residual native shallow donor in ZnO,” *Physical review letters*, vol. 82, no. 12, 1999.

[64] R. L. Jones, “Electrical properties of bulk ZnO,” *Solid state communications*, vol. 105, no. 6, pp. 399-401, 1998.

[65] C. SF et al., “Experimental confirmation of the predicted shallow donor hydrogen state in zinc oxide,” *Physical review letters*, vol. 86, no. 12, pp. 2601-2604, 2001.

[66] Y. M. Strzhemechny et al., “Remote hydrogen plasma doping of single crystal ZnO,” *Applied physics letters*, vol. 84, no. 14, 2004.

[67] C. G. V. de Walle, “Hydrogen as a cause of doping in zinc oxide,” *Physical review letters*, vol. 85, no. 5, pp. 1012-1015, 2000.

[68] J. P. Wiff, Y. Kinemuchi, and K. Watari, “Hall mobilities of Al- and Ga-doped ZnO polycrystals,” *Materials Letters*, vol. 63, no. 28, pp. 2470-2472, Nov. 2009.

[69] M.-C. Li, C.-C. Kuo, S.-H. Peng, S.-H. Chen, and C.-C. Lee, “Influence of hydrogen on the properties of Al and Ga-doped ZnO films at room temperature,” *Applied Optics*, vol. 50, no. 9, p. C197, Dec. 2010.

[70] T. Minami, “Transparent conducting oxide semiconductors for transparent electrodes,” *Semicond. Sci. Technol.*, vol. 20, p. S35-S44, 2005.

[71] G. F. Neumark, “Achievement of well conducting wide band gap semiconductors: Role of solubility and of nonequilibrium impurity incorporation,” *Physical review letters*, vol. 62, no. 15, pp. 1800-1803, 1989.

[72] D. J. Chadi, “Doping in ZnSe, ZnTe, MgSe, and MgTe wide band gap semiconductors,” *Physical review letters*, vol. 72, no. 4, pp. 534-537, 1994.

[73] S. B. Zhang, S. H. Wei, and A. Zunger, “Microscopic origin of the phenomenological equilibrium ‘doping limit rule’ in n-type III-V semiconductors,” *Physical review letters*, vol. 84, no. 6, pp. 1232-1235, 2000.

[74] S. B. Zhang, S. H. Wei, and A. Zunger, “A phenomenological model for systematization and prediction of doping limits in II-VI and I-III-VI2 compounds,” *Journal of applied physics*, vol. 83, no. 6, 1998.

[75] D. B. Laks, “Acceptor doping in ZnSe versus ZnTe,” *Applied physics letters*, vol. 63, no. 10, 1993.

[76] H. Kato, M. Sano, K. Miyamoto, and T. Yao, “Growth and characterization of Ga doped ZnO layers on a-plane sapphire substrates grown by molecular beam epitaxy,” *Journal of crystal growth*, vol. 237-239, no. 1, pp. 538-543, 2002.

[77] H. J. Ko, Y. F. Chen, S. K. Hong, H. Wenisch, T. Yao, and D. C. Look, “Ga-doped ZnO films grown on GaN templates by plasma-assisted molecular-beam epitaxy,” *Applied Physics Letters*, vol. 77, no. 23, p. 3761, Dec. 2000.

[78] M. Miyazaki, K. Sato, A. Mitsui, and H. Nishimura, “Properties of Ga-doped ZnO films,” *Journal of Non-Crystalline Solids*, vol. 218, pp. 323-328, Sep. 1997.

[79] Y. J. Park, H. N. Kim, and H. H. Shin, “Effects of deposition temperature on the crystallinity of Ga-doped ZnO thin films on glass substrates prepared by sputtering method,” *Applied Surface Science*, vol. 255, no. 17, pp. 7532-7536, Jun. 2009.

[80] H. . Lee, S. . Lau, Y. . Wang, K. . Tse, H. . Hng, and B. . Tay, “Structural, electrical and optical properties of Al-doped ZnO thin films prepared by filtered cathodic vacuum arc technique,” *Journal of Crystal Growth*, vol. 268, no. 3-4, pp. 596-601, Aug. 2004.

[81] X. Zi-qiang, D. Hong, L. Yan, and C. Hang, “Al-doping effects on structure, electrical and optical properties of c-axis-orientated ZnO:Al thin films,” *Materials Science in Semiconductor Processing*, vol. 9, no. 1-3, pp. 132-135, 2006.

[82] S. Mridha and D. Basak, “Aluminium doped ZnO films: electrical, optical and photoresponse studies,” *Journal of Physics D: Applied Physics*, vol. 40, no. 22, pp. 6902-6907, Nov. 2007.

[83] L. E. Mir, Z. B. Ayadi, M. Saadoun, H. J. von Bardeleben, K. Djessas, and A. Zeinert, “Optical, electrical and magnetic properties of transparent, n-type conductive Zn0.90− x V 0.10 Al x O thin films elaborated from aerogel nanoparticles,” *physica status solidi (a)*, vol. 204, no. 10, pp. 3266-3277, Oct. 2007.

[84] V. Musat, B. Teixeira, E. Fortunato, R. C. C. Monteiro, and P. Vilarinho, "Al-doped ZnO thin films by sol-gel method," *Surface and Coatings Technology*, vol. 180-181, pp. 659-662, 2004.

[85] A. Suzuki, T. Matsushita, N. Wada, Y. Sakamoto, and M. Okuda, "Transparent Conducting Al-Doped ZnO Thin Films Prepared by Pulsed Laser Deposition," *Japanese journal of applied physics*, vol. 35, p. L56-L59, 1996.

[86] H. Agura, A. Suzuki, T. Matsushita, T. Aoki, and M. Okuda, "Low resistivity transparent conducting Al-doped ZnO films prepared by pulsed laser deposition," *Thin solid films*, vol. 445, no. 2, pp. 263-267, 2003.

[87] B. M. Ataev, A. M. Bagamadova, A. M. Djabrailov, V. V. Mamedo, and R. A. Rabadanov, "Highly conductive and transparent Ga-doped epitaxial ZnO films on sapphire by CVD," *Thin solid films*, vol. 260, no. 1, pp. 19-20, 1995.

[88] C. H. Park, S. B. Zhang, and S.-H. Wei, "Origin of p-type doping difficulty in ZnO: The impurity perspective," *Physics review B*, vol. 66, no. 7, 2002.

[89] A. Kobayashi, O. F. Sankey, and J. D. Dow, "Deep energy levels of defects in the wurtzite semiconductors AIN, CdS, CdSe, ZnS, and ZnO," *Physics review B*, vol. 28, no. 2, pp. 946-956, 1983.

[90] C. G. V. de Walle, D. B. Laks, G. F. Neumark, and S. T. Pantelides, "First-principles calculations of solubilities and doping limits: Li, Na, and N in ZnSe," *Physics review B*, vol. 47, no. 15, pp. 9425-9434, 1993.

[91] J. C. C. Fan and J. B. Goodenough, "X-ray photoemission spectroscopy studies of Sn-doped indium-oxide films," *Journal of applied physics*, vol. 48, no. 8, pp. 3524-3531, 1977.

[92] A. E. Manouni et al., "Effect of aluminium doping on zinc oxide thin films grown by spray pyrolysis," *Superlattices and Microstructures*, vol. 39, no. 1-4, pp. 185-192, Jan. 2006.

[93] M. SUCHEA, S. CHRISTOULAKIS, N. KATSARAKIS, T. KITSOPOULOS, and G. KIRIAKIDIS, "Comparative study of zinc oxide and aluminum doped zinc oxide transparent thin films grown by direct current magnetron sputtering," *Thin solid films*, vol. 515, no. 16, pp. 6562-6566.

[94] G. M. Wu, Y. F. Chen, and H. C. Lu, "Aluminum-Doped Zinc Oxide Thin Films Prepared by Sol-Gel and RF Magnetron Sputtering," in *Proceedings of the VIII International Conference ION 2010*, 2011, vol. 120, no. 1, pp. 149-152.

[95] P. Drude, "Zur Elektronentheorie der Metalle," *Annalen der Physik*, vol. 306, no. 3, pp. 566-613, 1900.

[96] "Drude model." [Online]. Available: http://en.wikipedia.org/wiki/Drude_model.

[97] N. F. Mott, "Metal-Insulator transitions." Taylor & Francis, London, 1990.

[98] I. G. Austin and N. F. Mott, "Metallic and nonmetallic behavior in transition metal oxides," *Science*, vol. 168, no. 3927, 1970.

[99] N. F. Mott, "The transition to the metallic state," *Philosophical magazine*, vol. 6, no. 62, pp. 287-309, 1961.

[100] J. G. Lu and S. Fujita, "Carrier concentration dependence of band gap shift in n-type ZnO:Al films," *Journal of applied physics*, vol. 101, 2007.

[101]B. K. Meyer et al., "Bound exciton and donor-acceptor pair recombinations in ZnO," *Physica status solidi (B)*, vol. 241, no. 2, pp. 231-260, 2004.

[102] K. P. Bhuvana, J. Elanchezhiyan, N. Gopalakrishnan, and T. Balasubramanian, "Optimization of Zn1−xAlxO film for antireflection coating by RF sputtering," *Journal of Alloys and Compounds*, vol. 473, pp. 534-537, 2009.

[103] T. Yamamoto, T. Shiosaki, and A. Kawabata, "Characterization of ZnO piezoelectric films prepared by rf planar-magnetron sputtering," *Journal of applied physics*, vol. 51, no. 6, 1980.

[104] T. Mitsuyu, S. Ono, and K. Wasa, "Structures and SAW properties of rf-sputtered single-crystal films of ZnO on sapphire," *Journal of applied physics*, vol. 51, no. 5, 1980.

[105] A. Hachigo, H. Nakahata, K. Higaki, S. Fujii, and S. Shikata, "Heteroepitaxial growth of ZnO films on diamond (111) plane by magnetron sputtering," *Applied physics letters*, vol. 65, no. 20, 1994.

[106] J. G. E. Gardeniers, Z. M. Rittersma, and G. J. Burger, "Preferred orientation and piezoelectricity in sputtered ZnO films," *Journal of applied physics*, vol. 83, no. 12, 1998.

[107] S. K. Tiku, C. K. Lau, and K. M. Lakin, "Chemical vapor deposition of ZnO epitaxial films on sapphire," *Applied physics letters*, vol. 36, no. 4, 1980.

[108] M. Kasuga and M. Mochizuki, "Orientation relationships of zinc oxide on sapphire in heteroepitaxial chemical vapor deposition," *Journal of crystal growth*, vol. 54, no. 2, pp. 185-194, 1981.

[109] K.-K. Kim, J.-H. Song, H.-J. Jung, W.-K. Choi, and S.-J. Park, "The grain size effects on the photoluminescence of ZnO/alpha-Al2O3 grown by radio-frequency magnetron sputtering," *Journal of applied physics*, vol. 87, no. 7, 2000.

[110] Y. Chen et al., "Plasma assisted molecular beam epitaxy of ZnO on c -plane sapphire: Growth and characterization," *Journal of applied physics*, vol. 84, no. 7, 1998.

[111] R. D. Vispute et al., "Heteroepitaxy of ZnO on GaN and its implications for fabrication of hybrid optoelectronic devices," *Applied physics letters*, vol. 73, no. 3, 1998.

[112] Y. Liu et al., "Ultraviolet detectors based on epitaxial ZnO films grown by MOCVD," *Journal of Electronic Materials*, vol. 29, no. 1, pp. 69-74, 2000.

[113] Z. K. Tang et al., "Room-temperature ultraviolet laser emission from self-assembled ZnO microcrystallite thin films," *Applied physics letters*, vol. 72, no. 25, 1998.

[114] G. B. Murdoch, S. Hinds, E. H. Sargent, S. W. Tsang, L. Mordoukhovski, and Z. H. Lu, "Aluminum doped zinc oxide for organic photovoltaics," *Applied physics letters*, vol. 94, no. 21, 2009.

[115] K. Tarasov and O. Raccurt, "A wet chemical preparation of transparent conducting thin films of Al-doped ZnO nanoparticles," *Journal of Nanoparticle Research*, vol. 13, no. 12, pp. 6717-6724, Sep. 2011.

[116] Y. Galagan, R. Andriessen, E. Rubingh, N. Grossiord, and P. Blom, "Toward fully printed Organic Photovoltaics: Processing and Stability," *LOPE-C*, pp. 88-91, 2008.

[117] J. Wu, H. A. Becerril, Z. Bao, Z. Liu, Y. Chen, and P. Peumans, "Organic solar cells with solution-processed graphene transparent electrodes," *Applied Physics Letters*, vol. 92, no. 26, p. 263302, Jul. 2008.

[118] D. R. Uhlmann, G. Teowee, and J. Boulton, "The future of sol-gel science and technology," *Journal of Sol-Gel Science and Technology*, vol. 8, no. 1-3, pp. 1083-1091, Feb. 1997.

[119] J. Zarzycki, "Past and present of sol-gel science and technology," *Journal of Sol-Gel Science and Technology*, vol. 8, no. 1-3, pp. 17-22, Feb. 1997.

[120] S. Sakka, *Handbook of sol-gel science and technology: processing, characterization and applications*. Springer, 2005, p. 680.

[121] W. Tang and D. C. Cameron, "Aluminum-doped zinc oxide transparent conductors deposited by the sol-gel process," *Thin solid films*, vol. 238, no. 1, pp. 83-87, 1994.

[122] J. H. Lee, K. H. Ko, and B. O. Park, "Electrical and optical properties of ZnO transparent conducting films by the sol-gel method," *Journal of crystal growth*, vol. 247, no. 1-2, pp. 119-125, 2003.

[123] S. C. Lee, J. H. Lee, T. S. Oh, and Y. H. Kim, "Fabrication of tin oxide film by sol-gel method for photovoltaic solar cell system," *Solar energy materials and solar cells*, vol. 75, no. 3-4, pp. 481-487, 2003.

[124] K.-moh Lin and P. Tsai, "Growth mechanism and characterization of ZnO: Al multi-layered thin films by sol-gel technique," *Thin solid films*, vol. 515, no. 24, pp. 8601-8604, 2007.

[125] A. E. Jiménez-González, J. A. Soto Urueta, and R. Suárez-Parra, "Optical and electrical characteristics of aluminum-doped ZnO thin films prepared by solgel technique," *Journal of crystal growth*, vol. 192, no. 3-4, pp. 430-438, 1998.

[126] J. Chen, D. Chen, and Z. Chen, "Optimization of the process for preparing Al-doped ZnO thin films by sol-gel method," *Science in China Series E: Technological Sciences*, vol. 52, no. 1, pp. 88-94, 2009.

[127] K.-moh Lin and P. Tsai, "Parametric study on preparation and characterization of ZnO:Al films by sol-gel method for solar cells," *Materials Science and Engineering: B*, vol. 139, no. 1, pp. 81-87, 2007.

[128] M. Ohyama, H. Kozuka, and T. Yoko, "Sol-gel preparation of ZnO films with extremely preferred orientation along (002) plane from zinc acetate solution," *Thin solid films*, vol. 306, no. 1, pp. 78-85, 1997.

[129] K. E. Lee, M. Wang, E. J. Kim, and S. H. Hahn, "Structural, electrical and optical properties of sol-gel AZO thin films," *Current Applied Physics*, vol. 9, no. 3, pp. 683-687, 2009.

[130] G. G. Valle, P. Hammer, S. H. Pulcinelli, and C. V. Santilli, "Transparent and conductive ZnO:Al thin films prepared by sol-gel dip-coating," *Journal of the European Ceramic Society*, vol. 24, no. 6, pp. 1009-1013, 2004.

[131] J.-H. Lee and B.-O. Park, "Transparent conducting ZnO:Al, In and Sn thin films deposited by the sol-gel method," *Thin solid films*, vol. 426, no. 1-2, pp. 94-99, 2003.

[132] T. Ratana, P. Amornpitoksuk, and S. Suwanboon, "The wide band gap of highly oriented nanocrystalline Al doped ZnO thin films from sol-gel dip coating," *Journal of Alloys and Compounds*, vol. 470, no. 1-2, pp. 408-412, 2009.

[133] Y. Natsume and H. Sakata, "Zinc oxide films prepared by sol-gel spin-coating," *Thin solid films*, vol. 372, no. 1-2, pp. 30-36, 2000.

[134] C. Lizandara-Pueyo, M. W. E. van den Berg, A. D. Toni, T. Goes, and S. Polarz, "Nucleation and Growth of ZnO in Organic Solvents - an in Situ Study," *American Chemical Society*, 2008.

[135] C. J. Brinker and G. W. Scherer, "The physics and chemistry of sol-gel processing." Academic press, 1990.

[136] A. Goetzberger, C. Hebling, and H.-W. Schock, "Photovoltaic materials, history, status and outlook," *Materials Science and Engineering: R: Reports*, vol. 40, no. 1, pp. 1-46, 2003.

[137] R. M. Pasquarelli, D. S. Ginley, and R. O'Hayre, "Solution processing of transparent conductors: from flask to film.," *Chemical Society reviews*, vol. 40, no. 11, pp. 5406-41, Nov. 2011.

[138] M. A. Aegerter, J. Puetz, G. Gasparro, and N. Al-Dahoudi, "Versatile wet deposition techniques for functional oxide coatings," *Optical Materials*, vol. 26, no. 2, pp. 155-162, Jul. 2004.

[139] K. Norrman, A. Ghanbari-Siahkali, and N. B. Larsen, "6 Studies of spin-coated polymer films," *Annual reports - section c*, vol. 101, pp. 174-201, 2005.

[140] S. Mridha and D. Basak, "Thickness dependent photoconducting properties of ZnO films," *Chemical Physics Letters*, vol. 427, pp. 62-66, 2006.

[141] J. H. Kim, J. Jang, and W. C. Zin, "Thickness dependence of the glass transition temperature in thin polymer films ," *Langmuir*, vol. 17, no. 9, pp. 2703-2710, 2001.

[142] J. Q. Pham and P. F. Green, "The glass transition of thin film polymer/polymer blends: Interfacial interactions and confinement," *Journal of chemical physics*, vol. 116, no. 13, 2002.

[143] L. L. Spangler, J. M. Torkelson, and J. S. Royal, "Influence of solvent and molecular weight on thickness and surface topography of spin-coated polymer films," *Polymer engineering and science*, vol. 30, no. 11, pp. 644-653, 1990.

[144] A. Weill and E. Dechenaux, "The spin-coating process mechanism related to polymer solution properties," *Polymer engineering and science*, vol. 28, no. 15, pp. 945-948, 2004.

[145] H. Ko, W.-P. Tai, K.-C. Kim, S.-H. Kim, S.-J. Suh, and Y.-S. Kim, "Growth of Al-doped ZnO thin films by pulsed DC magnetron sputtering," *Journal of Crystal Growth*, vol. 277, no. 1-4, pp. 352-358, Apr. 2005.

[146] C. Periasamy and P. Chakrabarti, "Tailoring the Structural and Optoelectronic Properties of Al-Doped Nanocrystalline ZnO Thin Films," *Journal of Electronic Materials*, vol. 40, no. 3, pp. 259-266, Dec. 2010.

[147] H. Kim, J. . Horwitz, S. . Qadri, and D. . Chrisey, "Epitaxial growth of Al-doped ZnO thin films grown by pulsed laser deposition," *Thin Solid Films*, vol. 420-421, pp. 107-111, Dec. 2002.

[148] R. Chakravarty and C. Periasamy, "Effect of Aluminium Doping on Structural and Optoelectronic Properties of Sol–Gel Derived Nanocrystalline ZnO Thin Film," *Science of Advanced Materials*, vol. 3, pp. 276-283, 2011.

[149] X. Zi-qiang, D. Hong, L. Yan, and C. Hang, "Al-dopingeffects on structure, electrical and opticalproperties of c-axis-orientatedZnO:Althinfilms."

[150] C. J. B. Tobias Stubhan, Hyunchul Oh, Luigi Pinna, Johannes Krantz, Ivan Litzov, "Inverted organic solar cells using a solution processed aluminum-doped zinc oxide buffer layer," *Organic Electronics*, vol. 12, no. 9, pp. 1539-1543, 2011.

[151] Y. Li, L. Xu, X. Li, X. Shen, and A. Wang, "Effect of aging time of ZnO sol on the structural and optical properties of ZnO thin films prepared by sol–gel method," *Applied Surface Science*, vol. 256, no. 14, pp. 4543-4547, May 2010.

[152] S. P. Shrestha et al., "Properties of ZnO:Al Films Prepared by Spin Coating of Aged Precursor Solution," in *Bull. Korean Chem. Soc*, 2010, p. 112.

[153] A. K. K. Kyaw, X. W. Sun, C. Y. Jiang, G. Q. Lo, D. W. Zhao, and D. L. Kwong, "An inverted organic solar cell employing a sol-gel derived ZnO electron selective layer and thermal evaporated MoO[sub 3] hole selective layer," *Applied Physics Letters*, vol. 93, no. 22, p. 221107, Dec. 2008.

[154] Z. Hu, J. Zhang, Y. Liu, Y. Li, X. Zhang, and Y. Zhao, "Efficiency enhancement of inverted organic photovoltaic devices with ZnO nanopillars fabricated on FTO glass substrates," *Synthetic Metals*, vol. 161, no. 19-20, pp. 2174-2178, Oct. 2011.

[155] W. Ma, C. Yang, X. Gong, K. Lee, and A. J. Heeger, "Thermally Stable, Efficient Polymer Solar Cells with Nanoscale Control of the Interpenetrating Network Morphology," *Advanced Functional Materials*, vol. 15, no. 10, pp. 1617-1622, 2005.

[156] L. Li, J. S. Yu, S. L. Lou, W. Z. Li, Y. D. Jiang, and W. Li, "Surface modification and characterization of indium–tin oxide for organic light-emitting devices," *Journal of Materials Science: Materials in Electronics*, vol. 19, no. 12, pp. 1214-1221, Jan. 2008.

[157] M. Reyes-Reyes, K. Kim, and D. L. Carroll, "High-efficiency photovoltaic devices based on annealed poly(3-hexylthiophene) and 1-(3-methoxycarbonyl)-propyl-1-phenyl-(6,6)C[sub 61] blends," *Applied Physics Letters*, vol. 87, no. 8, p. 083506, Aug. 2005.

[158] B. Sernelius, K.-F. Berggren, Z.-C. Jin, I. Hamberg, and C. Granqvist, "Band-gap tailoring of ZnO by means of heavy Al doping," *Physical Review B*, vol. 37, no. 17, pp. 10244-10248, Jun. 1988.

[159]J. Tauc, "Absorption edge and internal electric fields in amorphous semiconductors," *Materials Research Bulletin*, vol. 5, no. 8, pp. 721-729, Aug. 1970.

[160] C. G. Granqvist, *Handbook of Inorganic Electrochronic Materials*. Amsterdam: Elsevier, 1995.

[161] P. P. Stallinga, *Electrical Characterization of Organic Electronic Materials and Devices*. John Wiley & Sons, Ltd., 2009, p. 29.

[162] F. M Smits, "Measurements of Sheet Resistivity with the Four-Point Probe," *Bell System Technical Journal*, vol. 37, no. 3, 1958.

[163] L. Valdes, "Resistivity Measurements on Germanium for Transistors," *Proceedings of the IRE*, vol. 42, no. 2, pp. 420-427, Feb. 1954.

[164] L. J. Guo and M.-G. Kang, "Nanostructured transparent metal electrodes for organic solar cells," *SPIE Newsroom*, pp. 10-12, 2009.

[165] E. H. Hall, *On a new Action of the Magnet on Electric Currents*. American Journal of Mathematics, 1879, pp. 287-292.

[166] A. ORTIZCONDE, F. GARCIASANCHEZ, and J. MUCI, “New method to extract the model parameters of solar cells from the explicit analytic solutions of their illuminated characteristics,” *Solar Energy Materials and Solar Cells*, vol. 90, no. 3, pp. 352-361, Feb. 2006.

[167] “http://en.wikipedia.org/wiki/Transparent_conducting_film.” [Online]. Available: http://en.wikipedia.org/wiki/Transparent_conducting_film.

[168] C. G. Granqvist and A. Hultåker, “Transparent and conducting ITO films: new developments and applications,” *Thin Solid Films*, vol. 411, no. 1, pp. 1-5, May 2002.

[169] R. Bel Hadj Tahar, T. Ban, Y. Ohya, and Y. Takahashi, “Tin doped indium oxide thin films: Electrical properties,” *Journal of Applied Physics*, vol. 83, no. 5, p. 2631, Mar. 1998.

[170] S.-S. Kim, S.-Y. Choi, C.-G. Park, and H.-W. Jin, “Transparent conductive ITO thin films through the sol-gel process using metal salts,” *Thin Solid Films*, vol. 347, no. 1-2, pp. 155-160, Jun. 1999.

[171] S. B. Khan, M. Faisal, M. M. Rahman, and A. Jamal, “Low-temperature growth of ZnO nanoparticles: photocatalyst and acetone sensor.,” *Talanta*, vol. 85, no. 2, pp. 943-9, Aug. 2011.

[172] Wikipedia, “Zinc.” 2009.

[173] “http://www.minormetals.com.” [Online]. Available: http://www.minormetals.com/.

[174] “http://www.metalprices.com/FreeSite/metals/zn/zn.asp.” [Online]. Available: http://www.metalprices.com/FreeSite/metals/zn/zn.asp.

[175] J. C. Bernède, L. Cattin, M. Morsli, and Y. Berredjem, “Ultra-thin metal layer passivation of the transparent conductive anode in organic solar cells,” *Solar energy materials and solar cells*, vol. 92, no. 11, pp. 1508-1515, 2008.

[176] S. Tasch, a. Niko, G. Leising, and U. Scherf, “Highly efficient electroluminescence of new wide band gap ladder-type poly(para-phenylenes),” *Applied Physics Letters*, vol. 68, no. 8, p. 1090, 1996.

[177] Z. Liu et al., “Organic thin film electroluminescent devices with ZnO:Al as the anode,” *Journal of Physics: Condensed Matter*, vol. 8, no. 18, pp. 3221-3228, Apr. 1996.

[178] H. Serier, M. Gaudon, and M. Ménétrier, “Al-doped ZnO powdered materials: Al solubility limit and IR absorption properties,” *Solid State Sciences*, vol. 11, no. 7, pp. 1192-1197, Jul. 2009.

[179] Z. B. Bahşi, M. H. Aslan, M. Ozer, and A. Y. Oral, “Sintering behavior of ZnO:Al ceramics fabricated by sol-gel derived nanocrystalline powders,” *Crystal Research and Technology*, vol. 44, no. 9, pp. 961-966, Sep. 2009.

[180] S. A. Ansari, A. Nisar, B. Fatma, W. Khan, and A. H. Naqvi, "Investigation on structural, optical and dielectric properties of Co doped ZnO nanoparticles synthesized by gel-combustion route," *Materials Science and Engineering: B*, vol. 177, no. 5, pp. 428-435, Mar. 2012.

[181] Z. Zhang, C. Bao, W. Yao, S. Ma, L. Zhang, and S. Hou, "Influence of deposition temperature on the crystallinity of Al-doped ZnO thin films at glass substrates prepared by RF magnetron sputtering method," *Superlattices and Microstructures*, vol. 49, no. 6, pp. 644-653, Jun. 2011.

[182] M. Wang, J. Wang, W. Chen, Y. Cui, and L. Wang, "Effect of preheating and annealing temperatures on quality characteristics of ZnO thin film prepared by sol–gel method," *Materials Chemistry and Physics*, vol. 97, no. 2-3, pp. 219-225, Jun. 2006.

[183] D. Bao, H. Gu, and A. Kuang, "Sol-gel-derived c-axis oriented ZnO thin films," *Thin Solid Films*, vol. 312, no. 1-2, pp. 37-39, Jan. 1998.

[184] H.-ming Zhou, D.-qing Yi, Z.-ming Yu, L.-rong Xiao, and J. Li, "Preparation of aluminum doped zinc oxide films and the study of their microstructure, electrical and optical properties," *Thin Solid Films*, vol. 515, no. 17, pp. 6909-6914, Jun. 2007.

[185] H. Kim et al., "Effect of aluminum doping on zinc oxide thin films grown by pulsed laser deposition for organic light-emitting devices," *Thin Solid Films*, vol. 377-378, pp. 798-802, Dec. 2000.

[186] P. Pieranski, "Colloidal crystals," *Contemporary Physics*, vol. 24, no. 1, pp. 25-73, 1983.

[187] "http://hyperphysics.phy-astr.gsu.edu/hbase/quantum/bragg.html." [Online]. Available: http://hyperphysics.phy-astr.gsu.edu/hbase/quantum/bragg.html.

[188] J. F. Moulder, W. F. Stickle, P. E. Sobol, and K. D. Bomben, *Handbook of X Ray Photoelectron Spectroscopy: A Reference Book of Standard Spectra for Identification and Interpretation of Xps Data*. Physical Electronics; Reissue edition, 1995, p. 261.

[189] M. Gao, X. Wu, J. Liu, and W. Liu, "The effect of heating rate on the structural and electrical properties of sol–gel derived Al-doped ZnO films," *Applied Surface Science*, vol. 257, no. 15, pp. 6919-6922, May 2011.

[190] M. Chen, Z. L. Pei, C. Sun, L. S. Wen, and X. Wang, "Formation of Al-doped ZnO films by dc magnetron reactive sputtering," *Materials Letters*, vol. 48, no. 3-4, pp. 194-198, Apr. 2001.

[191] C. D. Wagner, W. M. Riggs, L. E. Davis, J. F. Moulder, and G. E. Muilenberg, *Handbook of X-ray Photoelectron Spectroscopy*. Physical Electronics Division, Eden Prairie, 1979, pp. 50-51.

[192] L. Li, L. Fang, X. J. Zhou, Z. Y. Liu, L. Zhao, and S. Jiang, "X-ray photoelectron spectroscopy study and thermoelectric properties of Al-doped ZnO thin films," *Journal of Electron Spectroscopy and Related Phenomena*, vol. 173, no. 1, pp. 7-11, Jun. 2009.

[193] H. Tong et al., "Effects of post-annealing on structural, optical and electrical properties of Al-doped ZnO thin films," *Applied Surface Science*, vol. 257, no. 11, pp. 4906-4911, Mar. 2011.

[194] N. P. Dasgupta, S. Neubert, W. Lee, O. Trejo, J.-R. Lee, and F. B. Prinz, "Atomic Layer Deposition of Al-doped ZnO Films: Effect of Grain Orientation on Conductivity," *Chemistry of Materials*, vol. 22, no. 16, pp. 4769-4775, Aug. 2010.

[195] M. J. Alam and D. C. Cameron, "Preparation and properties of transparent conductive aluminum-doped zinc oxide thin films by sol–gel process," *Journal of Vacuum Science & Technology A: Vacuum, Surfaces, and Films*, vol. 19, no. 4, p. 1642, Jul. 2001.

[196] F. Li, C. Liu, Z. Ma, and L. Zhao, "New methods for determining the band gap behavior of ZnO," *Optical Materials*, vol. 34, no. 7, pp. 1062-1066, May 2012.

[197] J. G Lu et al., "Carrier concentration dependence of band gap shift in n-type ZnO:Al films," *Journal of Applied Physics*, vol. 101, no. 8, 2007.

[198] E. Burstein, "Anomalous Optical Absorption Limit in InSb," *Physical Review*, vol. 93, no. 3, pp. 632-633, Feb. 1954.

[199] K. J. Chen, F. Y. Hung, S. J. Chang, and Z. S. Hu, "Microstructures, optical and electrical properties of In-doped ZnO thin films prepared by sol–gel method," *Applied Surface Science*, vol. 255, no. 12, pp. 6308-6312, Apr. 2009.

[200] H. Oh, J. Krantz, I. Litzov, T. Stubhan, L. Pinna, and C. J. Brabec, "Comparison of various sol–gel derived metal oxide layers for inverted organic solar cells," *Solar Energy Materials and Solar Cells*, vol. 95, no. 8, pp. 2194-2199, Aug. 2011.

[201] S.-Y. Kuo et al., "Effects of RF power on the structural, optical and electrical properties of Al-doped zinc oxide films," *Microelectronics Reliability*, vol. 50, no. 5, pp. 730-733, May 2010.

[202] S. MAJUMDER, M. JAIN, P. DOBAL, and R. KATIYAR, "Investigations on solution derived aluminium doped zinc oxide thin films," *Materials Science and Engineering B*, vol. 103, no. 1, pp. 16-25, Sep. 2003.

[203] K. H. Kim, R. A. Wibowo, and B. Munir, "Properties of Al-doped ZnO thin film sputtered from powder compacted target," *Materials Letters*, vol. 60, no. 15, pp. 1931-1935, Jul. 2006.

[204] B. Thestrup, "Deposition of ITO and AZO thin films by laser ablation at 355 nm in a background atmosphere," 2000.

[205] J. Hun Park, “Deposition-Temperature Effects on AZO Thin Films Prepared by RF Magnetron Sputtering and Their Physical Properties,” *Scanning*, vol. 49, no. December, pp. 584-588, 2006.

[206] D. Sivalingam, J. B. Gopalakrishnan, and J. B. Balaguru Rayappan, “Influence of precursor concentration on structural, morphological and electrical properties of spray deposited ZnO thin films,” *Crystal Research and Technology*, vol. 46, no. 7, pp. 685-690, Jul. 2011.

[207] J. Bruneaux, H. Cachet, M. Froment, and A. Messad, “Structural, electrical and interfacialproperties of sprayed SnO2 films ☆.”

[208] M. N. Amalina and M. Rusop, “Effect of the precursor solution concentration of Copper (I) Iodide (CuI) thin film deposited by mister atomizer method,” in *2011 IEEE Symposium on Industrial Electronics and Applications (ISIEA)*, 2011, pp. 440-444.

[209] Z. Deng et al., *Effects of Al content on the properties of ZnO:Al films prepared by Al2O3 and ZnO co-sputtering*, vol. 21, no. 10. Springer New York, 2010, pp. 1030-1035.

[210] M. K. Puchert, “Postdeposition annealing of radio frequency magnetron sputtered ZnO films,” *Journal of Vacuum Science & Technology A: Vacuum, Surfaces, and Films*, vol. 14, no. 4, p. 2220, Jul. 1996.

[211] D. Marrocchelli, S. R. Bishop, H. L. Tuller, and B. Yildiz, “Understanding Chemical Expansion in Non-Stoichiometric Oxides: Ceria and Zirconia Case Studies,” *Advanced Functional Materials*, p. n/a-n/a, Feb. 2012.

[212] A. E. Rakhshani, “Al-doped zinc oxide films grown by successive chemical solution deposition,” *Applied Physics A*, vol. 92, no. 2, pp. 413-416, May 2008.

[213] G. J. Fang, D. Li, and B.-L. Yao, “Influence of post-deposition annealing on the properties of transparent conductive nanocrystalline ZAO thin films prepared by RF magnetron sputtering with highly conductive ceramic target,” *Thin solid films*, vol. 418, no. 2, pp. 156-162, 2002.

[214] H. Agura, A. Suzuki, T. Matsushita, T. Aoki, and M. Okuda, “Low resistivity transparent conducting Al-doped ZnO films prepared by pulsed laser deposition,” *Thin Solid Films*, vol. 445, no. 2, pp. 263-267, Dec. 2003.

[215] H. Kim, W. So, and S. Moon, “Effect of thermal annealing on the performance of P3HT/PCBM polymer photovoltaic cells,” *Journal Of The Korean Physical Society*, vol. 48, no. 3, 2006.

[216] R. Po, C. Carbonera, A. Bernardi, and N. Camaioni, “The role of buffer layers in polymer solar cells,” *Energy & Environmental Science*, vol. 4, no. 2, p. 285, 2011.

[217] H. Ma, H.-L. Yip, F. Huang, and A. K.-Y. Jen, “Interface Engineering for Organic Electronics,” *Advanced Functional Materials*, vol. 20, no. 9, pp. 1371-1388, Apr. 2010.

[218] Y.-fei Zhou et al., “Improved stability of OLEDs with mild oxygen plasma treated PEDOT:PSS,” *Journal of Luminescence*, vol. 122-123, pp. 602-604, Jan. 2007.

[219] C. Lee, R. P. Dwivedi, W. Lee, C. Hong, W. I. Lee, and H. W. Kim, “IZO/Al/GZO multilayer films to replace ITO films,” *Journal of Materials Science: Materials in Electronics*, vol. 19, no. 10, pp. 981-985, Oct. 2007.

[220] J. Kunert et al., “Advanced titania buffer layer architectures prepared by chemical solution deposition,” *Superconductor Science and Technology*, vol. 24, no. 8, p. 085018, Aug. 2011.

[221] C. Lee, A. Park, Y. Cho, M. Park, W. I. Lee, and H. W. Kim, “Influence of ZnO buffer layer thickness on the electrical and optical properties of indium zinc oxide thin films deposited on PET substrates,” *Ceramics International*, vol. 34, no. 4, pp. 1093-1096, May 2008.

[222] R. Po, C. Carbonera, A. Bernardi, and N. Camaioni, “The role of buffer layers in polymer solar cells,” *Energy & Environmental Science*, vol. 4, no. 2, p. 285, Nov. 2011.

[223] C. Tao et al., “Performance improvement of inverted polymer solar cells with different top electrodes by introducing a MoO[sub 3] buffer layer,” *Applied Physics Letters*, vol. 93, no. 19, p. 193307, Nov. 2008.

[224] V. D. Mihailetchi, P. W. M. Blom, J. C. Hummelen, and M. T. Rispens, “Cathode dependence of the open-circuit voltage of polymer:fullerene bulk heterojunction solar cells,” *Journal of Applied Physics*, vol. 94, no. 10, p. 6849, 2003.

[225] C. J. Brabec et al., “Origin of the Open Circuit Voltage of Plastic Solar Cells,” *Advanced Functional Materials*, vol. 11, no. 5, pp. 374-380, 2001.

[226] L.-M. Chen, Z. Xu, Z. Hong, and Y. Yang, “Interface investigation and engineering – achieving high performance polymer photovoltaic devices,” *Journal of Materials Chemistry*, vol. 20, no. 13, p. 2575, 2010.

[227] A. K. K. Kyaw, X. Sun, D. W. Zhao, S. T. Tan, Y. Divayana, and H. V. Demir, “Improved Inverted Organic Solar Cells With a Sol–Gel Derived Indium-Doped Zinc Oxide Buffer Layer,” *IEEE Journal of Selected Topics in Quantum Electronics*, vol. 16, no. 6, pp. 1700-1706, Nov. 2010.

[228] R. Janssen, “Introduction to polymer solar cells,” The Netherlands.

[229] S.-W. Oh, H. Woo Rhee, C. Lee, Y. Chul Kim, J. Kyeong Kim, and J.-W. Yu, “The photovoltaic effect of the p–n heterojunction organic photovoltaic device using a nano template method,” *Current Applied Physics*, vol. 5, no. 1, pp. 55-58, Jan. 2005.

[230] H. Cha et al., “Thermally stable amorphous polymeric semiconductors containing fluorene and thiophene for use in organic photovoltaic cells,” *Organic Electronics*, vol. 11, no. 9, pp. 1534-1542, Sep. 2010.

[231] R. Li et al., “Effect of mixture ratio on the performance of MDMO-PPV:PCBM bulk heterojunction solar cells: A numerical study,” *Materials Science and Engineering: B*, vol. 172, no. 3, pp. 305-310, Sep. 2010.

[232] W.-Y. Lee et al., “Effects of Acceptors on the Electronic and Optoelectronic Properties of Fluorene-Based Donor–Acceptor–Donor Copolymers,” *Macromolecular Chemistry and Physics*, vol. 208, no. 17, pp. 1919-1927, Sep. 2007.

[233] J. Y. Kim et al., “Efficient tandem polymer solar cells fabricated by all-solution processing.,” *Science (New York, N.Y.)*, vol. 317, no. 5835, pp. 222-5, Jul. 2007.

[234] S. Wu et al., “pH-neutral PEDOT:PSS as hole injection layer in polymer light emitting diodes,” *Organic Electronics*, vol. 12, no. 3, pp. 504-508, Mar. 2011.

[235] Z. Hu, J. Zhang, Y. Liu, Z. Hao, X. Zhang, and Y. Zhao, “Influence of ZnO interlayer on the performance of inverted organic photovoltaic device,” *Solar Energy Materials and Solar Cells*, vol. 95, no. 8, pp. 2126-2130, Aug. 2011.

[236] Y. Yang, K. Lee, K. Mielczarek, W. Hu, and A. Zakhidov, “Nanoimprint of dehydrated PEDOT:PSS for organic photovoltaics.,” *Nanotechnology*, vol. 22, no. 48, p. 485301, Dec. 2011.

[237] S. H. Eom et al., “Polymer solar cells based on inkjet-printed PEDOT:PSS layer,” *Organic Electronics*, vol. 10, no. 3, pp. 536-542, 2009.

[238] L. C. Olsen, H. Aguilar, and F. W. Addis, “CIS solar cells with ZnO buffer layers,” in *Conference Record of the Twenty Fifth IEEE Photovoltaic Specialists Conference - 1996*, 1996, pp. 997-1000.

[239] B. L. S. Roman, W. Mammo, L. A. A. Pettersson, M. R. Andersson, and O. Inganäs, “High Quantum Efficiency Polythiophene / C 60 Photodiodes,” *Ratio*, vol. 41296, no. 10, pp. 774-777, 1998.

[240] J. C. Scott et al., “Hole limited recombination in polymer light-emitting diodes,” *Applied Physics Letters*, vol. 74, no. 11, p. 1510, Mar. 1999.

[241] J. Huang, “Influence of thermal treatment on the conductivity and morphology of PEDOT/PSS films,” *Synthetic Metals*, vol. 139, no. 3, pp. 569-572, Oct. 2003.

[242] G.-F. Wang, X.-M. Tao, J. H. Xin, and B. Fei, “Modification of conductive polymer for polymeric anodes of flexible organic light-emitting diodes.,” *Nanoscale research letters*, vol. 4, no. 7, pp. 613-7, Jan. 2009.

[243] L. Groenendaal, F. Jonas, D. Freitag, H. Pielartzik, and J. R. Reynolds, “Poly(3,4-ethylenedioxythiophene) and Its Derivatives: Past, Present, and Future,” *Advanced Materials*, vol. 12, no. 7, pp. 481-494, Apr. 2000.

[244] T. Hori et al., “MoO3 buffer layer effect on photovoltaic properties of interpenetrating heterojunction type organic solar cells,” *Thin Solid Films*, vol. 518, no. 2, pp. 522-525, Nov. 2009.

[245] K. J. Reynolds, J. A. Barker, N. C. Greenham, R. H. Friend, and G. L. Frey, “Inorganic solution-processed hole-injecting and electron-blocking layers in polymer light-emitting diodes,” *Journal of Applied Physics*, vol. 92, no. 12, p. 7556, Dec. 2002.

[246] K. Morii, M. Omoto, M. Ishida, and M. Graetzel, “Enhanced Hole Injection in a Hybrid Organic–Inorganic Light-Emitting Diode,” *Japanese Journal of Applied Physics*, vol. 47, no. 9, pp. 7366-7368, Sep. 2008.

[247] F. Liu, S. Shao, X. Guo, Y. Zhao, and Z. Xie, “Efficient polymer photovoltaic cells using solution-processed MoO3 as anode buffer layer,” *Solar Energy Materials and Solar Cells*, vol. 94, no. 5, pp. 842-845, May 2010.

[248] V. Shrotriya, G. Li, Y. Yao, C.-W. Chu, and Y. Yang, “Transition metal oxides as the buffer layer for polymer photovoltaic cells,” *Applied Physics Letters*, vol. 88, no. 7, p. 073508, Feb. 2006.

[249] N. S. Kang, B.-K. Ju, C. Lee, J.-P. Ahn, B. D. Chin, and J.-W. Yu, “Partitioning of the organic layers for the fabrication of high efficiency organic photovoltaic devices,” *Organic Electronics*, vol. 10, no. 6, pp. 1091-1096, 2009.

[250] F.-C. Chen, J.-L. Wu, C.-L. Lee, Y. Hong, C.-H. Kuo, and M. H. Huang, “Plasmonic-enhanced polymer photovoltaic devices incorporating solution-processable metal nanoparticles,” *Applied Physics Letters*, vol. 95, no. 1, p. 013305, 2009.

[251] D. Y. Kim, J. Subbiah, G. Sarasqueta, F. So, H. Ding, and Y. Gao, “The effect of molybdenum oxide interlayer on organic photovoltaic cells,” *Applied Physics Letters*, vol. 95, no. 9, p. 093304, Sep. 2009.

[252]P. M. Allemand et al., “Two different fullerenes have the same cyclic voltammetry,” *Journal of the American Chemical Society*, vol. 113, no. 3, pp. 1050-1051, Jan. 1991.

[253] C.-C. Chang et al., “Effects of cathode buffer layers on the efficiency of bulk-heterojunction solar cells,” *Applied Physics Letters*, vol. 96, no. 26, p. 263506, Jun. 2010.

[254] P. P. Boix, J. Ajuria, I. Etxebarria, R. Pacios, G. Garcia-Belmonte, and J. Bisquert, “Role of ZnO Electron-Selective Layers in Regular and Inverted Bulk Heterojunction Solar Cells,” *The Journal of Physical Chemistry Letters*, vol. 2, no. 5, pp. 407-411, Mar. 2011.

[255] G. E. Jabbour et al., “Highly efficient and bright organic electroluminescent devices with an aluminum cathode,” *Applied Physics Letters*, vol. 71, no. 13, p. 1762, Sep. 1997.

[256] L. S. Hung, C. W. Tang, and M. G. Mason, “Enhanced electron injection in organic electroluminescence devices using an Al/LiF electrode,” *Applied Physics Letters*, vol. 70, no. 2, p. 152, Jan. 1997.

[257] T. M. Brown, R. H. Friend, I. S. Millard, D. J. Lacey, J. H. Burroughes, and F. Cacialli, “LiF/Al cathodes and the effect of LiF thickness on the device characteristics and built-in potential of polymer light-emitting diodes,” *Applied Physics Letters*, vol. 77, no. 19, p. 3096, Nov. 2000.

[258] J. Yoon, J.-J. Kim, T.-W. Lee, and O.-O. Park, “Evidence of band bending observed by electroabsorption studies in polymer light emitting device with ionomer/Al or LiF/Al cathode,” *Applied Physics Letters*, vol. 76, no. 16, p. 2152, Apr. 2000.

[259] S. E. Shaheen, C. J. Brabec, N. S. Sariciftci, F. Padinger, T. Fromherz, and J. C. Hummelen, “2.5% efficient organic plastic solar cells,” *Applied Physics Letters*, vol. 78, no. 6, p. 841, Feb. 2001.

[260] C. J. Brabec, S. E. Shaheen, C. Winder, N. S. Sariciftci, and P. Denk, “Effect of LiF/metal electrodes on the performance of plastic solar cells,” *Applied Physics Letters*, vol. 80, no. 7, p. 1288, Feb. 2002.

[261] J. Lee, Y. Park, D. Y. Kim, H. Y. Chu, H. Lee, and L.-M. Do, “High efficiency organic light-emitting devices with Al/NaF cathode,” *Applied Physics Letters*, vol. 82, no. 2, p. 173, Jan. 2003.

[262] S. E. Shaheen et al., “Bright blue organic light-emitting diode with improved color purity using a LiF/Al cathode,” *Journal of Applied Physics*, vol. 84, no. 4, p. 2324, Aug. 1998.

[263] S. K. M. Jönsson, E. Carlegrim, F. Zhang, W. R. Salaneck, and M. Fahlman, “Photoelectron Spectroscopy of the Contact between the Cathode and the Active Layers in Plastic Solar Cells: The Role of LiF,” *Japanese Journal of Applied Physics*, vol. 44, no. 6, pp. 3695-3701, 2005.

[264] B. Limketkai and M. Baldo, “Charge injection into cathode-doped amorphous organic semiconductors,” *Physical Review B*, vol. 71, no. 8, Feb. 2005.

[265] E. Ahlswede, J. Hanisch, and M. Powalla, “Comparative study of the influence of LiF, NaF, and KF on the performance of polymer bulk heterojunction solar cells,” *Applied Physics Letters*, vol. 90, no. 16, p. 163504, Apr. 2007.

[266] X. Jiang, H. Xu, L. Yang, M. Shi, M. Wang, and H. Chen, “Effect of CsF interlayer on the performance of polymer bulk heterojunction solar cells,” *Solar Energy Materials and Solar Cells*, vol. 93, no. 5, pp. 650-653, 2009.

[267] I. Tunc, M. Bruns, H. Gliemann, M. Grunze, and P. Koelsch, “Bandgap determination and charge separation in Ag@TiO2 core shell nanoparticle films,” *Surface and Interface Analysis*, vol. 42, no. 6-7, pp. 835-841, May 2010.

[268] J. Y. Kim et al., “New Architecture for High-Efficiency Polymer Photovoltaic Cells Using Solution-Based Titanium Oxide as an Optical Spacer,” *Advanced Materials*, vol. 18, no. 5, pp. 572-576, Mar. 2006.

[269] M. C. Scharber et al., “Design Rules for Donors in Bulk-Heterojunction Solar Cells—Towards 10 % Energy-Conversion Efficiency,” *Advanced Materials*, vol. 18, no. 6, pp. 789-794, Mar. 2006.

[270] J. H. Lee, S. Cho, A. Roy, H.-T. Jung, and A. J. Heeger, “Enhanced diode characteristics of organic solar cells using titanium suboxide electron transport layer,” *Applied Physics Letters*, vol. 96, no. 16, p. 163303, Apr. 2010.

[271] A. Tentorio and L. Canova, “Adsorption of α-amino acids on spherical TiO2 particles,” *Colloids and Surfaces*, vol. 39, no. 2, pp. 311-319, 1989.

[272] A. Hayakawa, O. Yoshikawa, T. Fujieda, K. Uehara, and S. Yoshikawa, “High performance polythiophene/fullerene bulk-heterojunction solar cell with a TiO[sub x] hole blocking layer,” *Applied Physics Letters*, vol. 90, no. 16, p. 163517, Apr. 2007.

[273] M. S. White, D. C. Olson, S. E. Shaheen, N. Kopidakis, and D. S. Ginley, “Inverted bulk-heterojunction organic photovoltaic device using a solution-derived ZnO underlayer,” *Applied Physics Letters*, vol. 89, no. 14, p. 143517, Oct. 2006.

[274] A. K. K. Kyaw, X. W. Sun, C. Y. Jiang, G. Q. Lo, D. W. Zhao, and D. L. Kwong, “An inverted organic solar cell employing a sol-gel derived ZnO electron selective layer and thermal evaporated MoO3 hole selective layer,” *Applied Physics Letters*, vol. 93, no. 22, p. 221107, 2008.

[275] G. Zhang, Y. Fu, Z. Xie, and Q. Zhang, “Synthesis and Photovoltaic Properties of New Low Bandgap Isoindigo-Based Conjugated Polymers,” *Macromolecules*, vol. 44, no. 6, p. 110204084214089, Feb. 2011.

[276] P. Ding, C.-C. Chu, Y. Zou, D. Xiao, C. Pan, and C.-S. Hsu, “New low bandgap conjugated polymer derived from 2, 7-carbazole and 5, 6-bis(octyloxy)-4, 7-di(thiophen-2-yl) benzothiadiazole: Synthesis and photovoltaic properties,” *Journal of Applied Polymer Science*, vol. 123, no. 1, pp. 99-107, Jan. 2012.

[277] M. Girtan and M. Rusu, “Role of ITO and PEDOT:PSS in stability/degradation of polymer:fullerene bulk heterojunctions solar cells,” *Solar Energy Materials and Solar Cells*, vol. 94, no. 3, pp. 446-450, Mar. 2010.

[278] C. Waldauf et al., “Highly efficient inverted organic photovoltaics using solution based titanium oxide as electron selective contact,” *Applied Physics Letters*, vol. 89, no. 23, p. 233517, 2006.

[279] H. Yan et al., “High-performance hole-transport layers for polymer light-emitting diodes. Implementation of organosiloxane cross-linking chemistry in polymeric electroluminescent devices.,” *Journal of the American Chemical Society*, vol. 127, no. 9, pp. 3172-83, Mar. 2005.

[280] Z. Feng, Y. Hou, and D. Lei, “The influence of electrode buffer layers on the performance of polymer photovoltaic devices,” *Renewable Energy*, vol. 35, no. 6, pp. 1175-1178, Jun. 2010.

[281] A. WATANABE and A. KASUYA, “Effect of atmospheres on the open-circuit photovoltage of nanoporous TiO/poly(3-hexylthiophene) heterojunction solar cell,” *Thin Solid Films*, vol. 483, no. 1-2, pp. 358-366, Jul. 2005.

[282] M. P. de Jong, L. J. van IJzendoorn, and M. J. A. de Voigt, “Stability of the interface between indium-tin-oxide and poly(3,4-ethylenedioxythiophene)/poly(styrenesulfonate) in polymer light-emitting diodes,” *Applied Physics Letters*, vol. 77, no. 14, p. 2255, Oct. 2000.

[283] Y. SAHIN, S. ALEM, R. DEBETTIGNIES, and J. NUNZI, “Development of air stable polymer solar cells using an inverted gold on top anode structure,” *Thin Solid Films*, vol. 476, no. 2, pp. 340-343, Apr. 2005.

[284] S. J. Jo et al., “Increase in indium diffusion by tetrafluoromethane plasma treatment and its effects on the device performance of polymer light-emitting diodes,” *Journal of Applied Physics*, vol. 103, no. 11, p. 114502, Jun. 2008.

[285] D. Lide, “CRC Handbook of Chemistry and Physics. 84th,” *Memory*, vol. 1989, 2002.

[286] C.-D. Wang and W. C. H. Choy, “Efficient hole collection by introducing ultra-thin UV–ozone treated Au in polymer solar cells,” *Solar Energy Materials and Solar Cells*, vol. 95, no. 3, pp. 904-908, Mar. 2011.

[287] K. Norrman, M. V. Madsen, S. A. Gevorgyan, and F. C. Krebs, “Degradation patterns in water and oxygen of an inverted polymer solar cell.,” *Journal of the American Chemical Society*, vol. 132, no. 47, pp. 16883-92, Dec. 2010.

[288] K. Norrman, N. B. Larsen, and F. C. Krebs, “Lifetimes of organic photovoltaics: Combining chemical and physical characterisation techniques to study degradation mechanisms,” *Solar Energy Materials and Solar Cells*, vol. 90, no. 17, pp. 2793-2814, Nov. 2006.

[289] S. A. Gevorgyan, M. Jørgensen, and F. C. Krebs, “A setup for studying stability and degradation of polymer solar cells,” *Solar Energy Materials and Solar Cells*, vol. 92, no. 7, pp. 736-745, Jul. 2008.

[290] E. Nasybulin, S. Wei, M. Cox, I. Kymissis, and K. Levon, “Morphological and Spectroscopic Studies of Electrochemically Deposited Poly(3,4-ethylenedioxythiophene) (PEDOT) Hole Extraction Layer for Organic Photovoltaic Device (OPVd) Fabrication,” *The Journal of Physical Chemistry C*, vol. 115, no. 10, pp. 4307-4314, Mar. 2011.

[291] W. Osikowicz, X. Crispin, C. Tengstedt, L. Lindell, T. Kugler, and W. R. Salaneck, “Transparent low-work-function indium tin oxide electrode obtained by molecular

scale interface engineering," *Applied Physics Letters*, vol. 85, no. 9, p. 1616, Aug. 2004.

[292] G. Li, C.-W. Chu, V. Shrotriya, J. Huang, and Y. Yang, "Efficient inverted polymer solar cells," *Applied Physics Letters*, vol. 88, no. 25, p. 253503, Jun. 2006.

[293] S. G. Ihn et al., "ITO-free inverted polymer solar cells using a GZO cathode modified by ZnO," *Solar Energy Materials and Solar Cells*, vol. 95, no. 7, pp. 1610-1614, Jul. 2011.

[294] N. Sekine, C.-H. Chou, W. L. Kwan, and Y. Yang, "ZnO nano-ridge structure and its application in inverted polymer solar cell," *Organic Electronics*, vol. 10, no. 8, pp. 1473-1477, Dec. 2009.

[295] D. C. Olson, S. E. Shaheen, R. T. Collins, and D. S. Ginley, "The Effect of Atmosphere and ZnO Morphology on the Performance of Hybrid Poly(3-hexylthiophene)/ZnO Nanofiber Photovoltaic Devices," *Journal of Physical Chemistry C*, vol. 111, no. 44, pp. 16670-16678, Nov. 2007.

[296] F. C. Krebs and K. Norrman, "Analysis of the failure mechanism for a stable organic photovoltaic during 10000 h of testing," *Progress In Photovoltaics*, vol. 15, no. 8, pp. 697-712, 2007.

[297] Z. Xu et al., "Vertical Phase Separation in Poly(3-hexylthiophene): Fullerene Derivative Blends and its Advantage for Inverted Structure Solar Cells," *Advanced Functional Materials*, vol. 19, no. 8, pp. 1227-1234, Apr. 2009.

[298] A. K. K. Kyaw, X. Sun, D. W. Zhao, S. T. Tan, Y. Divayana, and H. V. Demir, "Improved Inverted Organic Solar Cells With a Sol–Gel Derived Indium-Doped Zinc Oxide Buffer Layer," *IEEE Journal of Selected Topics in Quantum Electronics*, vol. 16, no. 6, pp. 1700-1706, 2010.

[299] M. T. Dang, L. Hirsch, and G. Wantz, "P3HT:PCBM, Best Seller in Polymer Photovoltaic Research," *Advanced Materials*, vol. 23, no. 31, p. n/a-n/a, Jul. 2011.

[300] D. W. Zhao, P. Liu, X. W. Sun, S. T. Tan, L. Ke, and A. K. K. Kyaw, "An inverted organic solar cell with an ultrathin Ca electron-transporting layer and MoO[sub 3] hole-transporting layer," *Applied Physics Letters*, vol. 95, no. 15, p. 153304, Oct. 2009.

[301] C.-Y. Li et al., "An inverted polymer photovoltaic cell with increased air stability obtained by employing novel hole/electron collecting layers," *Journal of Materials Chemistry*, vol. 19, no. 11, p. 1643, Mar. 2009.

[302] V. D. Mihailetchi, P. W. M. Blom, J. C. Hummelen, and M. T. Rispens, "Cathode dependence of the open-circuit voltage of polymer:fullerene bulk heterojunction solar cells," *Journal of Applied Physics*, vol. 94, no. 10, p. 6849, Nov. 2003.

[303] Z. Hu, J. Zhang, Y. Liu, Z. Hao, X. Zhang, and Y. Zhao, "Influence of ZnO interlayer on the performance of inverted organic photovoltaic device," *Solar Energy Materials and Solar Cells*, vol. 95, no. 8, pp. 2126-2130, Aug. 2011.

[304] L.-M. Chen, Z. Hong, G. Li, and Y. Yang, "Recent Progress in Polymer Solar Cells: Manipulation of Polymer:Fullerene Morphology and the Formation of Efficient Inverted Polymer Solar Cells," *Advanced Materials*, vol. 21, no. 14-15, pp. 1434-1449, Apr. 2009.

[305] L. Vayssieres, "Growth of Arrayed Nanorods and Nanowires of ZnO from Aqueous Solutions," *Advanced Materials*, vol. 15, no. 5, pp. 464-466, Mar. 2003.

[306] R. B. Peterson, C. L. Fields, and B. A. Gregg, "Epitaxial Chemical Deposition of ZnO Nanocolumns from NaOH Solutions," *Langmuir*, vol. 20, no. 12, pp. 5114-5118, Jun. 2004.

[307] O. Kunz, J. Wong, J. Janssens, J. Bauer, O. Breitenstein, and A. G. Aberle, "Shunting problems due to sub-micron pinholes in evaporated solid-phase crystallised poly-Si thin-film solar cells on glass," *Progress in Photovoltaics: Research and Applications*, vol. 17, no. 1, pp. 35-46, Jan. 2009.

[308] A. M. Peiro et al., "Hybrid polymer/metal oxide solar cells based on ZnO columnar structures," *Journal of Materials Chemistry*, vol. 16, no. 21, p. 2088, May 2006.

[309] E. M. Kaidashev et al., "High electron mobility of epitaxial ZnO thin films on c-plane sapphire grown by multistep pulsed-laser deposition," *Applied Physics Letters*, vol. 82, no. 22, p. 3901, Jun. 2003.

[310] E. Centurioni and D. Iencinella, "Role of front contact work function on amorphous silicon/crystalline silicon heterojunction solar cell performance," *IEEE Electron Device Letters*, vol. 24, no. 3, pp. 177-179, Mar. 2003.

[311] D. W. Zhao, P. Liu, X. W. Sun, S. T. Tan, L. Ke, and A. K. K. Kyaw, "An inverted organic solar cell with an ultrathin Ca electron-transporting layer and MoO[sub 3] hole-transporting layer," *Applied Physics Letters*, vol. 95, no. 15, p. 153304, 2009.

[312] I. D. Parker, "Carrier tunneling and device characteristics in polymer light-emitting diodes," *Journal of Applied Physics*, vol. 75, no. 3, p. 1656, Feb. 1994.

[313] C. Y. Jiang, X. W. Sun, D. W. Zhao, A. K. K. Kyaw, and Y. N. Li, "Low work function metal modified ITO as cathode for inverted polymer solar cells," *Solar Energy Materials and Solar Cells*, vol. 94, no. 10, pp. 1618-1621, Oct. 2010.

[314] J. Nunzi, "Organic photovoltaic materials and devices," *Comptes Rendus Physique*, vol. 3, no. 4, pp. 523-542, 2002.

[315] B. Kang, L. W. Tan, and S. R. P. Silva, "Fluoropolymer indium-tin-oxide buffer layers for improved power conversion in organic photovoltaics," *Applied Physics Letters*, vol. 93, no. 13, p. 133302, Sep. 2008.

[316] M. Y. Chan et al., “Efficient organic photovoltaic devices using a combination of exciton blocking layer and anodic buffer layer,” *Journal of Applied Physics*, vol. 100, no. 9, p. 094506, Nov. 2006.

[317] F. C. Krebs, “Air stable polymer photovoltaics based on a process free from vacuum steps and fullerenes,” *Solar Energy Materials and Solar Cells*, vol. 92, no. 7, pp. 715-726, Jul. 2008.

[318] M.-C. Choi, Y. Kim, and C.-S. Ha, “Polymers for flexible displays: From material selection to device applications,” *Progress in Polymer Science*, vol. 33, no. 6, pp. 581-630, Jun. 2008.

[319] H.-chiang You and S.-jun Zhang, “Al-Doped ZnO Thin Film Transistors by Thermal Evaporation,” *Glass*, pp. 4-6.

[320] Y. Sobajima, S. Kato, T. Matsuura, T. Toyama, and H. Okamoto, “Study of the light-trapping effects of textured ZnO:Al/glass structure TCO for improving photocurrent of a-Si:H solar cells,” *Journal of Materials Science: Materials in Electronics*, vol. 18, no. 1, pp. 159-162, Mar. 2007.

[321] T. Minami, T. Miyata, Y. Ohtani, and T. Kuboi, “Effect of thickness on the stability of transparent conducting impurity-doped ZnO thin films in a high humidity environment,” *physica status solidi (RRL) – Rapid Research Letters*, vol. 1, no. 1, p. R31-R33, Jan. 2007.

[322] T. Minami, “New n-Type Transparent Conducting Oxides,” *MRS Bulletin*, vol. 25, no. 8, pp. 38-44, Aug. 2000.

[323] M. Wang et al., “Thickness dependence of the MoO(3) blocking layers on ZnO nanorod-inverted organic photovoltaic devices.,” *Applied physics letters*, vol. 98, no. 10, p. 103305, Mar. 2011.

[324] H. Lu, “Enhanced emission in organic light-emitting diodes using Ta2O5 buffer layers,” *Solid-State Electronics*, vol. 47, no. 8, pp. 1409-1412, Aug. 2003.

[325] A. Hayakawa, O. Yoshikawa, T. Fujieda, K. Uehara, and S. Yoshikawa, “High performance polythiophene/fullerene bulk-heterojunction solar cell with a TiO[sub x] hole blocking layer,” *Applied Physics Letters*, vol. 90, no. 16, p. 163517, 2007.

[326] H. J. Snaith, N. C. Greenham, and R. H. Friend, “The Origin of Collected Charge and Open-Circuit Voltage in Blended Polyfluorene Photovoltaic Devices,” *Advanced Materials*, vol. 16, no. 18, pp. 1640-1645, Sep. 2004.

[327] B. Sun, H. J. Snaith, A. S. Dhoot, S. Westenhoff, and N. C. Greenham, “Vertically segregated hybrid blends for photovoltaic devices with improved efficiency,” *Journal of Applied Physics*, vol. 97, no. 1, p. 014914, Dec. 2005.

[328] P. Peumans, S. Uchida, and S. R. Forrest, “Efficient bulk heterojunction photovoltaic cells using small-molecular-weight organic thin films.,” *Nature*, vol. 425, no. 6954, pp. 158-62, Sep. 2003.

[329] H. KIM, W. SO, and S. MOON, “The importance of post-annealing process in the device performance of poly(3-hexylthiophene): Methanofullerene polymer solar cell,” *Solar Energy Materials and Solar Cells*, vol. 91, no. 7, pp. 581-587, Apr. 2007.

[330] G. Li et al., “High-efficiency solution processable polymer photovoltaic cells by self-organization of polymer blends,” *Nature Materials*, vol. 4, pp. 864-868, 2005.

[331] M. O. Reese, M. S. White, G. Rumbles, D. S. Ginley, and S. E. Shaheen, “Optimal negative electrodes for poly(3-hexylthiophene): [6,6]-phenyl C61-butyric acid methyl ester bulk heterojunction photovoltaic devices,” *Applied Physics Letters*, vol. 92, no. 5, p. 053307, Feb. 2008.

[332] H. Lin, W. Xia, H. N. Wu, and C. W. Tang, “CdS/CdTe solar cells with MoO[sub x] as back contact buffers,” *Applied Physics Letters*, vol. 97, no. 12, p. 123504, Sep. 2010.

[333] C. Luan et al., “Facile solution growth of vertically aligned ZnO nanorods sensitized with aqueous CdS and CdSe quantum dots for photovoltaic applications.,” *Nanoscale research letters*, vol. 6, no. 1, p. 340, Jan. 2011.

[334] Q. Zhang, C. S. Dandeneau, X. Zhou, and G. Cao, “ZnO Nanostructures for Dye-Sensitized Solar Cells,” *Advanced Materials*, vol. 21, no. 41, pp. 4087-4108, Nov. 2009.

[335] R. C. Pillai and J. T. Thirukonda Anandha Vijayan, “Growth of Undoped and Metal Doped ZnO Nanostructures by Solution Growth,” *Nanocrystals*, pp. 31-44, 2010.

[336] I. Mora-Seró, S. Giménez, F. Fabregat-Santiago, E. Azaceta, R. Tena-Zaera, and J. Bisquert, “Modeling and characterization of extremely thin absorber (eta) solar cells based on ZnO nanowires.,” *Physical chemistry chemical physics□: PCCP*, vol. 13, no. 15, pp. 7162-9, Apr. 2011.

[337] A. Mere, A. Katerski, T. Dedova, I. Oja Acik, and M. Krunks, “Extremely thin absorber layer nanostructured solar cell by chemical spray pyrolysis,” in *23rd European Photovoltaic Solar Energy Conference*, 2008, pp. 2147 - 2150.

[338] R. Tena-Zaera, M. A. Ryan, A. Katty, G. Hodes, S. Bastide, and C. Lévy-Clément, “Fabrication and characterization of ZnO nanowires/CdSe/CuSCN eta-solar cell,” *Comptes Rendus Chimie*, vol. 9, no. 5-6, pp. 717-729, May 2006.

[339] R. Tena-Zaera, A. Katty, S. Bastide, C. Lévy-Clément, B. O’Regan, and V. Muñoz-Sanjosé, “ZnO/CdTe/CuSCN, a promising heterostructure to act as inorganic eta-solar cell,” *Thin Solid Films*, vol. 483, no. 1-2, pp. 372-377, Jul. 2005.

[340] D. C. Olson, J. Piris, R. T. Collins, S. E. Shaheen, and D. S. Ginley, “Hybrid photovoltaic devices of polymer and ZnO nanofiber composites,” *Thin Solid Films*, vol. 496, no. 1, pp. 26-29, Feb. 2006.

[341] W. J. E. Beek, M. M. Wienk, and R. A. J. Janssen, “Hybrid polymer solar cells based on zinc oxide,” *Journal of Materials Chemistry*, vol. 15, no. 29, p. 2985, 2005.

[342] W. J. E. Beek, M. M. Wienk, and R. A. J. Janssen, “Hybrid Solar Cells from Regioregular Polythiophene and ZnO Nanoparticles,” *Advanced Functional Materials*, vol. 16, no. 8, pp. 1112-1116, May 2006.

[343] R. S. Aga et al., “Enhanced photoresponse in ZnO nanowires decorated with CdTe quantum dot,” *Applied Physics Letters*, vol. 91, no. 23, p. 232108, Dec. 2007.

[344] K.-T. Kuo, D.-M. Liu, S.-Y. Chen, and C.-C. Lin, “Core-shell CuInS2/ZnS quantum dots assembled on short ZnO nanowires with enhanced photo-conversion efficiency,” *Journal of Materials Chemistry*, vol. 19, no. 37, p. 6780, 2009.

[345] Y. Tang, X. Hu, M. Chen, L. Luo, B. Li, and L. Zhang, “CdSe nanocrystal sensitized ZnO core-shell nanorod array films: Preparation and photovoltaic properties,” *Electrochimica Acta*, vol. 54, no. 10, pp. 2742-2747, Apr. 2009.

[346] K. S. Leschkies et al., “Photosensitization of ZnO nanowires with CdSe quantum dots for photovoltaic devices.,” *Nano letters*, vol. 7, no. 6, pp. 1793-8, Jun. 2007.

[347]F. W. Wise, “Lead Salt Quantum Dots: the Limit of Strong Quantum Confinement,” *Accounts of Chemical Research*, vol. 33, no. 11, pp. 773-780, Nov. 2000.

[348] J. H. Warner, E. Thomsen, A. R. Watt, N. R. Heckenberg, and H. Rubinsztein-Dunlop, “Time-resolved photoluminescence spectroscopy of ligand-capped PbS nanocrystals.,” *Nanotechnology*, vol. 16, no. 2, pp. 175-9, Mar. 2005.

[349] A. A. R. Watt, P. Meredith, J. D. Riches, S. Atkinson, and H. Rubinsztein-Dunlop, “A PbS quantum-cube: conducting polymer composite for photovoltaic applications,” *Current Applied Physics*, vol. 4, no. 2-4, pp. 320-322, Apr. 2004.

[350] M. T. Nenadovic, M. I. Comor, V. Vasic, and O. I. Micic, “Transient bleaching of small lead sulfide colloids: influence of surface properties,” *The Journal of Physical Chemistry*, vol. 94, no. 16, pp. 6390-6396, Aug. 1990.

[351] M. J. Fernée, J. Warner, A. Watt, S. Cooper, N. R. Heckenberg, and H. Rubinsztein-Dunlop, “Polarized photoluminescence from surface-passivated lead sulfide nanocrystals,” *Nanotechnology*, vol. 15, no. 1, pp. 16-22, Jan. 2004.

[352] C. Wadia, A. P. Alivisatos, and D. M Kammen, “Materials availability expands the opportunity for large-scale photovoltaics deployment.,” *Environmental science technology*, vol. 43, no. 6, pp. 2072-2077, 2009.

[353] C. H. Henry, “Limiting efficiencies of ideal single and multiple energy gap terrestrial solar cells,” *Journal of Applied Physics*, vol. 51, no. 8, p. 4494, Aug. 1980.

[354] H. Reuter and H. Schmitt, “Efficiencies of single and graded gap solar cells at terrestrial solar spectra,” *Journal of Applied Physics*, vol. 71, no. 12, p. 5957, Jun. 1992.

[355] J. FAN and B. PALM, “Optimal design of amorphous single-junction and tandem solar cells,” *Solar Cells*, vol. 10, no. 1, pp. 81-98, Oct. 1983.

[356] J. Cox, “A quantum paintbox,” *Chemistry in Britain*, vol. 39, no. 9, pp. 21-25, 2003.

[357] C. Honsberg and S. Bowden, “PV Education.”

[358] J. M. Luther, J. Gao, M. T. Lloyd, O. E. Semonin, M. C. Beard, and A. J. Nozik, “Stability assessment on a 3% bilayer PbS/ZnO quantum dot heterojunction solar cell.,” *Advanced materials (Deerfield Beach, Fla.)*, vol. 22, no. 33, pp. 3704-7, Sep. 2010.

[359] J. E. Murphy et al., “PbTe colloidal nanocrystals: synthesis, characterization, and multiple exciton generation.,” *Journal of the American Chemical Society*, vol. 128, no. 10, pp. 3241-7, Mar. 2006.

[360] R. Debnath et al., “Ambient-processed colloidal quantum dot solar cells via individual pre-encapsulation of nanoparticles.,” *Journal of the American Chemical Society*, vol. 132, no. 17, pp. 5952-3, May 2010.

[361] E. J. D. Klem, D. D. MacNeil, P. W. Cyr, L. Levina, and E. H. Sargent, “Efficient solution-processed infrared photovoltaic cells: Planarized all-inorganic bulk heterojunction devices via inter-quantum-dot bridging during growth from solution,” *Applied Physics Letters*, vol. 90, no. 18, p. 183113, May 2007.

[362] G. I. Koleilat et al., “Efficient, stable infrared photovoltaics based on solution-cast colloidal quantum dots.,” *ACS nano*, vol. 2, no. 5, pp. 833-40, May 2008.

[363] J. M Luther et al., “Schottky solar cells based on colloidal nanocrystal films.,” *Nano Letters*, vol. 8, no. 10, pp. 3488-3492, 2008.

[364] J. Gao, J. M. Luther, O. E. Semonin, R. J. Ellingson, A. J. Nozik, and M. C. Beard, “Quantum dot size dependent J-V characteristics in heterojunction ZnO/PbS quantum dot solar cells.,” *Nano letters*, vol. 11, no. 3, pp. 1002-8, Mar. 2011.

[365] P. R. Brown et al., “Improved current extraction from ZnO/PbS quantum dot heterojunction photovoltaics using a MoO3 interfacial layer.,” *Nano letters*, vol. 11, no. 7, pp. 2955-61, Jul. 2011.

[366] J. J. Choi et al., “PbSe nanocrystal excitonic solar cells.,” *Nano letters*, vol. 9, no. 11, pp. 3749-55, Nov. 2009.

[367] K. S Leschkies, T. J Beatty, M. S. Kang, D. J Norris, and E. S Aydil, “Solar cells based on junctions between colloidal PbSe nanocrystals and thin ZnO films.,” *ACS nano*, vol. 3, no. 11, pp. 3638-3648, 2009.

[368] K. S. Leschkies, A. G. Jacobs, D. J. Norris, and E. S. Aydil, “Nanowire-quantum-dot solar cells and the influence of nanowire length on the charge collection efficiency,” *Applied Physics Letters*, vol. 95, no. 19, p. 193103, Nov. 2009.

[369] A. G. Pattantyus-Abraham et al., “Depleted-heterojunction colloidal quantum dot solar cells.,” *ACS nano*, vol. 4, no. 6, pp. 3374-80, Jun. 2010.

[370] B. E. N. G Streetman and S. K. Banerjee, “Solid State Electronic Devices,” *Macromolecular Bioscience*, vol. 10, no. 1, pp. 1-608, 2006.

[371] S. A. McDonald et al., “Solution-processed PbS quantum dot infrared photodetectors and photovoltaics.,” *Nature materials*, vol. 4, no. 2, pp. 138-42, Feb. 2005.

[372] A. Maria, P. W. Cyr, E. J. D. Klem, L. Levina, and E. H. Sargent, “Solution-processed infrared photovoltaic devices with >10% monochromatic internal quantum efficiency,” *Applied Physics Letters*, vol. 87, no. 21, p. 213112, Nov. 2005.

[373] I. Mora-Seró et al., “Factors determining the photovoltaic performance of a CdSe quantum dot sensitized solar cell: the role of the linker molecule and of the counter electrode.,” *Nanotechnology*, vol. 19, no. 42, p. 424007, Oct. 2008.

[374] D. A. R. Barkhouse et al., “Depleted Bulk Heterojunction Colloidal Quantum Dot Photovoltaics.,” *Advanced materials (Deerfield Beach, Fla.)*, vol. 23, no. 28, pp. 3134-8, May 2011.

[375] H. Liu et al., “Electron Acceptor Materials Engineering in Colloidal Quantum Dot Solar Cells,” *Advanced Materials*, vol. 23, no. 33, pp. 3832-3837, Jul. 2011.

[376] J. Gao et al., “n-Type Transition Metal Oxide as a Hole Extraction Layer in PbS Quantum Dot Solar Cells.,” *Nano letters*, vol. 11, no. 8, pp. 3263-3266, Jun. 2011.

[377] J. Tang et al., “Colloidal-quantum-dot photovoltaics using atomic-ligand passivation,” *Nature Materials*, vol. 10, no. 10, pp. 765-771, Sep. 2011.

[378] W. A. Tisdale, K. J. Williams, B. A. Timp, D. J. Norris, E. S. Aydil, and X.-Y. Zhu, “Hot-electron transfer from semiconductor nanocrystals.,” *Science (New York, N.Y.)*, vol. 328, no. 5985, pp. 1543-7, Jun. 2010.

[379] M. S. Kang, A. Sahu, D. J. Norris, and C. D. Frisbie, “Size-dependent electrical transport in CdSe nanocrystal thin films.,” *Nano letters*, vol. 10, no. 9, pp. 3727-32, Oct. 2010.

[380] J. M. Luther et al., “Schottky solar cells based on colloidal nanocrystal films.,” *Nano letters*, vol. 8, no. 10, pp. 3488-92, Oct. 2008.

[381] S. Giménez et al., “Improving the performance of colloidal quantum-dot-sensitized solar cells.,” *Nanotechnology*, vol. 20, no. 29, p. 295204, Jul. 2009.

[382] J. J. Choi et al., “Solution-Processed Nanocrystal Quantum Dot Tandem Solar Cells.,” *Advanced materials (Deerfield Beach, Fla.)*, vol. 23, no. 28, pp. 3144-8, Jun. 2011.

[383] X. Wang et al., “Tandem colloidal quantum dot solar cells employing a graded recombination layer,” *Nature Photonics*, vol. 5, no. 8, pp. 480-484, Jun. 2011.

[384] A. K. Rath, M. Bernechea, L. Martinez, and G. Konstantatos, “Solution-Processed Heterojunction Solar Cells Based on p-type PbS Quantum Dots and n-type Bi(2) S(3) Nanocrystals.,” *Advanced materials (Deerfield Beach, Fla.)*, vol. 23, no. 32, pp. 3712-7, Jul. 2011.

[385] M. Law, M. C. Beard, S. Choi, J. M. Luther, M. C. Hanna, and A. J. Nozik, “Determining the internal quantum efficiency of PbSe nanocrystal solar cells with the aid of an optical model.,” *Nano letters*, vol. 8, no. 11, pp. 3904-10, Nov. 2008.

[386] J. Tang et al., “Quantum dot photovoltaics in the extreme quantum confinement regime: the surface-chemical origins of exceptional air- and light-stability.,” *ACS nano*, vol. 4, no. 2, pp. 869-78, Feb. 2010.

[387] Y. Liu et al., “Dependence of carrier mobility on nanocrystal size and ligand length in PbSe nanocrystal solids.,” *Nano letters*, vol. 10, no. 5, pp. 1960-9, May 2010.

[388] M. H. Zarghami, Y. Liu, M. Gibbs, E. Gebremichael, C. Webster, and M. Law, “p-Type PbSe and PbS quantum dot solids prepared with short-chain acids and diacids.,” *ACS nano*, vol. 4, no. 4, pp. 2475-85, Apr. 2010.

[389] G. Sarasqueta, K. R. Choudhury, and F. So, “Effect of Solvent Treatment on Solution-Processed Colloidal PbSe Nanocrystal Infrared Photodetectors,” *Chemistry of Materials*, vol. 22, no. 11, pp. 3496-3501, Jun. 2010.

[390] Y. Kim, T. Pietsch, A. Erbe, W. Belzig, and E. Scheer, “Benzenedithiol: a broad-range single-channel molecular conductor.,” *Nano Letters*, vol. 11, no. 9, pp. 3734-3738, 2011.

[391] F. Xu, X. Ma, C. R. Haughn, J. Benavides, M. F. Doty, and S. G. Cloutier, “Efficient Exciton Funneling in Cascaded PbS Quantum Dot Superstructures.,” *ACS nano*, vol. 5, no. 12, pp. 9950-9957, Nov. 2011.

[392] J. M. Luther, M. Law, Q. Song, C. L. Perkins, M. C. Beard, and A. J. Nozik, “Structural, optical, and electrical properties of self-assembled films of PbSe nanocrystals treated with 1,2-ethanedithiol.,” *ACS nano*, vol. 2, no. 2, pp. 271-80, Feb. 2008.

[393] Y. Liu et al., “Dependence of carrier mobility on nanocrystal size and ligand length in PbSe nanocrystal solids.,” *Nano letters*, vol. 10, no. 5, pp. 1960-9, May 2010.

[394] J. Dharma and A. Pisal, “Simple Method of Measuring the Band Gap Energy Value of TiO2 in the Powder Form using a UV/Vis/ NIR Spectrometer,” Shelton.

[395]I. Moreels et al., “Size-dependent optical properties of colloidal PbS quantum dots.,” *ACS nano*, vol. 3, no. 10, pp. 3023-3030, 2009.

[396] S. W. Buckner, R. L. Konold, and P. A. Jelliss, “Luminescence quenching in PbS nanoparticles,” *Chemical Physics Letters*, vol. 394, no. 4-6, pp. 400-404, Aug. 2004.

[397] H. J. Snaith, A. Stavrinadis, P. Docampo, and A. A. R. Watt, “Lead-sulphide quantum-dot sensitization of tin oxide based hybrid solar cells,” *Solar Energy*, vol. 85, no. 6, pp. 1283-1290, Jun. 2011.

[398] D. A. R. Barkhouse, I. J. Kramer, X. Wang, and E. H. Sargent, “Dead zones in colloidal quantum dot photovoltaics: evidence and implications,” *Optics Express*, vol. 18, no. 3, p. A451, Sep. 2010.

[399] I. Kramer and E. H. Sargent, “Colloidal Quantum Dot Photovoltaics: A Path Forward.,” *ACS nano*, vol. 5, no. 11, pp. 8506-8514, Oct. 2011.

[400] K. W. Johnston et al., “Efficient Schottky-quantum-dot photovoltaics: The roles of depletion, drift, and diffusion,” *Applied Physics Letters*, vol. 92, no. 12, p. 122111, Mar. 2008.

[401] D. A. R. Barkhouse, A. G. Pattantyus-Abraham, L. Levina, and E. H. Sargent, “Thiols passivate recombination centers in colloidal quantum dots leading to enhanced photovoltaic device efficiency.,” *ACS nano*, vol. 2, no. 11, pp. 2356-62, Nov. 2008.

[402] J. Gao, J. M. Luther, O. E. Semonin, R. J. Ellingson, A. J. Nozik, and M. C. Beard, “Quantum dot size dependent J-V characteristics in heterojunction ZnO/PbS quantum dot solar cells.,” *Nano letters*, vol. 11, no. 3, pp. 1002-8, Mar. 2011.

[403] S. Cox et al., “Experimental Confirmation of the Predicted Shallow Donor Hydrogen State in Zinc Oxide,” *Physical Review Letters*, vol. 86, no. 12, pp. 2601-2604, Mar. 2001.

[404] D. Hofmann et al., “Hydrogen: A Relevant Shallow Donor in Zinc Oxide,” *Physical Review Letters*, vol. 88, no. 4, Jan. 2002.

[405] F. Oba, A. Togo, I. Tanaka, J. Paier, and G. Kresse, “Defect energetics in ZnO: A hybrid Hartree-Fock density functional study.”

[406] E. Lavrov, F. Börrnert, and J. Weber, “Photoconductivity and infrared absorption study of hydrogen-related shallow donors in ZnO,” *Physical Review B*, vol. 72, no. 8, Aug. 2005.

[407] B. Li et al., “Defects in ZnO transparent conductors studied by capacitance transients at ZnO/Si interface,” *Applied Physics Letters*, vol. 98, no. 8, p. 082101, Feb. 2011.

[408] E. Likovich, R. Jaramillo, K. Russell, S. Ramanathan, and V. Narayanamurti, “Scanning tunneling microscope investigation of local density of states in Al-doped ZnO thin films,” *Physical Review B*, vol. 83, no. 7, Feb. 2011.

[409] R. Collins and D. Thomas, “Photoconduction and Surface Effects with Zinc Oxide Crystals,” *Physical Review*, vol. 112, no. 2, pp. 388-395, Oct. 1958.

[410] F. Verbakel, S. C. J. Meskers, and R. A. J. Janssen, “Electronic memory effects in diodes from a zinc oxide nanoparticle-polystyrene hybrid material,” *Applied Physics Letters*, vol. 89, no. 10, p. 102103, Sep. 2006.

[411] K. S. Leschkies, M. S. Kang, E. S. Aydil, and D. J. Norris, “Influence of Atmospheric Gases on the Electrical Properties of PbSe Quantum-Dot Films,” *The Journal of Physical Chemistry C*, vol. 114, no. 21, pp. 9988-9996, Jun. 2010.

[412] K. S. Leschkies, M. S. Kang, E. S. Aydil, and D. J. Norris, “Influence of Atmospheric Gases on the Electrical Properties of PbSe Quantum-Dot Films,” *The Journal of Physical Chemistry C*, vol. 114, no. 21, pp. 9988-9996, Jun. 2010.

[413] L. Vayssieres, “Growth of Arrayed Nanorods and Nanowires of ZnO from Aqueous Solutions,” *Advanced Materials*, vol. 15, no. 5, pp. 464-466, Mar. 2003.

[414] A. Stavrinadis, J. M. Smith, C. A. Cattley, A. G. Cook, P. S. Grant, and A. A. R. Watt, “SnS/PbS nanocrystal heterojunction photovoltaics.,” *Nanotechnology*, vol. 21, no. 18, p. 185202, May 2010.

[415] J. Tang et al., “Schottky quantum dot solar cells stable in air under solar illumination.,” *Advanced materials (Deerfield Beach, Fla.)*, vol. 22, no. 12, pp. 1398-402, Mar. 2010.

[416] M. Sykora et al., “Effect of air exposure on surface properties, electronic structure, and carrier relaxation in PbSe nanocrystals.,” *ACS nano*, vol. 4, no. 4, pp. 2021-34, Apr. 2010.

[417] S. W. Buckner, R. L. Konold, and P. A. Jelliss, “Luminescence quenching in PbS nanoparticles,” *Chemical Physics Letters*, vol. 394, no. 4-6, pp. 400-404, Aug. 2004.

[418] G. SOMORJAI, “Charge transfer controlled surface interactions between oxygen and CdSe films,” *Journal of Physics and Chemistry of Solids*, vol. 24, no. 2, pp. 175-186, Feb. 1963.

[419] B. Sun, A. T. Findikoglu, M. Sykora, D. J. Werder, and V. I. Klimov, “Hybrid photovoltaics based on semiconductor nanocrystals and amorphous silicon.,” *Nano letters*, vol. 9, no. 3, pp. 1235-41, Mar. 2009.

[420] K. W. Johnston et al., “Schottky-quantum dot photovoltaics for efficient infrared power conversion,” *Applied Physics Letters*, vol. 92, no. 15, p. 151115, Apr. 2008.

[421] G. Konstantatos et al., “Ultrasensitive solution-cast quantum dot photodetectors.,” *Nature*, vol. 442, no. 7099, pp. 180-183, 2006.

[422] G. Konstantatos, J. Clifford, L. Levina, and E. H. Sargent, “Sensitive solution-processed visible-wavelength photodetectors,” *Nature Photonics*, vol. 1, no. 9, pp. 531-534, Sep. 2007.